2mif
p

R-746

SIRU DEVELOPMENT - FINAL REPORT
VOLUME I
SYSTEM DEVELOPMENT

by

J.P. Gilmore
R.J. Cooper

July 1973

(NASA-CR-136033) SIRU DEVELOPMENT. N74-10616
VOLUME 1: SYSTEM DEVELOPMENT Final
Report (Massachusetts Inst. of Tech.)
~~[illegible]~~ p HC $13.75 CSCL 17G Unclas
231 G3/21 15585

The Charles Stark Draper Laboratory, Inc.
Cambridge, Massachusetts 02139

R-746

SIRU DEVELOPMENT - FINAL REPORT
VOLUME I
SYSTEM DEVELOPMENT

by

J. P. Gilmore
R. J. Cooper

July 1973

CHARLES STARK DRAPER LABORATORY, INC.
CAMBRIDGE, MASSACHUSETTS

Approved: J P Gilmore
J. P. GILMORE

Approved: N E Sears
N. E. SEARS

Approved: N Sears for D Hoag
D. G. HOAG

ACKNOWLEDGEMENT

This report was prepared under our Project No. 55-32600, sponsored by the Lyndon B. Johnson Space Center of the National Aeronautics and Space Administration through Contract No. NAS9-8242.

The successful development of the SIRU system to its present state of hardware, software and analytical maturity results from the dedicated efforts of many from the NASA L. B. Johnson Space Center and the C. S. Draper Laboratory, Inc.

The technical and historical material presented in this volume of the SIRU Development Final Report was to a large extent contributed by the people who performed the original design and evaluation tasks. The major contribution by the authors has been in the collection, composition, direction and editing control of assembled material.

Special mention is due to the following for major contributions pertaining to their area of interest

Julius Feldman
Richard McKern
David Brown
John Oehrle
Richard Blaha
David Fairbanks

David Swanson
Siegbert Katz
Arthur Boyce
Howard Musoff
Martin Landey
Thomas Shuck

and to Robert Booth whose knowledge and assistance in preparation of this report has been invaluable.

The work performed by Stephen Helfant with Linda Willy and Angela Desmond in editing and preparing the document for publication deserves special recognition. To the Apollo Publications Group with special mention to Ellen Hurley goes our sincere appreciation.

The publication of this report does not constitute approval by the National Aeronautics and Space Administration of the findings or the conclusions contained herein. It is published only for the exchange and stimulation of ideas.

R-746

SIRU DEVELOPMENT FINAL REPORT

ABSTRACT

This report presents a complete description of the development and initial evaluation of the Strapdown Inertial Reference Unit (SIRU) system sponsored by the NASA Johnson Space Center under Contract NAS9-8242.

The SIRU configuration is a modular inertial subsystem with hardware and software features that achieve fault tolerant operational capabilities. The SIRU redundant hardware design is formulated about a six gyro and six accelerometer instrument module package. The modules are mounted in this package so that their measurement input axes form a unique symmetrical pattern that corresponds to the array of perpendiculars to the faces of a regular dodecahedron. This six axes array provides redundant independent sensing and the symmetry enables the formulation of an optimal software redundant data processing structure with self-contained fault detection and isolation (FDI) capabilities.

This report consists of four volumes.

Volume I, System Development, documents the system mechanization with the analytic formulation of the FDI and processing structure; the hardware redundancy design and the individual modularity features; the computational structure and facilities; and the initial subsystem evaluation results.

Volume II, Gyro Module, is devoted specifically to the Gyro Module, the inertial instrument and its digital strapdown torque-to-balance loop, the mechanical, thermal, and electronic design and function, test procedures and test equipment and performance results and analysis.

Volume III, Software, documents the basic SIRU software coding system used in the DDP-516 computer. The documentation covers the instrument compensation software, reorganizational and FDI processing, and the inertial attitude and velocity algorithm routines as well as servicing, input/output, etc. software.

Volume IV, Accelerometer Module, is devoted specifically to the Accelerometer Module, the inertial instrument and its digital strapdown torque-to-balance loop, the mechanical, thermal and electronic design and function and performance results and analysis, as it differs from the Gyro Module.

In addition to this report, SIRU Utilization Report R-747, has been issued documenting analyses, software and evaluation activities in the application of advanced statistical FDI algorithms, calibration and alignment techniques to the SIRU system.

April 1973

Table of Contents

Table of Contents (Cont)

Table of Contents (Cont)

List of Illustrations

List of Illustrations (Cont)

List of Illustrations (Cont)

List of Illustrations (Cont)

List of Illustrations (Cont)

PRECEDING PAGE BLANK NOT FILMED

Dictionary of Terms

AC	Alternating Current
AD	Acceleration-Dependent
A/D	Analogue to Digital
ADIA	Acceleration-Dependent Gyro Drift Due to Acceleration Along the Input Axis
ADOA	Acceleration-Dependent Gyro Drift Due to Acceleration Along the Output Axis
ADSRA	Acceleration-Dependent Gyro Drift Due to Acceleration Along the Spin Reference Axis
BD	Bias Drift
BeO	Beryllium Oxide
BITE	Built-in Test Equipment
CRT	Cathode Ray Tube
CSDL	Charles Stark Draper Laboratory, Inc.
DC	Direct Current
DCA	Digital Computational Assembly
DOS	Disc Operating System
ERC	Electronic Research Center
EA	Electronics Assembly
FDICR	Failure Detection, Isolation, Classification and Recompensation
FDI	Failure Detection and Isolation
FO-FO-FS	Fail Operational-Fail Operational-Fail Safe
GNC	Guidance, Navigation and Control
GSE	Ground Support Equipment
H	Angular Momentum about the Spin Axis
HX	Heat Exchanger
IA	Input Axis
IC	Inertial Components
ICB	Interconnect Box
ID	Independent Drift
INT	Interrogate Pulse
I/O	Input/Output

Dictionary of Terms (Cont)

IRIG	Inertial Reference Integrating Gyro
ISS	Inertial Subsystem
K	Compliance
+LDFF	Positive Level Detect Flip-Flop
LEB	Lower Equipment Bay
LOS	Line of Sight
MAC	Machine Aided Compiler
MIT	Massachusetts Institute of Technology
MSC	Manned Space Center (now L. B. Johnson Space Center)
MSI	Medium Scale Integration
MTBF	Mean-Time-Between Failures
NASA	National Aeronautics and Space Administration
NAV	Navigation
NBD	Normal Bias Drift
OA	Output Axis
PGNC	Primary Guidance Navigation and Control
PIP	Pulsed Integrating Pendulum
PIPA	Pulsed Integrating Pendulous Accelerometer
PIRIG	Pulsed Inertial Reference Integrating Gyro
PMT	Permanent Magnet Torquer
PPM	Part Per Million
PPS	Pulses Per Second
PTE	Pulse Torque Electronics
PTTB	Pulse Torque-to-Balance
PVR	Precision Voltage Reference
RIP	Redundant Instrument Package
SA	Spin Axis
S/C	Spacecraft
SDF	Single Degree-of-Freedom
SF	Scale Factor
SG	Signal Generator
SIRU	Strapdown Inertial Reference Unit
S/N	Signal-to-Noise
SPC	Single Position Calibration

Dictionary of Terms (Cont)

SPOT	Strapdown System Performance Optimization Test Evaluations
SRA	Spin Reference Axis
TG	Torque Generator
TIM	Thermal Interface Material
TJB	Table Junction Box
TMSFF	Torque Motor Set Flip-Flop
TP	Test Point
TSE	Total Squared Error
TSRFF	Torque Switch Reset Flip-Flop
W_{IA}	Angular Rate about the Input Axis

1.0 Introduction

This SIRU Development Final Report is the first of two SIRU system final reports. The second, SIRU Utilization Report R-747, is summarized briefly in this introductory section.

The SIRU Development Final Report provides an overview of the SIRU project, including historical background, design concept, hardware mechanization, software, test equipment, reliability and initial test results. In general, it describes the activities and achievements accomplished during the period from May, 1968 through November, 1971. At that time a complete operational system had been functional for five months and both hardware and software had been debugged and consistent system operation demonstrated. The report is presented in four volumes as follows:

Volume I - System Development
Volume II - Gyro Modules
Volume III - Software Documentation
Volume IV - Accelerometer Module (CONFIDENTIAL)

Volume I contains a complete description of the SIRU system concentrating on the system hardware but covering in adequate detail system mechanization, computational software and facilities, test facilities, test results and a reliability appraisal. Program milestones and conclusions and recommendations are also included.

Volume II presents in greater detail the design, operation and test results applicable to the gyro modules and Volume IV provides the same information applicable to the accelerometer modules. Volume III provides a documentation of the base-line system software including assembly listings and flowcharts.

The SIRU Utilization Report presents the results of the additional analysis, software development and testing activities provided for under Amendment 7S to the basic SIRU contract. The report is presented in three volumes as follows:

Volume I - Theory, Development and Test Evaluations
Volume II - Software Documentation
Volume III - System Log

Volume I contains a complete description of the theory, analysis, implementation and test results for each of the tasks, namely:

1. Statistical Failure Detection Isolation Classification and Recompensation (FDICR)
2. Error Source Propagation Characteristics
3. System Single Position Self-Calibration
4. SIRU Self-Alignment (Gyro Compassing)
5. Local Level Navigator Performance Demonstrations

Volume II provides documentation for the additional or modified software including assembly listings and flowcharts. Volume III contains a log of significant system events from the beginning of the system testing program.

1.1 Background

A major requirement for guidance, navigation, and control systems designed for future spacecraft and aircraft applications is high reliability. As a means for fulfilling this requirement, attention in recent system studies has been focused on the use of redundancy concepts with fault tolerant features to achieve an order of magnitude or better improvement in reliability.

In the Apollo spacecraft, each "primary" system was complemented by a "backup" system which had limited mission-mode capabilities. For future space missions this concept, predicated on a fail-safe return to earth, will not suffice; it fails to provide the necessary reliability and operational capabilities for extended missions. In commercial and military aircraft, duplex or triplex redundancy in guidance, navigation, and control systems has become commonplace. In these applications failure isolation decisions and system reconfiguration selection are for the most part assigned to the human operator. Advanced guidance and navigation systems to meet improved air traffic control requirements undoubtedly will incorporate automatic failure detection and adaptation—especially in critical guidance phases.

Obtaining an optimum redundant guidance and navigation system can be approached in several ways. A basic decision, however, will involve the geometric arrangement of the inertial sensors. The choice is between instrument redundancy along common orthogonal axes and a non-orthogonal array of instruments; in either case the objective is to provide a comprehensive array of measurement data. In both approaches the mechanization should be free from single point failure possibilities, and provide a self-contained failure detection, isolation and processing reorganization capability. The operation of the failure detection and isolation technique must achieve time critical system reliability by eliminating faulty data from instruments or their electronics before the faulty measurements data affects successful mission performance, and the remaining data and processing structure, after reorganization, must have satisfactory mission performance capabilities.

1.2 Historical Background

On May 7, 1968 the Charles Stark Draper Laboratory[*] at the Massachusetts Institute of Technology submitted a Technical Proposal, in response to NASA RFP #BG 731-47-8-533P, to the Manned Spacecraft Center of the National Aeronautics and Space Administration for the design, analysis and development of a redundant Strapdown Inertial Reference Unit (SIRU). This unit was intended to replace corresponding assemblies in the Primary Guidance Navigation and Control System (PGNC) which the laboratory had designed and developed for the Apollo program.

This contractual activity marked the culmination of a research and development effort to determine and define the fundamental aspects of redundant strapdown inertial guidance, navigation and control systems. The redundancy concept was based on a dodecahedron configuration for the inertial instruments that had been proposed and delineated in an MIT masters thesis published in 1967.[**] During the next two years under NASA sponsorship (contract NAS 9-6823) a base of supporting strapdown technology was created including an inertial grade high torque gyroscope, improved torque-to-balance servo techniques and higher order computational algorithms.

As stated in the May 1968 Technical Proposal, the purpose of the SIRU effort was "to design, assemble, and test an inertial reference unit suited to the operational reliability requirements of long-term manned space flights. Redundant, structure mounted inertial components (strapdown) should be used to provide high reliability and freedom from operational constraints (e.g., gimbal lock)".

The SIRU was to be configured to interface with the spacecraft planned for the Apollo Application Program (since modified and renamed Skylab). Specifically,

---

[*] The former Instrumentation Laboratory of the Department of Aeronautics and Astronautics at M.I.T.

[**] "A Non-Orthogonal Gyro Configuration", Jerold P. Gilmore, T-472, Instrumentation Laboratory, MIT, January, 1967.

the SIRU would replace the Apollo PGNC system Inertial Measurement Unit, the Coupling Display Unit, and the inertial section of the Power and Servo Assembly. The new assemblies would interface with the Apollo Guidance Computer and then the spacecraft to achieve fully redundant guidance, navigation, and control.

Work under Contract NAS 9-8242 commenced June 27, 1968. The Statement of Work specified that the contract's purpose was to develop and deliver one SIRU, whose production version would "meet the reliability requirement for long-term manned space flights." The reliability requirement was defined as "the capability to perform a 120-day mission with a .999 mission success probability and a one-half hour reentry phase at the end of 120 days with a .9999 mission success probability."

The SIRU was to consist of an Inertial Component Sensor Assembly with the associated electronics and power supplies necessary to meet the interface requirements. A Digital Computational Assembly package to verify the operational capability of the modified Guidance, Navigation and Control system was also prescribed. As a design goal, the complete package (including associated hardware and harnesses) was to weigh less than 80 lbs with a power requirement of less than 250 watts.

1.3 Development Summary

The SIRU system consists of a Redundant Instrument Package (RIP) and an Electronics Assembly (EA). The geometric redundancy concept is mechanized in the Redundant Instrument Package, which contains six single degree-of-freedom gyroscope modules and six linear accelerometer modules. Geometric redundancy is achieved by using a non-orthogonal mounting configuration in which the instrument input axes (IAs) are oriented to correspond to the array of normals to the faces of a dodecahedron, Fig. 1.3.1. This arrangement yields a unique symmetry in which all instrument input axes are at a spherical angle (63.4°) from each other.

In the particular implementation used, pairs of gyro or accelerometer axes lie in the orthogonal planes of a reference triad and are displaced about the principle triad axes by an angle. This symmetry yields optimal redundant reorganizational data processing with minimum error propagation. Moreover, by means of instrument output comparisons, self-contained failure isolation of up to two out of six of both instrument types is achieved and a third failure of each may be detected. With the aid of additional diagnostics, the processing structure still allows continued operation after three failures on both of the six gyro and six accelerometer measurement axes.

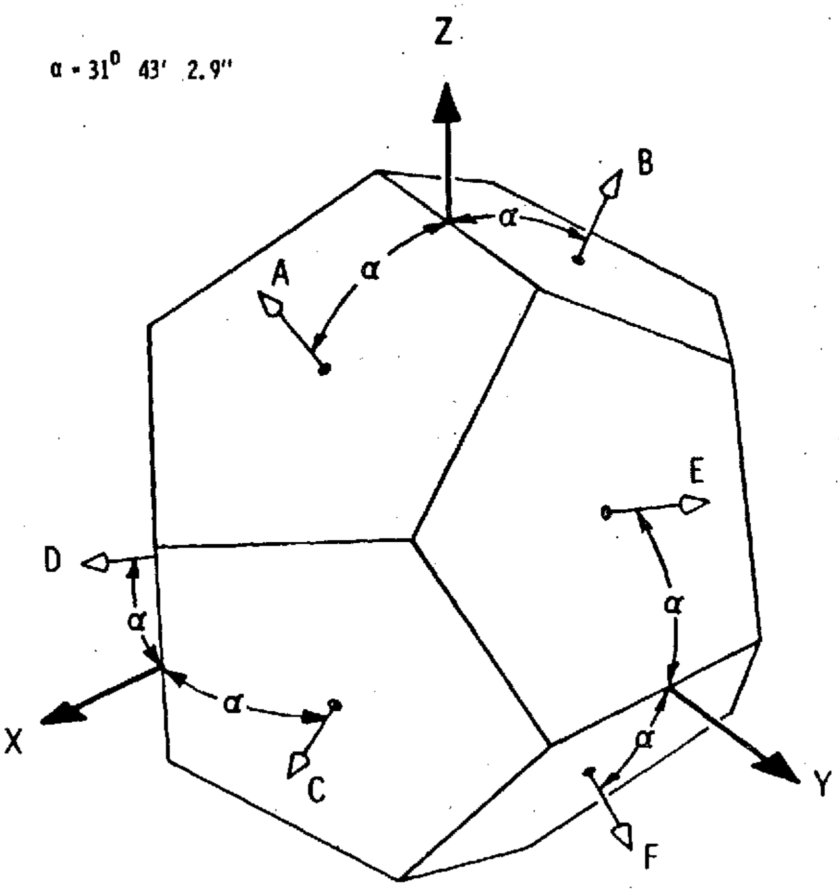

Fig. 1.3.1 Instrument Input Axes Orientation Relative to The Instrument Frame Triad and the Dodecahedron

The RIP is an assembly of gyro and accelerometer modules in which each module is a prealigned and normalized assembly. The modules are interchangeable and include the instrument and its pulse torque-to-balance control electronics, temperature controller, etc. The gyro module is scaled to be compatible with a 1 rad/sec input and the accelerometer module is compatible with an Apollo 19 g's capability. Redundant concepts are also applied in the supporting EA (power supplies, clock and scalers, etc.). The levels of redundancy used in the EA are based upon the relative reliability of functional circuits and circuit isolation concepts. For example, to maintain the inherent reliability of the instrument configuration such features as triple clock voting, dual scaler channels and six functional power supplies are employed.

With respect to reliability, insight into the relative merit of different sensor geometric configurations is provided by a normalized reliability comparision. The variation of probability of mission success with normalized time for several sensor arrangements is illustrated in Fig. 1.3.2. Time (t) is normalized by the mean-time-between-failures (MTBF) of a sensor axis, i.e., the instrument and its functionalized electronics. In the illustration, all system sensor axes are assumed to have the same MTBF. For reference, a reliability curve is shown for a conventional orthogonal triad package of three sensor axes. The other curves correspond to systems with self-contained failure isolation features, i.e., three triads (where mission success is attained by majority agreement); a single triad with three instruments on each axis (with majority agreement per axis); and the dodecahedron array (which allows the failure of any two axes). Note that a marked reliability advantage for the SIRU configuration is clearly observable. Further, if external failure isolation is assumed so that operation continues until all three triad systems fail or a fourth SIRU axis fails, SIRU reliability is 0.999 compared to 0.98 for a normalized time (t/T) of 0.1. It is important to note that redundancy alone does not supply a complete solution to the problem of system reliability. Each element in the system must be selected and conservatively applied in a manner that is consistent with the environment and the mission duration; there is no substitute for quality engineering. Similarly, an element's statistical MTBF of one million hours does not preclude its failure, on a random or defect basis. Thus, the system must be configured to avoid total failure resulting from the failure of a single element.

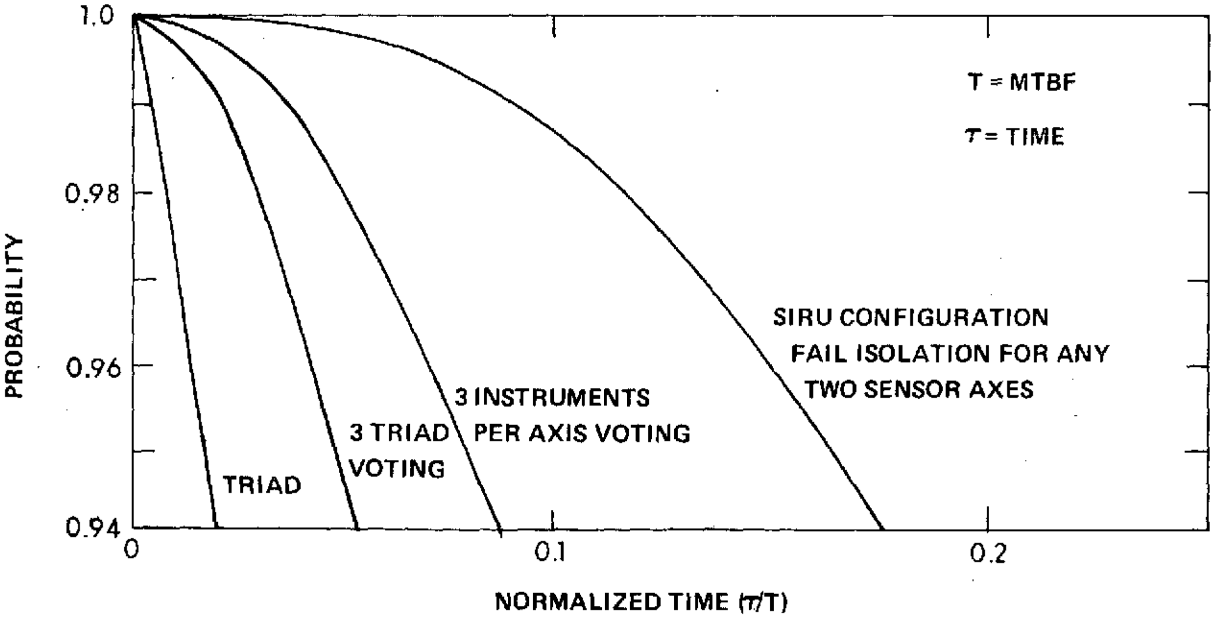

Fig. 1.3.2 Mission Success Probability

A Digital Computational Assembly (DCA) design was formulated concurrently with the development of the inertial sensor and electronics packages. A representative engineering design was developed to fulfill the processing and strapdown algorithm system requirements and a breadboard unit built. The DCA design concept was based on a general purpose computer with duplex processors, memories and I/O sequencers. It was configured to achieve the system high reliability requirements and it incorporated multiple error checking, single instruction restart capabilities, micro-programmed sequence generation, and the use of a serial time multiplexed input/output. The fabrication of a prototype DCA was not undertaken in this program due to cost considerations. A report describing the work performed and results achieved under the DCA task has been published as MIT Engineering Report E-2590, December, 1970.

A general purpose computation and control facility was developed and expanded to support system RIP and EA testing, data reduction and analysis as well as operational software development and evaluation. This facility was also used for the development and coding of DCA software. It was developed around a general purpose commercial mini-computer, the Honeywell DDP-516, which is software compatible with the Honeywell 601 airborne computer. The DDP-516 is a representative state-of-the-art general purpose machine, employing a 16-bit word with a memory cycle time of 0.96 microseconds, a high-speed arithmetic package and 16,384 words of core memory. The peripherals used include: two disc drives; a teletype unit, a CRT display; a high-speed paper tape reader and an incremental magnetic tape unit.

Ground support equipment (GSE) consisting of a GSE console with power supplies and monitoring and control capabilities, an Interconnect Box and Table Junction Box for table interconnections across the test table slip rings, a RIP test box and an auxiliary monitor console for signal monitoring and test table control functions were assembled and combined with the other system hardware.

The computer was interfaced with the SIRU outputs and the test table encoder and is operated with the system on-line and in real-time. The following specific software has been developed and debugged and are routinely operating with the SIRU system.

1. Interface software to operate in real-time with the SIRU outputs and to display and record the desired computational algorithm outputs.
2. Strapdown attitude and velocity algorithms compatible with general purpose computer structure and speed.

3. Static and dynamic instrument error model (e.g., BD, ADIA, etc., SF and OA coupling, etc.) compensation routines that are also compatible with failure conditions, (e.g., gyro compensation independent of accelerometer failure status, etc.).
4. An adaptive instrument data processing structure using least-squares triad body rate and accelerometer estimation with restructuring based on instrument failure status i.e., by reducing the number of dodecahedron measurement axes that are processed (six, five, four or three axes) to reflect the current failure status. A least-squares triad solution is thereby obtained that uses only those measurement axes that are performing to an acceptable standard.
5. A failure detection and isolation (FDI) structure based on the total squared error (TSE) ratio test and parity equations to provide sequential FDI of any two gyro or accelerometer soft* performance failures(equivalent to approximately ten times the nominal uncertainties). Isolation ambiguities are limited to two certain simultaneous failures of the same measurement type that have equivalent failure levels in one FDI test period. FDI is effected prior to every algorithm interaction cycle. Thus if a hard failure (catastrophic in nature, e.g., full on output) or a soft failure (error characteristics several orders of magnitude above the FDI threshold levels) occurs, it is possible to detect and isolate it prior to a single iteration period (10 ms at 100/sec) with no error propagation in the attitude or velocity algorithm outputs. In both cases soft and hard failure detection of a third failure is achieved.
6. System static and dynamic instrument calibration programs that acquire and process raw data in the calibration test sequence and generate printouts in engineering units as well as calibration loads in machine language for the real-time compensation routines.
7. Programs to provide algorithm output recording and test programs for performance and simulation testing.
8. A disc operated system with assembler, compiler, and program editor providing self-contained development and debugging of operational and test software suitable for the DCA as well as for the DDP-516.
9. Programs for fine grained analysis of performance test results on the IBM 360.

---

*A soft failure is performance degradation requiring measurement comparisons to detect. A hard failure is defined as one which is generally catastrophic in nature, probably could be detected and isolated by Hardware Self Test (BITE) techniques, and tends to be gross in nature.

In summary, the SIRU program accomplished the following major achievements.

1. Implemented in hardware a redundant strapdown inertial system based on the dodecahedron symmetry, incorporating effective FDI and efficient automatic redundancy management.
2. Designed, fabricated and assembled a modularized, redundant instrument package consisting of six normalized gyro and accelerometer modules supported by an EA possessing interchangeable functional modularity consisting of six axes power supplies, dual power bus and triple clock redundancy to eliminate single point failure sources. Feasibility of interchangeable modularity was successfully demonstrated.
3. Developed and demonstrated software to provide redundancy management and strapdown processing including automatic fault detection and isolation, static and dynamic instrument compensation, attitude and velocity algorithms, self alignment and calibration and real-time data acquisition and analysis.
4. Demonstrated a full-up and continuously operating system reliability record covering a period in excess of 20,000 hours since July, 1970.
5. Demonstrated over this period operational capabilities and performance consistent with and exceeding the requirements for the "fail operational/ fail safe" concepts now specified for the Space Shuttle even though its intended application was for the earlier Apollo Applications (Skylab) mission.

2.0 System Mechanization

This section describes in detail the mechanization of the strapdown redundant system including normal processing and failure detection and isolation (FDI) techniques. Software requirements including compensation programs are defined. Analyses of error propagation and resulting performance forecasts are presented. The first half of the section deals with all these elements as they apply to the geometric redundancy and the second half shows the extension of the concept to the electronics design.

2.1 Computational Functional Flow

2.1.1 Redundant Instrument Processing

The measurement data, derived from the gyros and accelerometers whose input axes are colinear with the dodecahedron vectors A through F in Fig. 1.3.1 in Chapter 1, must be related to a reference triad, XYZ. For a gyro set, the orientation yields a relationship between the angular rate inputs (W) about the triad axes and the gyro measurements (m) that may be expressed in matrix form in terms of the geometry as:

$$\underline{m} = \underline{H}\underline{b} \tag{2.1}$$

where

$$\underline{b}^T = [W_X W_Y W_Z]$$

$$\underline{m}^T = [m_a \; m_b \; m_c \; m_d \; m_e \; m_f]$$

$$\underline{H}^T = \begin{bmatrix} s & -s & c & c & o & o \\ o & o & s & -s & c & c \\ c & c & o & o & s & -s \end{bmatrix}$$

$$c = \cos\left(\frac{5+\sqrt{5}}{10}\right)^{1/2} \cong 0.851$$

$$s = \sin\left(\frac{5+\sqrt{5}}{10}\right)^{1/2} \cong 0.526$$

These relationships reflect the dodecahedron configuration shown in Fig. 1.3.1. In the specific mechanization adopted for SIRU the Y axis is reversed compared to the dodecahedron which introduces sign changes in the equations. For the SIRU configuration the corresponding matrix H^T is given by:

$$H^T = \begin{bmatrix} s & -s & -c & -c & o & o \\ o & o & -s & s & c & -c \\ c & c & o & o & s & s \end{bmatrix}$$

All the following equations in this volume are representative of this specific SIRU configuration. As seen from the equation, each instrument provides a measure of redundant data, e.g., instruments A, B, C, and D sense a component of input along the X triad axis. By algebraic solution of the equations, equivalent triad axis rate or acceleration solutions can be obtained from any three gyros or accelerometers. Subsequent discussion illustrates that it is possible to isolate up to two failures of either type instrument and to detect a third failure through self-contained instrument output comparisons.

The processing structure used to obtain equivalent triad solutions from the dodecahedron array corresponds to a weighted least-squares solution form:

$$\underline{\hat{b}} = (\underline{H}^T \underline{\psi}^{-1} \underline{H})^{-1} \underline{H}^T \psi^{-1} \underline{m} \tag{2.2}$$

where $\hat{b}$ is defined as the "best" triad solution estimate and ψ^{-1} corresponds to a diagonal 6×6 matrix whose terms represent the individual instrument variances. This solution provides a best estimate where both the geometric properties of the configuration and the individual instrument performance statistics are considered. For the dodecahedron array the computational implementation allows the selection of the appropriate triad solution in accordance with the operational status of the instruments in that ψ can be modified to reflect either degraded or failed instrument performance. However, for efficient computational usage and time-critical decision and error propagation minimization, only a "go-no go" criterion has been implemented (a study to determine the feasibility of generating continuously a weighted least-squares estimate in an adaptive fashion has been conducted). Thus, processing reorganization is achieved by replacement of ψ^{-1} by a status matrix, λ, in which all diagonal elements are unity when all instruments perform satisfactorily*. By setting the appropriate elements to zero when failures are detected, a least-squares triad solution can be defined for any combination of instruments (i.e., 5, 4, and 3 gyro or accelerometer combinations). (The actual processing matrices appropriate

---

* An additional contract task documented in Report R-747 covered the implementation of a statistical approach which, when combined with the current λ implementation, provides higher resolution FDI using a recursive statistical algorithm which also classifies the fault (mean or variance change) and if the fault corresponds to a stable mean performance change, recompensates it.

for each combination of gyros or accelerometers are presented in Appendix A). In the computer mechanization, this approach is implemented by storage of common parametric elements that may be assembled to form the appropriate least-squares solution based on the status of the instruments, λ. This structure is regenerative in that, if instrument "healing" is observed in the failure isolation process, the instrument may be reinstated. Thus, the failure isolation criteria enables adaptive data processing.

As noted previously, the self-contained FDI to be discussed in subsequent paragraphs illustrates that the dodecahedron symmetry enables isolation (determination of the faulty measurement axes, λ_i, λ_j) and thereby automatic processing reconfiguration for up to two of either type of instrument axes failures through self-contained output comparisons. In addition, dependent upon the order and magnitude of failures in a sequence of failures, self-contained isolation of a third failure is also achieved. Under all circumstances self-contained detection of a third failure of the same type measurement axis is provided. External monitors may also be used to provide additional λ status data to allow continued operation after as many as three gyro or accelerometer axes failures.

The advantage of the dodecahedron self-detection and isolation capabilities is clearly illustrated when one considers that a system employing duplex instrument redundancy on orthogonal axes experiences total failure with two gyro or two accelerometer failures on the same axis, and self-contained isolation of performance degradation between two instruments on the same axis is not possible. Even with three independent triads, only one fault can be isolated when axis-by-axis voting is precluded (as when the triad orientations are not precisely aligned with respect to each other or if a fault occurs in a triad system that causes multiple failures in that subsystem). Using triple component orthogonal redundancy in a single system with failure isolation by instrument "voting" between the three instrument signals on the same axis provides limited capability. A second failure on the same axis cannot be isolated. The SIRU skewed configuration yields the most efficient redundant use of six single-degree-of-freedom measurement axes for failure isolation and reliability improvement.

In principle, any six-instrument, skewed configuration possesses similar redundant measurement and failure isolation capabilities. The advantage of the dodecahedron array results from its unique symmetry, whereby the six measurement axes are spherically distributed with equal angles between all axes. This feature minimizes geometric error amplification, simplifies failure isolation and optimizes the response characteristics to provide equalized performance at all attitudes.

Independent studies by Weinstein[*], have demonstrated that equivalent performance is not attainable with triads that are rotated with respect to each other to obtain a six axes measurement array.

The relative performance of the SIRU configuration under various failure conditions may be identified clearly by comparing the SIRU reference triad solution statistics to the corresponding statistics for an operational three axis system. In each case, all instrument axes are assumed to have identical and independent measurement error characteristics. The statistical performance characteristics of the failure-free, three axis system are defined as having a standard measurement deviation of σ along any axis and a total three-dimensional rss measurement deviation of $(3)^{1/2}\sigma$. In comparison, when all six axes of SIRU are operational, the error statistics of its triad solution provide an axis standard measurement deviation of 0.707σ and an rss system deviation of $(1.5)^{1/2}\sigma$. Similarly, deviations for the SIRU triad solutions for the various five, four, and three instrument combinations may also be compared to the basic triad's statistics. These combinations represent SIRU performance, with failed instruments detected and isolated, i.e., the failed axes no longer being used in the triad solution processing.

In general, the error propagation of a non-orthogonal array with instruments deleted is such that its triad solution performance statistics reflect both the reduction in measurement data and the deterioration in geometry. Thus, dependent on the geometric positions of the deleted (failed) axes, the solution tends to have a maximum standard deviation along a specific axis (worst-case) and certain failure combinations have more pronounced rss error amplification than others. However, as illustrated in Table 2.1.1., SIRU error propagation is bounded and performance is not significantly affected by processing with reduced instruments.

Table 2. 1. 1

SIRU Performance with Instrument Failures
Versus
An Operational Triad System

Instrument Failures	Standard Deviation (Worst-Case Axis Solution)	Ratio of Deviation (SIRU Solution to a 3-axis System)
None	0.707σ	0.707
1 (6 Combinations)	0.927σ	0.816
2 (15 Combinations)	1.349σ	1.000
3A (10 Combinations)	1.349σ	1.176
3B (10 Combinations)	2.890σ	1.902

---

[*] Weinstein, Warren D., Optimum Skew Angle Between Redundant Inertial Systems, Grumman Aerospace Corporation, Bethpage, L. I., N. Y.

The first column of Table 2.1.1 corresponds to the SIRU processing status, i.e., operation with all instruments, down to combinations of failures on three instrument axes. For each of these states, the table shows the SIRU worst-case single axis triad solution standard deviation and the ratio of the SIRU solution rss deviation to an equivalent triad system rss deviation. Note that SIRU performance with one failure is statistically better than an unfailed triad system and for all two-failure and ten three-failure combinations performance is essentially identical to an unfailed triad. For the remaining worst three-failure combinations, the maximum single axis solution standard deviation in comparison to a good triad axis standard deviation degrades by a factor of three while the corresponding total rss performance degrades by only a factor of two.

2.1.2 Failure Isolation

The self-contained failure isolation algorithm is based upon a simple comparison of measurement outputs. The unique symmetrical properties of the array allow one to implement two different but correlated FDI algorithms. One algorithm is based on the development of a series of "parity equations" and the other on a set of equations derived from the conical representation of the dodecahedron. Both algorithms are directly related; for example, the conical equation representation for the two-failure case is identical to the parity equations. The parity equations consist of a series of 15 equations, each equation representing a comparison of four measurements. All the equations will have a zero output (ϵ) if all instruments are operating properly. The derivations of these equations are presented in MIT/IL Report T-472, A Non-Orthogonal Gyro Configuration by J. Gilmore, January, 1967. Table 2.1.2 lists the 15 equations. Each m term in the equations corresponds to an accumulated θ count or velocity over some comparison interval. If, however, an instrument along A has malfunctioned, Eqs. 2.1 through 2.10 will show a non-zero total, while Eqs. 2.11 through 2.15 equate to zero, thereby isolating the failure. If a second instrument failure occurs, inspection of the remaining equations (2.11 through 2.15) allows another level of failure isolation. If a third failure occurs and none of the equations show a zero total, the failure is detected but not isolated.

The conical technique was originally synthesized in the computational software, but parity equations were subsequently used for the third-fail detect function and in the statistical FDI algorithms described in the SIRU Utilization Report Volume II, R-747. The conical technique is displayed in Fig. 2.1.1. Note that each of the five vectors (B, C, D, E, F) is symmetrically displaced in a conical array about the central vector A. This relationship is identical for all orientations because of the symmetry of the dodecahedron array.

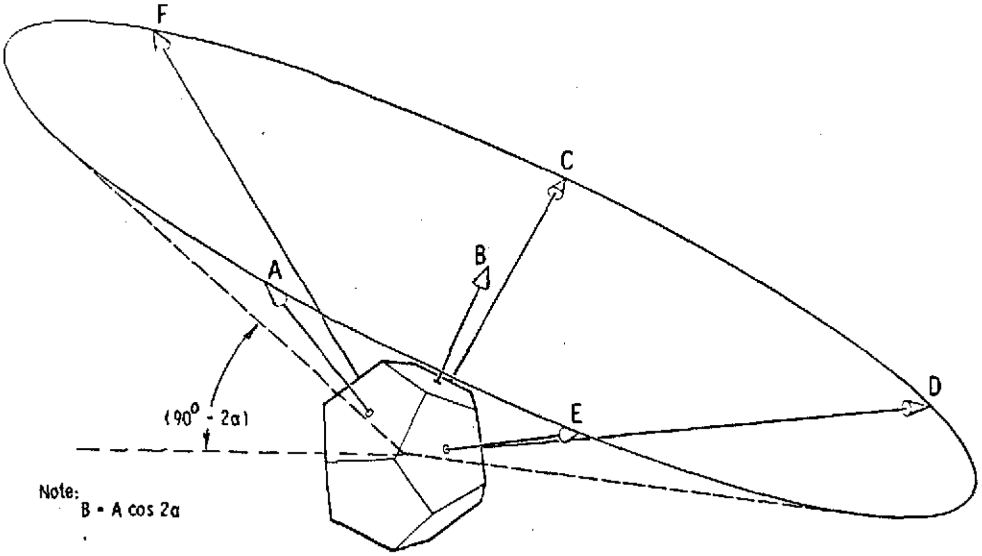

Note:
$B = A \cos 2\alpha$
.
.
.
$F = A \cos 2\alpha$

Or

$\hat{A} = \frac{(B + \ldots + F)}{5 \cos 2\alpha}$

$E_A = A - \hat{A}$

$\tan 2\alpha = 2$
$\cos 2\alpha = \frac{1}{\sqrt{5}}$

Fig. 2.1.1 Conical Representation of Dodecahedron Normals

Table 2.1.2 SIRU Parity Equations

No.	Instruments	
1	ABCD	$(m_a - m_b) c + (m_c + m_d) s = \|\epsilon\|$
2	ABCE	$(m_b - m_c) c - (m_a + m_e) s = \|\epsilon\|$
3	ABCF	$-(m_a + m_c) c + (m_b + m_f) s = \|\epsilon\|$
4	ABDE	$-(m_a + m_d) c + (m_b + m_e) s = \|\epsilon\|$
5	ABDF	$(m_b - m_d) c - (m_a + m_f) s = \|\epsilon\|$
6	ABEF	$(m_e + m_f) c - (m_a + m_b) s = \|\epsilon\|$
7	ACDE	$(m_d - m_e) c + (m_a - m_c) s = \|\epsilon\|$
8	ACDF	$(m_c - m_f) c + (m_a - m_d) s = \|\epsilon\|$
9	ACEF	$(m_a - m_f) c + (m_c - m_e) s = \|\epsilon\|$
10	ADEF	$(m_a - m_e) c + (m_d - m_f) s = \|\epsilon\|$
11	BCDE	$(m_c + m_e) c - (m_b + m_d) s = \|\epsilon\|$
12	BCDF	$-(m_d + m_f) c + (m_b + m_c) s = \|\epsilon\|$
13	BCEF	$(m_b - m_e) c - (m_c + m_f) s = \|\epsilon\|$
14	BDEF	$(m_b - m_f) c - (m_d + m_e) s = \|\epsilon\|$
15	CDEF	$(m_c - m_d) c + (m_e - m_f) s = \|\epsilon\|$

Note: m_a = measurement of axis A accelerometer or gyro
c = cos (α)
s = sin (α)
ϵ = Threshold Level

Using spherical representation one can directly derive the relationship between each vector and the central vector A:

$$\begin{aligned} m_b &= m_a \cos 2\alpha \\ &\vdots \\ m_f &= m_a \cos 2\alpha \end{aligned} \tag{2.3}$$

where:

$$\cos 2\alpha = \sqrt{.2}$$

When all six instruments are assumed to be operating, six equations, Eq. 2.4, are obtained by considering each vector A, B . . . , F and the corresponding conical array of the other five vectors that surround it:

$$\begin{aligned} \hat{E}_a &= \left[m_a - \sqrt{0.2}\,(m_b - m_c - m_d + m_e + m_f)\right] \\ \hat{E}_b &= \left[m_b - \sqrt{0.2}\,(m_a + m_c + m_d + m_e + m_f)\right] \\ \hat{E}_c &= \left[m_c - \sqrt{0.2}\,(-m_a + m_b + m_d - m_e + m_f)\right] \\ \hat{E}_d &= \left[m_d - \sqrt{0.2}\,(-m_a + m_b + m_c + m_e - m_f)\right] \\ \hat{E}_e &= \left[m_e - \sqrt{0.2}\,(m_a + m_b - m_c + m_d - m_f)\right] \\ \hat{E}_f &= \left[m_f - \sqrt{0.2}\,(m_a + m_b + m_c - m_d - m_e)\right] \end{aligned} \tag{2.4}$$

For each case the individual equations, Eq. 2.3 above, are then combined. For example $\hat{E}_a$ in Eq. 2.4, corresponding to the A vector, is derived by determining $\hat{A}$ from Eq. 2.3.

$$\hat{A} = \frac{m_b - m_c - m_d - m_e - m_f}{5 \cos 2\alpha} = \frac{1}{5 \cos 2\alpha} = \sqrt{.2} \tag{2.5}$$

where A is the estimate of what m_a should read based on m_b, m_c . . . , m_f. The estimated error E_a in what A is reading may be derived by simply:

$$\hat{E}_a = m_a - \hat{A} \tag{2.6}$$

For the situation where a failure is already known (second "fail search") the procedure is identical except the known "bad" measurement is not included; scaling may be adjusted accordingly and only five equations used. For processing ease, if A were known to have failed, m_a would be substituted for A in each of the original six equations, Eq. 2.4. Mathematically these same relationships may be obtained by using the best-estimate solution for b in Eq. 2.2. For example, the best-estimate of what the instrument measurements should be:

$$\underline{\hat{m}} = \underline{H}\hat{b} \tag{2.7}$$

$$\underline{\hat{m}}^T = \left[\hat{m}_a \ \hat{m}_b \ldots \hat{m}_f\right]$$

A comparison of the actual measurement (m) with the estimated measurement ($\hat{m}$) yields an estimate of the measurement error for all six instruments (E_o).

$$\underline{\hat{E}}_o = \underline{m} - \underline{\hat{m}} \tag{2.8}$$

where:

$$\hat{E}_o{}^T = \left[\hat{E}_a \ \hat{E}_b \ \hat{E}_c \ \hat{E}_d \ \hat{E}_e \ \hat{E}_f\right]$$

The estimated error in the measurement of the six axes is given by the same equations as those listed in Eq. 2.4, except that they are multiplied by 1/2.

The measurement error variance (TSE_o) of the six instruments is:

$$TSE_o = \hat{E}_o{}^T \hat{E}_o = \hat{E}_a{}^2 + \hat{E}_b{}^2 + \hat{E}_c{}^2 + \hat{E}_d{}^2 + \hat{E}_e{}^2 + \hat{E}_f{}^2 \tag{2.9}$$

If no instrument errors exist, both equations reduce to zero. If an instrument failure occurs, the error propagates through Eqs. 2.8 and 2.9. It is dominant in the faulty instruments' error estimate but is also reflected at reduced magnitude in the other instrument error estimates. If one knew which instrument was at fault and adapted the processing structure, the corresponding five-instrument variance (TSE_j) with the faulty instrument omitted would then equal zero. It can be shown that the relationship between TSE_j, the faulty instrument error E_j, and the TSE_o is:

$$TSE_j = TSE_o - 2(\hat{E}_j)^2 \tag{2.10}$$

Thus (from Eq. 2.10), if a failure exists, the failed instrument's squared error (E_j^2) corresponds to 50% of the total six-instrument variance (TSE_o).

If a prior failure has been detected and isolated, a new equation set must be used to enable a second failure detection and isolation capability. This set must omit the data from the already known bad axis. The new set is obtained by using the same equations for E_a through E_f (Eq. 2.8 as detailed in Eq. 2.4) but replacing the known failed instrument measurement by the calculated estimate for that axis using information derived from the remaining five units. For example, if A had failed previously, m_a would be replaced by an estimate of A given by the remaining five instruments. A (Eq. 2.5) and the error equations become:

$$
\begin{aligned}
\hat{E}_{aa} &= \frac{1}{2}\,\hat{A} - \hat{A} = o \\
\hat{E}_{ab} &= \frac{1}{2}\left[m_b - \sqrt{0.2}\,(\hat{A} + m_c + m_d + m_e + m_f)\right] \\
\hat{E}_{ac} &= \frac{1}{2}\left[m_c - \sqrt{0.2}\,(-\hat{A} + m_b + m_d - m_e + m_f)\right] \\
\hat{E}_{ad} &= \frac{1}{2}\left[m_d - \sqrt{0.2}\,(-\hat{A} + m_d + m_c + m_e + m_f)\right] \\
\hat{E}_{ae} &= \frac{1}{2}\left[m_e - \sqrt{0.2}\,(\hat{A} + m_b - m_c + m_d - m_f)\right] \\
\hat{E}_{af} &= \frac{1}{2}\left[m_f - \sqrt{0.2}\,(\hat{A} + m_b + m_c - m_d - m_e)\right]
\end{aligned}
\qquad (2.11)
$$

The corresponding measurement error variance is:

$$TSE_a = \hat{E}_a{}^T \hat{E}_a = \hat{E}_{ab}{}^2 + \hat{E}_{ac}{}^2 + \hat{E}_{ad}{}^2 + \hat{E}_{ae}{}^2 + \hat{E}_{af}{}^2 \qquad (2.12)$$

The general formulation for the new equation set E_{jk}, derived with the previously failed instrument (j) not used, corresponds to:

$$TSE_{jk} = TSE_j - 2.5\,(\hat{E}_{jk})^2 \qquad (2.13)$$

The $\underline{\lambda}_{jk}$ is a unity matrix except that the λ_{jk} term equals 0.

The corresponding variance TSE_j is:

$$\underline{\hat{E}}_{jk} = \underline{m} - \underline{m}_j$$

where:

$$\underline{\hat{m}}_j = \underline{H}\underline{\hat{b}}_j \text{ and } \underline{\hat{b}}_j = (\underline{H}^T \underline{\lambda}_{jk} \underline{H})^{-1}\, \underline{H}^T \underline{\lambda}_{jk} \underline{m}$$

If no second failure exists, TSE_j reduces to zero, i.e., no errors. If a second failure, l, occurs, an error propagates in the instrument error estimate E_{jk}, Eq. 2.13 and TSE_j. The error is dominant in E_{jl} but is also reflected at reduced magnitude in the other instrument estimates. If the originally failed instrument, j, and the new failed instrument, l, are deleted from the processing, a corresponding four-instrument variance TSE_{jk} would be computed and would reduce to zero. It can be shown that the relationship between TSE_{jk}, the faulty instrument error E_{j1} and TSE_j is:

$$TSE_j = \hat{E}^T_{jk} \quad \hat{E}_{jk} \tag{2.14}$$

Thus, from Eq. 2.14, the second failed instrument's squared error E^2_{j1} corresponds to 40% of the 5 instrument variance TSE_j. The computer's failure isolation algorithm implements these concepts in the following manner. First, all six individual errors are computed and Eq. 2.9 is used to calculate TSE_o. The total squared error is compared to an allowable threshold, which may be varied as a function of the mission requirement and the dynamic environment. If the system is operating within the acceptable TSE_o criteria, no further activity is required until the next failure isolation iteration. If the TSE_o threshold is exceeded, the ratio of each individual instrument error, Eq. 2.4, is squared and taken with respect to the TSE_o. If, for example, E^2_a is a significant percentage of TSE_o exceeding a selected magnitude, the failure of instrument A is indicated.

The presence of a second failure is detected when the TSE_j threshold is exceeded. This failure is isolated by taking the ratio of E^2_{jk} to TSE_j and if E_{j1} exceeds a selected magnitude, the failure is isolated to the 1 instrument.

While the theoretical maximum squared error $(E_j)^2$ for the first failure corresponds to 50% of TSE, Eq. 2.10, and (E^2_{jk}) for the second failure corresponds to 40% of TSE_j, Eq. 2.14, practical considerations require that an isolation ratio threshold be chosen which is lower than these theoretical values. The isolation ratio threshold is defined as R_o equals E_o/TSE_o for the first failure, and for the second failure, R_1 equals E_{jk}/TSE_j. Since the use of quantized data and the acceptable noise and residuals associated with the instrument population increase all the E terms and the TSE, use of the theoretical values would result in undetected failures. The use of too low a value would result in false alarms.

A plot is shown in Fig. 2.1.2A which provides an indication of the safe region for quantifying the detection and isolation thresholds.

This plot shows the largest magnitude ratio, R_o for an instrument E_n which has not failed (Curve 1) and the corresponding smallest ratio R_o for an instrument E_j which has failed (Curve 2). These ratios are plotted for a normalized signal to noise expression N that is the ratio of the instrument axis accumulated output (signal) to the maximum noise magnitude (quantization, uncompensated residuals, etc.) that may be expected in that output. Thus N is the ratio of a failure measurement error to the background noise or error residuals of good instruments. In these plots the magnitude of the noise is a maximum (±1) but its signs (+ or -) are considered to be equally probable. The curves in the figure result from averaging all of the worst-case noise values assuming + and - to be equally probable.

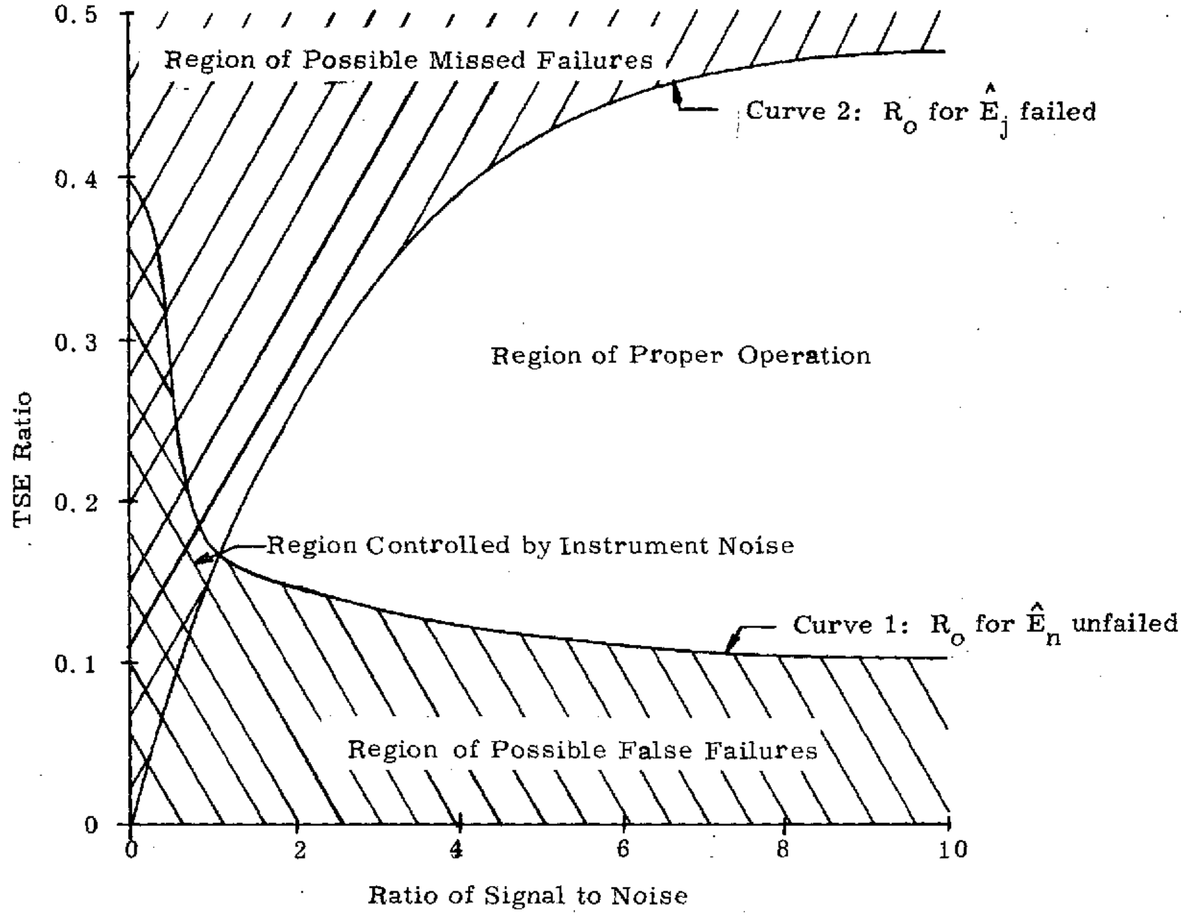

Fig. 2.1.2A TSE vs Signal-to-Noise Ratio Operating Range-First Fail

Viewing Fig. 2.1.2A, note that if the R_o ratio for failure isolation were selected below Curve 1, false alarms would routinely occur, (i.e. an unfailed instrument could yield a E_n/TSE_o greater than the selected R_o). Similarly, if the R_o ratio were selected above Curve 2, missed alarms would occur, i.e. a failed instrument could not yield E_j/TSE_o greater than the selected R_o. Thus, to assure reliable failure isolation a R_o should be selected in the region between the two curves. Note that the crossover point of the two curves occurs at 1.

As expected, in the region to the left of this crossover no decisions can be made since the signal and the worst-case noise are equal. As noted previously, the FDI cycle is initiated when the TSE threshold is exceeded, providing identification that a failure exists. The discussion on the curves thus far has reflected on those regions of R_0 selection that yield reliable failure isolation.

Combined FDI operation is a function of the selection of both of these thresholds. The TSE threshold is selected on the basis of the anticipated signal to noise (S/N) ratio. The TSE flags the presence of a failure when it is large enough to assure that noise can not cause an erroneous isolation decision. For the first fail search, the TSE must correspond at a minimum to a S/N ratio of 1. Conservatively, since crossover at a higher S/N ratio is possible, a larger S/N criteria should be used. For example, if all the outputs have a maximum noise component, the specific worst-case sign polarity (probability of 0.03), and an accumulation in which polarity occurred at every iteration throughout the FDI period (probability approaching zero), the crossover in Fig. 2.1.2A would move to approximately a S/N of 5.5. Similarly the lower Curve 1, would move up and become asymptotic to a ratio of 0.2. In practice, to provide adequate detection reliability margin, a TSE threshold criteria of approximately $2 \times 6\Delta\theta^2$ or $2 \times 6\Delta\theta^2$ error or greater is used. (The factor of 2 is derived from Eq. 2.10, where TSE $= 2E_j^2$). In a static environment, with gyro drift residuals bounded within 0.10°/hr, a 6 min accumulator used with the TSE $= 2 \times 6(\Delta\theta)^2$ threshold would correspond to approximately 0.15°/hr degradation detection where $\Delta\theta = 5.5\ \widehat{\text{sec}}$. To accomodate for dynamics, an effective $\Delta\theta$ of approximately 20 $\widehat{\text{sec}}$ has typically been used.

The combined first fail FDI uses a TSE criteria that reflects an S/N ratio greater than 6 and a failure isolation ratio, R, greater than 0.35. Empirically, laboratory testing has demonstrated that a ratio as high as 0.44 provides highly sensitive and reliable FDI performance.

A second set of curves, see Fig. 2.1.2B, applicable to the second FDI is developed using the same approach. Note that the crossover point of the two curves in Fig. 2.1.2B also occurs at 1. This second fail search FDI curve also reflects a worst-case noise situation and illustrates a somewhat reduced safe R_1 selection region (area between Curve 1 and 2) since the lower Curve 1 is asymptotic to 0.15 vs 0.1 on Fig. 2.1.2A. Similarly the true fail ratio asymptote (Curve 2) has reduced from 0.5 to 0.4. For the absolute worst-case condition (the sign of all noise terms having a specific polarity distribution), the crossover for this second fail case moves to a S/N ratio of approximately 9 and the Curve 1 asymptote is 0.3. These factors illustrate that second fail detection and isolation threshold selection does not have as much margin as the first fail FDI. This finding is intuitively obvious since there are fewer comparative measurements. Conversely, if one wishes the same second fail FDI reliability, some degradation in fault isolation resolution capability will occur. For example, FDI reliability equivalent to the previously discussed illustration of a 0.1°/hr fail degradation isolation would correspond to a 0.15°/hr (TSE$_{jk}$ = 2 × 9$\Delta\theta^2$ capability in the second fail search.

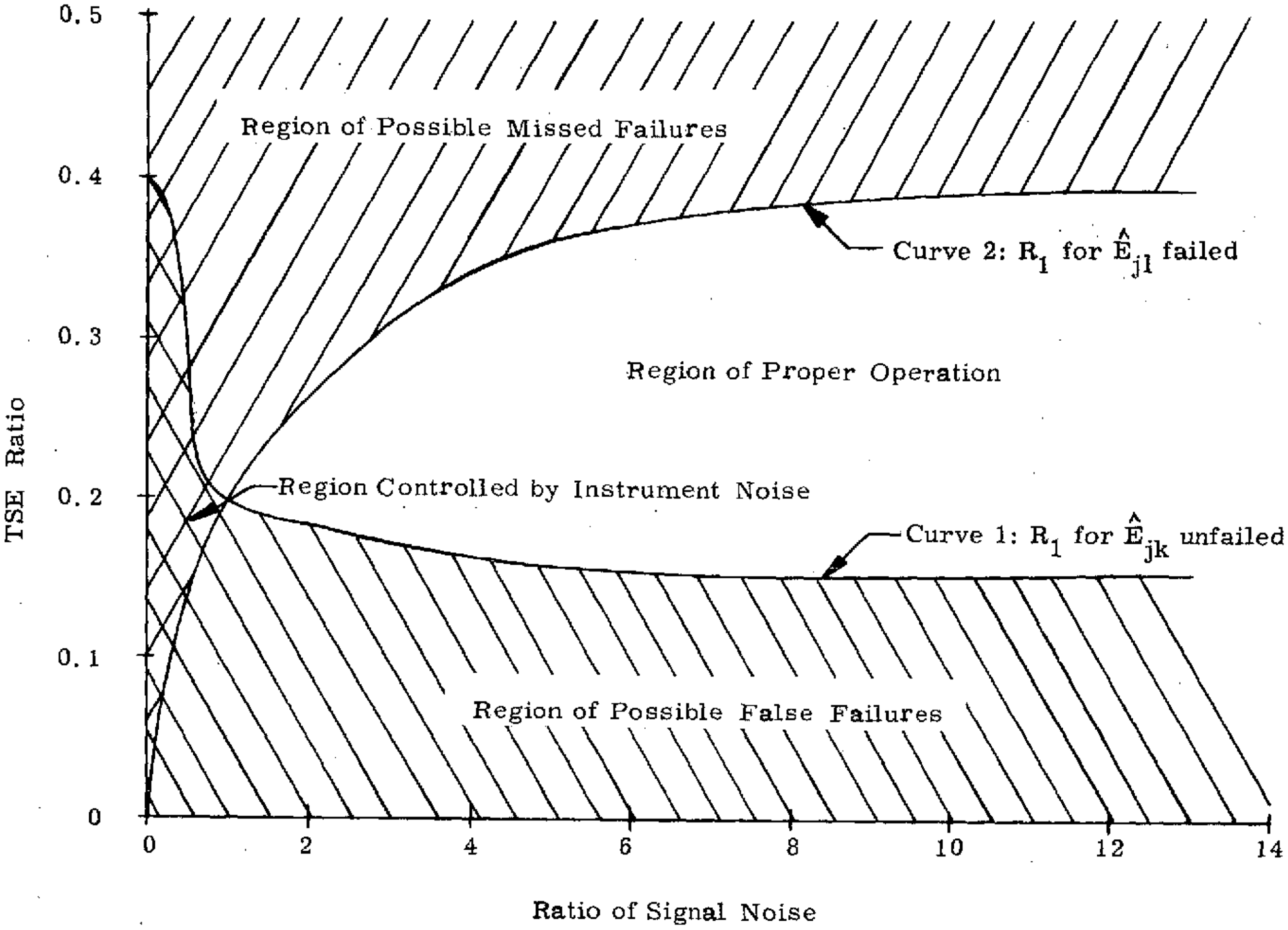

Fig. 2.1.2B TSE vs Signal-to-Noise Ratio Operating Range-Second Fail

In testing, a second fail isolation ratio of 0.38 has been used with good resolution and high reliability. A 20 $\widehat{\text{sec}}$ effective $\Delta\theta$ has been used in the TSE$_{jk}$ criterion to allow for dynamic environment noise. Detailed analyses that provide definitive assessment of the FDI reliability are presented in the SIRU Utilization Report, R-747.

Redundancy Management

The software redundancy management system implements the FDI concepts and equations discussed above in the following manner. Prior to each attitude and velocity algorithm iteration, the failure detection and isolation algorithms operate on measurements accumulated at the system iteration rate (100 iterations/sec and 50 iterations/sec have been mechanized in the SIRU software). Thus the FDI algorithms operate to detect and isolate a failure prior to each system iteration. If a failure is detected, the least-squares matrix processing, Eq. 2.2, is modified to reflect the failure and only the current good data is processed through to the attitude and velocity algorithms. Thus, no known bad data is used. The FDI algorithm uses individual accumulators for each instrument's measurement data. The accumulators are incremented at each iteration by the new data sample. Thus, at each iteration, the accumulator represents the sum of past and new data. The extent of storage, i.e., past data accumulation, is selected on the basis of the desired FDI resolution (e.g., for the gyros, an equivalent drift). Periodically, all the accumulators are simultaneously purged of an equal time interval of their oldest data. The finest detection and isolation resolution is therefore obtained at the FDI test just prior to a purging (the maximum interval storage capability). The minimum resolution is obtained at the FDI test of the accumulator data remaining just after a purging. In test demonstrations a six minute accumulator, purged of old data every two minutes, has been used. These time parameters are selectable based on the desired resolution. The tradeoff considerations are discussed later in this report.

After a first failure is detected and isolated, a search is made for a second failure. The data used in this search does not include the measurement data in the accumulator corresponding to the axis that was identified as failed in the prior first fail search. However, the prior failure is continuously examined (its accumulator continues to be incremented) by returning to the original first fail search equation. This operation allows recertification (use again in forward processing) should the failure heal (e.g. the failure may have been due to a transient condition). Thus the first fail search is continuously repeated. Similar provision is made for recertifying a second failure. After a second failure has been isolated, the appropriate parity equation is also examined for a third failure detection.

The ranking of failures for the purpose of failure management is as follows. If there are two failures, that failure which exceeds the isolation threshold ratio, computed using data from all six instruments, is ranked first and is considered to be the worst failure. The other instrument failure is ranked second. If there is a third failure, the second ranked failure and the third failure are included in the isolation ratio computation using data from five instruments (the first ranked failure is excluded). The instrument exceeding the isolation threshold ratio is ranked second. If it is the same instrument that was previously ranked second, the failure detection alarm is continued and the third failure cannot be isolated by software alone. On the other hand, if the third failure exceeds the second fail isolation threshold ratio (in the 5 instrument test), it is ranked second and taken off-line. The previously second ranked instrument is now ranked third and remains off-line. In this case a third failure has been successfully self-isolated. This capability was successfully demonstrated toward the end of the SIRU Utilization program by an example in which the third failure was approximately 10 times greater than the original second failure.

An illustration of the error detection process is shown in Fig. 2.1.3 using data from an actual test on the SIRU system. This figure shows a plot of the E_j^2 magnitude output (in pulses squared) for all instrument axes as a function of test time. The detection TSE threshold used in this test sequence corresponded to $2 \times 12\Delta\theta^2$ pulses where $\Delta\theta$ was 5.5 $\widehat{\text{sec}}$ (an E_j error of 66 $\widehat{\text{sec}}$). The failure isolation ratio used was 0.44. A simulated failure was introduced in the A axis gyro (bias miscompensated by 25 meru after 120 seconds of normal system operation). Note that the E_a^2 error magnitude increases until the failure detection threshold is exceeded, 150 seconds after the failure was introduced. At that point the failure is isolated to the A gyro. After isolation, the A gyro data is no longer processed, and the error propagation in the estimate of B through F instrument errors is reduced significantly. The resultant system attitude error during this time interval, Fig. 2.1.4, shows the gyro drift rate error propagating as an attitude error until detection and isolation occur. The total error accumulation caused by this A gyro failure is less than 15 $\widehat{\text{sec}}$ in both the X and Z axes. Note that the failure detection is time-dependent since it is based on the magnitude of accumulated E_j^2 pulses, but the attitude error is bounded within 28 $\widehat{\text{sec}}$ (for the particular magnitude of TSE$_\phi$ used in this test demonstration) for an isolated failure regardless of the magnitude of the instrument drift rate error.

It should be noted that the propagation of an error into the system attitude output, as shown in Fig. 2.1.4, occurs because the processing of data continues until sufficient error develops to enable a failure detection and isolation decision. In other words, a finite time is required to accumulate sufficient data to enable a FDI decision. During this time (until the TSE criteria is exceeded) the error propagates through the least-squares processing to the attitude algorithm. The bounded maximum error for the first FDI corresponds to the instrument angle error E_j times one half the cosine of the dodecahedron half angle, 0.425 (see Appendix A). This reduction in the error propagation magnitude is attributable to the least-squares processing, six instruments being weighted geometrically, thereby reducing the effect of a single instrument's measurement error. Generally, this attitude error propagation has negligible influence on a mission since the basic drift detection resolution must be compatible with acceptable performance over an entire mission phase. Thus, if 0.37°/hr drift uncertainty performance is the limit

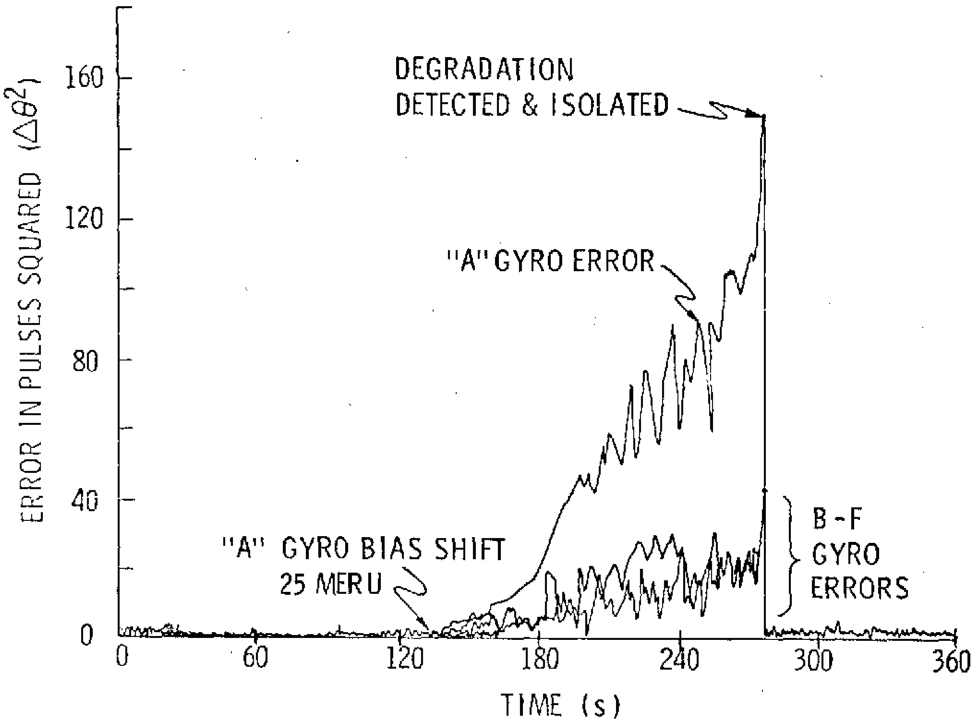

Fig. 2.1.3 Failure Simulation - SIRU

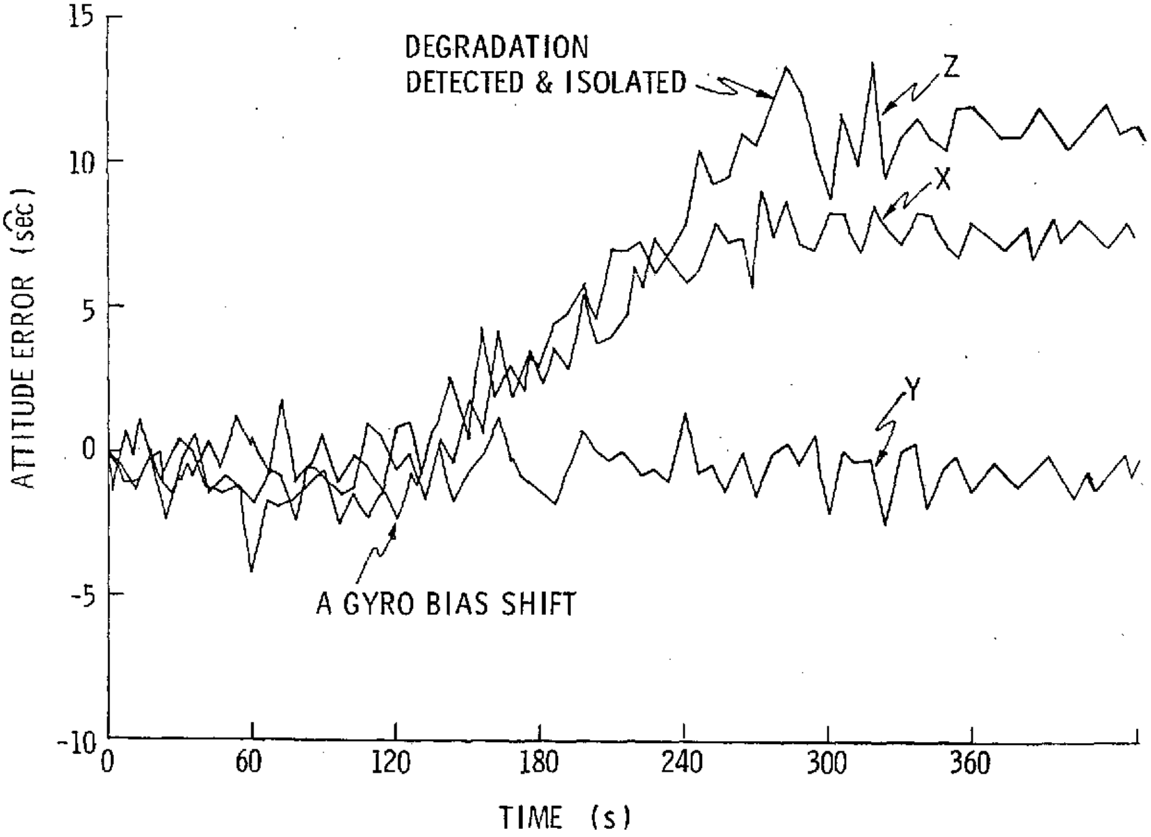

Fig. 2.1.4 Failure Simulation - SIRU

for acceptable drift performance during a mission phase, the influence of a 15 $\widehat{\text{sec}}$ error associated with the FDI of a 0.38°/hr drift error is negligible. Clearly, the relative performance resolution capabilities are therefore the principle interest. The resolution, given a specific TSE criteria, is a function of the system noise, the calibration residuals, and the FDI accumulator storage time. The tradeoffs involved in the choice of these parameters are discussed in the next section. It should be noted, however, that dependent on the computational complex supporting the instrument hardware configuration, processing schemes can be implemented that would not yield a resultant attitude error when a performance degradation failure above the FDI thresholds occurs. For example, in a three computer complex all data from the six measurement axes could be used in all computers for FDI, but only selected sets of four axes of data would be processed in each computer through the least-squares matrix. Thus, an attitude error due to the time the failure took to be detected and isolated would appear in only those computers that were using in its four axes processing the specific instrument that had failed. At least one computer for a single failure case would not reflect an attitude or velocity error due to this failure and all computers, since they were using all axes in their FDI processing, would know which axes had failed. Therefore, each computer would know the relative status of its data. The velocity and attitude status of the affected computers could be reinitialized, and the processing equation sets reorganized to assure that a second failure could be tolerated in the same manner by at least one unaffected computer.

FDI Threshold Tradeoff Considerations

In the present implementation, the gyro failure isolation criteria achieves detection and isolation in 35 seconds for a performance deterioration equivalent to a 100 meru change in bias. Proportionately longer times are required for detection of smaller performance changes. With the current 6 minute accumulator and a 4 cm/sec pulse weight, accelerometer bias changes equivalent to a 0.1 cm/sec^2 can also be detected and isolated. Equivalent detection and isolation is achieved for instrument scale factor (SF) and alignment degradation.

Because of the nature of the nominal uncertainties associated with SF and alignment in strapdown error propagation, special FDI considerations are required for operation in the laboratory where continuous test revolutions are often imposed.

Scale factor or alignment degradation corresponds to a change from the calibrated $\Delta\theta$ or ΔV pulse weight or an angular change in an instrument's input axis orientations from its previous calibrated orientation. Errors due to these types of degradation do not propagate, however, until rotation (for the gyro) or a specific force (for the accelerometer) is sensed. Thus, a SF or alignment change in combination with, for example, a slew (constant rate) input results in an angle error. This angle represents an equivalent drift magnitude during the slew period. Of significance in a mission, however, is the attitude error resulting from a SF or alignment change and its effect on guidance and navigation. The attitude or velocity error for the ternary loops used in SIRU is proportional to the total attitude maneuver or velocity change. In a static environment with only earth rate and gravity inputs, the error associated with a 1000 ppm SF shift in a single gyro (sensing the major portion of earth rate) corresponds to 0.015°/hr drift. This type of error propagation is within the calibration uncertainties of drift terms. Representative SF calibration uncertainties consistent with current moderate performance technological capabilities is on the order of 100 ppm and in the SIRU configuration 20 ppm performance has been achieved. For many applications an uncertainty on the order of 200-300 ppm at the start of the mission and over the entire maneuver profile may prove satisfactory. For example, from the Space Shuttle trajectory once around abort studies error coefficients, presented in Appendix A of the SIRU Utilization Report, R-747, a 200 ppm gyro SF error in the worst axis would correspond to approximately a 4.4 nautical mile cross track error at the 100,000 foot entry altitude. Clearly, in a static prelaunch environment large SF deviations can exist, while due to the nature of their propagation characteristics in this environment, the corresponding attitude error would be perfectly acceptable. Similarly, since the TSE type FDI uses individual axis body frame attitude error estimate accumulations over a finite period, relatively large gyro SF and alignment errors would not cause the failure threshold levels to be exceeded. For example, with an $E_j^2 = 37\ \widehat{\text{sec}}^2$ criteria ($6\Delta\theta^2$ where $\Delta\theta = 5.5\ \widehat{\text{sec}}$) and a six minute accumulation and, if all the earth rate is about the specific gyro, a failure would be identified only if the SF has degraded by at least 6,800 ppm (corresponding to approximately 0.1°/hr drift). Operation in such an environment with this type of degradation is perfectly acceptable. On the other hand, if one were to apply an input to a system rate test of 5°/sec, a SF degradation of only 5.7 ppm could cause the FDI thresholds to be exceeded in only six minutes. Even if $E_j^2 = 132\ \widehat{\text{sec}}^2$ was used in the FDI logic, the failure threshold would be exceeded for a SF degradation of only 20 ppm. In both cases SF uncertainties of this magnitude are perfectly acceptable while the FDI indications would be a nuisance. Clearly, the FDI goal is to detect and isolate a SF degradation level in SIRU in excess of 100 ppm. Thus to circumvent nuisance problems and achieve a detection capability consistent with a realistic SF and alignment degradation

FDI goal, an algorithm was implemented that increased the TSE limit on the basis of the dynamic input environment. The technique used was to open the threshold on the TSE based upon the magnitude of a triad solution body angle accumulation. That is, the TSE is increased by an amount proportional to the magnitude of the θ_x, θ_y, θ_z body angle traversed in the same six minute FDI accumulation period. For simplicity, however, rather than generating a vector magnitude, the TSE increment (ΔTSE in $\widehat{sec}^2$) was made proportional to the sum of the magnitude of the individual triad body axis accumulations, e.g.: the ΔTSE is synchronized with the FDI accumulators and it updates the TSE limits prior to each FDI test.

The scaler K, during the test program, was set so that the TSE was increased by 44 $\widehat{sec}^2$ for every 1/8 radian accumulated. This scaling is equivalent to opening the TSE to allow for a SF degradation of approximately 150 ppm (i.e. if rotation was essentially about the degraded axis) under a constant slew test. The considerations applicable to alignment shifts are essentially identical and the scaling corresponds to approximately a 30 $\widehat{sec}$ alignment shift detection capability.

The isolation resolution performance capability of the SIRU system TSE technique as a function of the FDI accumulator storage time for different effective quantization ($\Delta\theta$) levels is illustrated in Fig. 2.1.5. Quantization levels of 44 $\widehat{sec}$, 20 $\widehat{sec}$ and 6 $\widehat{sec}$ are shown in the figure. The limiting condition is for 6 $\widehat{sec}$ resolution corresponding approximately to the present SIRU gyro interpolator quantization. Note in the figure that when the storage time exceeds 600 seconds, all of the curves flatten out and there is little to be gained by longer accumulator storage time. During the test program, storage times used varied between 3 and 6 minutes. In the six minute accumulation, for convenience, the old data was purged every 2 minutes. (One minute purge cycles were implemented with the 3 minute accumulation). The six minute accumulation represented the maximum accumulation storage time and therefore the highest resolution FDI. The 4 minute value remaining immediately after the oldest two minute portion of data had been purged represented the lowest resolution FDI for the six minute accumulation. These values (360 and 240 seconds respectively) occur at the knee of the 6 $\widehat{sec}$ quantization curve and for this value of quantization the accumulator storage times are therefore optimum. The theoretical performance isolation resolution corresponding to these storage times is on the order of 0.1°/hr. This 0.1°/hr value corresponds to using six times the 5.5 $\widehat{sec}$ quantization noise for E_j in the TSE threshold and a 6 minute accumulator storage time.

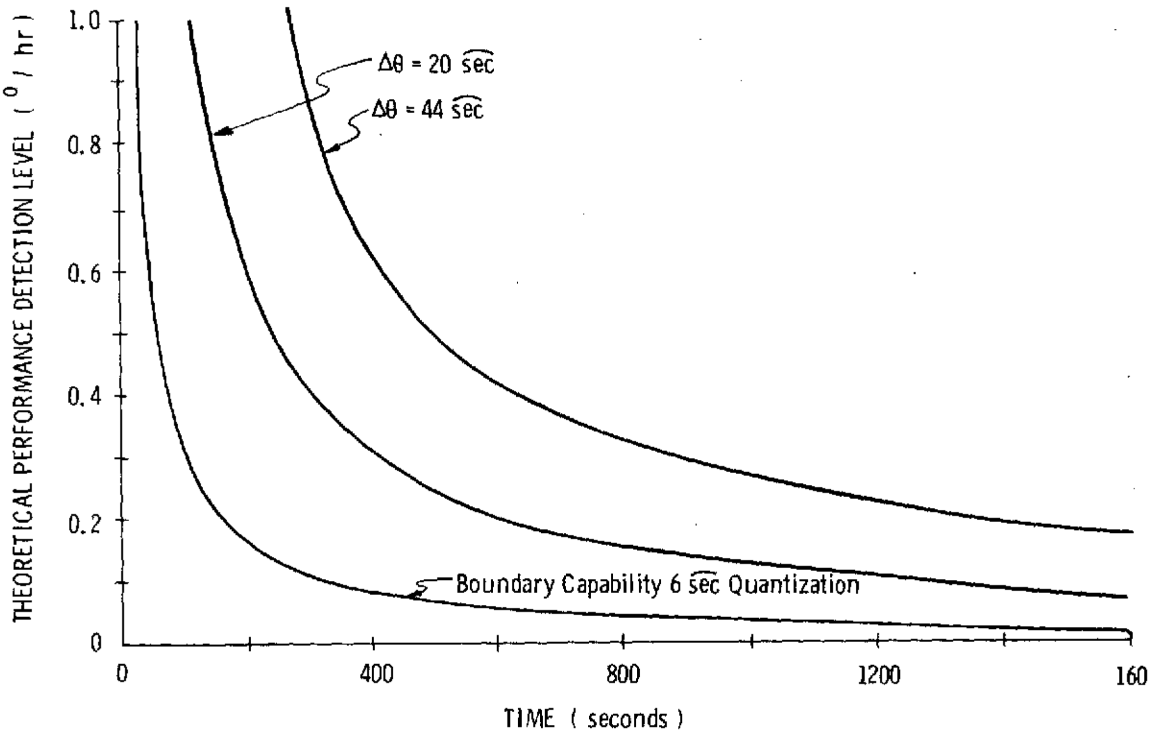

Fig. 2.1.5 Isolation Capability vs Accumulator Storage Time

In the SIRU hardware testing, use of a TSE based on the 6 $\widehat{\text{sec}}$ quantization has resulted in occasional "false alarms", i.e., failure indication of a specific instrument on a transient basis where no failure has actually occurred. This phenomenon was traced to the occurrance of a spurious burst of 2-3 pulses which resulted in no net integrated angle but did, in the presence of other residuals, cause the TSE to be exceeded during an FDI accumulation cycle time. Thus, on a transient basis, an instrument was taken out of the data processing structure until the accumulator purged the transient data burst and requalified the instrument (approx. 120-180 sec later). The noise effect, although random and infrequent, was traced to the long cable run, (approx 50') and the table slip ring interface between the gyro module outputs and the computer. An effective quantization corresponding to the $\Delta\theta$ = 20 $\widehat{\text{sec}}$ curve in Fig. 2.1.5 was used initially to allow for this noise phenomena, equivalent to operating with a TSE of approximately $2 \times 24\Delta\theta^2$ with $\Delta\theta$ equal to 5.5 $\widehat{\text{sec}}$. Subsequent dynamic testing illustrated that an equivalent noise in a two minute accumulation period on the order of 18 $\widehat{\text{sec}}$ could be induced by 1 Hz, $1/2^{\circ}$p-p oscillations. Therefore the $2 \times 132\,\widehat{\text{sec}}^{2}$ TSE criteria was retained as a nominal threshold. The accumulator structure was not optimized to correspond to a more sensitive drift resolution (from Fig. 2.1.5 ten minutes would be more optimal) since the software was sufficient to demonstrate the FDI mechanization and the new statistical FDI did not require this type of accumulation approach. During static tests, however, finer resolution capabilities were demonstrated, e.g., Fig. 2.1.3 illustrates a 2 x 66 $\widehat{\text{sec}}^2$ TSE criteria corresponding to an effective $\Delta\theta$ quantization of 11 $\widehat{\text{sec}}$. A 0.1°/hr FDI with a six minute accumulator was demonstrated in static tests when drift residual uncertainties were bounded within approximately 0.015°/hr. Figure 2.1.6 shows the error propagation in attitude ($\widehat{\text{sec}}$) as a function of the TSE

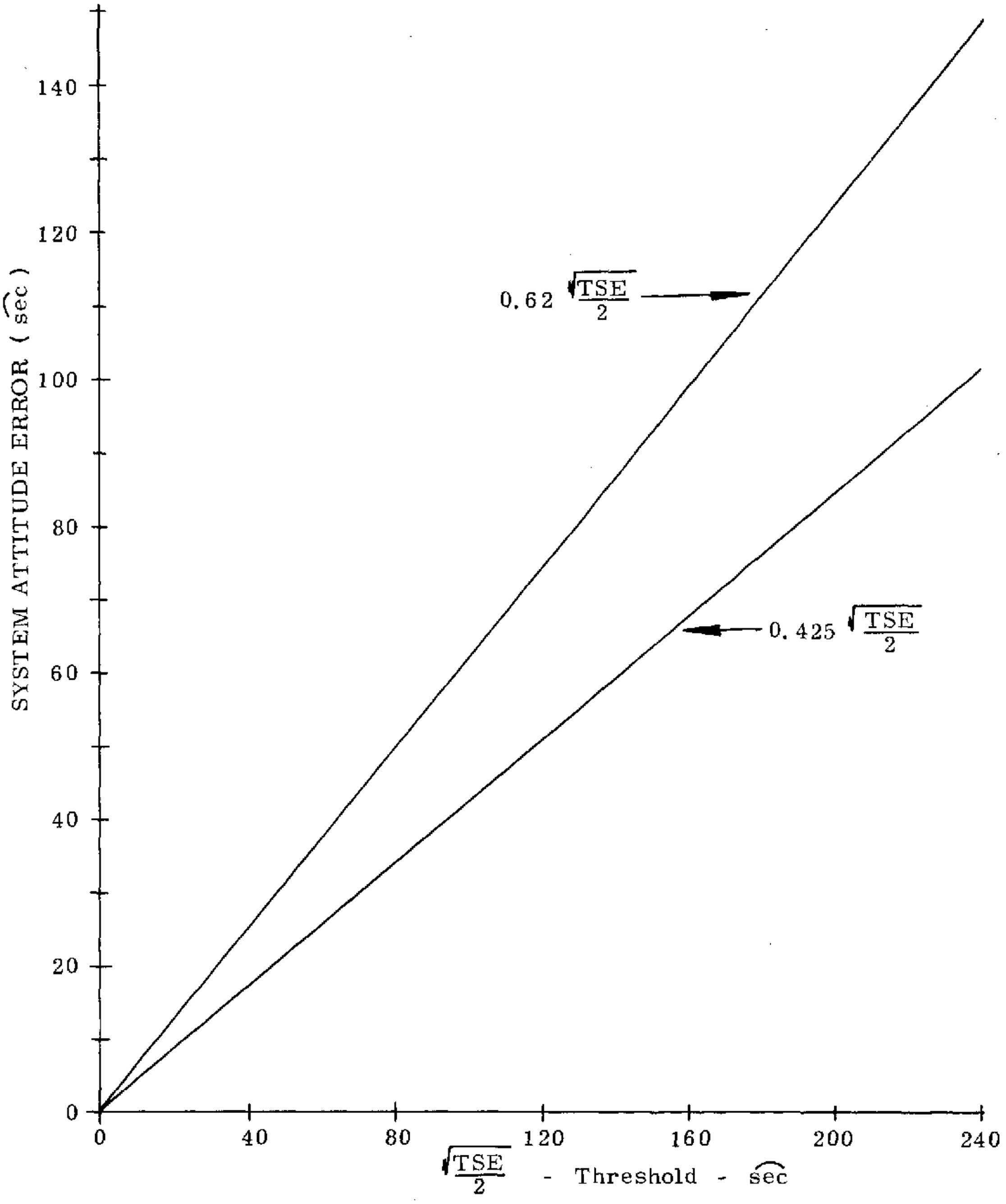

Fig. 2.1.6 Fault Isolation Threshold vs System Error Propagation (Single Soft Fault)

detection threshold (in $\widehat{\text{sec}}$)^2. As discussed previously, an attitude error is propagated until the failure is detected and isolated. This curve shows the linear relationship of the maximum system attitude error (resulting from the least-squares processing). The maximum error reflected in a single triad reference axis corresponds to 0.425 and 0.62 of the instrument error (E_j) that is accumulated prior to exceeding the TSE threshold and to isolation of a first and second fail respectively (Appendix A). As the effective quantization noise is lowered, the system attitude error propagation is also lowered since the detection threshold can be lowered. With 6 $\widehat{\text{sec}}$ quantization, the attitude error is less than 20 $\widehat{\text{sec}}$. When the effective noise is 20 $\widehat{\text{sec}}$ the system attitude error propagation is about 50 $\widehat{\text{sec}}$. A quantization of 44 $\widehat{\text{sec}}$, used prior to the incorporation of the torque loop interpolator, results in an error propagation of 112 $\widehat{\text{sec}}$. The second failure condition reflects a somewhat higher magnitude of attitude error propagation since, after the first failure, the least-squares processing uses the remaining five axes of data. Thus, when another failure occurs, the smoothing effect degrades. As noted previously, if a redundant computer implementation was used, simple logical utilization of different sets of measurement axes data in different computers for the algorithm processing would assure that at least one computer would be identified as retaining a non-degraded system output.

Table 2.1.3 Demonstrated Redundancy Capabilities

Fault Detection and Isolation

Filter	No False Alarms 3 Min	6 Min
Soft Failure:	0.75°/hr	0.375°/hr
(Drift Change)	0.2 cm/sec^2	—

100 ppm SF as low as 0.05 rad/sec input

Quantization Limit:	(Random False Alarms on Noise Burst)	
$\Delta\theta$ = 6 $\widehat{\text{sec}}$	0.18°/hr	0.09°/hr
ΔV = 4 cm/sec	0.13 cm/sec^2	0.065 cm/sec^2

Demonstrated Results—Hard or Soft Failure:

	No False Alarms	Random False Alarm
System Attitude Error	~60 $\widehat{\text{sec}}$	16 $\widehat{\text{sec}}$
Velocity Error	~15 cm/sec	

Table 2.1.3 summarizes the significant performance values for the SIRU TSE detection and isolation methods for both gyros and accelerometers. For gyros, the

drift and bias levels have been reliably detected and isolated. They correspond to the resolution associated with the full six minute accumulator storage time. If occasional random false alarms are allowed, the detection and isolation thresholds can also be lowered. For accelerometers, the static FDI operation is essentially limited by the pulse quantization used. SIRU was scaled for the Apollo mission to preserve a 19 g capability, resulting in a ΔV quantization of 4 cm/sec. Dynamic errors introduced when large angular rate inputs are applied are the primary cause for random accelerometer false alarms.

The FDI technique described in this text has been limited to the TSE and parity equation approach. In late 1971 concepts for improving FDI resolution by specifying the coverage (reliability) and classifying the nature of the performance degradation (random or stable bias, etc.) with a subsequent recalibration were conceived. These techniques were based on a statistical FDI algorithm. During the late 1971-72 period the statistical technique was developed and matured. Significant performance resolution improvement with reduced data storage was achieved. For example, FDI resolutions equivalent to 1.5 times the population's standard deviation was demonstrated. Recalibration with high accuracy was also demonstrated. The statistical technique is described in the SIRU Utilization Report, R-747.

2.1.3 General System Software Description

A general purpose computer (Honeywell DDP-516) is used to verify the redundant SIRU system software design by providing an instrument calibration and real-time system evaluation capability. The DDP-516 is a 16-bit machine with memory cycle time of 0.96 microsecond, a high-speed arithmetic package and 16,384 words of core memory. Peripherals used include: two disc drives, each capable of storing 34 million words; a teletype unit; a CRT character display and a high-speed paper tape reader. The DDP-516 has been interfaced with the test table encoder as well as the SIRU instrument module outputs and thereby provides a capability for real-time system evaluation.

The basic SIRU software flow is shown in Fig. 2.1.7. A detailed software coding listing and description is presented in Volume III of this report. As shown in Fig. 2.1.7, the individual gyro and accelerometer outputs ($\Delta\theta$s and ΔVs) are compensated to provide corrected body rotation and body velocity. This information is subjected to the FDI test prior to each algorithm iteration and failed axes data are not utilized by the matrix processor (reorganization). As previously discussed, provision for recertification (reapplication of "healed" instruments) is an automatic feature of the TSE FDI. Recalibration (recompensation of stable performance changes), however, is incorporated as part of the statistical FDI technique and is covered in the SIRU Utilization report. The accelerometer and gyro failure status is also available for display. The corrected body incremental motion change as released for updating is utilized in the matrix processor in which the least-squares solution to transform the corrected individual instrument $\Delta\theta$s and ΔVs into a X, Y, and Z body frame is performed. The outputs of the matrix processors are used in attitude and velocity algorithms to update a quaternion transformation into the inertial frame. The transformation is accomplished using a third-order Taylor series which achieves high performance at low iteration rates. An analysis of the use of the third-order quaternion is presented in both the SPOT Final Report, R-743, and Control, Guidance and Navigation for Advanced Manned Missions, Volume IV, Inertial Subsystems, R-600 and is not repeated here.

As noted, the first step in the processing structure relates to compensation of known instrument calibration parameters and dynamic error sources. The gyro and accelerometer compensation algorithms accumulate pulses from the torquing electronics and corrects them for the various error sources intrinsic to each instrument. The result of the compensation yields corrected rotational and velocity increments in the body frame. The gyro compensation algorithm corrects for the gyro scale factor, the drift components (acceleration sensitive and non-sensitive) major compliance, misalignment angles and OA coupling. The accelerometer compensation algorithm corrects for scale factor, null bias, misalignment angles and centripetal acceleration normalization. A detailed discussion of the compensation techniques is presented in Appendix B.

Shown in Fig. 2.1.7 are the compensation algorithms and their integration with the other algorithms used in the SIRU system. The pulse torque increments are accumulated for a period of time determined by the iteration cycle (e.g., 10 ms for 100 iterations per second). The gyro and accelerometer iteration cycles are of equal length, but are staggered such that the accelerometer-derived velocity data is available half way through the gyro cycle (and vice versa). This implementation increases the efficiency of data processing and algorithm performance.

The accumulated input of raw torque pulses is sequentially corrected for each parameter by incrementally modifying the count by an amount that is dependent upon the magnitude of the error parameter. After all parameters have been compensated, two state vectors are derived which represent the body rotation and velocity increments in the dodecahedron reference frame.

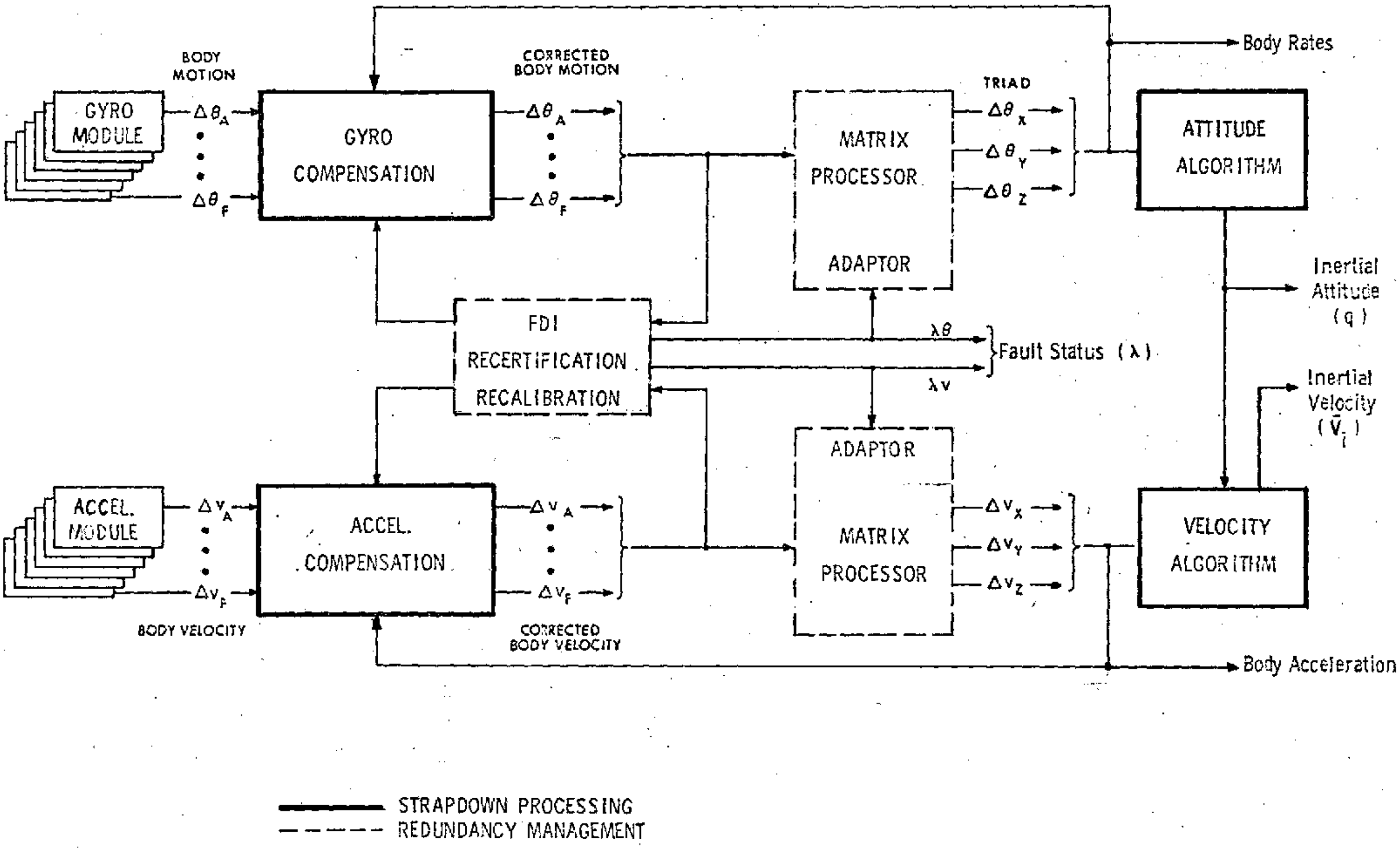

Fig. 2.1.7 Basic Software Flow Diagram

This incremental data is processed by the FDI algorithm to indicate instrument failures and by an adaptive matrix processor to transpose the incremental data from the dodecahedron frame of reference to a triad frame of reference. Transformation from the dodecahedron to the triad reference frame is accomplished with a least-squares estimator operating on the six axes of body data. If an instrument failure occurs, the matrix processor rejects that instrument's output and accurately compiles the triad data from the remaining instruments' data. Thus, redundant performance is exhibited in the triad data.

The triad data is used to furnish estimates of the environment when required to compensate the appropriate parameters (as examples, acceleration sensitive gyro drift, misalignment angles and OA coupling). Because the triad data is immune to instrument failures, the compensation scheme is also immune to instrument failure. Thus the inherent redundancy features are maintained by the use of the triad data for compensation. For example, since the A-gyro's ADIA term (as determined in static test) is corrected for g level by using a triad solution derived acceleration resolved back into the A-gyro IA axis, the loss of the A-accelerometer does not degrade the compensation of the A-gyro.

The computer memory and percent of machine time required to accomplish the data processing described above is summarized in Tables 2.1.4A, 2.1.4B, 2.1.4C.

Table 2.1.4A shows the memory requirement for all of the routines applicable to the operating SIRU system, and Table 2.1.4B shows the percentage of computer time required at selected iteration rates. The system was initially put into operation at an iteration rate of 100 updates/second and is presently operating at 50 updates/second. 20 updates/second has been proposed as an acceptable iteration rate for several representative applications of the SIRU system.

Table 2.1.4C shows the memory presently required for servicing and overhead routines implemented to aid in the checkout and development of the SIRU system. These elements would not exist in a functional installation.

The basic SIRU memory requirement (4280 words) can be correlated to the load map shown in Volume III by adding to it the overhead of 1859 words and the blank 243 words of memory between the Digistore output routine and the centripetal acceleration, $R\omega^2$, compensation to total 6392 words (14370 octal).

Summary descriptions of the SIRU routines are contained in Chapter 4 of Volume I and full descriptions, plus load map and listings, are contained in Volume III.

Table 2.1.4A Basic SIRU Software

Operation	Memory Words
Gyro Compensation	514
Accelerometer Compensation	378
Gyro Matrix Processor	124
Accelerometer Matrix Processor	86
Failure Detection and Isolation and Matrix Generator	1706
Attitude Transformation Algorithm	278
Quaternion Unifier	176
Velocity Transformation Algorithm	378
Base Sector*	512
Read Routines	138
Total Memory	4290

*The base sector is used to store static coefficient compensation, misalignment compensation, error accumulators, delta theta and delta V registers, quaternion, fail status and other often used items.

Table 2.1.4B % Machine Time—Basic SIRU

Update Rate	% Machine Time
20/sec	16.6
50/sec	42
100/sec	83

Table 2.1.4C Laboratory Overhead Software

Operation	Memory Words	
Earth Rate Compensation	70	
Machine Control Executive	230	
Output Routines		
Magnetic Tape	101	1559
CRT Display	468	
Teletype	91	
Output Handler	899	
	1859	

2.2 Electronics

2.2.1 Redundant Mechanization

The previous discussions have described SIRU's redundant data processing and failure isolation concepts. In this section, the manner in which these concepts are extended to the electronics is reviewed. Discussion of the electronic design features of these circuits is presented in Chapter 3.

Redundant techniques are employed in the electronic mechanization to provide circuit functions that are free from single-point failure mechanisms. Figure 2.2.1 illustrates the basic features of the mechanization. Functional axes have been defined that correspond to each dodecahedron measurement axis. Each axis consists of a gyro and an accelerometer module supported by common power supplies. These power sources include: a 2 phase 800 Hz gyrowheel power supply; a 9600 Hz supply for suspension and signal generator excitation and a dc axis supply. The dc axis supply provides the modules' torque electronics with the required logic (5v) and amplifier (+10v) voltage levels and a separate floating excitation (15v) for each precision voltage reference (PVR). This per-axis implementation enables the isolation of any failure to a specific instrument axis or, at most, to a functional axis . The functional axis concept was implemented for ac and floating dc power

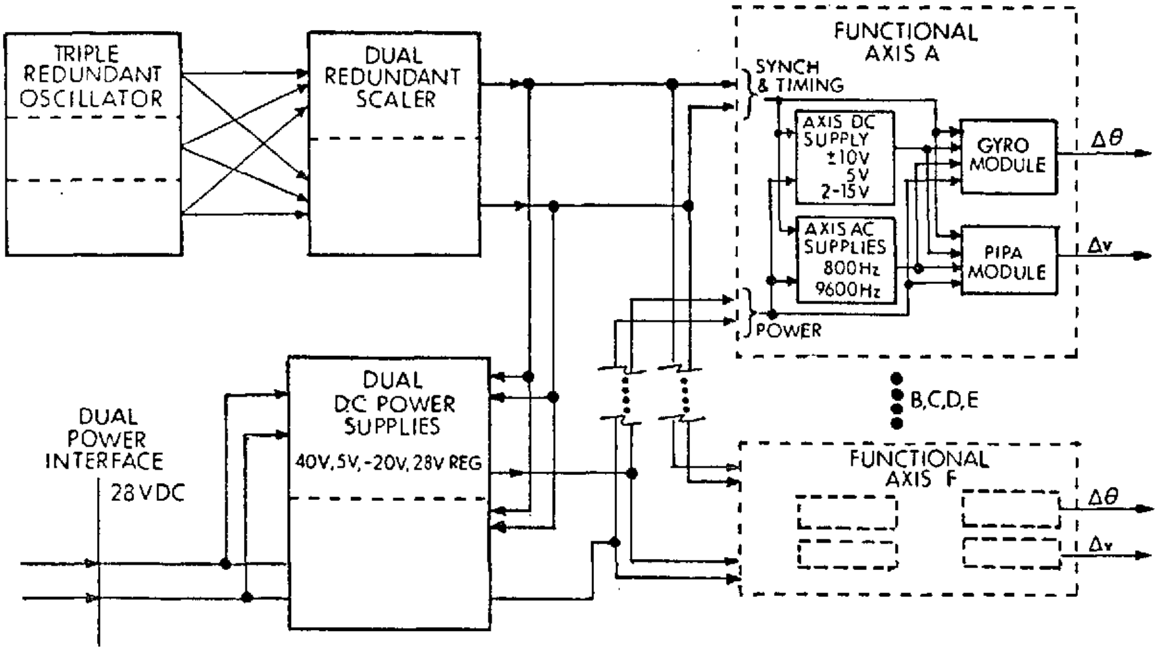

Fig. 2.2.1 Block Diagram of SIRU System

The timing control pulses for the torque electronics and synchronization functions for the various power supplies are redundantly implemented. The oscillators are mechanized in a triple-redundant configuration with output frequency comparisons by individual failure detectors.

Dual redundancy is employed in the scaler implementation, and high/low frequency detectors test both the 115.2 kpps and 200 pps outputs. The control pulses to the torquing electronics are also tested for their presence and proper sequence. The selection logic gates only one scaler at a time to the system functional axes and power supplies, but both scalers are continuously operated and monitored by their detectors. The scaler output lines are separately buffered to assure fail-safe operation. In both the scaler and oscillator implementation, provisions for test sequencing of all the combinations are included.

It is important to note that with respect to the dc power supply and the scaler, the electronic system configuration was mechanized to provide only fail-safe isolation characteristics because the relative reliability of the particular functional elements was used to determine the redundancy level to be implemented. For example, the estimated failure rate of a 40v power supply is less than 10 failures per million hours whereas a gyro module failure rate estimate might range between 100 and 200 failures per million hours, determined principally by the inertial instrument and the torque electronics. Thus, dual redundancy is sufficient for the dc power supply; it does not compromise the end-to-end system reliability index and still provides fail-safe operation. Similar considerations were applicable to the dual implementation of scalers. Inclusion of a third scaler and dc power supply would represent a relatively simple design modification.

2.2.2 Module Electronics

Each gyro and accelerometer module includes its own temperature controller, preamplifier, torque control loop, etc. Scale factor stability and linearity performance on the order of 3 and 20 ppm respectively has been achieved with the present instrument control loop within a 1 rad/sec design range.

A functional block diagram of the gyro module is shown in Fig. 2.2.2. Note that an Interpolator/Compensator is included in the ternary torque-to-balance loop function.

supplies because a dual-redundant implementation would have necessitated a complex and possibly unreliable system of independent failure detection monitors and switching networks. Each gyro and accelerometer module includes its own temperature controller, ternary torque-to-balance control loop and other specialized instrument electronics.

The mechanization allows for the incremental $\Delta\theta$ and ΔV outputs of each instrument module to be stored redundantly in an interface multiplexer. The multiplexer would then transmit data and receive control and sampling messages from the computer assembly on dual buses. A serial data transmission format would be used. The multiplexer included provisions for digitized analog data (voltages, etc.) for automatic monitoring to enable more extensive fault localization, e.g. to replaceable modules. The multiplexer was designed but not incorporated in the SIRU system due to program funding limitations.

Redundant dc power distribution to the functional axes is achieved by the use of dual dc power supplies. These supplies are designed so that each can independently support the total load of all functional axes. They are isolated from each other by diode networks to provide fail-safe operation. Provisions were made to allow for the addition of another dc power axis if further contingency planning was desired, i.e., Fail Operational/Fail Safe.

Discussion of the design implementation of the dual 40v supply which provides power for the gyro torquing current, provides insight into the special design considerations that are required to avoid a system failure due to a single-point failure mechanism. First and most obvious, the diode interconnection is provided on a per-axis basis to assure the availability of 40v power to the gyro modules if either of the two supplies fails due to a low output level or to an internal short circuit ahead of the diode. Similarly, to protect against a gyro module short circuit, fusing is incorporated on a per-axis basis. This feature assures that the 40v distribution to all other gyro modules (a solid-state fuse design has been formulated) is not influenced by a loading fault. Another more subtle reliability design requirement, fail-safe voltage regulation feedback, has been incorporated to insure that the 40v input to the gyro module torque loops remains within regulation limits. If the 40v were to go above the regulation limit, performance degradation could occur on all axes. Therefore, each 40v module has dual-redundant feedback loops that regulate and limit its maximum output voltage. The dual feedback loops operate to insure that if one loop fails the remaining loop will prevent the module voltage from exceeding the regulation limit. Other design features allow 100% continuous overload without affecting regulation of the module output.

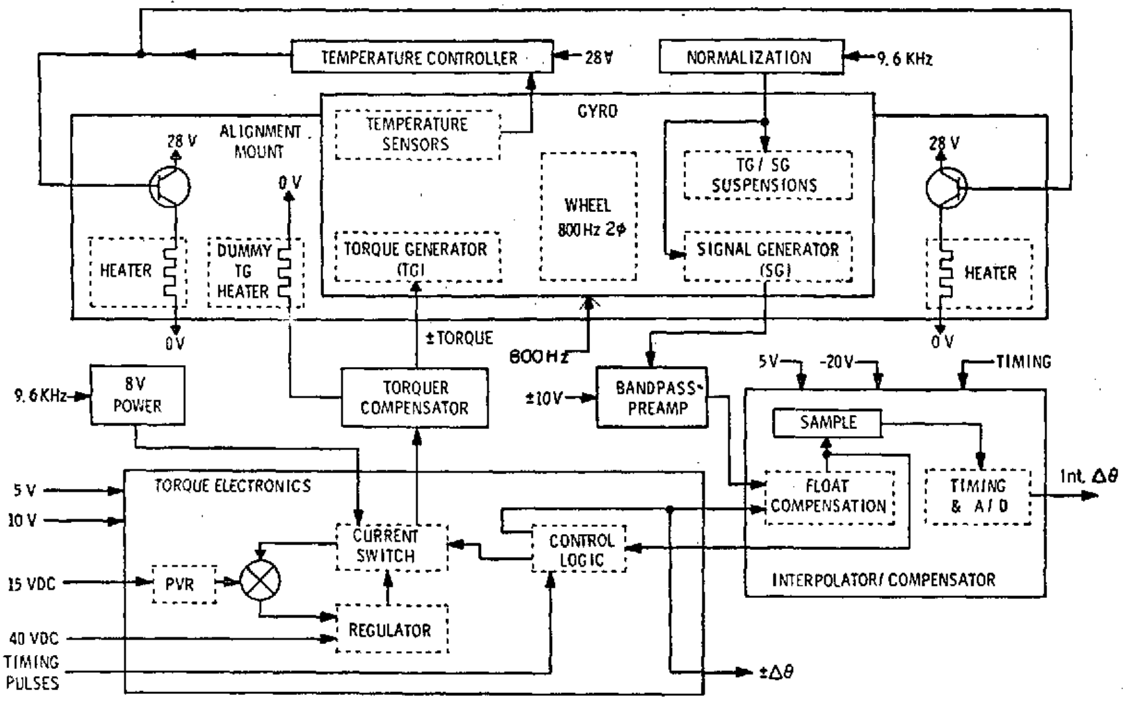

Fig. 2.2.2 A Functional Block Diagram of the Gyro Module

In standard ternary loop operation, the gyro signal generator (SG) output is sampled and, when the SG signal reaches a given threshold, the control logic applies a torque current pulse to the gyro torque generator to return the gyro float to its null position. Timing pulses to the logic control the current pulse width, and precision current amplitude control is effected by a current feedback loop that operates on the basis of a comparison between the PVR and a current sampling resistor.

The Interpolator/Compensator provides a dual function. As a compensator it substantially eliminates the effect of the dynamic characteristics of the gyro float and linearizes the gyro torque loop output response to the applied input rates. Without this compensation, lagging gyro float response to a torque pulse can result in multiple pulsing. In the uncompensated ternary pulse torque-to-balance control loop at an interrogation rate of 4800 pps and with a float inertia to output axis damping ratio (I/C) of 330 microseconds, multiple pulsing does occur. In the accelerometer loop, with the 16 PIP Mod B I/C ratio so much smaller than for the gyro, compensation for float dynamics was not considered necessary. As an interpolator, at each interrogation period the unit samples and holds the analog, compensated SG signal, performs an A/D conversion, shifts in parallel the digital data pulses into a serial register and finally sends them to the computer accompanied by an end-of-data pulse. The digital data is quantized such that each pulse is equivalent to approximately 5.5 arc seconds or 1/8 of the 44 arc second torque pulse. Explanation of the operation of the Interpolator/Compensator is provided in further detail in Chapter 3.

The torquer compensation module includes RC networks that tune the torquer so that it is a resistive load for the current switch and provides a trim resistor for the "dummy" TG load. In the ternary torque loop when torque is not required, the current is applied to a "dummy" load which is also a heater (equal in resistance to the torquer) located on the gyro TG alignment end mount. The purpose of this module is to minimize transients in the current control loop. The switching of the current to the "dummy" load minimizes these transients in two ways. When no torque is required to be applied to the gyro the same current level is fed through the "dummy"; thus the dc amplifier sees essentially a constant voltage, regardless of the torquing state. In addition using this "dummy" as a heater on the TG end mount tends to maintain a relatively constant thermal input to the gyro, reducing loop transients and thermal gradients as well. The 8v power supply is also located within the module to minimize lead capacitance which affects switching time in the current switch.

A dc temperature control loop is used in the gyro and accelerometer module. It is novel in that the control power includes the output transistor's dissipation. The applied power, therefore, is a linear function of control current and a more efficient power mechanization results. This efficiency is achieved by mounting the output power transistor on the instrument alignment mounts (where the heater is also located) permitting the transistor dissipation power to serve also as control power.

The accelerometer module electronic configuration is similar to the gyro module, except that the Interpolator/Compensator function is not incorporated. The SIRU torque loop scaling characteristics are listed in Table 2.2.1. The features of the electronics design are described in further detail in Chapter 3.

Table 2.2.1 SIRU Instrument Torque Loop Characteristics

A) Gyro Torque Loop	
Type:	Linearized Ternary Pulse Torque-to-Balance
Dynamic Range:	1 rad/sec
Torque Loop Quantization:	44 $\widehat{\text{sec}}$/pulse
Interpolator Quantization:	5 $\widehat{\text{sec}}$/pulse
Torquer Power:	2.94 watts—1 rad/sec
B) Accelerometer Torque Loop	
Type:	Ternary Pulse Torque-to-Balance
Dynamic Range:	19 g
Torque Loop Quantization:	4 cm/sec per pulse
Torquer Power:	0.78 watt—19.5 g

3.0 System Hardware

3.1 Electronics Assembly and Redundant Instrument Package

The configuration that has been developed for the SIRU system embodies its reliability features in a modular implementation for improved maintainability. The system is configured as two separate assemblies; the Redundant Instrument Package (RIP) and the Electronics Assembly (EA).

The RIP consists of a mounting and alignment structure, commonly referred to as the π-frame, upon which the six gyro and six accelerometer modules mount. The assembled instrument package is shown in Fig. 3.1.1.

Each module consists of a prealigned gyro or accelerometer that is normalized and packaged with its calibrated electronics in a sealed unit. The instrument's input axis (IA) is offset at an angle, α (31.7°), with respect to its module base. Thus, when the modules are mated to the π-frame's precision mounting surfaces, which lie in orthogonal planes, the instrument's IAs are aligned to the desired dodecahedron symmetry. This mounting configuration allows all units to be prealigned in exactly the same manner, and all modules of each type are replaceable and interchangeable. Offsets from module instrument alignment to system alignment measurements after mounting on the π-frame have averaged less than 10 $\widehat{\text{sec}}$. Maintenance is further enhanced by the π-frame configuration that allows direct access to every instrument from the front of the package.

One interesting aspect of this mechanical configuration is that all instrument output axes (OAs) are colinear with the reference orthogonal triad. This circumstance permits compensation for errors introduced by dynamic inputs about the OA using calculations developed from the triad solutions without additional geometric resolution.

The accelerometer module has been designed about the MIT developed size 16 Permanent Magnet (PM) Pulsed Integrating Pendulum (PIP), a single degree-of-freedom specific-force receiver operated in a torque-to-balance mode. It is primarily distinguished from its predecessor, the Apollo PIP, by a permanent magnet torquer and a solid float.

The gyro module has been designed about the size 18 Inertial Reference Integrating Gyroscope (18 IRIG) Mod B, a single degree-of-freedom gyroscope

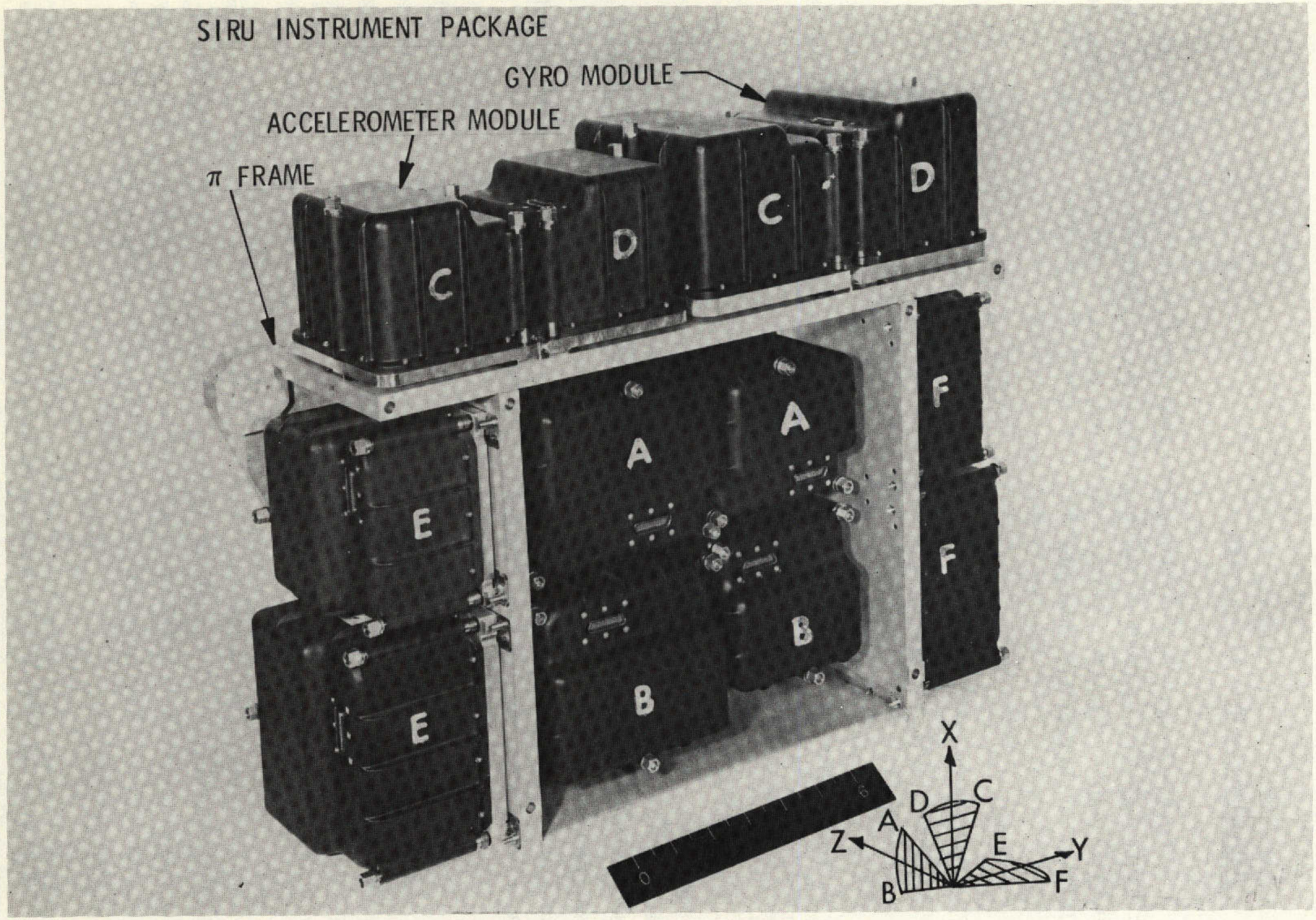

Fig. 3.1.1 SIRU Instrument Package

developed by MIT/DL specifically for strapdown application. Its PM torquer is scaled for torque-to-balance operation with input rates up to one rad/sec, and the OA suspension capability is sized to limit radial side loading at this rate to a negligible value. It contains a gas bearing wheel package, with a greater than 5 rad/sec slew and a multiple stop-start capability. A final report covering the design and development of this instrument has been published as MIT Draper Laboratory Report R-664 dated June 1970.

The packaging system developed by the U.S. Naval Avionics Facility, Indianapolis (NAFI) was used in the design of the EA as shown in Fig. 3.1.2. This approach was selected because, among other features, it permitted the definition of the π-frame structural design independently of the status of the electronic module designs and packaging. The EA design was configured so that functional redundant elements are completely separate mechanically and electrically. Thus, an oscillator module or portions of a scaler, etc., may be removed without disabling the system.

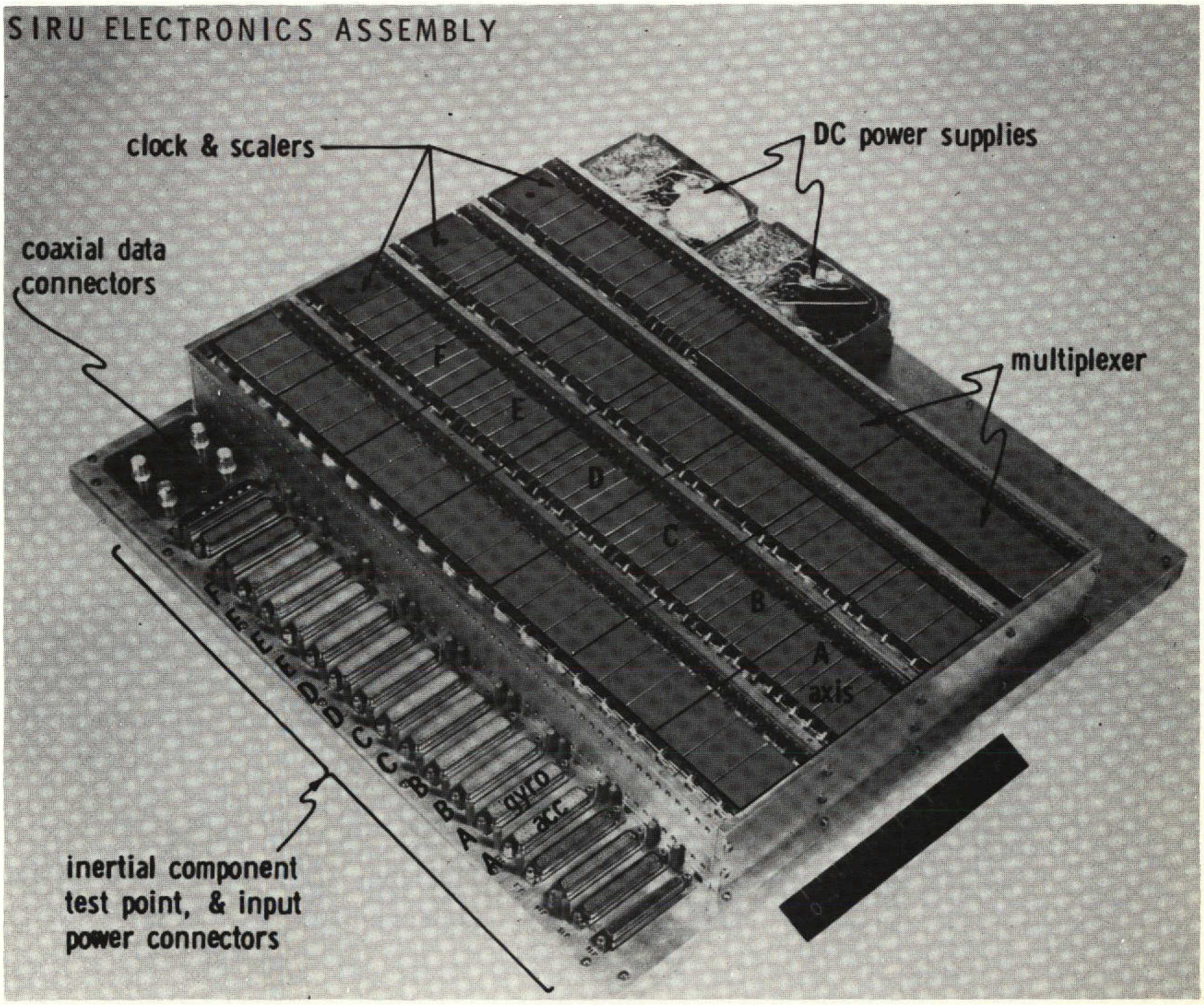

Fig. 3.1.2 SIRU Electronics Assembly.

3.1.1 Weight, Volume, and Power

The weight, volume and power requirements of the RIP and the EA are shown in Table 3.1.1. Project funding did not permit the development of microminiature electronics and the interface requirements limited possible size reductions. A production design without these restrictions would result in significant weight, volume and power reductions. A further breakdown of the components of the RIP is shown in Table 3.1.2.

Table 3.1.1 SIRU Weight, Power, and Volume

Assembly	Weight (lb)	Volume (in^3)	Power (watts)
Redundant Instrument Package (RIP)	62.94	1753.84	182.4
Electronics Assembly (EA)	33.50	1155.00	124.0
RIP—EA Harness	6.25	—	—
Totals	102.7	2908.84	306.4

Table 3.1.2 Redundant Instrument Package

Assembly	Qty	Dimensions (in)	Weight (lb)	Power (watts)
Gyro Module	6	5 1/4×4 3/8×4	4.35	23.0
Accelerometer Module	6	4 1/4×3 7/8×3 9/16	2.64	7.4
π-Frame	1	20 1/ 4×15 1/16×5 3/4	21.00	—

The SIRU configuration satisfies manned spacecraft design considerations (vacuum, thermal by conduction, etc.) and can be compared with the Apollo Inertial Subsystem (ISS) which has similar packaging density. The total Apollo equivalent ISS weight, volume and power is 93 lbs, 2654 in^3 and 216 watts, respectively. To achieve the same relative reliability as SIRU, such as would be required for the space shuttle, three to four such systems would be required.

As a development model constrained by the time line, fiscal and interface factors specified in the authorizing contract, the present RIP does not represent an ultimate design miniaturization, although it is a realizable competitive equipment configuration (the use of hybrid medium scale integrated electronic packaging techniques, for example, could reduce the system weight by over 50%). It serves to demonstrate the redundancy, the failure detection and isolation capability and the performance level to be expected from this type of equipment using a high reliability, low risk packaging technique.

3.2 Redundant Instrument Package

3.2.1 Inertial Component Mounting Concept

The formulation of a mounting concept for the inertial components (ICs) in the SIRU system was finalized after examination of all design objectives and constraints. The basic considerations were mounting frame complexity, instrument environmental sensitivities, module normalization requirements and interchangeability goals. Each of these basic considerations included supplementary elements that had to be considered with respect to each other without violating the objectives of in-flight maintainability and of form factor compatibility with the Apollo Command Module Lower Equipment Bay.*

Figure 3.2.1 shows one possible conceptual approach. This mechanization aligns the gyros such that all spin axes (SAs) are normal to the Z axis. The resulting advantage lies in the elimination of one of the g-sensitive drift terms during thrusting along the Z axis. The major drawback to this configuration is the degree of complexity required in the mounting frame. Figure 3.2.2 presents the concept that was implemented. The simple box shaped schematic reflects the ability to position the instruments in three orthogonal planes while maintaining each instrument's IA aligned normal to the face of a regular dodecahedron.

Using the "box" approach, several choices were available for the arrangement which provides the dodecahedron angle. Figure 3.2.3 illustrates two methods. In the first, the IA is aligned normal to its mounting base and the angle is machined into the mounting structure. In the second, which was the method selected, the dodecahedron angle is achieved at the module level. Figure 3.2.4 shows the IA

---

*The contract required mechanical and electrical interface compatibility with the Apollo GN&C equipment (see Chapter 1, Introduction).

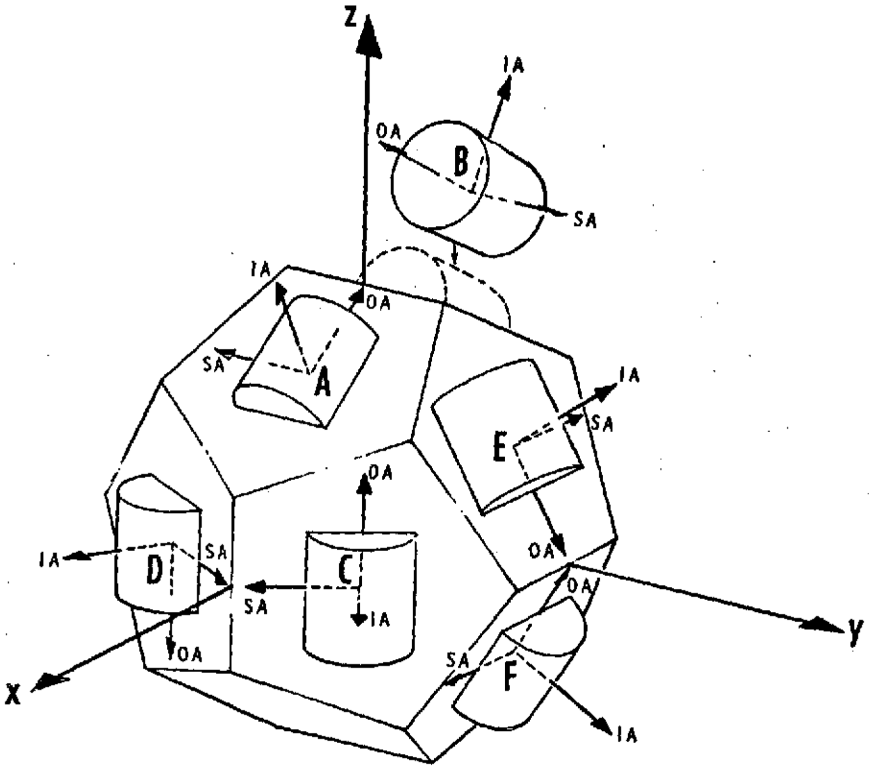

Fig. 3.2.1 Alternative Layout Gyro Spin Axes Normal to Z Axis

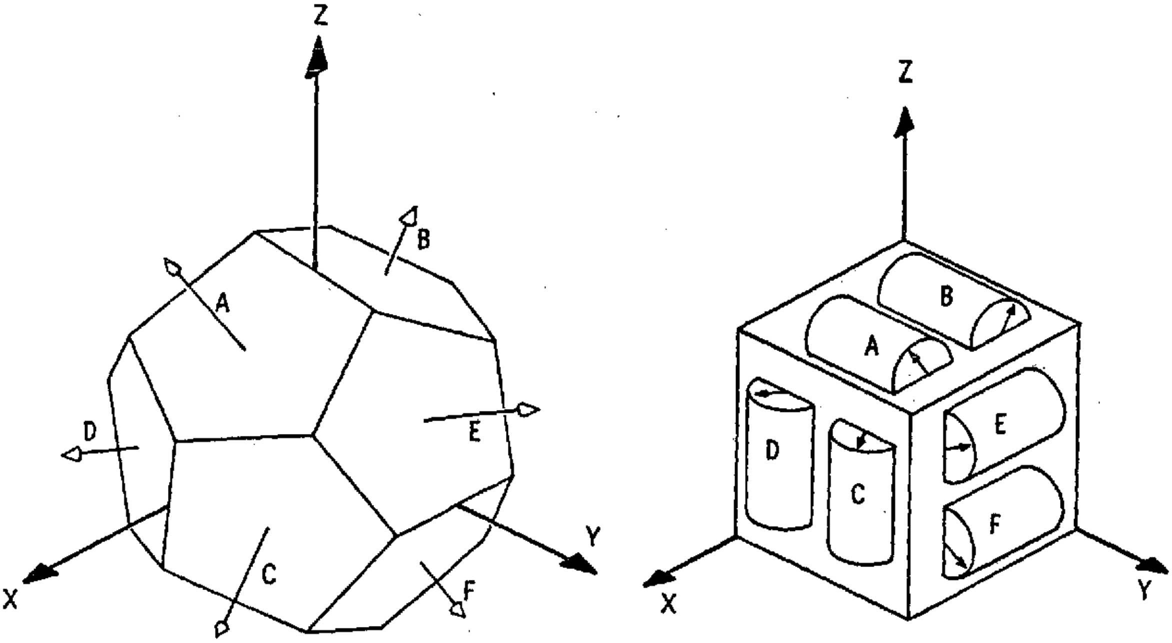

Fig. 3.2.2 Implemented Layout IAs Normal to Dodecahedron Faces

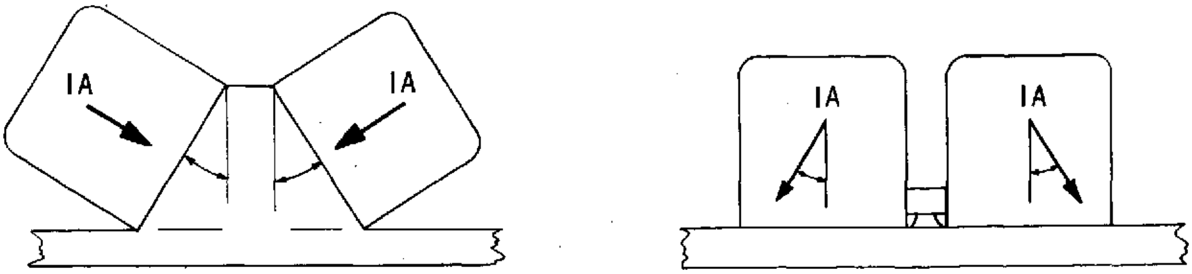

IA Aligned ⊥ Base No Alignment Pins Required.

ALTERNATIVE DESIGN
(a)

Aligned on Fixture with SIRU Angle Alignment Pins Required.

IMPLEMENTED DESIGN
(b)

Fig. 3.2.3 Possible I/C to π-Frame Interfaces

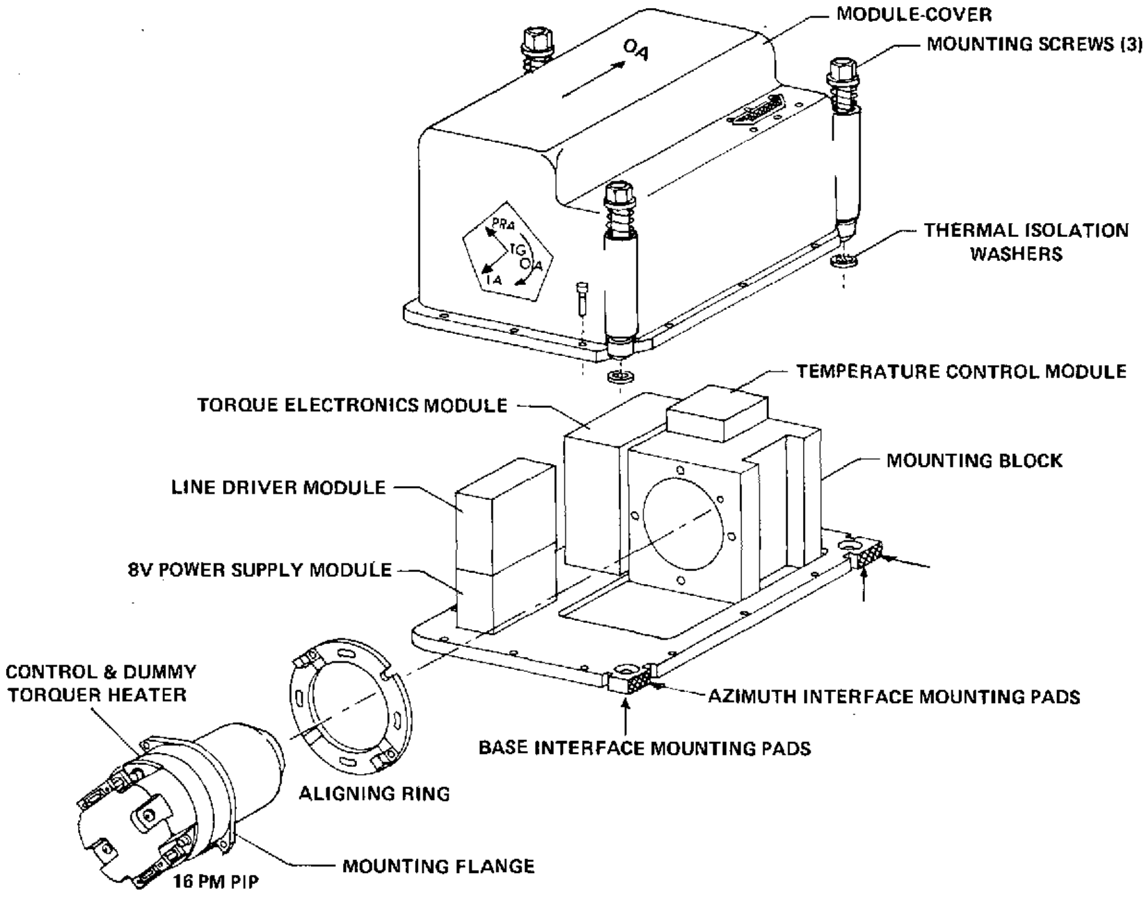

Fig. 3.2.4 Accelerometer Module Mounting & Alignment

alignment of the accelerometers and Fig. 3.2.5 illustrates the fixturing and test method utilized to achieve the proper IA alignment for the gyros. The arrangement finally chosen represented a modification of the "box" approach which placed all the instrument modules on the front face with the coldplate heat exchanger mounting from the rear. The resulting structure is referred to as the π-frame.

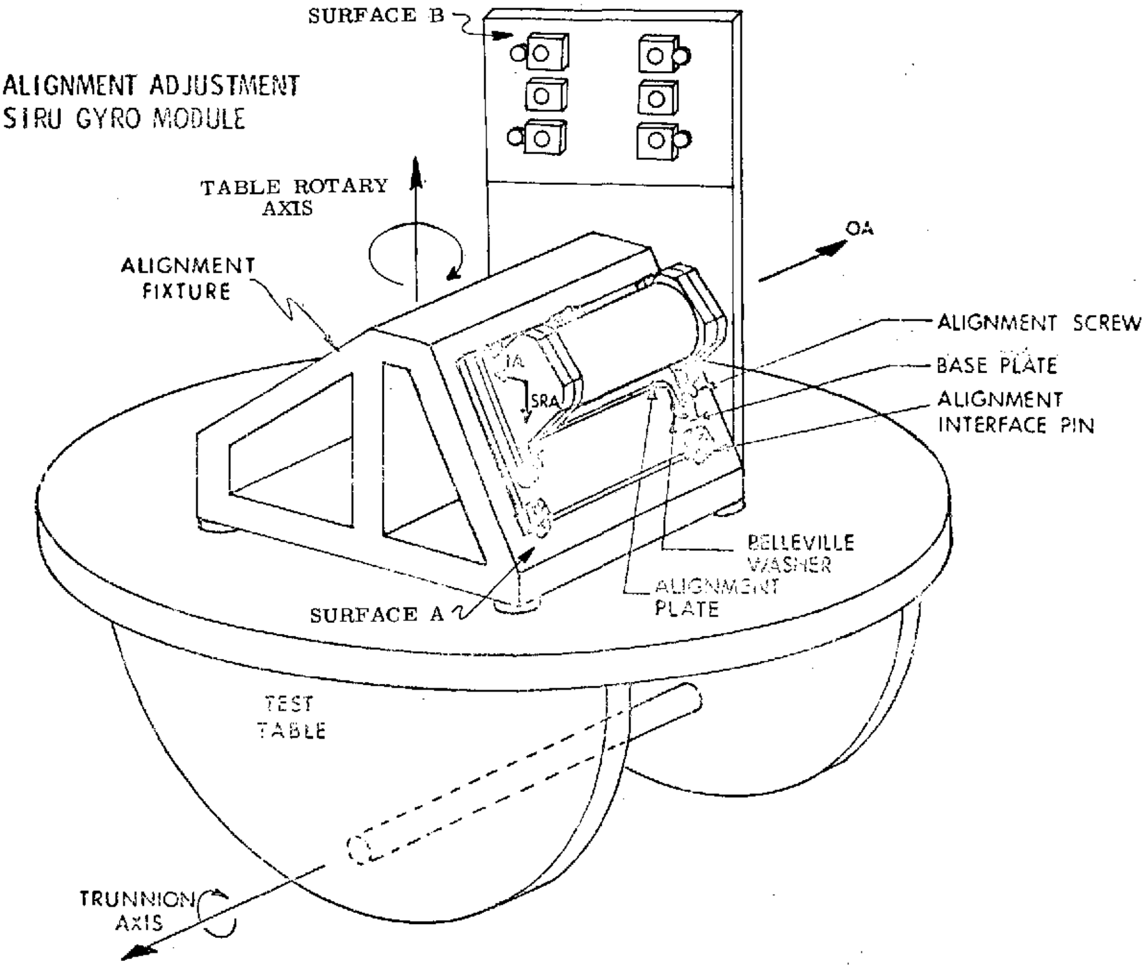

Fig. 3.2.5 Alignment Adjustment SIRU Gyro Module

The selection of this configuration resulted in the simplest design of the mounting structure with no sacrifice in interchangeability and performance. Experience has shown that replacement of a module in the system can be accomplished in less than ten minutes with a minimum possibility of damage and with an alignment repeatability better than 20 $\widehat{\text{sec}}$.

3.2.2 Mechanical Design of SIRU Redundant Instrument Package

The SIRU RIP assembly layout is shown in Fig. 3.2.6 with its wiring harness removed. This assembly consists of a π-frame, six gyro modules, six accelerometer modules, and a coldplate with overall dimensions of 19-7/8 inches by 15-1/16 inches by 5-3/4 inches and a weight of 70 lbs. with its harness.

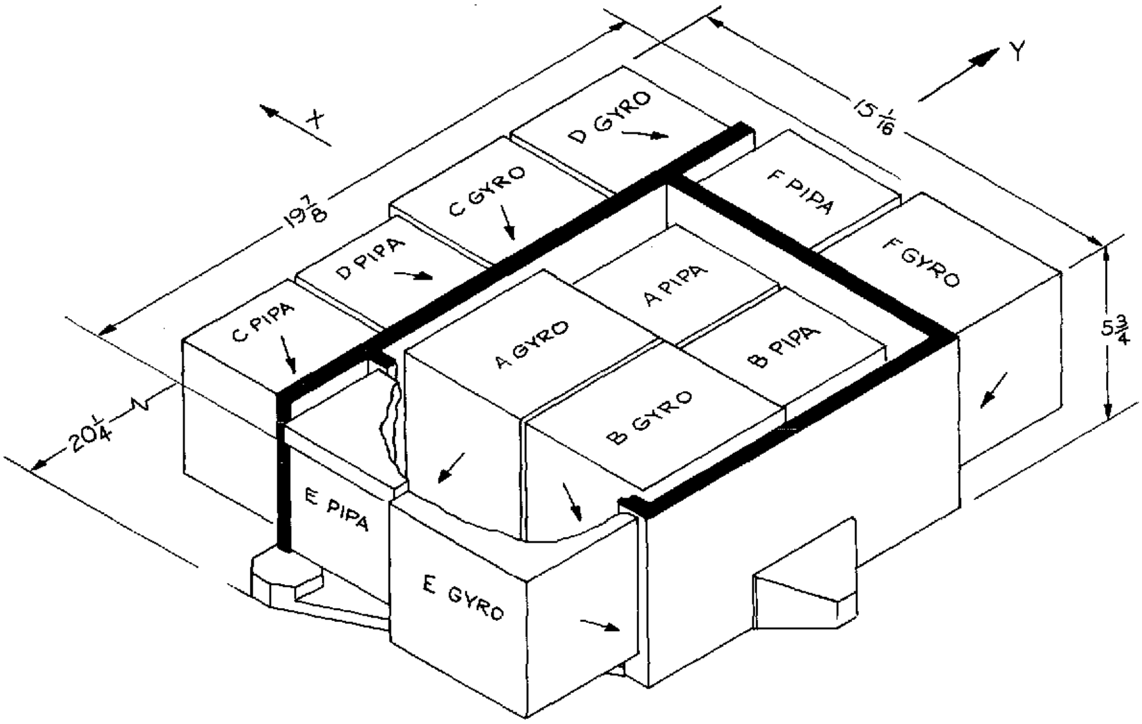

Fig. 3.2.6 SIRU RIP

The design objectives shown in Table 3.2.1 determined the RIP configuration. It was originally intended to be mounted within the Apollo Command Module Lower Equipment Bay with the coldplate connected to the spacecraft coolant lines. The RIP was to be removable without breaking these coolant lines. The frame was made as symmetrical as possible to obtain the structural rigidity and mounting stability necessary to maintain the alignment accuracies required for a strapdown system in a flight environment. This symmetry also contributed to good thermal design, providing minimum thermal gradients from component to component. A three-ball kinematic mounting arrangement was used to mount the RIP to the navigation base or to the test base. The parts used in this mounting arrangement are identical to the Apollo Optics Assembly mounting hardware. The ICs were prealigned and modularized for interchangeability. The frame design was constrained to be as simple as possible for ease of fabrication. Structural dimensioning and design tolerances necessary to meet the mechanical requirements shown in Table 3.2.2 were implemented. Figure 3.2.7 shows the π-frame consisting of a 6061 aluminum dip-brazed structure with inserts for mounting the instrument modules. The ICs are mounted on four mutually perpendicular planes (the Y axis plane is split in two to keep the design compact and symmetrical). An optical cube mounted on the under side of the Z axis plane is visible through a hole in the plane and from the X and Y directions. A flat mirror is also mounted on each of the IC mounting planes. These mirrors were used for alignment and positioning checks during tests. Different insert materials are used for mounting the gyros than are used for the accelerometers because of the difference in power dissipations; the gyro pads require a larger thermal resistance because of higher dissipation. Both materials had to be hardenable and suitable for lapping to meet the tolerance requirements. Carpenter 455 stainless steel for the accelerometers and beryllium copper #25 for the gyros are the materials employed.

Table 3.2.1 SIRU Design Objectives

1. STRUCTURAL RIGIDITY AND STABILITY
2. THERMAL BALANCE AND GRADIENTS
3. PREALIGNED AND INTERCHANGEABLE I/C MODULES
4. FIT APOLLO LEB WITH S/C HEAT EXCHANGER
5. TOLERANCED TO MEET DESIGN OBJECTIVE ACCURACIES
6. PRODUCIBILITY

Table 3.2.2. Mechanical Design Requirements.

RIP AXES TO OPTICS LOS	20 s$\widehat{\text{ec}}$s
PI FRAME TO NAV BASE	5 s$\widehat{\text{ec}}$s
PADS AND PINS, X TO Y TO Z TO OPTICAL CUBE	5 s$\widehat{\text{ec}}$s
THERMAL GRADIENTS	5 s$\widehat{\text{ec}}$s
STRUCTURAL LOADING AND STABILITY	10 s$\widehat{\text{ec}}$s

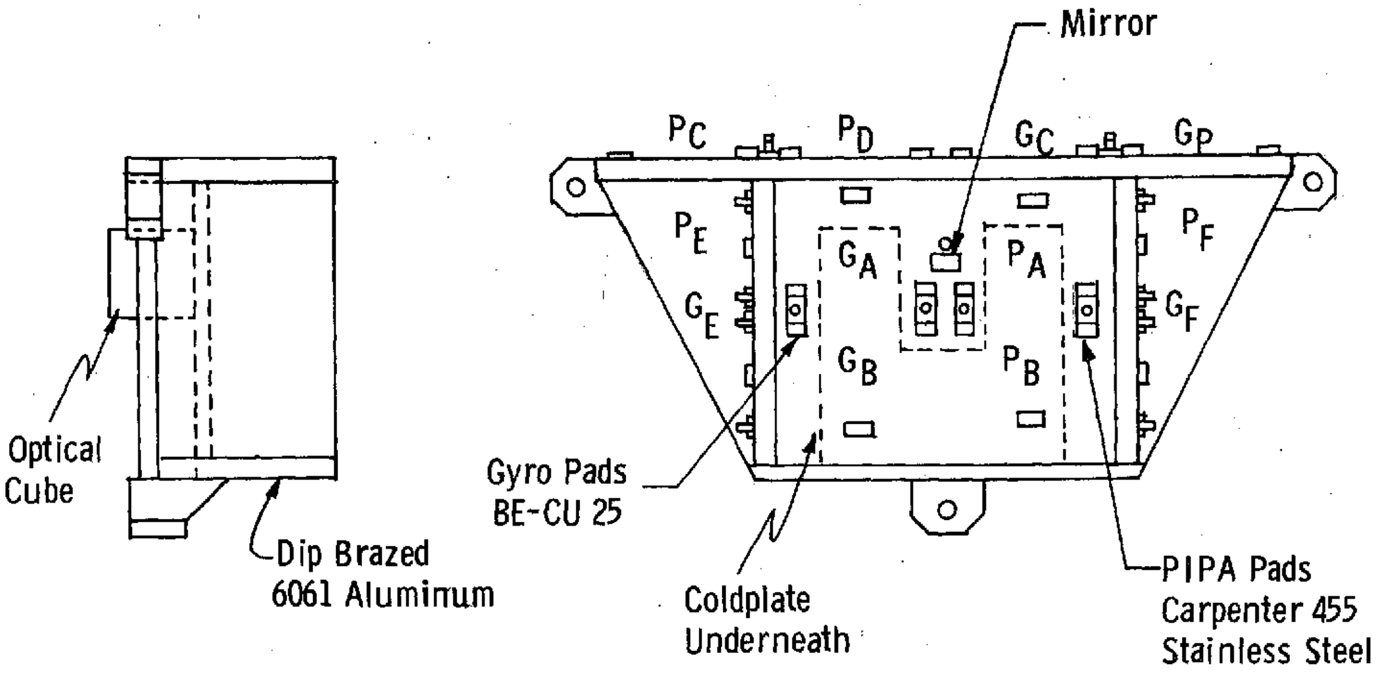

Fig. 3.2.7 SIRU π Frame

Figure 3.2.8 shows a cross section through an IC mounting pad including the tungsten carbide alignment pins which maintain alignment about the axis perpendicular to the mounting plane. Typical tolerances required to meet the mechanical design requirements of Table 3.2.2 are: flatness—50 microinches; perpendicularity and parallelism —100 microinches; and finish—4 to 8 microinches.

System tests were performed to determine π-frame distortion under extreme thermal gradients.

The testing was accomplished by mounting "dummy" thermal gyro and accelerometer modules on the π-frame and running the following sequence of tests.

1. Power to modules on right half of structure
2. Power to modules on left half of structure
3. Power to all modules
4. No power

The results shown in Table 3.2.3 proved the π-frame to be relatively insensitive to even large thermal gradients.

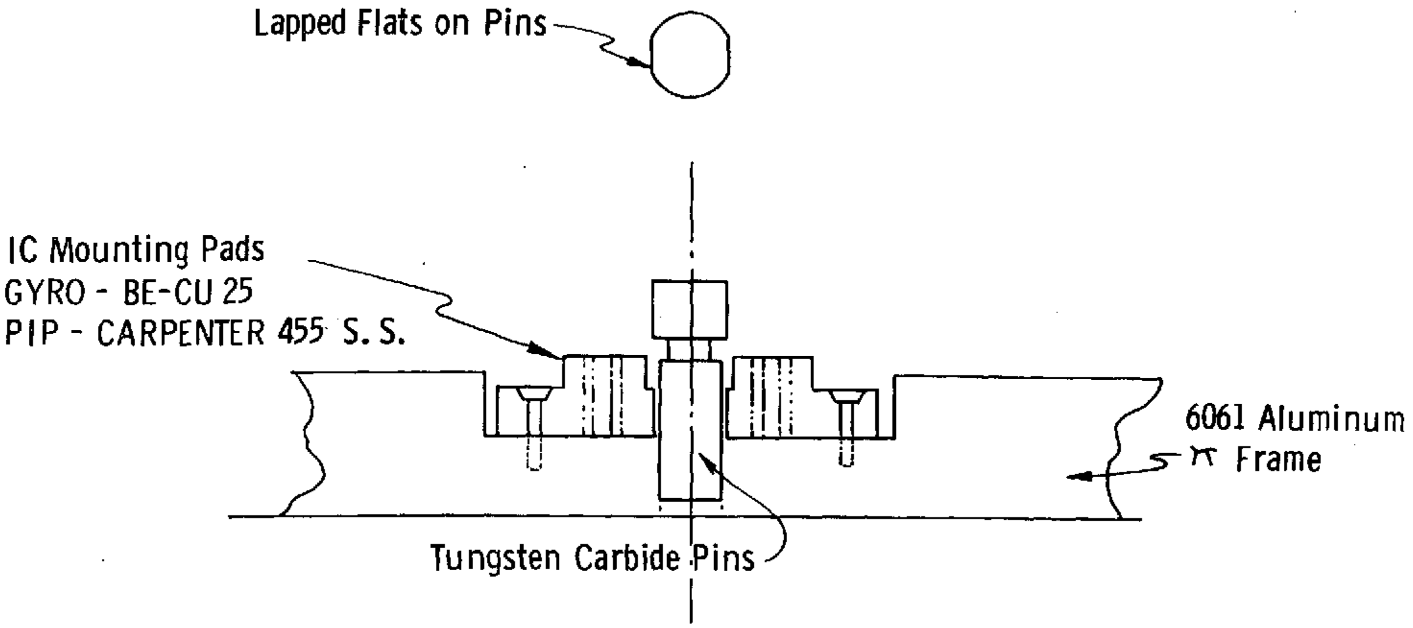

Fig. 3.2.8 IC Mounting Pads

Table 3.2.3 π-Frame Thermal Test Results

GYRO MODULE: 21 WATTS
ACC MODULE: 7 WATTS

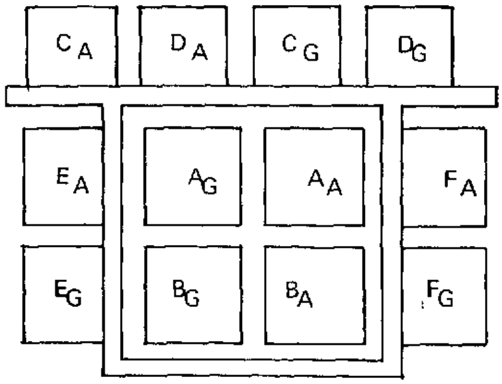

TEST CONDITION			MISALIGNMENT ARC SEC	
	MODULES EXCITED	COOLANT FLOW	X – X	Y – Y
I.	ACCS: A, B, F GYROS:C, D, F	OFF	–10.2	+ 7.1
		ON	– 9.7	– 1.8
II.	ACCS: C, D, E GYROS:A, B, E	OFF	+ 11.2	– 11.0
		ON	+ 10.6	– 3.5
III.	ACCS: C, D, GYROS: C, D	OFF	– 5.6	+ 4.0
		ON	– 4.7	+ 14.4
IV.	ACCS: ALL GYROS: ALL	ON	+ 1.4	– 6.2
V.	——	ON	+ 1.4	+ 0.5

3.2.3 Modularized Assemblies

The function of the gyro module is to sense the component of rotation being applied along its IA and deliver as its output a sequence of weighted pulses which defines the magnitude and sign of the rotation. The action is accomplished by closing a ternary loop around the gyro by means of precision current pulses to the gyro torquer. The general specification requirements for the gyro module including scale factor and drift parameters, input and output power and signal characteristics and tolerances, thermal limitations and other system features are provided in Appendix C.

Modularized IC assemblies were incorporated in the SIRU system to meet the requirement for in-flight maintenance. The modules are configured mechanically, thermally, and electrically to make replacement as simple and straightforward as possible. To accomplish a removal it is only necessary to loosen three screws conveniently located on the module, disengage a single multi-pole connector and lift the module from the π-frame. Replacement reverses the procedure. This capability for simple in-flight replacement depends on the prealigned, normalized condition of each module, the accuracy of the remount alignment provision, the rugged construction of the assembly, the accuracy and stability of the prealignment operation and the self-calibration features of the SIRU.

The following is a technical description of the gyro module. Substantially the same description, accompanied by test results, performance analysis and comparisons, including a description of the gyro module test equipment and procedures, is presented in Volume II of this report. The accelerometer module concept is very similar; a 16 PM PIP Accelerometer (PIPA) is substituted for the 18 IRIG Mod B gyroscope. The accelerometer is also used in a Navy project and the material describing the accelerometer module performance is presented in Volume IV (classified CONFIDENTIAL).

The functional block diagram of the gyro module is shown in Fig. 3.2.9. The gyro module consists of the following components:

1. Gyro - 18 IRIG Mod B
2. Gyro Pulse Torque Electronics (PTE)
3. Interpolator/Compensator
4. 8 Volt Power Supply
5. Torquer Tuning Network
6. Bandpass Preamplifier
7. Temperature Controller
8. Normalization Assembly

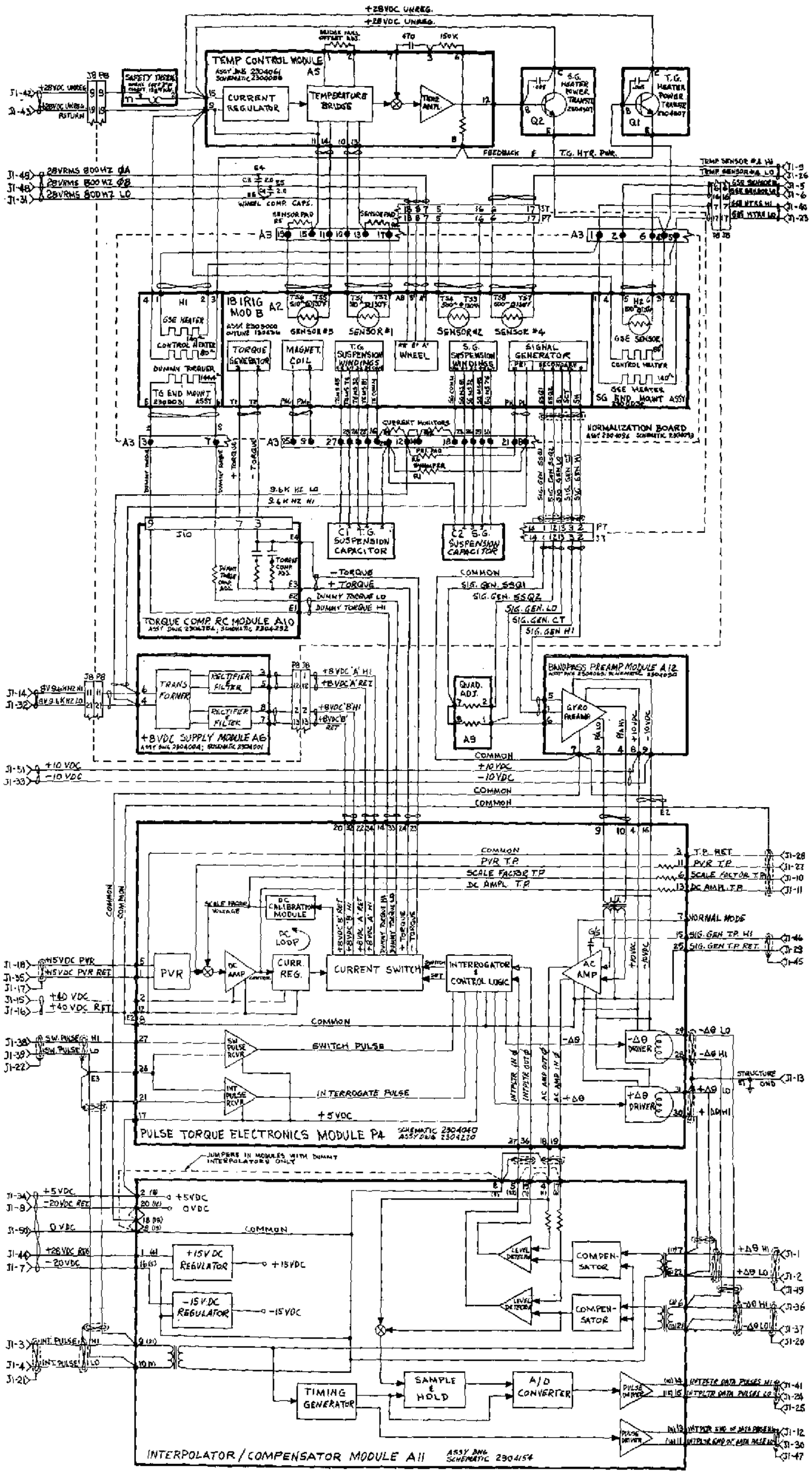

Fig. 3.2.9 A Functional Block Diagram of the Gyro Module

A description of the function and principal features of each component follows. Additional information may be found in Volume II.

1. Gyro - 18 IRIG Mod B

General Description

The 18 IRIG Mod B is an advanced design, gas bearing instrument specifically designed by the Draper Laboratory for the strapdown application. Fig. 3.2.10 is a cutaway view of the 18 IRIG Mod B 420 series gyroscope showing the various components. The wheel, made from a fine-grained, hot pressed, alumina ceramic, rotates at 24,000 rpm on a spool type gas bearing generating an angular momentum of 150,000 gm-cm^2/sec. The ceramic encapsulated motor stator enhances float mass stability, and reduces the possibility of condensed contaminants on the bearing surfaces.

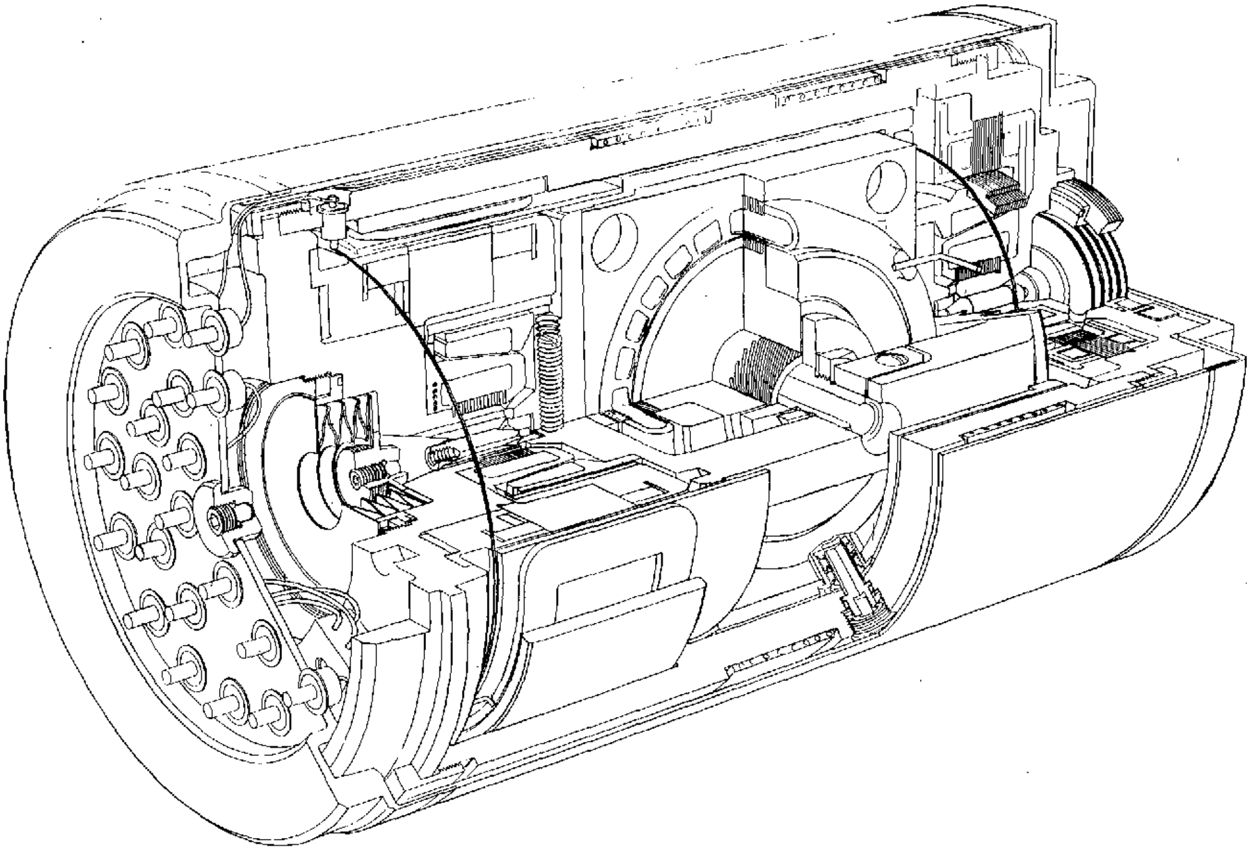

Fig. 3.2.10 18 IRIG Mod B

The float, which houses the wheel and stator, is fabricated from a high precision-elastic-limit beryllium which combines low density with excellent stability. It is surrounded by and floated in a high density, controlled viscosity, chemically inert dielectric fluid maintained at a precisely controlled temperature. The fluid isolates the float from environmental inputs and provides the damping which is an essential characteristic of the single degree-of-freedom (SDF) integrating gyroscope. The float inertias and compliances about the SA are matched to those of the IA to minimize dynamic errors from these sources.

The permanent magnet torquer (PMT) is capable of developing 150,000 dyne-cm of torque, sufficient to balance an input rate of one rad/sec. Tapered electromagnetic suspensions provide radial and axial stiffness capable of restraining the float at the rated input angular velocity. The angular position of the float from its null location is measured by a multiple E type signal generator (SG). SG sensitivity when excited by an 8v, 9600 Hz source is 20 mv/milliradian.

The instrument is hermetically sealed within a Mumetal shroud to augment magnetic isolation, aid heat transfer control and protect the gyro from unauthorized adjustment. Temperature control and monitoring are provided by four nickel wire wound sensors controlling heaters which are located on the gyro end mounts. The complete instrument measures approximately 2 inches in diameter and 3 7/8 inches long. Weight is 1.15 pounds. A summary of the characteristics of the 18 IRIG Mod B gyro is presented in Table 3.2.4.

Pulse Torque-to-Balance Operation

The gyro in the SIRU system operates in a closed loop where the torques on the float are restrained by torques developed by the torque generator (TG). See Fig. 3.2.11.

An angular rate imposed about the IA of the gyro produces a torque about its OA and causes the float to rotate from the SG null position. The direction and magnitude of the float rotation are detected by the SG, and when the SG output voltage reaches a given threshold level, a discriminator provides a positive or negative set signal, depending on the polarity of the SG output voltage. These set signals are interrogated at a given frequency to switch a current pulse of fixed amplitude and duration to the TG winding. In the control loop mechanization, a principle error source is inaccuracy in the torque pulse area. For example, a torque pulse of 100 ma amplitude and 200 microseconds width exhibiting a variation from nominal

Table 3.2.4 18 IRIG Gyroscope Characteristics

Single Degree of Freedom Floated Gyroscope

Weight: 1.15 lbs (523 gms)

Size: 2 inch (5.08 cm) Diam. 3.86 inch (9.8 cm) Long

- Wheel:

Self acting spool type gas bearing (Aluminum oxide)

Angular Momentum - 150,000 gm-cm^2/ sec (24000 RPM)

Maximum Capabilities - 5 Rad/sec about IA
> 50 g's 60-400Hz

Synchronous Motor - 4 pole 2ϕ 28v 800Hz
2.6 watts/ ϕ running

Drift Sensitivity - 0.004°/ Hr per Volt

- TORQUER:

Permanent Magnet - 8 poles, Alnico V IX, ring poles
1 Rad / sec at 3 watts

- COIL HOLDER - 8 coils on Beryllium Oxide holder

- SF SENSITIVITIES TO FLOAT MOTION:

Radial - 50ppm for 0.4×10^{-3} inches,
Equiv. to 1.0 Rad / sec about OA

Axial - 50ppm for 0.25×10^{-3} inches,
Equiv. to 10g accel or 2° F off flotation

Rotational - 50ppm mill i Rad
i.e. 3ppm for

Thermal - 10ppm / °F

- STABLE MAGNET CHARACTERISTICS

Decay 60ppm per decade
(magnetized after assembly)

- LOW DRIFT SENSITIVITY- For Torque Power Cycling

Table 3.2.4 IRIG Gyroscope Characteristics (Cont)

- Thermal:
  - Flotation Temperature - 132°F
  - Drift Sensitivity - <.03°/ Hr per °F
  - Storage 20°F - 180°F nominal
- Miscellaneous
  - Gyro Elastic Restraint <0.1 dyn cm per mr
  - Float & Housing - Beryllium
  - Fluid - Brominated fluorocarbon
  - Magnetic - vacuum shroud
- Suspension:
  - 8 Pole - Electromagnetic Tapered Suspension

    Prevents radial side-loading ≤1 Rad/ sec - OA
    Prevents axial loading < 20g 2° F
    Reaction torque sensitivity < 0.015°/ Hr - 1% Excitation
  - Excitation - 8V - 9600Hz 0.83 watts
- Signal Generator:
  - Microsyn - 12 Pole E Type
  - Sensitivity - 4.4mv/ mr (IA) $\Delta\theta \sim 0.9$mv
  - Noise - pickup 800Hz < 160 microvolts

    modulated ± 1.6KHz < 10 microV
  - Excitation - 8V - 9600Hz 7 ma

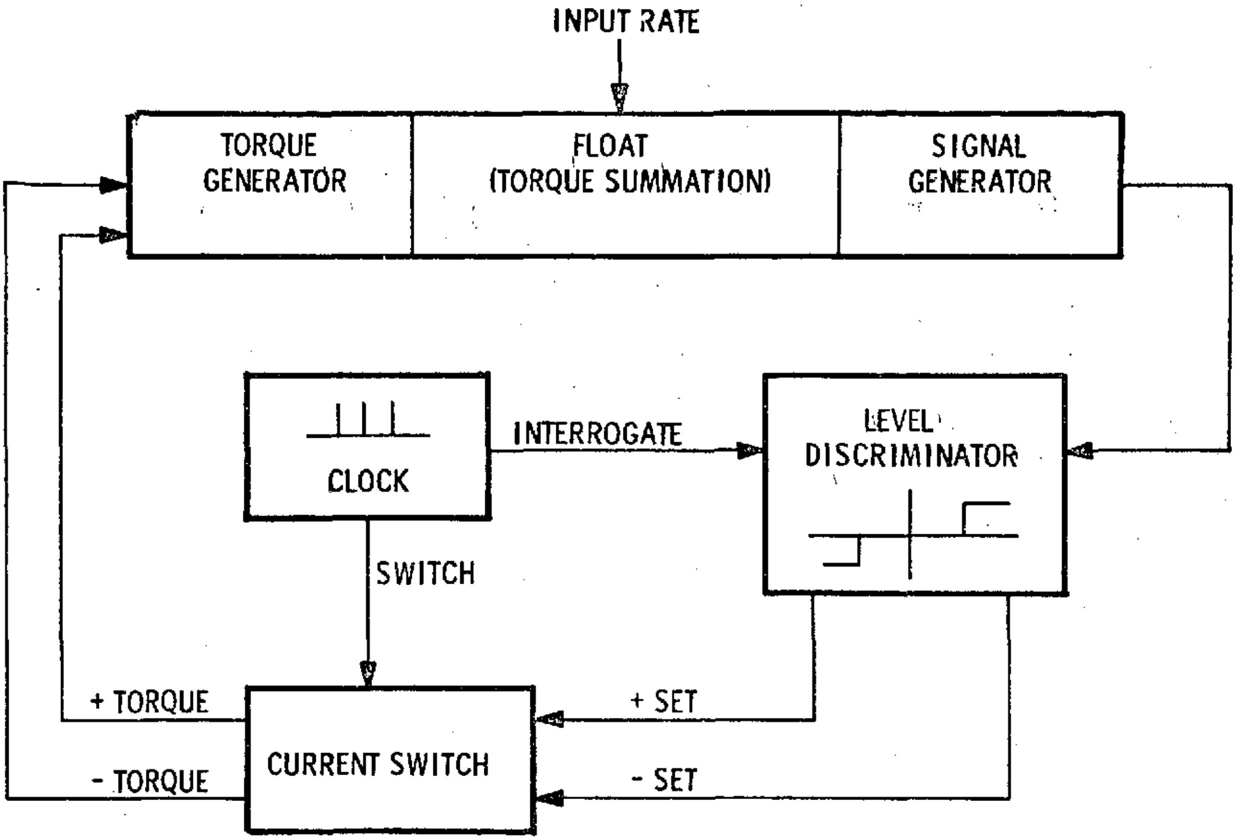

Fig. 3.2.11 Block Diagram-18 IRIG Closed Loop

of 10^{-4} ma in amplitude or 2×10^{-10} sec in width will cause an error in scale factor of one ppm.

Gyro and accelerometer module specifications and input/output characteristics are provided in Appendix C. The gyro module electrical schematic is Dwg. No. 2304040 and the corresponding schematic for the accelerometer module is Dwg. No. 2640424.

2. Gyro Pulse Torque Electronics

The function of the gyro PTE is to receive the output from the gyro SG, evaluate the threshold level in the torque control logic and, if ordered, supply current pulses to the gyro TG as required to reduce the SG signal below the threshold. The width of the current pulse is controlled by timing pulses transmitted by the torque control logic and the amplitude of the current pulse is maintained by a feedback loop involving the comparison of a precision voltage reference (PVR) and a current sampling resistor. The current pulse is transmitted to the gyro TG through a current switch which is set by the torque control logic to provide the appropriate polarity. The operation of the PTE is described in detail below.

The output signal from the gyroscope is first amplified by a bandpass preamplifier, fed into the ac amplifier (x10) in the PTE and then to a comparator or threshold device (essentially a strobed Schmitt trigger).

As shown in the Timing Diagrams, Figs. 3.2.12 and 3.2.13, and the logic diagram, Fig. 3.2.14, the comparator is strobed by the leading edge of the 4800 pps interrogate pulse (INT) which coincides with the peak of the 9600 Hz signal at the comparator. A phase shift adjustment is made in each module to the SG signal in the bandpass amplifier to insure this relationship. If, (referring to Fig. 3.2.14) at the instant of strobe (INT), the peak level of the amplified SG voltage exceeds the positive threshold level (equivalent to 44 $\widehat{\text{sec}}$ input) and is in phase with the INT pulse, a positive level detect signal is generated which sets the positive level detect flip-flop (+LDFF) to its positive state. The output of the +LDFF then sets the torque motor set flip-flop (TMSFF), (Fig. 3.2.15), to its negative state (S2,4=-; S3,5=+). The positive output of the TMSFF turns on Q3 and Q5 which sets up the current switch for a negative torque current command.

The output of the +LDFF is also summed with the reset and INT pulses in the positive $\Delta\theta$ AND gate to generate a $\Delta\theta$ pulse upon receipt of the reset pulse. This $\Delta\theta$ pulse goes to the computer.

The output of the +LDFF also goes to the torque switch AND gate where it is summed with the INT and the switch pulses. When the switch pulse occurs, a torque switch pulse is generated which sets the torque switch reset flip-flop (TSRFF) to its switch state so that its output turns on Q6 and turns off Q7. This sets up the current switch to send current to the torquer winding instead of to the "dummy" torquer.

After 195.33 microseconds, the INT pulse (4 microseconds wide) starts, followed 2 microseconds later by the reset pulse (0.4 microseconds wide). These pulses are summed in the torque reset AND gate which sends a pulse to the TSRFF switching it back to its reset state so that Q6 turns off and Q7 switches on, returning the current flow to the "dummy" torquer load.

A similar sequence occurs when the negative threshold level is exceeded except that a positive torque current and a negative $\Delta\theta$ are generated.

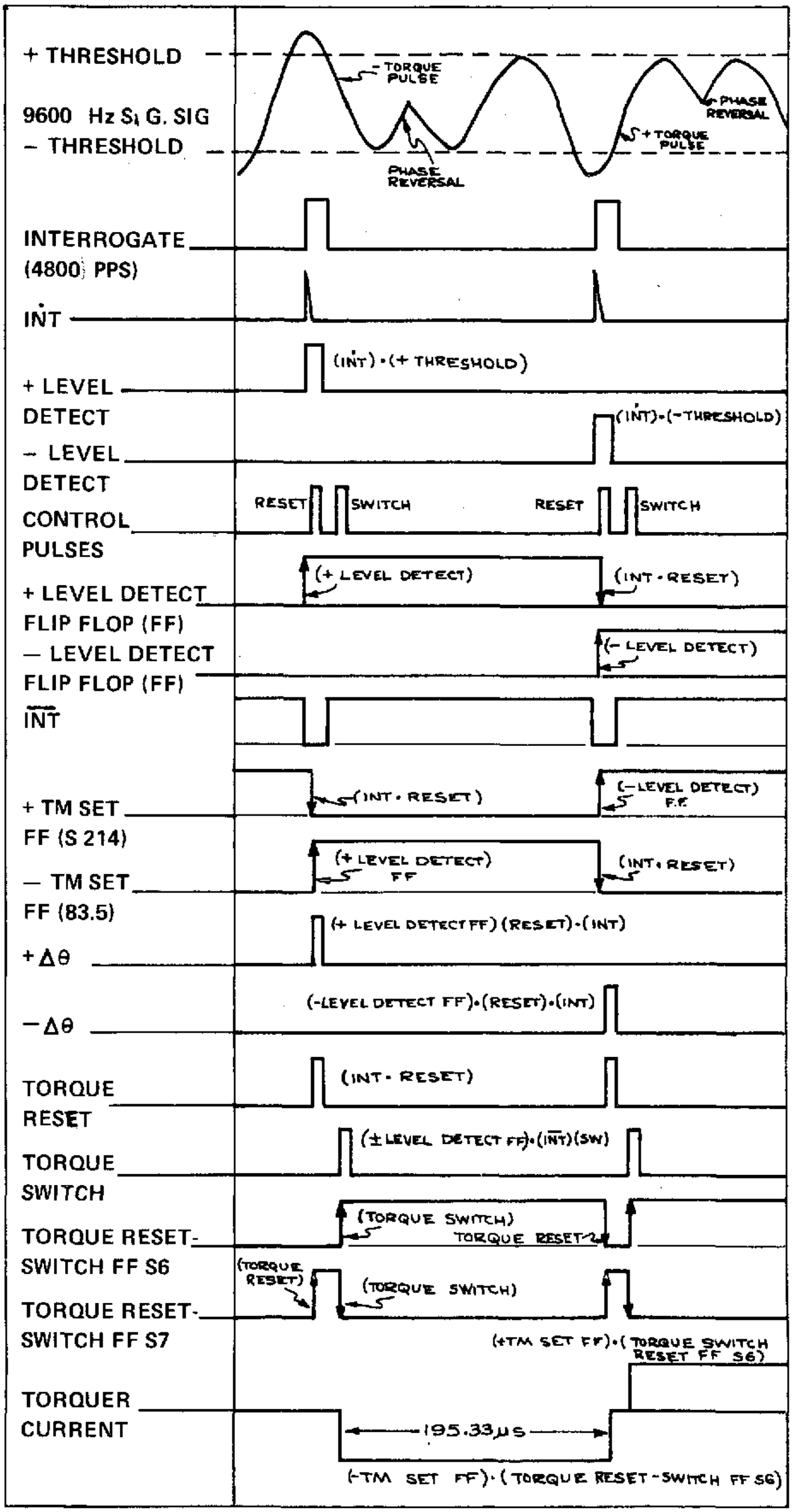

Fig. 3.2.12 PTE Timing Diagram

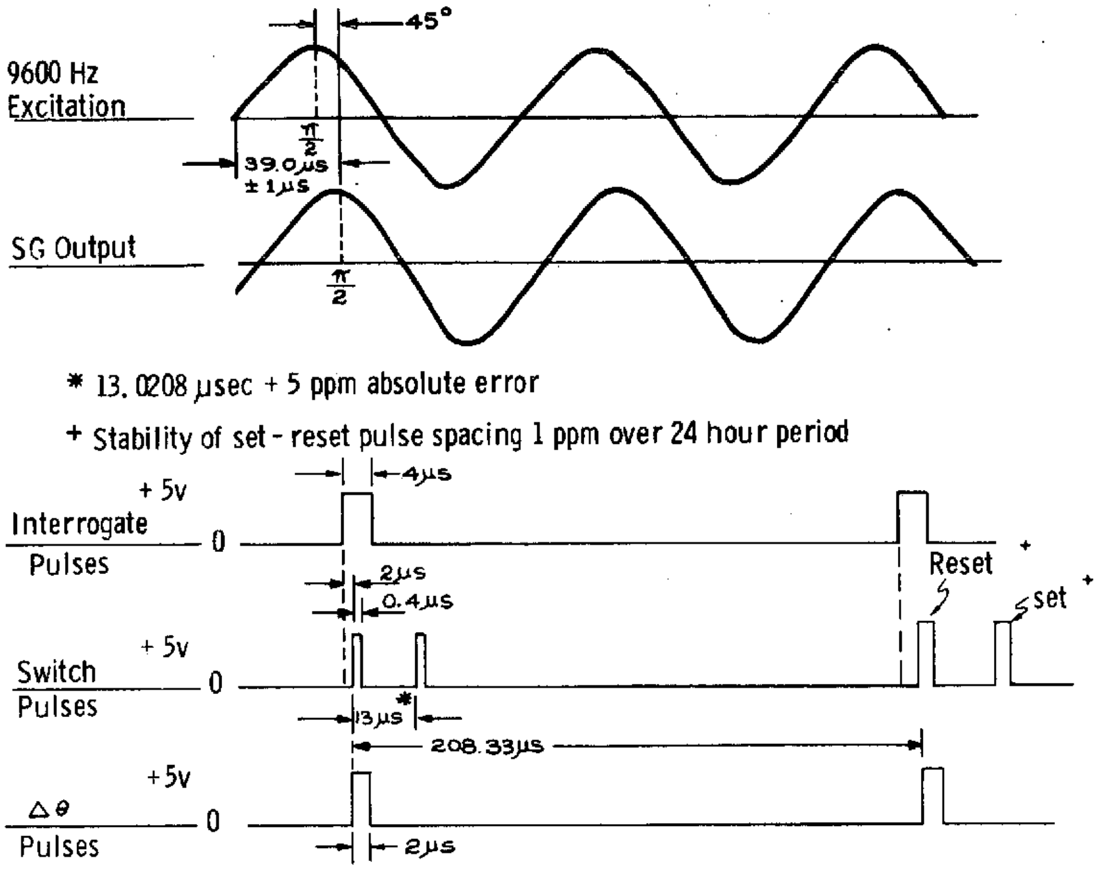

* 13.0208 µsec + 5 ppm absolute error

+ Stability of set - reset pulse spacing 1 ppm over 24 hour period

Fig. 3.2.13 SIRU Gyro Module—Timing

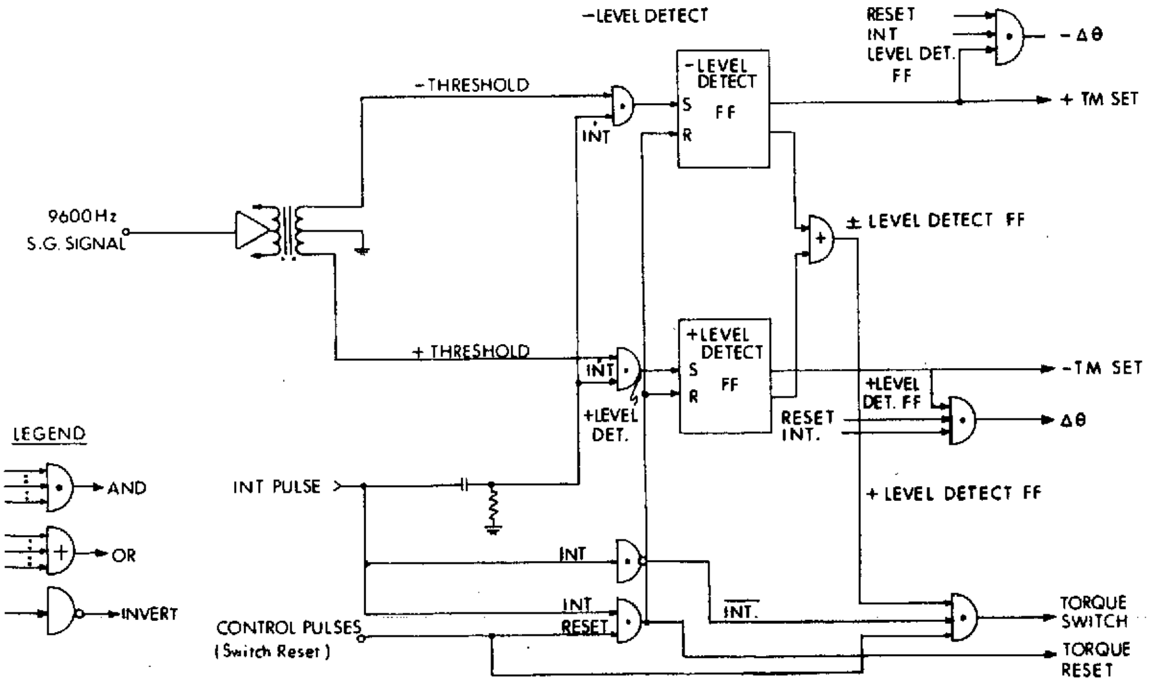

Fig. 3.2.14 PTE Logic

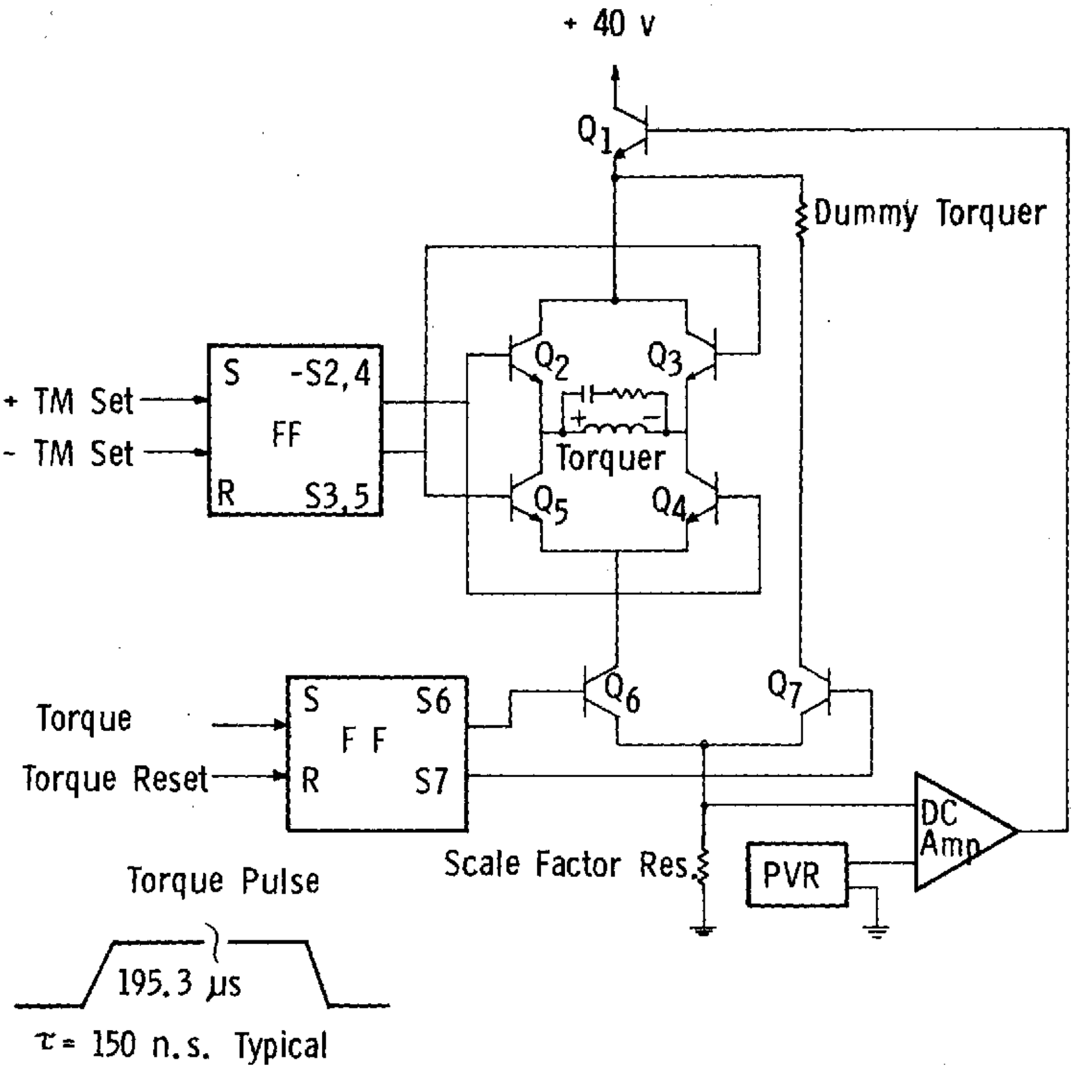

Fig. 3.2.15 PTE "H" Switch.

The torque delivered to the gyro is a function of the duration and amplitude of the torque current pulse. The pulse width and gyro torquer sensitivity define the pulse scale factor (SF) quantization (44 $\widehat{\text{sec}}$). The pulse duration is determined by the time between the reset and switch pulses and is 13.028 microseconds ± 5 ppm. A stability of 1 ppm over a period of 24 hours is characteristic of the SIRU performance. The amplitude is maintained by the Torque Current Loop, Fig. 3.2.16. This control loop compares the voltage drop across a precision (standards quality) resistor with the PVR. The difference voltage is amplified by the high gain dc amplifier and fed back to Q1 which controls the torque current supply to maintain a constant current amplitude.

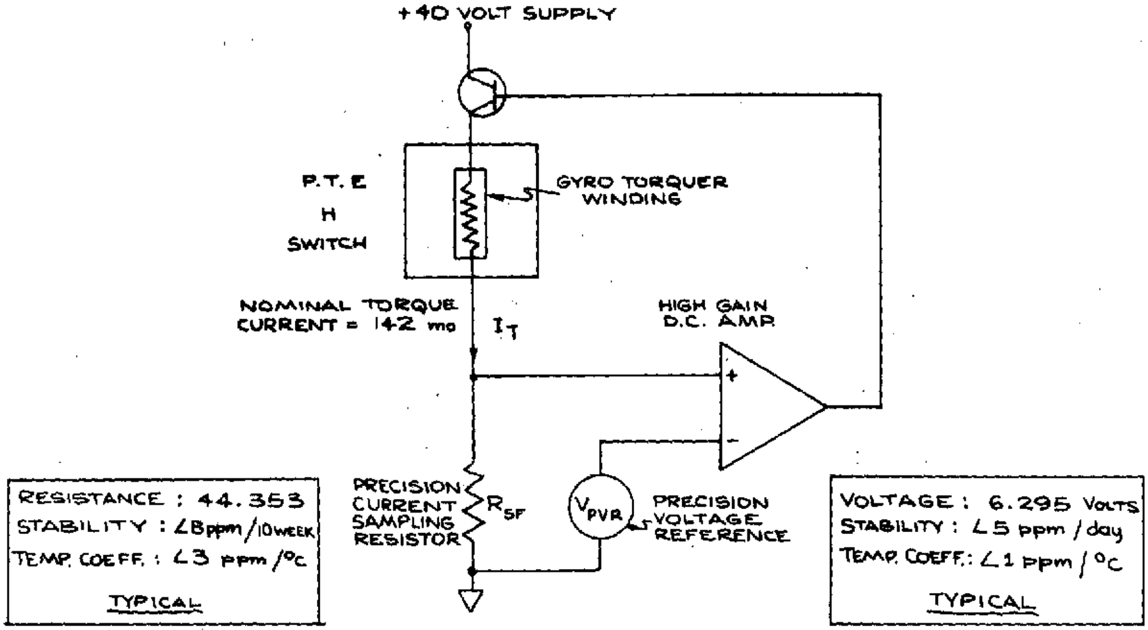

Fig. 3.2.16 Torque Current Loop

The stability and absolute magnitude of the torque current are, therefore, established by the PVR, the current sampling resistor (scale factor) and the high gain dc amplifier. For a given PVR and dc amplifier, the absolute magnitude of the current is determined by the SF resistor which is selected to match the measured gyro SF within 200 ppm. The SIRU loop has demonstrated a long term amplitude stability of 10 ppm.

The mode of operation for the accelerometer loop is intrinsically identical. Minor parameter differences result from the relative torquer requirements and normalization practices at the instrument level. The general characteristics of the accelerometer and its module are shown in Table 3.2.5.

The timing inputs to the torque control logic are reshaped by means of pulse receivers, one for the interrogate and one for the switch pulse train. The calibration stability of the module is largely dependent on the rise time characteristics of the pulse trains. Low noise performance is achieved using a single diode level "standoff" coupled to a fast rise, two stage pulse amplifier. Output $\Delta\theta$ lines are transmitted to the computer through line drivers to compensate for possible variation in transmission line length, performance characteristics and pickup. The line drivers consist of blocking oscillators designed to provide ground decoupling and a high level of cable drive power.

Table 3.2.5 SIRU Module/PIPA Characteristics

PIPA Module

1. Dimensions	4.3 in. x 3.9 in. x 3.6 in.
2. Volume	58.4 in.^{3}
3. Weight	1170 gm
4. Power	9 watts

PIPA

1. Physical Description	
a) Length	2.1 in.
b) Diameter	1.6 in.
c) Weight	354 gm
2. Configuration	
a) Signal Generator Type	Microsyn
b) Torque Generator Type	Permanent Magnet
c) Pendulum Support	Floated and Magnetic Suspension
3. Pendulosity	1 gm cm
4. Damping Coefficient	120,000 dyne-cm/rad/sec
5. Operating Temperature	130°F
6. Torque Parameters	
a) Mode	Pulsed—Ternary
b) Nominal Scale Factor	4 cm/sec/pulse
c) Interrogation Rate	4800 pps
d) Maximum Torque Rebalance Capability	19.0 g
7. Power	
a) Signal Generator	0.04 watts
b) Torque Generator	0.75 watts
c) Magnetic Suspension	0.6 watts

3. Interpolator/Compensator

The Interpolator/Compensator (schematic Dwg. No. 2304154) provides a dual function. As a compensator it substantially eliminates the effect of the dynamic characteristics of the gyro float and linearizes the gyro torque loop pulse output response to the applied input rates. Without this compensation, lagging gyro float response to a torque pulse can result in multiple pulsing. In the uncompensated

SIRU pulse torque-to-balance control loop at an interrogation rate of 4800 pps and with a ratio of float inertia to OA damping of 330 microseconds, multiple pulses do occur. In the accelerometer the ratio is much smaller and compensation for float dynamics was not considered necessary.

The float response to a single torque pulse provides insight into this effect of lagged response on closed loop operation. Less than one fifth of the total float motion response to a single, fixed magnitude torquing pulse, 195 microseconds in duration, occurs in the first sampling period (at the 4800 pps interrogation rate). Thus, if the angular rate about the gyro IA is in excess of 15% of the full-on torque loop capability, the torque loop will always pulse again because only 15% of the commanded return travel has occurred before the next interrogation. Over a total indicated angle the pulse bursting results in an instantaneous reading error and the base $\Delta\theta$ resolution is not realized. A compensation technique to eliminate this problem is shown in Fig. 3.2.17. Analog voltages, ±E Comp, are developed by generating a 206.3 microsecond pulse from a flip-flop circuit which is set and reset by the $\Delta\theta$ and interrogate pulses, respectively. This pulse, which is approximately the same length as the torque command (195.3 microseconds) is integrated by an RC network to generate a voltage of the proper phase and magnitude so that when summed with the gyro SG signal, the combined signal compensates for the gyro float time constant and eliminates the multiple pulsing.

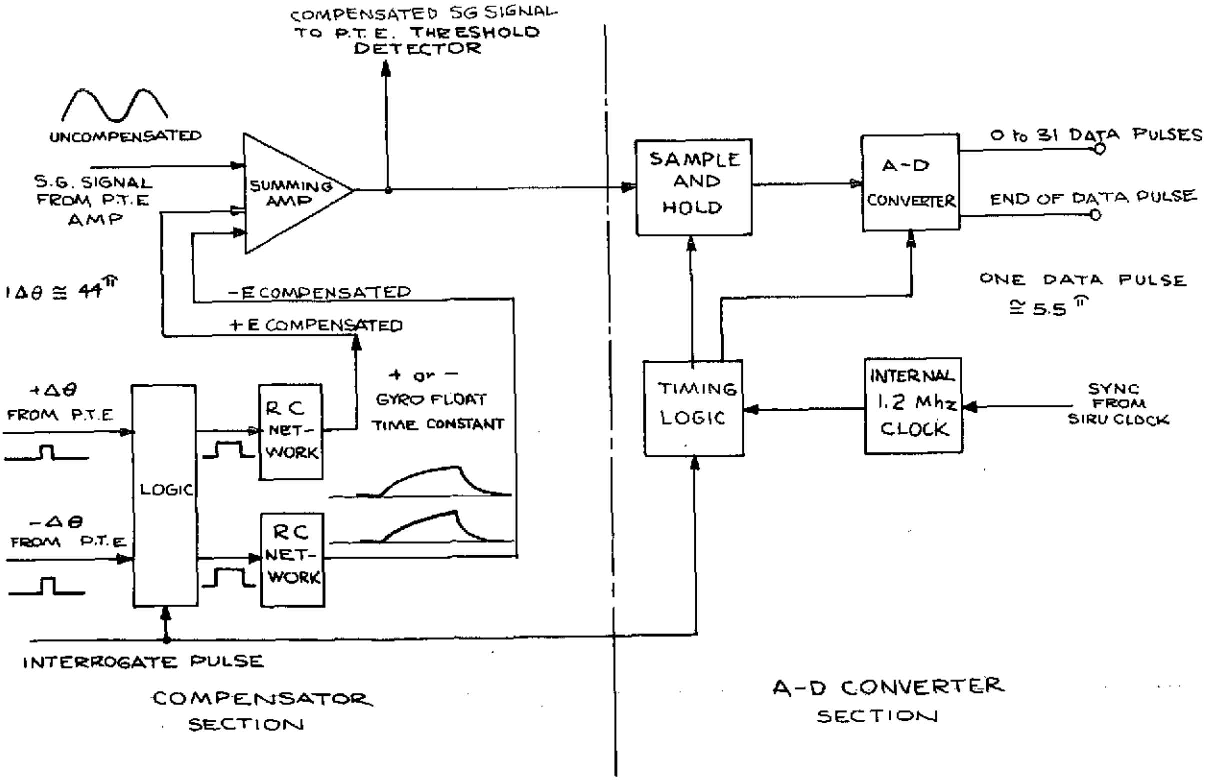

Fig. 3.2.17 Interpolator Block Diagram

The effectiveness of this technique is illustrated in Table 3.2.6. This table presents the distribution of the pulse torque patterns for the compensated and uncompensated loop of a SIRU gyro module when operated at 1/4 of maximum rate (.25 rad/sec) and at an interrogation frequency of 4800 pps. The first column represents the number of times that a particular mode occurred; the second and third columns are the number of ON pulses and OFF pulses for that particular mode.

Table 3. 2. 6 SIRU Gyro Module Moding Patterns at 4800 Hz
Input Rate: 0. 25 rad/sec

Number of Occurrances	Torquer	
	On	Off
Without Compensation		
1678	2	6
205	2	7
382	3	8
4095	3	9
With Compensation		
1132	1	2
4095	1	3
1937	1	4

The data shows a predominant 3 to 1 ratio of OFF to ON pulses and that the uncompensated data has characteristically a burst of 3 ON pulses followed by 9 OFF pulses compared to 1 ON and 3 OFF for the compensated data. The spread of pulse patterns is attributable to noise and variations in table rate. This data illustrates that compensating the system has removed the spurious output generated by the limit cycle.

As an interpolator, once each interrogation period, the unit samples and holds the analog compensated, SG signal, performs an A/D conversion, parallel shifts the digital data pulses into a serial register and finally sends the data, accompanied by an end-of-data pulse, to the computer. The data is quantized such that each data pulse is approximately 5.5 $\widehat{sec}$ or 1/8th of a 44 $\widehat{sec}$ $\Delta\theta$ pulse.

The timing of the data pulses and the end of data pulse are shown in Fig. 3. 2. 18.

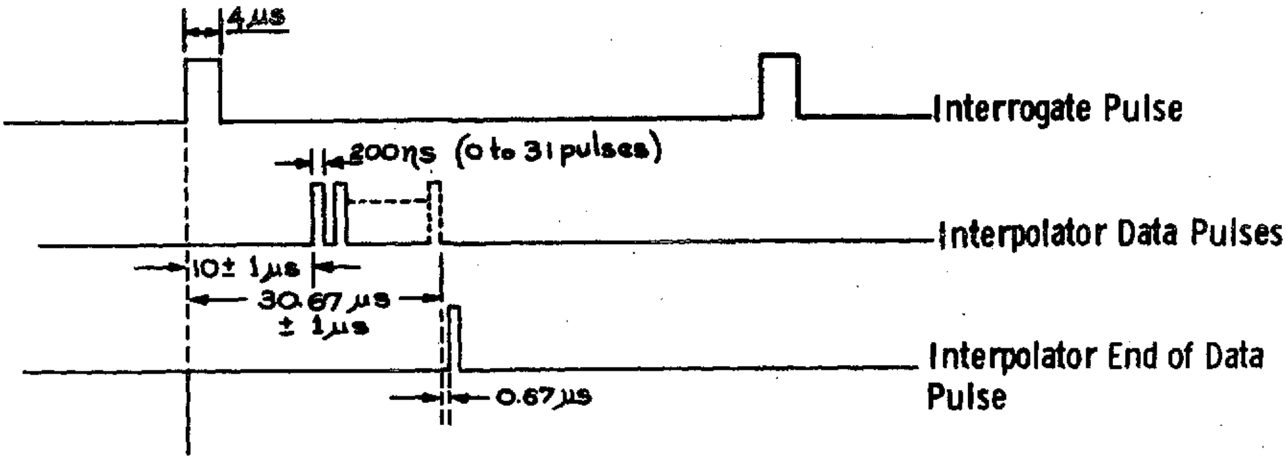

A) +Δθ (+5 Vdc amplitude, 2 µsec wide)

B) -Δθ (+5 Vdc amplitude, 2 µsec wide)

C) Interpolator Data Pulses. 4.5 Vdc, 0 to 31 pulses at 1.5 mc rate

D) Interpolator End of Data Pulse. 4.5 Vdc, 200 n sec pulse width, 208.33 µsec repetition rate

Fig. 3.2.18 SIRU Gyro Module Electrical Interface Output Signal Requirements

4. 8 Volt Power Supply

The 8v power supply is a dual dc source with identical floated and isolated outputs. One +8v output provides excitation to the polarity determining logic of the H switch (see Fig. 3.2.15) and the other +8v output excites the torque-torque reset logic of the H switch.

The 8v power supply was located within the module to minimize line capacitance that affects torquing performance. In addition, to further reduce capacitance to ground and minimize switching transients, the input transformer in the supply is designed for minimum interwinding capacitance.

The 9600 Hz excitation is used for the 8v power supply because of its availability in the module, simplifying the module wiring interface. Because of the good regulation of the 9600 Hz supply and the relatively high frequency, the size of the transformer and the filter components in the supply can be small. The schematic Dwg. No. is 2304009.

5. Torquer Tuning Network

This section contains two series RC networks which are connected in parallel with the gyro TG coil (see Fig. 3.2.19). The networks' function is to tune the coil so that minimum SF deviation with rate is achieved. The unit also contains a trim resistor which is in series with the "dummy" torquer mounted on the gyro. The trim resistor is used to adjust the "dummy" torquer resistance to the actual dc resistance of the torquer. This "dummy" torquer is a non-inductive heater whose resistance is approximately equal to the actual torquer dc resistance. The heater is located on the gyro end mount in the module at the torquer end of the gyro. When no torquer current is needed, the "dummy" is energized by the PTE torque-no torque logic (Fig. 3.2.15). This transfer provides a constant load to the current source. It also provides a thermal input to the gyro equivalent to that seen by the gyro when torquing is commanded. This action minimizes thermal transients in the gyro by delivering constant power to the gyro regardless of the torquing requirements.

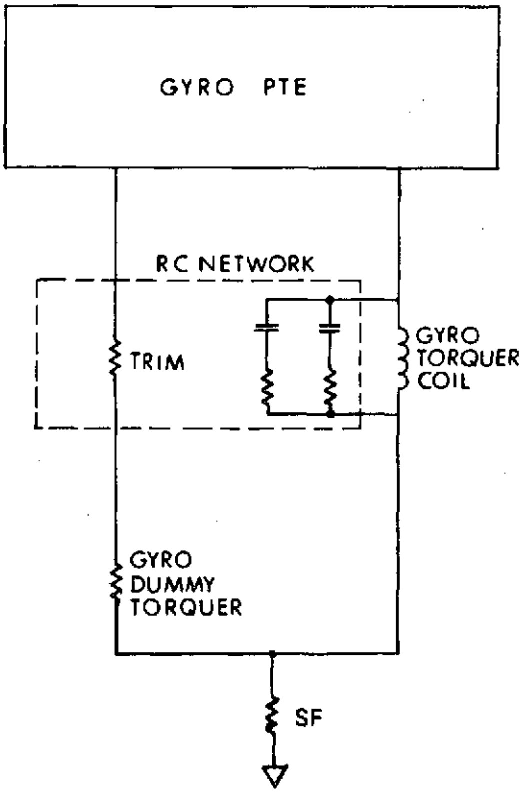

Fig. 3.2.19 Gyro Module RC Network

6. Bandpass Preamplifier

This amplifier provides the necessary gain to raise the level of the gyro SG error signal to be compatible with the PTE input circuit. It also provides bandpass filtering to minimize the unwanted 800 Hz pickup induced by the gyro wheel excitation. An adjustment is provided in the unit to correct the phasing of the SG signal so that it matches the timing of the interrogate pulse (see Fig. 3.2.13). The schematic Dwg. No. is 2304030.

7. Temperature Controller

The function of this unit is to minimize temperature sensitive gyro drift terms by maintaining the gyro temperature constant within ± 0.1°F over a range of ambient temperatures, wheel power variations, and other thermal disturbances. The controller contains two legs of a dc resistance bridge; the other two legs being temperature sensitive resistors located in the gyro. The bridge is balanced at the operating temperature (132°F) of the gyro. Any deviation from this temperature unbalances the bridge and generates an error voltage. This error is then amplified by a low level, high gain, dc, integrated circuit operational amplifier. This amplifier contains an integrated circuit temperature control loop which keeps the dc amplifier circuit at constant temperature in order to minimize dc drift due to temperature variations within the amplifier. This amplifier then drives another amplifier which drives power output transistors which, in turn, deliver power to a heater located on the gyro (See Fig. 3.2.20). The power transistors are assembled into the gyro end mounts so that the power dissipated in the power transistor is transferred to the gyro. Since the controller is essentially a series dc proportional regulator, the sum of the power dissipated in the transistor and the power dissipated in the gyro heaters is linearly proportional to the gyro heater current. This mechanization is in contrast to the usual situation where the power transistor dissipation is not part of the control heat (not located at the gyro) so that gyro thermal control is only by heater power which is proportional to the square of the heater current. This linear operation simplifies the dynamic compensation of the control loop and provides for maximum thermal efficiency of the controller output circuitry. Dynamic loop compensation is achieved by the use of a series of RC networks connected between the emitter of the TG end mount power transistor and the input to the high gain amplifier. The time constant and gain of the RC network are chosen so as to stabilize the control loop which would otherwise be unstable due to the high loop gain and the thermal lags between the heater and sensor. The network also optimizes the transient response to thermal disturbances. The schematic Dwg. No. is 2304058.

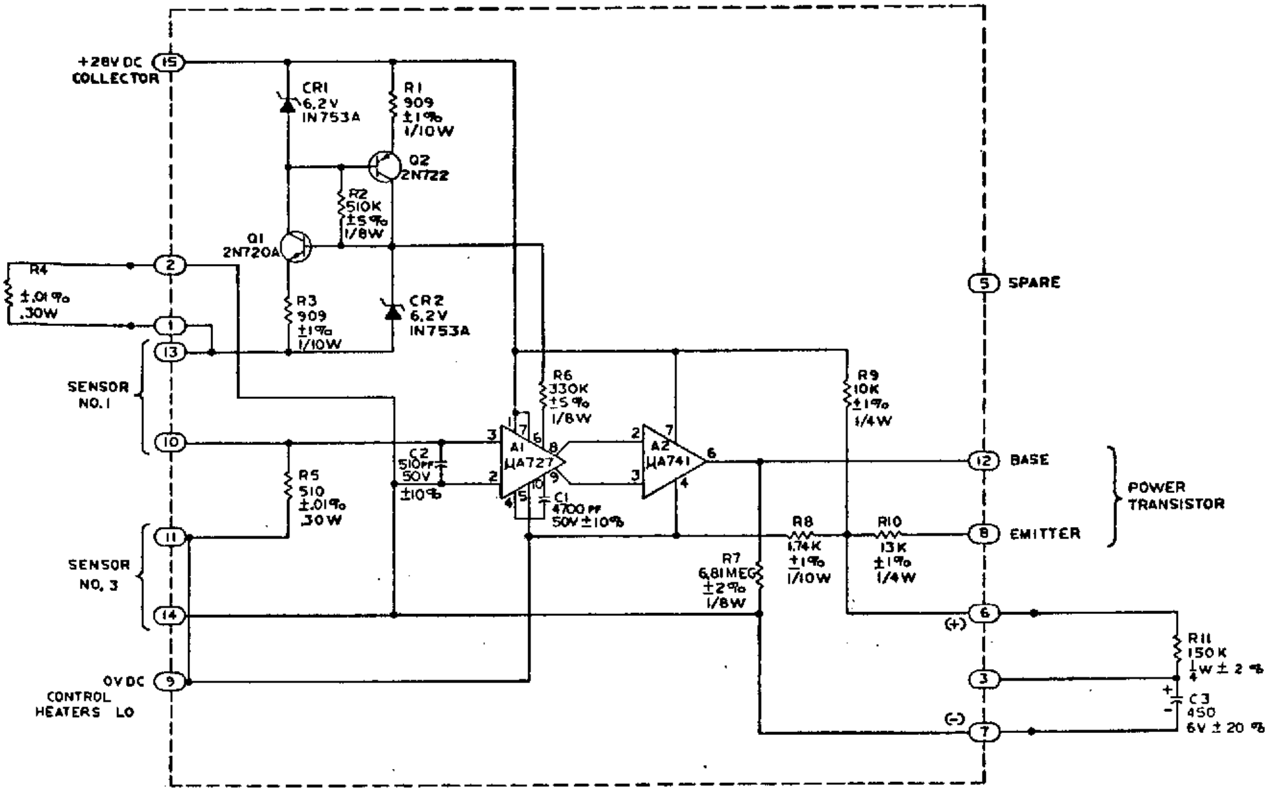

Fig. 3.2.20 Gyro Temperature Controller Schematic

8. Normalization Assembly

All of the components necessary to normalize the various gyro parameters are located in this assembly. These parameters are the gyro temperature sensor resistance, the SG phase shift, the suspension "Q", the suspension stiffness and the SG quadrature. In addition, the two resistors used for suspension current monitoring are located in this module. The required values of the components located in this module are determined during the appropriate phases of gyro and gyro module testing. The schematic drawing number is 2304093.

The location of the above components in an assembled module is shown in Fig. 3.2.21. The module is constructed in sections to simplify assembly, maintenance and repair. These subassemblies are shown in Fig. 3.2.22. This figure also shows a fully assembled module (lower left) and a covered module (upper center).

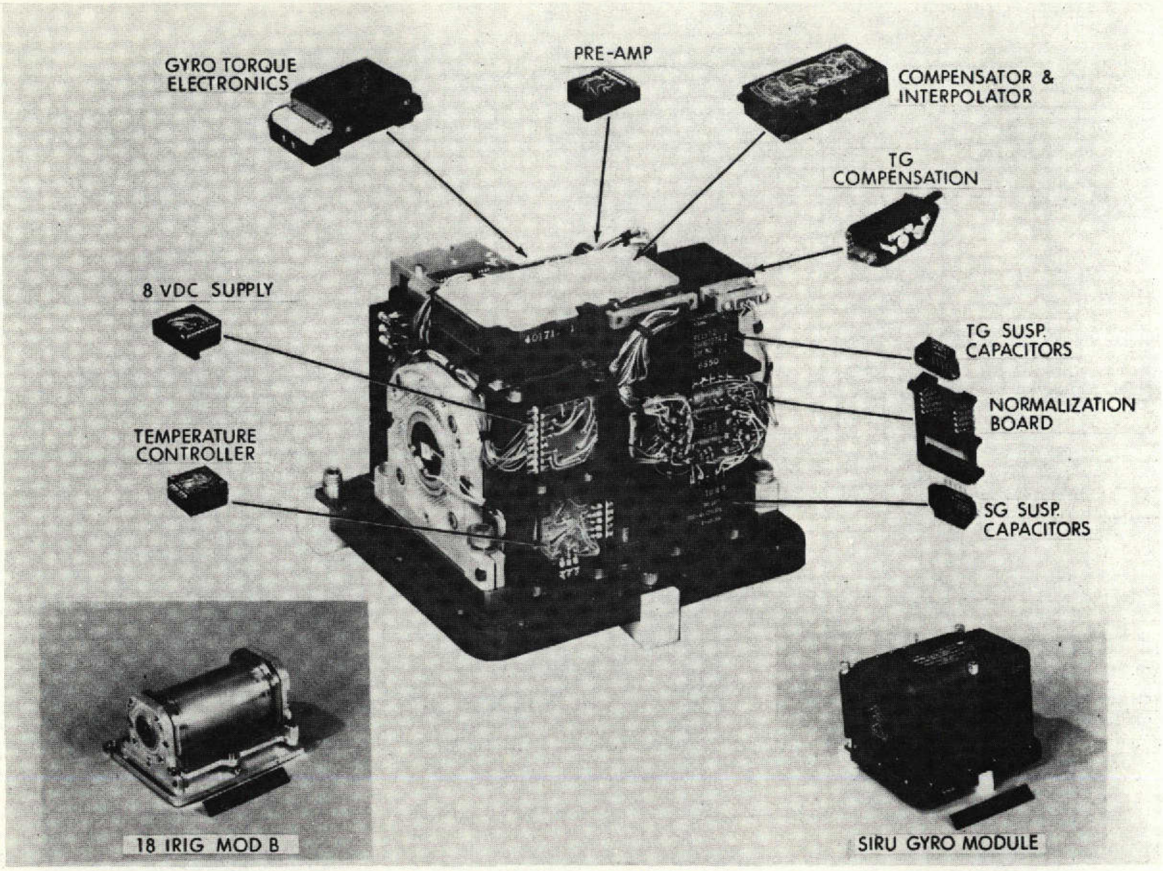

Fig. 3.2.21 Gyro Module Components

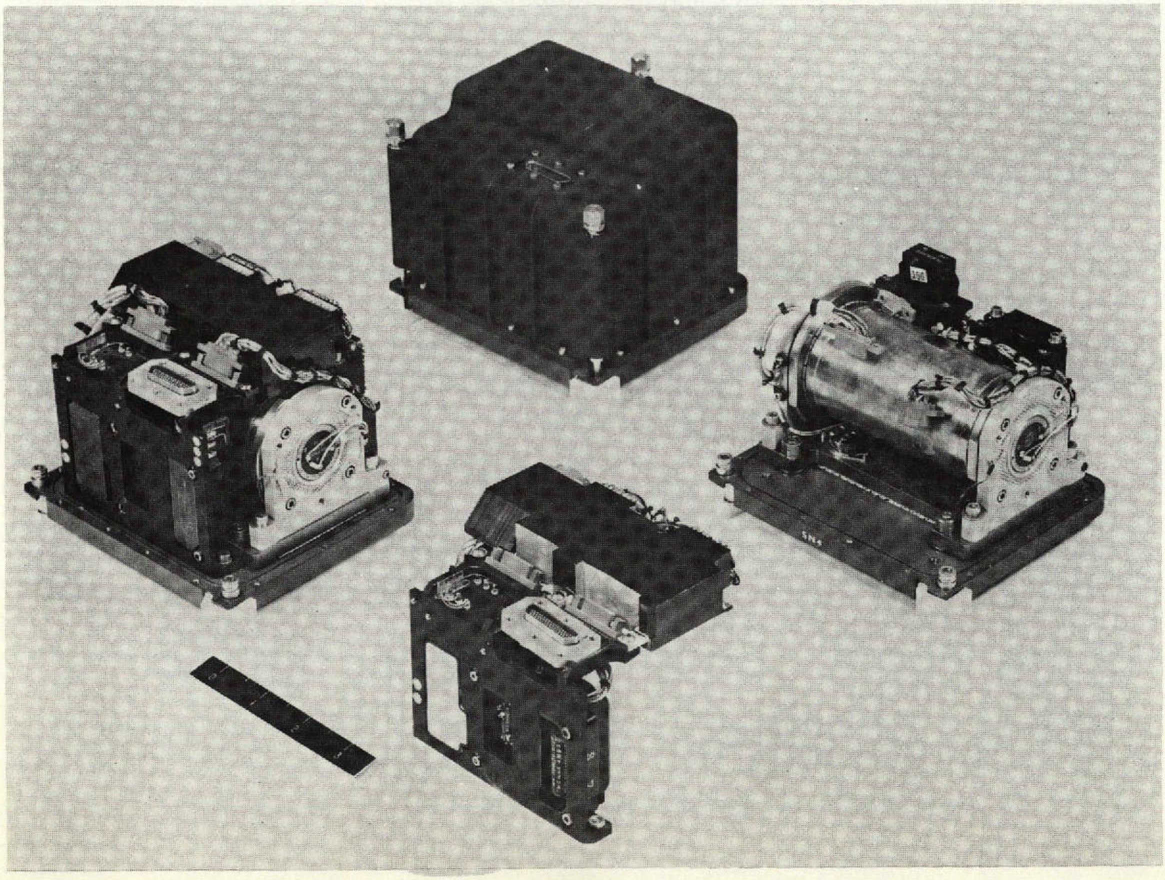

Fig. 3.2.22 Gyro Module Subassemblies

3.3 Electronic Assembly

The EA contains all of the system electronics circuitry not included in the gyro and accelerometer modules. The electronic elements can be classified as either axis-dedicated elements or general electronic function elements (see Fig. 2.2.1).

The axis-dedicated elements consist of one each (six total) axis dc power supply, 9600 Hz ac suspension and SG excitation supply, two phase 800 Hz ac gyro wheel supply and fuse and diode module. The other electronic functions are appropriately redundant; 40v 5v, -20v supplies (2 total) and the scalers (clock countdown chains for timing pulses, etc., 2 total) are implemented in a dual redundant fashion. The oscillators are triple redundant (3 total).

All elements except the dual dc power supplies are individual plug-in NAFI modules arranged for easy access and convenient identification. IC test point connectors, axial data connectors and input power connectors are also accessible from the top of the assembly. During laboratory testing an extruded aluminum, finned plate, heat exchanger assembly was used for the EA instead of a coldplate. (The exchanger is removed for access to the NAFI modules and the connectors).

3.3.1 Axis-Dedicated Electronic Functions

Electronic functions that are axis-dedicated are grouped by axis in the EA tray. Each function is repeated six times, once for each instrument axis, except as noted. As shown in Fig. 3.3.1, these functions are the ac power supplies consisting of a two-phase 800 Hz wheel supply for each gyro, and a 9600 Hz suspension supply for each gyro and each accelerometer, the fuse and diode modules, and the axis supporting dc supplies. The failure of any one of these functions affects only the axis to which it is dedicated (see Table 3.3.1 for specifications and sources).

1) AC Power Supplies

The waveform produced by the ac power supplies is a synthesized sinewave, formed by first generating a stepped series of outputs (see Figs. 3.3.2, 3.3.3 and 3.3.4). This stepped output utilizes the transistors in the output stage of the supply in a switching mode rather than in a linear mode with a corresponding reduction in the power dissipated in the transistor. This technique achieves an efficiency greater than 70%.

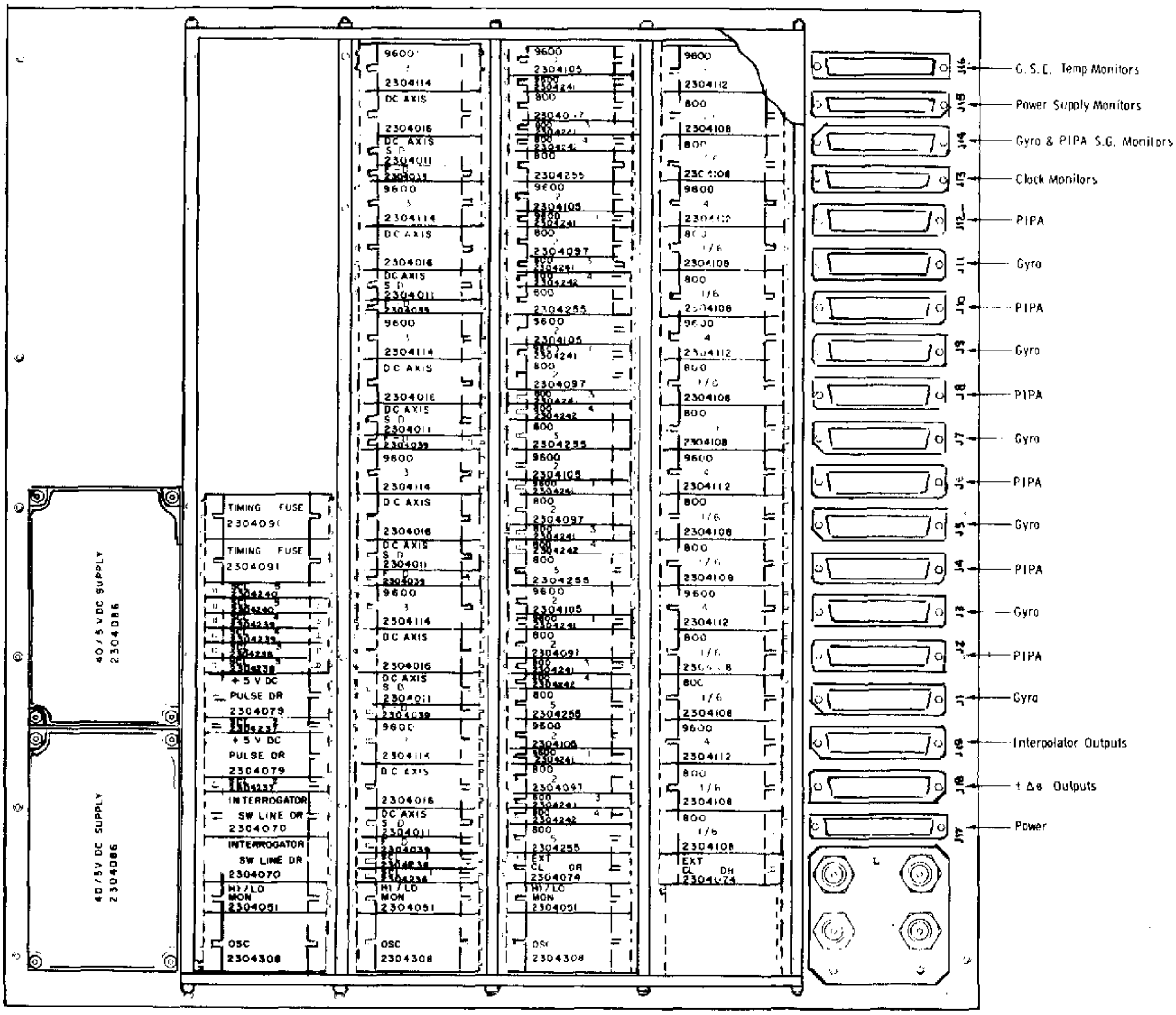

Fig. 3.3.1 Electronic Assembly Layout

Table 3.3.1 Axis Supply Specifications

800 Hz TWO PHASE WHEEL SUPPLY	Output:	Two Phase 800 Hz stepped sinewave 28 V RMS 2.6 W each phase
	Regulation:	5%
	Supply Type:	Sinewave synthesized from square-wave
9600 HZ POWER SUPPLY	Output (9600 Hz P. S.)	9600 Hz, 4 V RMS 1.6 W 9600 Hz, 8 V RMS 2.5 W
	Regulation:	1%
	Harmonic Content:	2% Max.
	Supply Type:	Sinewave synthesized from square-waves
DC AXIS SUPPLY	Outputs:	Two 15 ± 0.008 Vdc at 11.0 ma (for PVR excitation in one gyro module and one PIP module) +10 ± 0.8 Vdc at 50 ma -10 ± 0.8 Vdc at 50 ma +5.2 ± 0.3 Vdc at 0.7 A
	Ripple: (Switching Spikes)	0.6 Vp-p (15 V) (switching spikes) 0.5 Vp-p (10 V. -10 V) 0.4 Vp-p (5.2 V)
	Noise:	0.003 Vp-p (15 V)

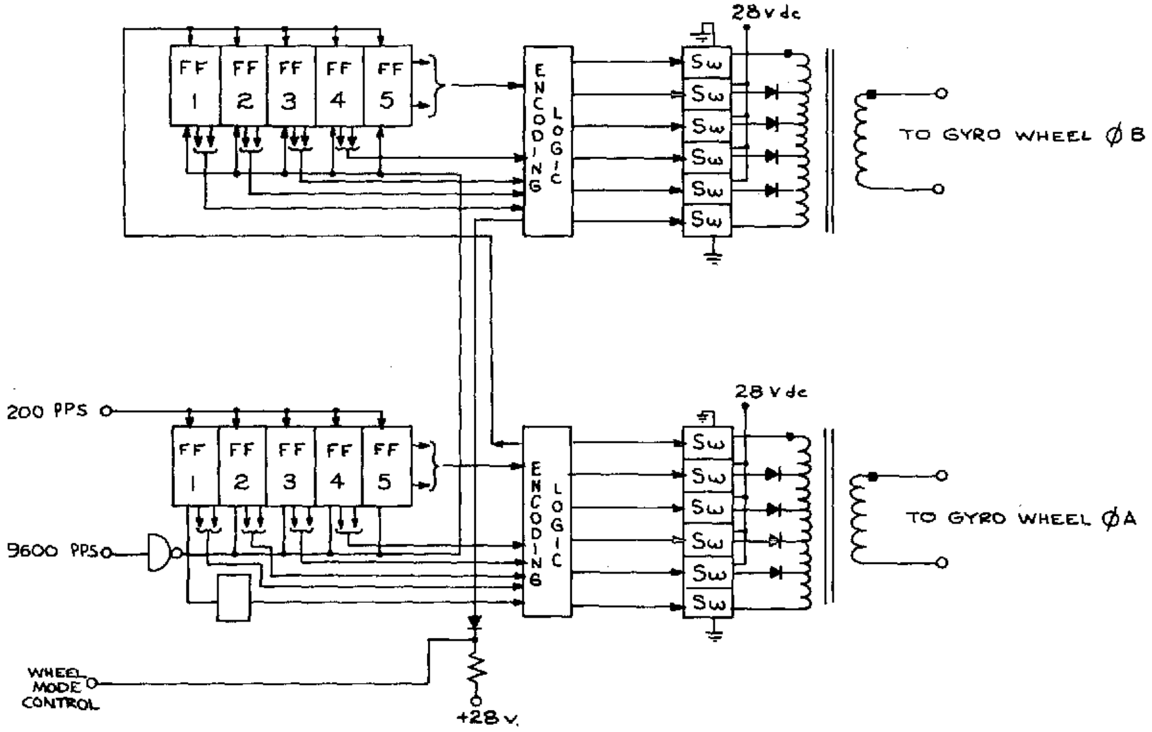

Fig. 3.3.2 800 Hz Gyro Wheel Supply

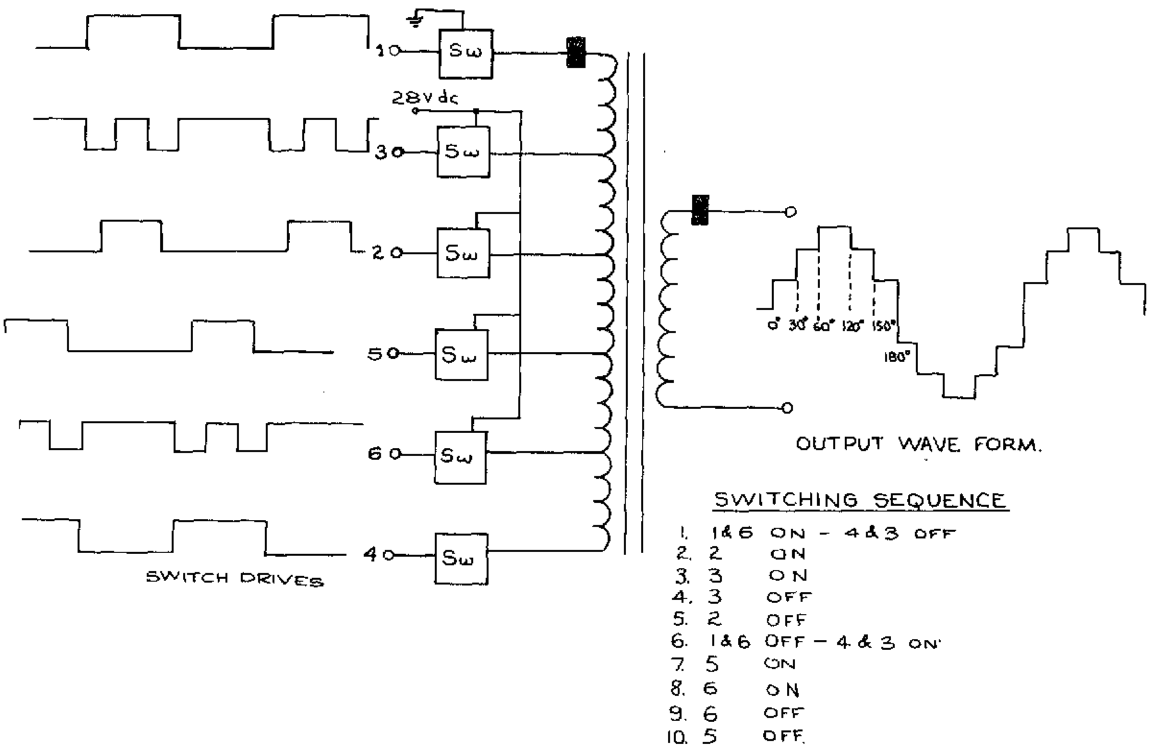

Fig. 3.3.3 800 Hz Wheel Supply Waveforms

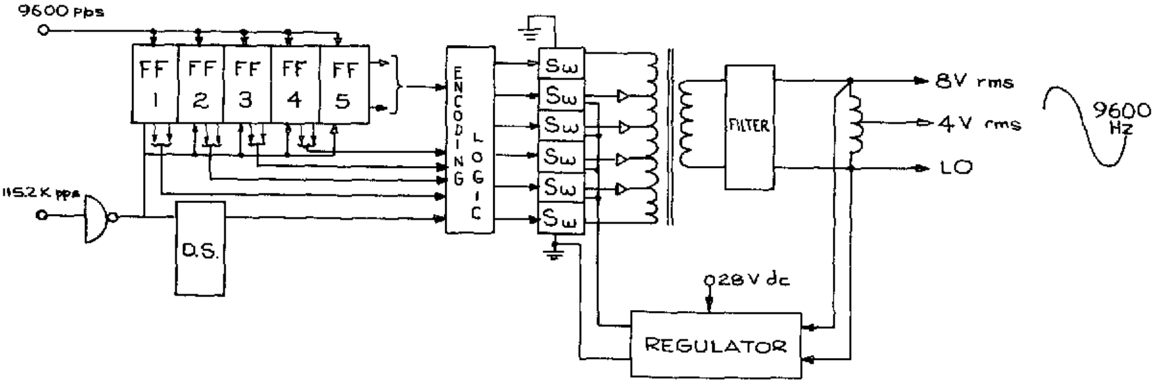

Fig. 3.3.4 9600 Hz Suspension Supply

By generating a 5 step waveform, the third and fifth harmonics are eliminated. In the 9600 Hz supply, this waveform is passed through an LC filter to reduce the harmonic content to less than 2% (see Fig. 3.3.4). In the 800 Hz supply, the inductive gyro wheel load is tuned by a capacitor in the gyro module reducing the harmonic content to less than 20%. While the 9600 Hz supply contains an active regulator to obtain 1% regulation, the 800 Hz supply relies on the regulation of the 28 vdc input which provides a regulation of 5%.

The 9600 Hz supply is redundantly clocked from the scaler at 115.2 kpps and synchronously locked by redundant 9.6 kpps lines from the scaler to hold the main 9600 Hz waveform in phase with the interrogate and switch pulse trains.

2) Fuse and Diode Modules

The purpose of the fuse and diode module is to insure fail-safe operation of the gyro Interpolator/Compensator from the dual redundant -20 vdc power supplies and the gyro pulse torque electronics from the dual redundant +40 vdc supplies (see Fig. 3.3.5). It also insures fail-safe isolation of the gyro temperature controller from the accelerometer temperature controller operating from a common +28 vdc unregulated supply, and fail-safe isolation of the gyro Interpolator/Compensator from the accelerometer pulse torque electronics operating from a common +28 vdc regulated source. One fuse and diode module is provided for each functional axis.

Fail-safe operation of the redundant dc supplies is provided by the action of the blocking diodes (CR1, CR2, CR3, and CR4) which prevent one supply from forcing current in a reverse direction into the other supply in the event of a low voltage failure. In case of a high voltage failure, the fuses (F1, F2, F3, and F4) protect the loads, while blocking diodes again prevent the other supply from reversing the current until the fuse blows and removes the failed supply from the circuit. In the event of an overload type failure, the fuses protect the individual supplies.

Fail-safe isolation of the gyro and accelerometer loads operating from a common or redundant supply is provided by fuses (F5, F6, F7, and F8). In the event of an overload failure, the blowing of one of these fuses removes the circuit it feeds from the supply, permitting continuing operation of the other circuit. The diodes are not needed in this circuit since there is no failure mechanism which would cause reverse current to flow into the supply. They are incorporated, however, into the circuit along with other fuses and diodes (not shown) to permit operation from dual +28 vdc supplies (if incorporated) in a manner similar to the -20 vdc and +40 vdc supplies.

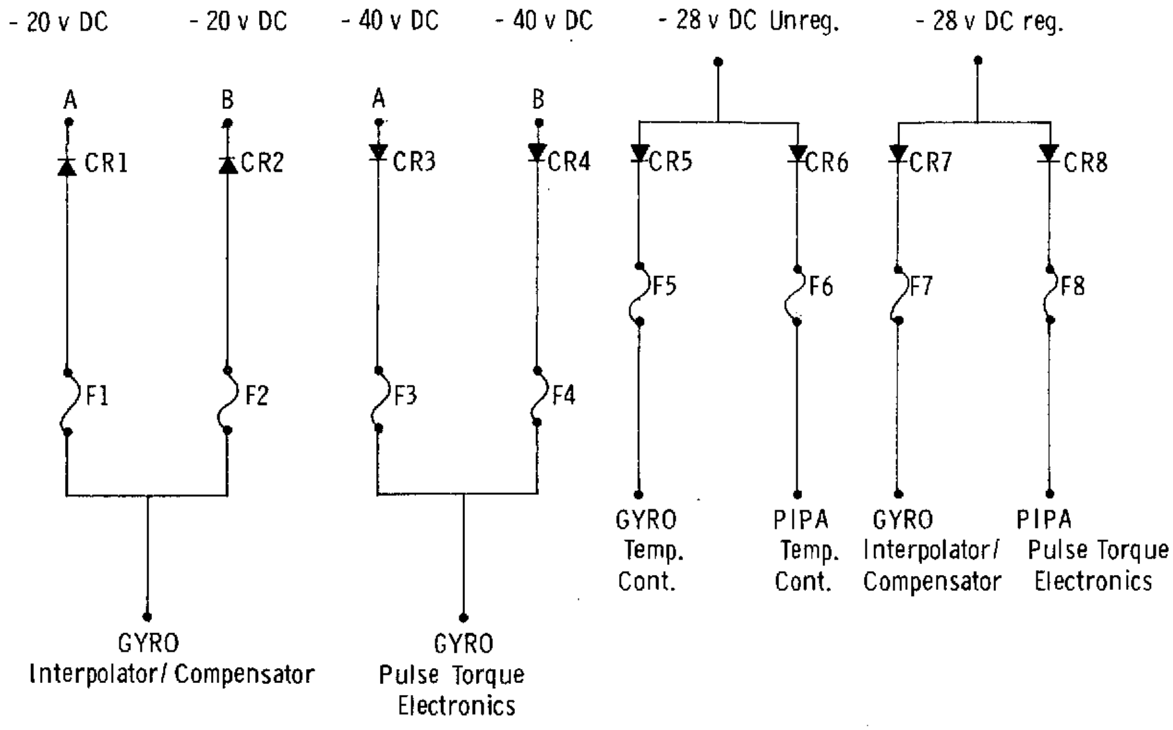

Fig. 3.3.5 Fuse and Diode Module

An advanced, semiconductor, self-resetting fuse was studied for use in this module instead of the fusible metal type fuse currently employed, but limited funding did not permit its further development and incorporation into SIRU. Although there was initial concern that fuse life itself might represent a reliability problem, no fusing failures have occurred in almost three years of continuous testing, except for two operator-induced failures.

3) Axis dc Supplies

See Fig. 3.3.6 and Table 3.3.2 for the schematic and output characteristics of the axis dc supplies.

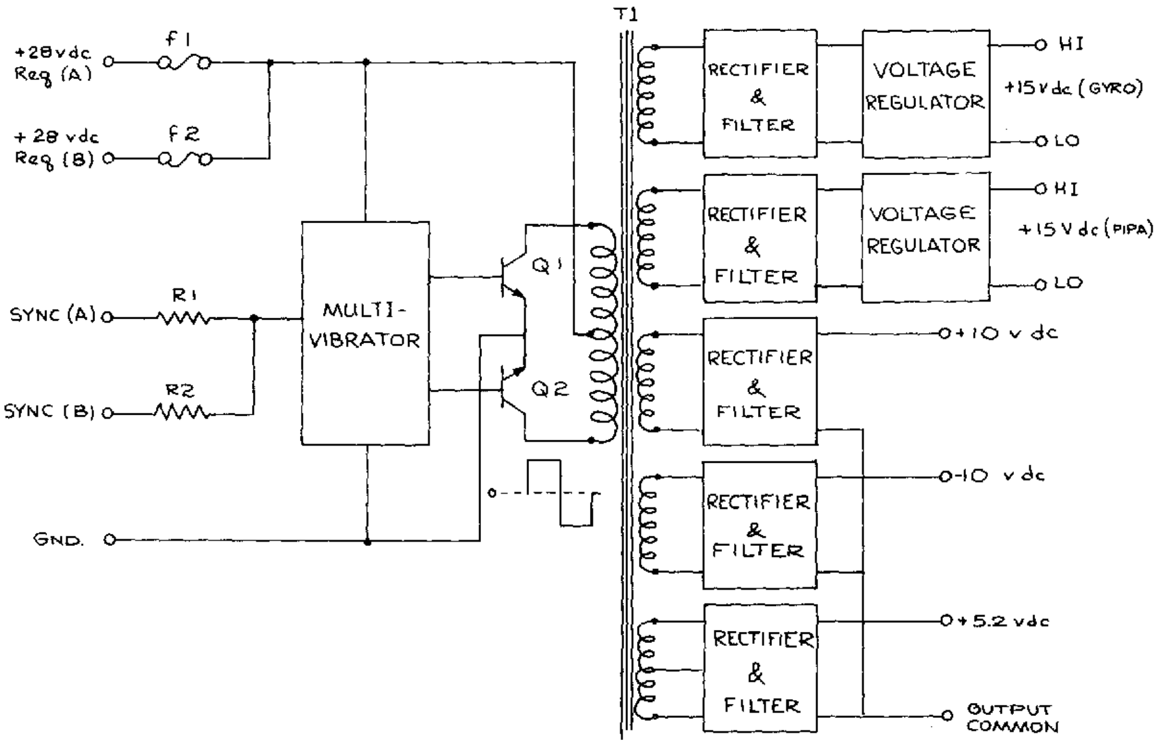

Fig. 3.3.6 Block Diagram—DC Axis Supply

Table 3.3.2 Measured Parameters—DC Axis Supply

I. OUTPUT VARIATIONS

A. 15 Vdc Outputs

1. Load Regulation - ±3 mv for ±10% Load Variation
2. Ripple - 0.1 Vp-p
3. Line Regulation ±1 mv for ±5% B + Variation
4. Temperature Coefficient - -100 ppm/C^0

B. +10 and -10 Vdc Outputs

1. Load Regulation - ±0.1 V for ±10% Load Variation
2. Ripple - 0.5 Vp-p
3. Temperature Coefficient - -200 ppm/C^0

C. +5.2 Vdc Output

1. Load Regulation - ±0.1 V for ±10% Load Variation
2. Ripple - 0.07 Vp-p
3. Temperature Coefficient - -300 ppm/C^0

II. EFFICIENCY - >65%

The accelerometer and gyro associated with each axis share an axis dc supply. The supply provides +10v, -10v and 5.2v as well as two independent 15v outputs to provide an independent excitation for the PVR in each module. The ±10v supplies excite operational amplifiers in the instrument modules while the 5.2v excite the logic elements in these modules.

3.3.2. General Electronic Functions

All of the non-axis-dedicated electronic functions are located in the EA; two are tri-redundant, the oscillators and the Hi/Lo detectors; and two are dual-redundant, the 40/20/5 vdc regulated supplies and the scalers. (It should be noted that the regulated 28 vdc supplies, while not considered to be a portion of the SIRU system, are required to be dual redundant in order to preserve the fault-tolerant character of the system). The EA provides for connection to the redundant 28 vdc system input with suitable fusing and steering diodes in the fuse and diode modules and in other 28 vdc-dependent functions.

1) Clock Oscillators

Figure 3.3.7 shows the block diagram of the clock oscillator and scaler as an array of coordinated functions. The oscillator is a proprietary design developed by Bulova. Essentially it is a 3.6864 mega Hz crystal oscillator stable to 0.5 ppm under all the environmental conditions anticipated for the SIRU system.

The tri-redundancy requirement for the clock results from the following considerations. The system calibration is dependent upon the accuracy and stability of the clock. Crystal clocks are susceptible to failure by excessive drift; and two clocks do not provide a voting capability for failure identification. Therefore, a three-clock redundancy is required to achieve the one failure fault tolerance for a drift isolation using voting. In addition, Hi/Lo frequency detectors in each oscillator circuit are provided to isolate large changes for a second failure detection capability.

2) Hi/Lo Detector

The output of each oscillator must be monitored and tested continuously and the detector operation must be confirmed to preserve the integrity of the system performance.

C2

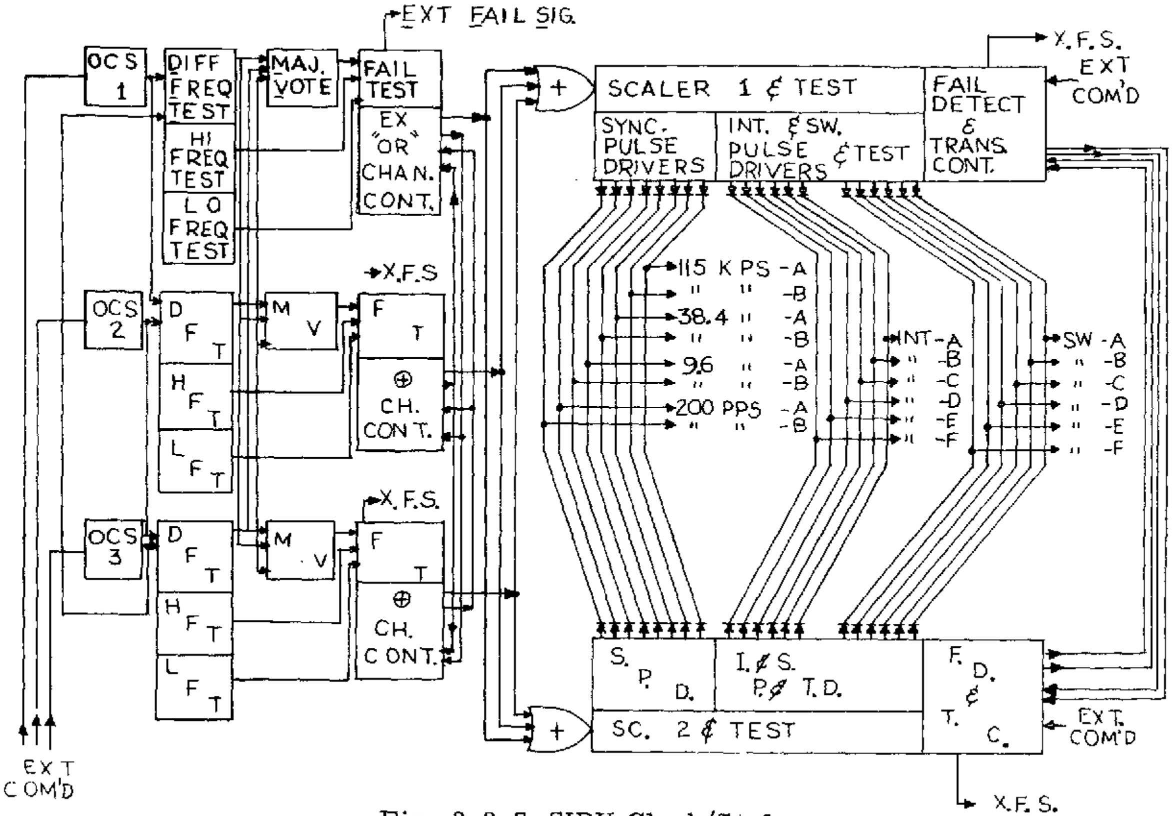

Fig. 3.3.7 SIRU Clock/Scaler

Oscillators may fail or appear to fail under four possible conditions:

1) Frequency too high
2) Frequency too low or non-existent
3) Differential frequency increasing
4) Monitor failure

The Hi/Lo detectors provide tri-redundant monitoring of the condition of the individual oscillator outputs.

Figure 3.3.8 shows the functional diagram of the Hi/Fail test circuit. This "fail high" mode arises from two possible sources. The first results from an alternate design of the oscillator preferred by some manufacturers. In this alternate design the crystals are cut to operate at twice the Bulova frequency and circuitry is provided to divide down to the required value. The SIRU system is designed to accept this alternate design and the Hi/Fail test monitors the possible failure of the flip-flop used to halve the crystal frequency. The Bulova oscillators currently used in SIRU are not susceptible to this particular failure mode.

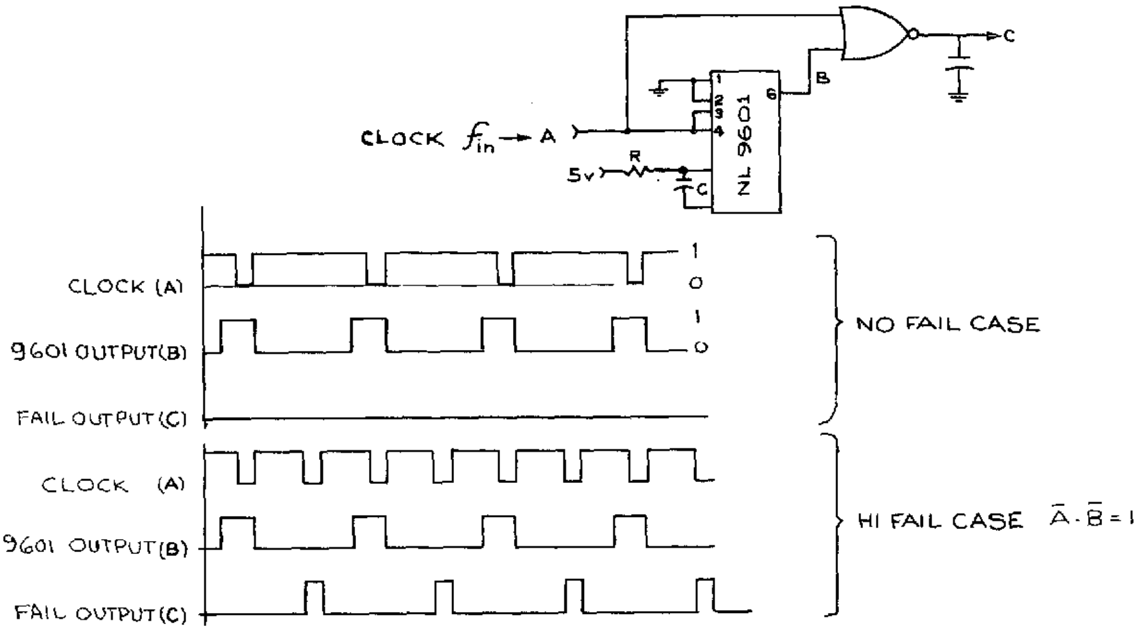

Fig. 3.3.8 Typical Hi Fail Test

The other failure mode monitored by the Hi/Fail test is a condition of a significantly higher frequency output from the oscillator due to failures of the tuned circuit components in the oscillator circuit control loop. As identified in Fig. 3.3.8 input A is the clock input pulse train. These pulses are used to trigger a monostable, retriggerable multivibrator. The output pulse width (B) is determined by the RC circuit. The output B is combined with input A in a NON gate. From the waveform diagram it can be seen that neither A nor B go to zero at the same time if the clock frequency is normal. Thus the inputs to the NON gate are not at zero at the same time and the output of the gate is zero. If, however, the clock frequency becomes significantly higher (≅ 50%) than the multivibrator frequency (as determined by the RC network) the inputs will be at zero at the same time and produce an output at C at the clock frequency. This output is a Hi/Fail indication and is transmitted to the failure logic.

The Lo/Fail circuit, Fig. 3.3.9, works in a manner similar to the Hi/Fail circuit. In this case the multivibrator frequency is set at a frequency lower than the clock frequency by an RC network. The clock pulses, occurring at a rate faster than the 9601 frequency, keep the gate triggered ON producing a steady state logical "1" at the output. If the clock frequency drops below the multivibrator frequency the output returns to logical "0" at the end of its pulse width before being triggered to logical "1" by the clock. The resulting train of pulses at the clock frequency is transmitted to the failure logic.

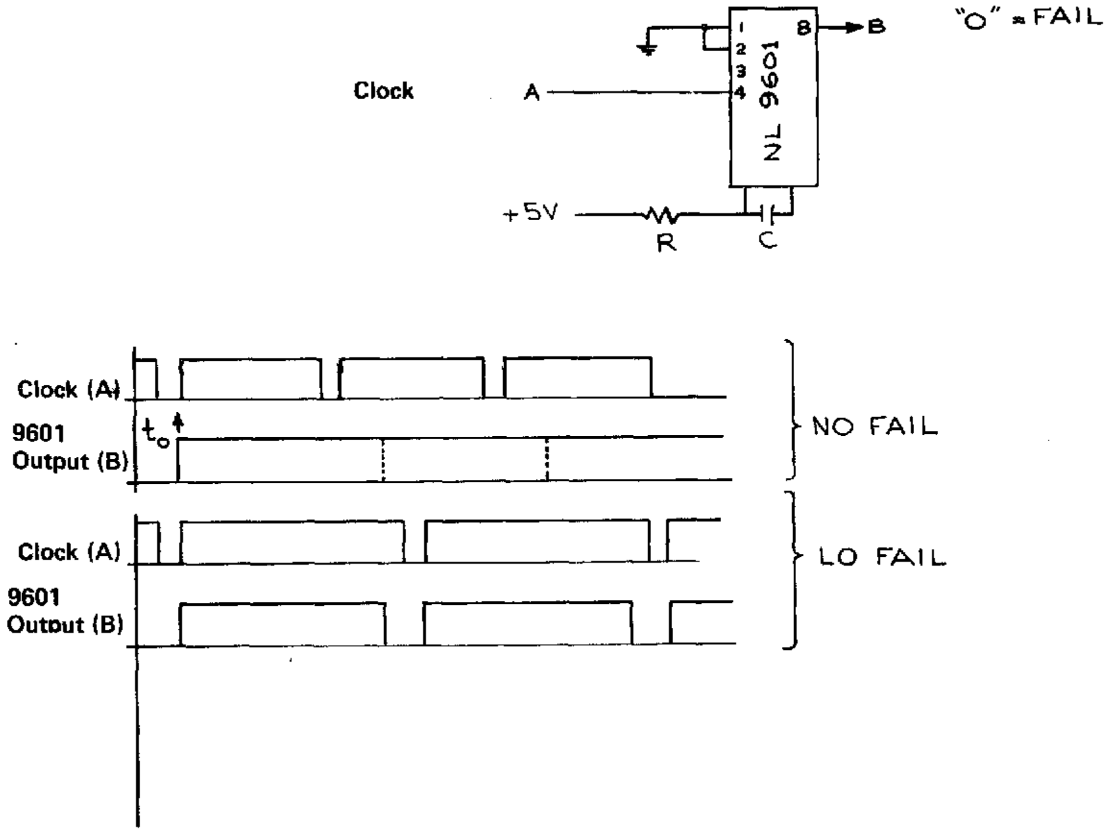

Fig. 3.3.9 Typical Lo Fail Test

Figure 3.3.10 shows the functional diagram for the differential test. This "differential" mode applies to excessive drift in the oscillator. As shown in the circuit diagram a D flip-flop samples the output of one oscillator while being strobed by the squared output of another oscillator (clock B). In other words, clock A sets the output to a "1" while clock B resets it to "0". If the two clocks are at the same frequency, these two events will occur simultaneously and there will be no change in the output. If they are at different frequencies an output will be produced at the difference frequency. A hysteresis circuit is also included, the function of which is to minimize the noise output of the differential circuit. The difference frequency goes to a modified Hi/Fail test circuit with capabilities as previously described. The remaining circuits are similarly tested in pairs. Differences between any channels exceeding 4 ppm results in "majority vote" logic action to isolate and "lockout" the highest difference channel. While the differential circuit could be used to detect Hi/Lo failures directly, the reaction time is so relatively slow (milliseconds) that the alternate circuits (nanosecond reaction time) are preferred for these tests.

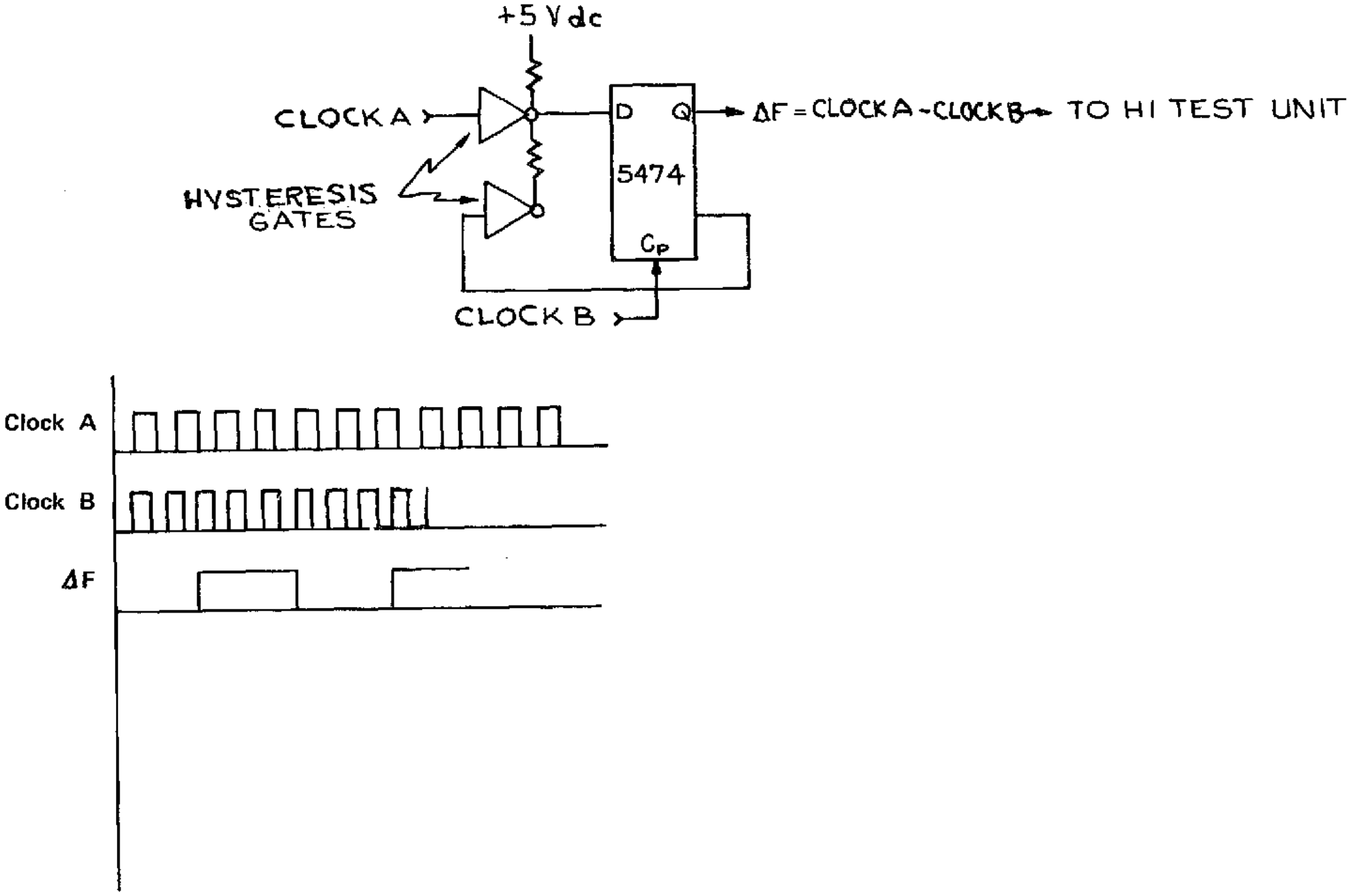

Fig. 3.3.10 Typical Differential Test

The Hi/Lo monitors are configured to be self-testing for power and logic failures within the module. Failures not associated with frequency tests result in automatic channel transfer. Channel transfers may also be commanded externally by the ground support equipment (GSE) or the computer.

In the previous discussion of the Hi/Lo detectors, the use of the term "transfer" implies that the oscillator channel being tested is the channel in control. The probability of failure on the channel in control is only one in three. Therefore, in two cases out of three the failed channel will not induce a transfer and the only notice of failure will be to the fail status line to the computer.

Any failure will always produce the "lockout" signal. "Lockout", however, is not of a latched or permanent type. A failed channel is still tested and if the failure clears, the channel is again ready for use. Transient failures which are self-clearing result in only temporary disablement.

3) 40/20/5 dc Supplies

These supplies are provided as dual redundant non-axis-dedicated functions located in the EA. Each supply is capable of supporting the entire SIRU system demand for 40 vdc, +5 vdc and -20 vdc power. The 40 vdc provides power to the H switches of the module PTEs. The -20v provides power for the gyro module Interpolator/Compensator. The 5v power is used for the logic excitations of the EA functions such as the scaler, and the logic elements of the 800 and 9600 Hz supplies. Table 3.3.3 details the summary specification and Fig. 3.3.11 shows the circuit block diagram. A dual feedback circuit in each supply prevents high voltage runaway. This protection assures that if a feedback line failed open, the other line would hold the supply voltage to prevent an increase to a Hi/Fail limit. An excessively high voltage at the gyro module PTE 40 vdc H switch circuits could exceed the regulation limits of the PTE dc current control loop causing performance degradation. The dual feedback provision prevents this possible failure mode.

A coupling scheme is provided with the dual supplies so that balanced loading of both supplies exists when no failures are present. This balanced loading results in better regulation of the 5 vdc logic supply. This improved regulation is due to the fact that the +5v logic supply does not have an independent regulator but depends on the regulation of the 40v dc supply. The diode coupling arrangement, shown in Fig. 3.3.12, connects three axes to supply No. 1 through a single diode drop and the remaining three axes to supply No. 1 through two series diode drops. Conversely, the three axes connected to supply No. 1 through the single diode drop are connected to supply No. 2 through two series diode drops, and the remaining three axes are connected to supply No. 2 through a single diode drop. This load steering scheme applies only to the 40 vdc lines which carry the principle system loads. Each 40 vdc supply has the capability of supplying double the system load; thus in normal balanced operation with both supplies functioning, each is operating at 25% of full load capacity.

4) Scaler

Scalers are provided as a dual redundant non-axis-dedicated function located on the EA. The scaler block diagram is shown in Fig. 3.3.13 and the clock/scaler redundancy block diagram is shown in Fig. 3.3.14. The principle functions of the scaler circuit consist of the following:

1. Generation of necessary synchronizing signals for all electronic functions
2. Self test of scaler circuits and outputs
3. Transfer to backup scaler upon failure

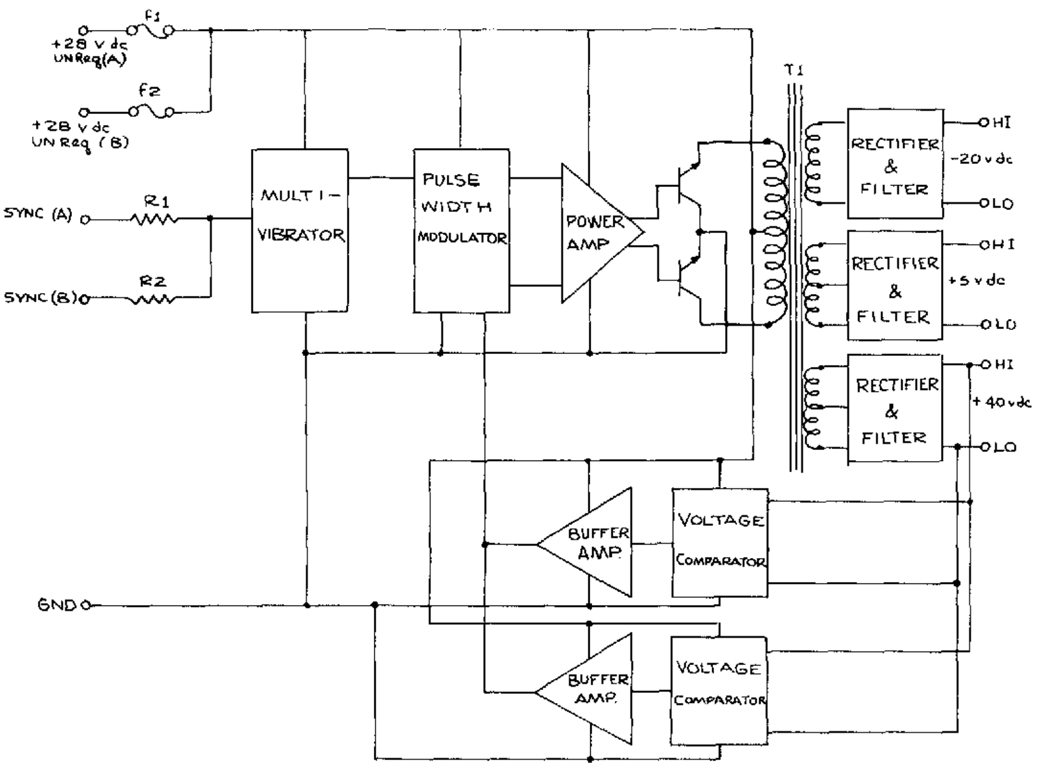

Fig. 3.3.11 Block Diagram—40/5 vdc Supply

Table 3.3.3 Measured Parameters—40/5 vdc Supply

I. OUTPUT VARIATIONS

A. 40 Vdc Output

1. Load Regulation - ±0.05 V for ±10% Load Variation
2. Ripple - 0.5 V p-p
3. Line Regulation - ±0.02 V for ±20% B+ Variation
4. Temperature Coefficient - +250 ppm/C°

B. -20 Vdc Output

1. Load Regulation - ±0.05 V for ±10% Load Variation
2. Ripple - 0.1 V p-p
3. Line Regulation - ±0.01 V for ±20% B+ Variation
4. Temperature Coefficient - +250 ppm/C°

C. 5 Vdc Output

1. Load Regulation - ±0.05 V for ±10% Load Variation
2. Ripple - 0.3 V p-p
3. Line Regulation - ±0.003 V for ±20% B+ Variation
4. Temperature Coefficient - +500 ppm/C°

II. EFFICIENCY - >70%

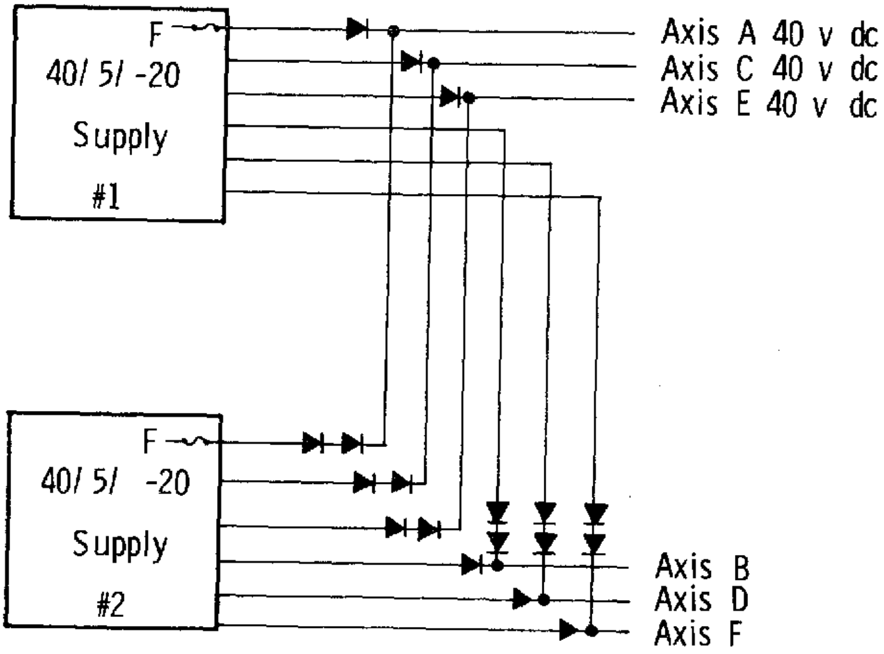

Fig. 3.3.12 Diode Load Steering Scheme

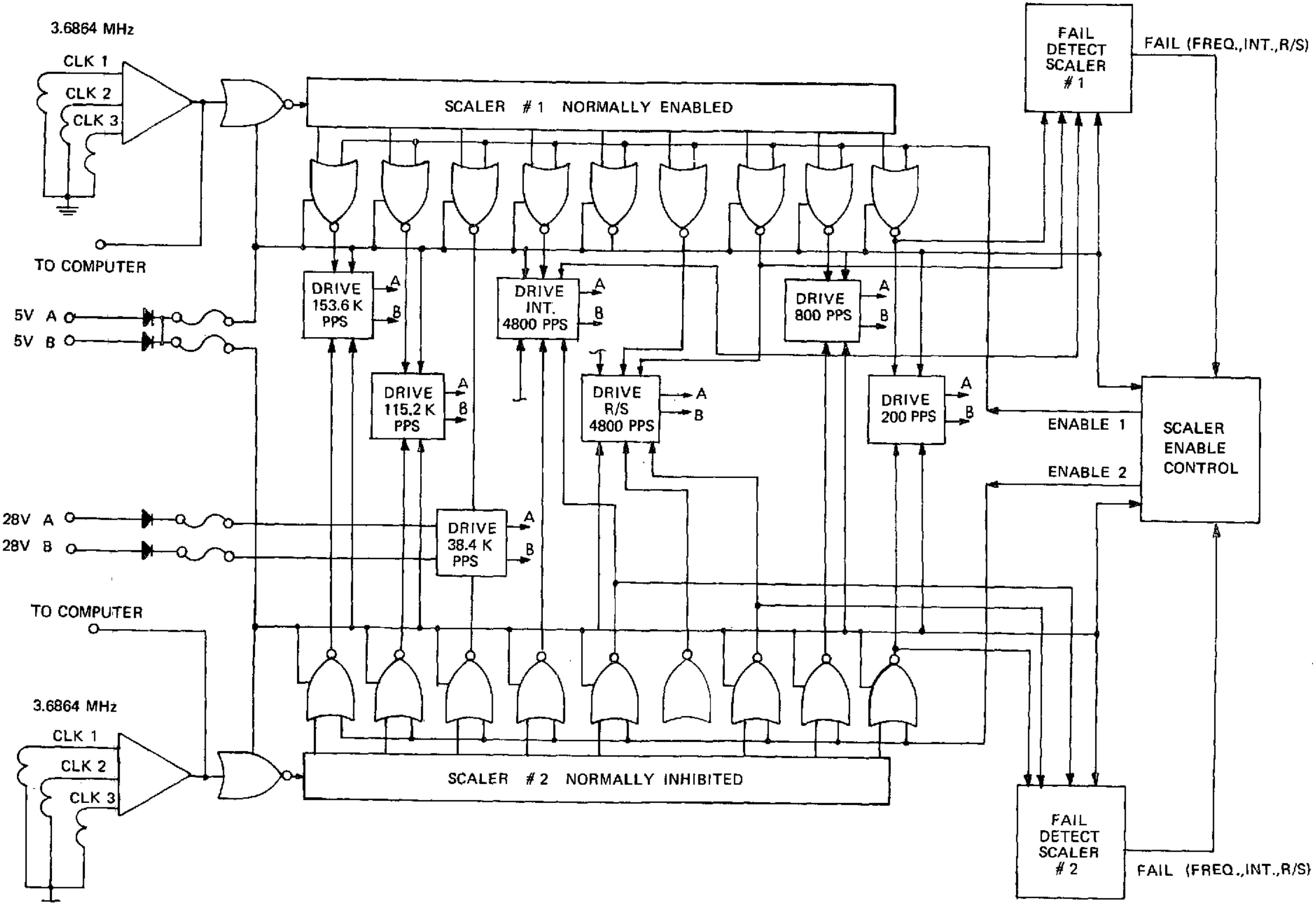

Fig. 3.3.13 Block Diagram-Duplex Scaler

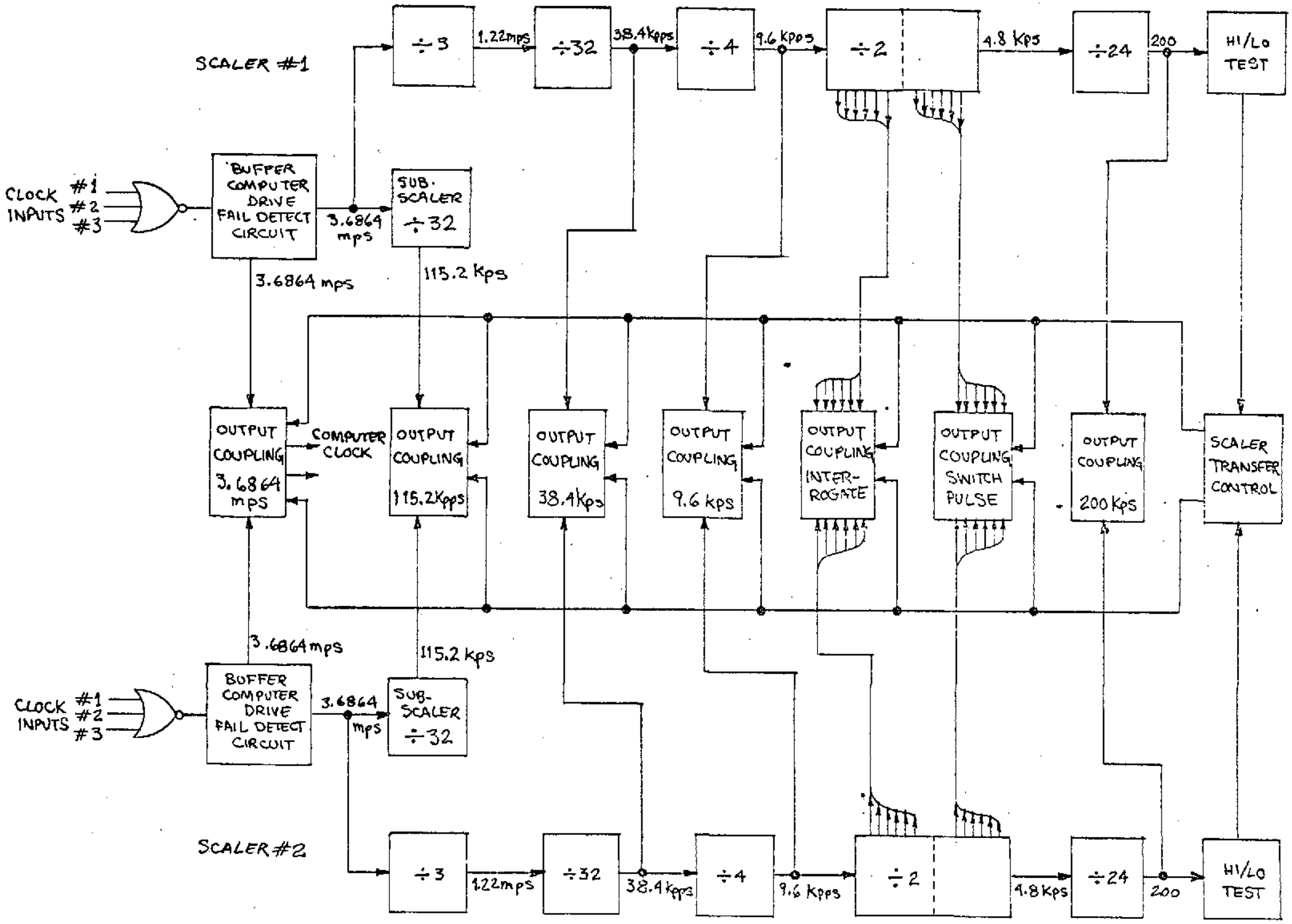

Fig. 3.3.14 Block Diagram—Clock Scaler Redundancy

The following descriptions are presented for each of the functions identified above.

1. Generation of Signals

   a) Module PTE timing signals—interrogate and switch pulses, 4.8 kpps.
   b) EA suspension and SG 9600 Hz supplies—a 115.2 kpps pulse train and a 9.6 kpps synchronizing signal provide clocking for the 9600 Hz suspension power supplies. The 9.6 kpps signal synchronizes the 9600 Hz "zero+" crossover for suspension lock control.
   c) EA dc axis and 40/5v dc power supplies—A 38.4 kpps signal clocks and synchronizes all the dc power supplies.
   d) EA 800 Hz wheel supplies—A 9.6 kpps synchronization signal for waveform generation and a 200 pps synchronization pulse signal is provided for the 800 Hz supplies.
   e) Other timing functions—The 9.6 kpps signal also serves as a clean pulse for testing the interrogate and switch pulse train within the scaler.

The 200 pps signal also is available to the computer as a timing signal.

All of the output signals are steered from the scaler to the using circuit by pulse drivers which are integral parts of the scaler. The pulse driver configuration is shown in Fig. 3.3.15. Each signal originates at an SN 5401 gate driving dual transformer coupled lines resulting in redundantly bussed signals (signals on either Bus A or Bus B). Either scaler may drive these buses since they are diode isolated and when connected in parallel will generate logic "OR".

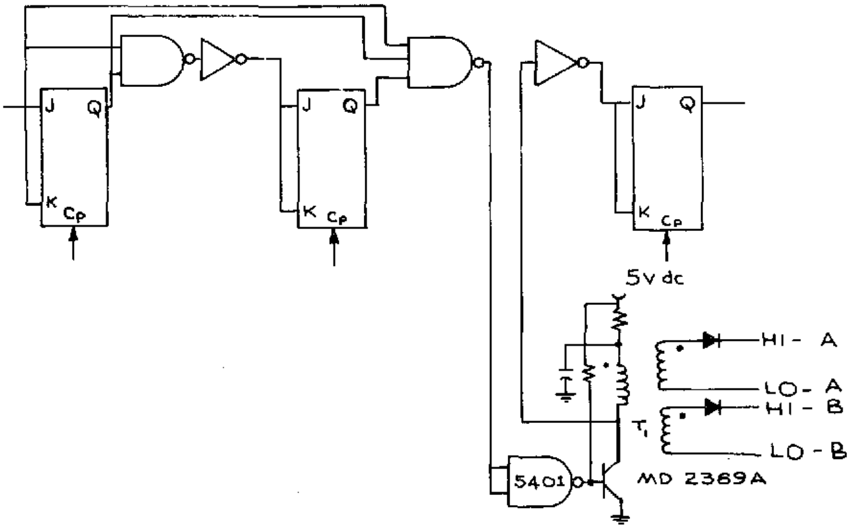

Fig. 3.3.15 Typical Sync Driver

The SN 5401 gate output also drives a switch transistor the collector of which feeds serially to enable the succeeding flip-flop in the divide down chain of a conventional synchronous counter. This arrangement permits a failure of the SN 5401 gate to cause failure of the succeeding scaler sections. This failure is detected by a simple end-of-counter failure detection circuit which will be described later. No further test circuits are required for this sequence of signals. The synchronizing pulses derived by these techniques are approximately 400 nanoseconds wide.

2. Self-Test of Scaler

Each scaler has a main scaler that divides down to 200 pps. In the main scaler, the 38.4 kpps, 9.6 kpps and 200 pps output signals are derived by conventional countdown techniques driven as described above. The lowest frequency, 200 pps, is fed to a Hi/Lo retriggerable one shot circuit similar to that described for the Hi/Lo monitor. A failure in an internal gate or flip flop of a synchronous scaler will result in locking the Enable of a next succeeding state change to either logical one (1) or zero (0) For the first state (1) the result will be an increase in the lowest frequency equal to 2^N where $1 < N < M$ and M is the highest number of flip-flops sharing one clock frequency. The Hi/Fail test circuit will reveal this condition effectively. For the second state (0) the lowest scaler frequency becomes zero which is detected in the Lo/Fail circuit previously described. Thus, the operation of the main scaler is tested by applying the 200 pps signal to one Hi/Fail and one Lo/Fail circuit.

The 115.2 kpps signal is derived from a subscaler linked synchronously with the main scaler. Self-test is by means of a separate Hi/Lo test section. The outputs of these test sections are logically "OR" connected to one "FAIL" gate for the scaler.

The fault tolerance capabilities and test provisions for the two line drivers which pass signals from the scaler to six separate interrogate and the six separate switch pulse line drivers are shown schematically in Fig. 3.3.16. The drivers are designed to operate four interrogate and switch pulse lines with up to two lines "dead" shorted without serious degradation. A failure in any one line (due to a transformer or other failure) will fail that axis of the SIRU system. Failure of a driver transistor or other component will be detected by the test feedback line and cause transfer of control to the back up scaler. The test feedback circuit is shown in Fig. 3.3.17. The test feedbacks from both the interrogate and switch driver are fed to a sequence detector circuit. If the proper sequence of interrogate leading edge, switch pulse #1, interrogate lagging edge, switch pulse #2 and the 9.6 kpps

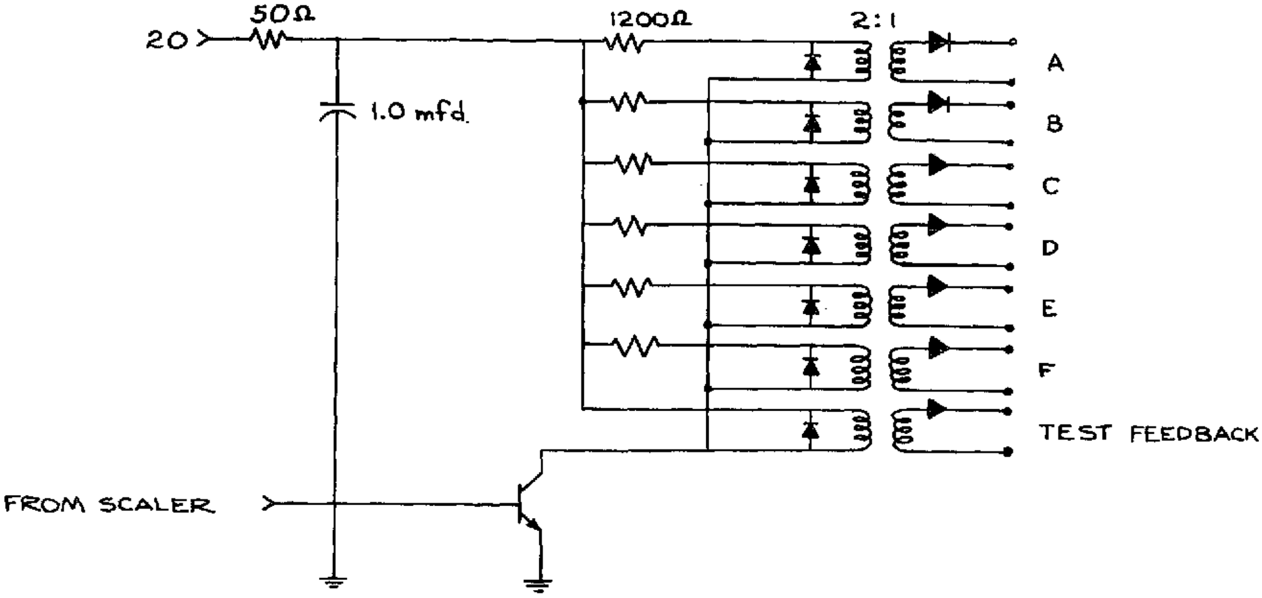

Fig. 3.3.16 Switch or Interrogate Drivers

SECTION ① INTERROGATE PULSE LEADING EDGE

② RESET SWITCH PULSE

③ INTERROGATE PULSE LAGGING EDGE

④ SET PULSE

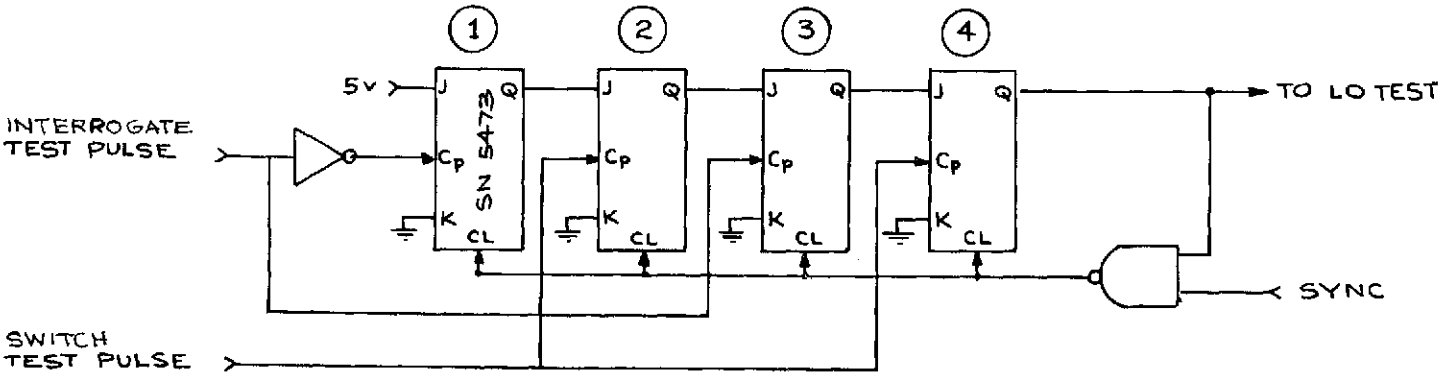

Fig. 3.3.17 Interrogate & Switch Sequence Test

synchronizing pulse is not present or fails to occur, the 4800 Hz output to a Lo/Fail test circuit will become quiescent, actuate an "OR" to the scaler "FAIL" gate, and transfer control to the "backup" scaler.

3. Transfer to "Backup" Scaler

A simplified form of the scaler transfer circuit is shown in Fig. 3.3.18. The circuit is a SR flip-flop shared between scalers. When the system is activated initially, if there are FAIL inputs (no scaler fails) into both 5401s, the choice of scalers (output of 5401s) is random and an INHIBIT command is sent to one scaler and not to the other. If a FAIL signal appears at the input to the 5401 which is not issuing an INHIBIT command, it will change its state to INHIBIT, and cause the other 5401 to reverse its state. This action locks out the failed scaler and activates the functioning scaler. The 5 vdc power on separately fused lines is cross strapped to effect transfer in the event of power failure. External commands or override options are also possible.

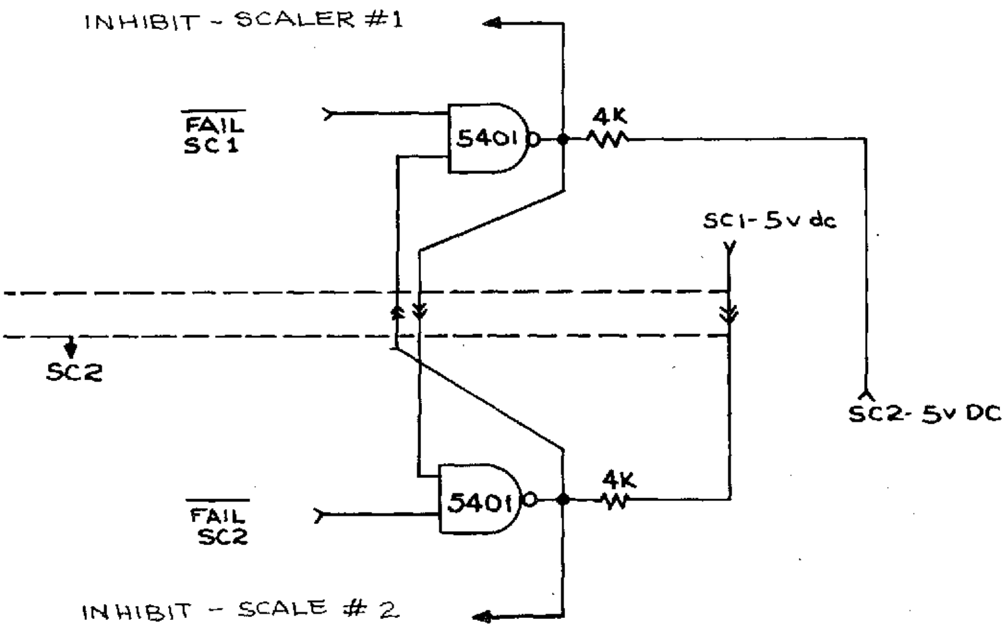

Fig. 3.3.18 Typical Transfer Circuit

4. 3.6864 mega Hz Optional Clock Drivers

Originally intended as clock lines to a dedicated computer, simplex "OR" gate outputs are power amplified to drive a redundant "Coax A" and "Coax B" bus. The design and test provisions are the same as for the drivers previously described.

5. Power Requirement Summary

Table 3.3.4 presents a Power/Efficiency Summary for the EA. The total load identified under the heading "Power Out" includes all channel (wheels, PTE, etc.) power. The variable power for the temperature controllers is excluded, but under normal control conditions a total of 6 watts is required for the gyro temperature control power and a total of 3 watts is required for the accelerometer temperature control power.

Table 3.3.4. Power Dissipation in Electronic Assembly.

Circuit	Power In	Power Out	Dissipation per Circuit	Total Dissipation	Efficiency	Modules
9600 Hz Microsyn	28 volt ~ 9W 5 volt ~ 1.15W	4.2W	5.95W	35.7W	41%	4 each 24 total
800 Hz Wheel	28 volt ~ 7W		1.8W	10.8W	75%	6 each 36 total
DC Axis Supply	28 volt ~ 12.3W	5.2W	4.3W	25.8W	65%	2 each 12 total
40/5 Volt Supply	28 volt ~ 112W	78.5W	33.5W	40W	70%	1 each 2 total
Oscillators	28 volt ~ 0.18W	-	0.18W	0.54W		1 each 3 total
Clock						
Scaler #1	5.0 volt #1 5.7W	-	12.18W	12.18W		21 total
Scaler #2	5.0 volt #2 3.8W					
Hi/Lo #1	5.0 volt #1 0.95W					
Hi/Lo #2	5.0 volt #2 0.98W					
Hi/Lo #3	5.0 volt #3 0.75W					

3.4 SIRU Thermal Design

3.4.1 Introduction

Temperature control of the SIRU system, to reduce the effect of the temperature sensitivity of the inertial sensors and some of the electronics modules, was accomplished by separately controlling the temperature of each gyro and accelerometer module and maintaining the mounting base structure (π-frame) nearly isothermal (coarse control) by means of a liquid-to-air heat exchanger cooling loop. The EA is forced-air cooled in laboratory operations; in a spacecraft installation, a coldplate would be mounted on the top or bottom of the EA. EA cooling provisions assure that the junction temperature of the silicon devices are nominally held well below the limits required for reliable operation (Figs. 3.4.1 and 3.4.2).

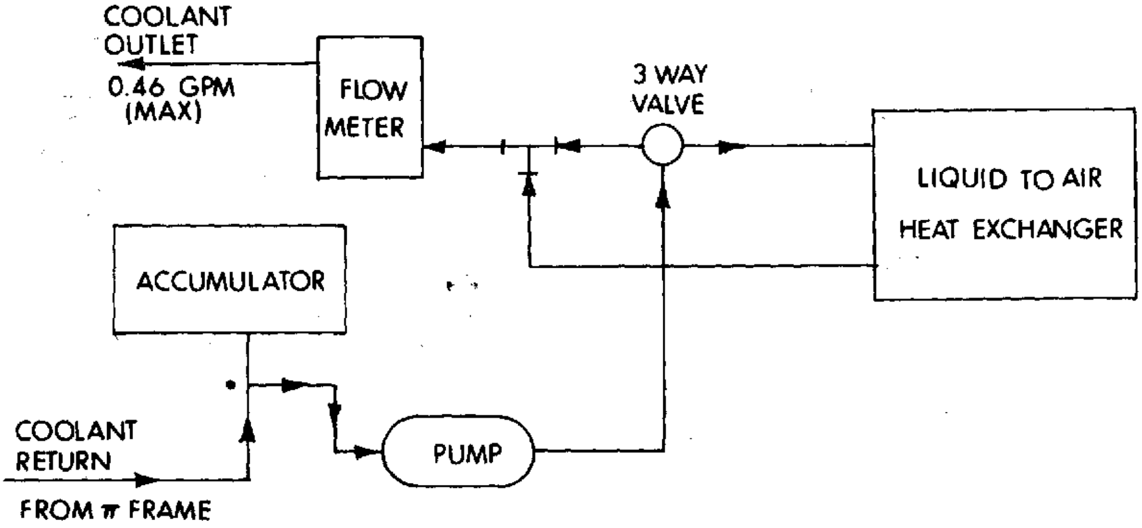

Fig. 3.4.1 SIRU Liquid-to-Air Heat Exchanger Flow Diagram

3.4.2 System Description

The SIRU system had to be designed to operate on spacecraft coolant lines and be removable without breaking these coolant lines, as well as to operate in a system test laboratory environment at minimum cost. These conditions required several compromises in the thermal design.

The approach taken was to design the RIP and the EA as flyable equipment and the heat exchanger (HX) for the RIP and cooling mechanism for the EA as rotary table mounted laboratory apparatus. For operation in the test laboratory in a 75°

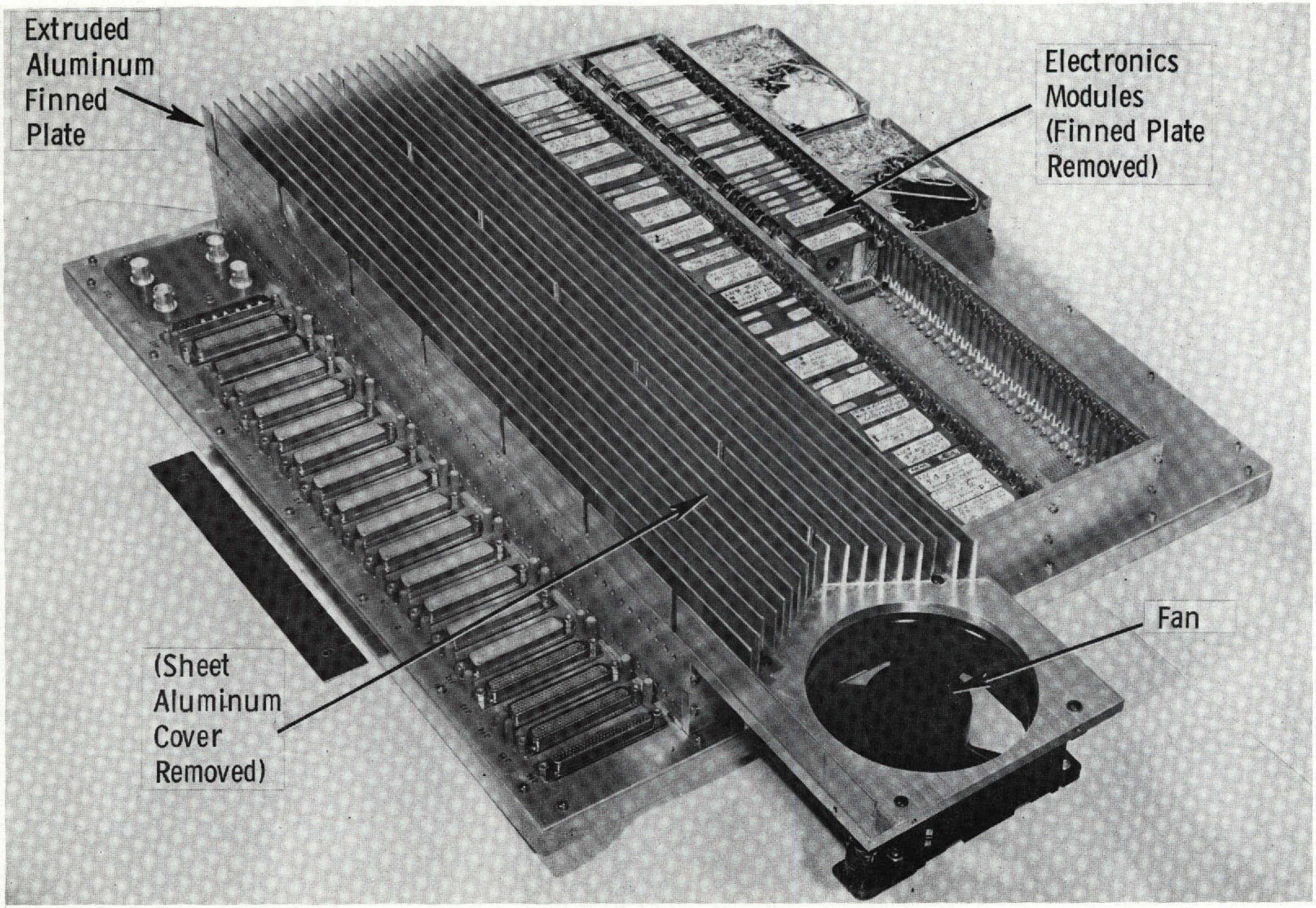

Fig. 3.4.2 SIRU Forced-Air Cooled Electronics Assembly

F environment, the liquid cooling HX package, Fig. 3.4.3, was designed to maintain the RIP π-frame at a slight temperature rise above ambient, thus avoiding the need for a refrigeration unit on the rotary table. The liquid-to-air HX package is mounted on the test table, making liquid slip rings unnecessary.

Each inertial sensor module has its individual temperature controller, and the mounting provisions for each module provide both alignment and thermal path control (thermal resistance). Controlling the heat flow by means of high thermal resistance minimizes thermal coupling between the inertial sensor modules and reduces the control power requirement. Coarse temperature control of some of the inertial sensor, module mounted, electronics circuits is achieved as a by-product of the inertial sensor temperature control by means of module thermal resistance design. Maximum thermal resistance to ambient as required in a spacecraft environment would be achieved by an insulating cover (thermal shroud) for the RIP.

The mounting pad materials for the gyro and accelerometer modules were selected to make the thermal impedances between modules and π-frame compatible; i.e. both gyro and accelerometer modules operate at the same percentage of maximum control power of their individual temperature controller circuit. The EA is forced-air cooled to meet laboratory test needs. For spacecraft use it could be connected to the liquid cooling loop or mounted on a heat-sinked structure, depending on the allowable spacecraft temperature range.

Mechanically the thermal design can be considered as consisting of four different control areas, namely: RIP, EA, gyro module and accelerometer module.

3.4.3 System Thermal Design Concept

Individual temperature control for each IC is not only consistent with the redundant implementation but allows for unsymmetrical thermal changes. Examples of these unsymmetrical changes are position sensitivity, module mounting thermal resistance variations, single component wheel power variation and random inputs such as torque commands.

In order to provide maximum isolation of the controlled element, the heaters are located at the IC mounting surfaces within the modules. The liquid cooling loop to the RIP coldplate develops a reasonably constant thermal sink. The RIP coldplate mounts to the back of the RIP π-frame in the central well area. Hold down screws accessible from the front of the RIP allow attachment of the coldplate

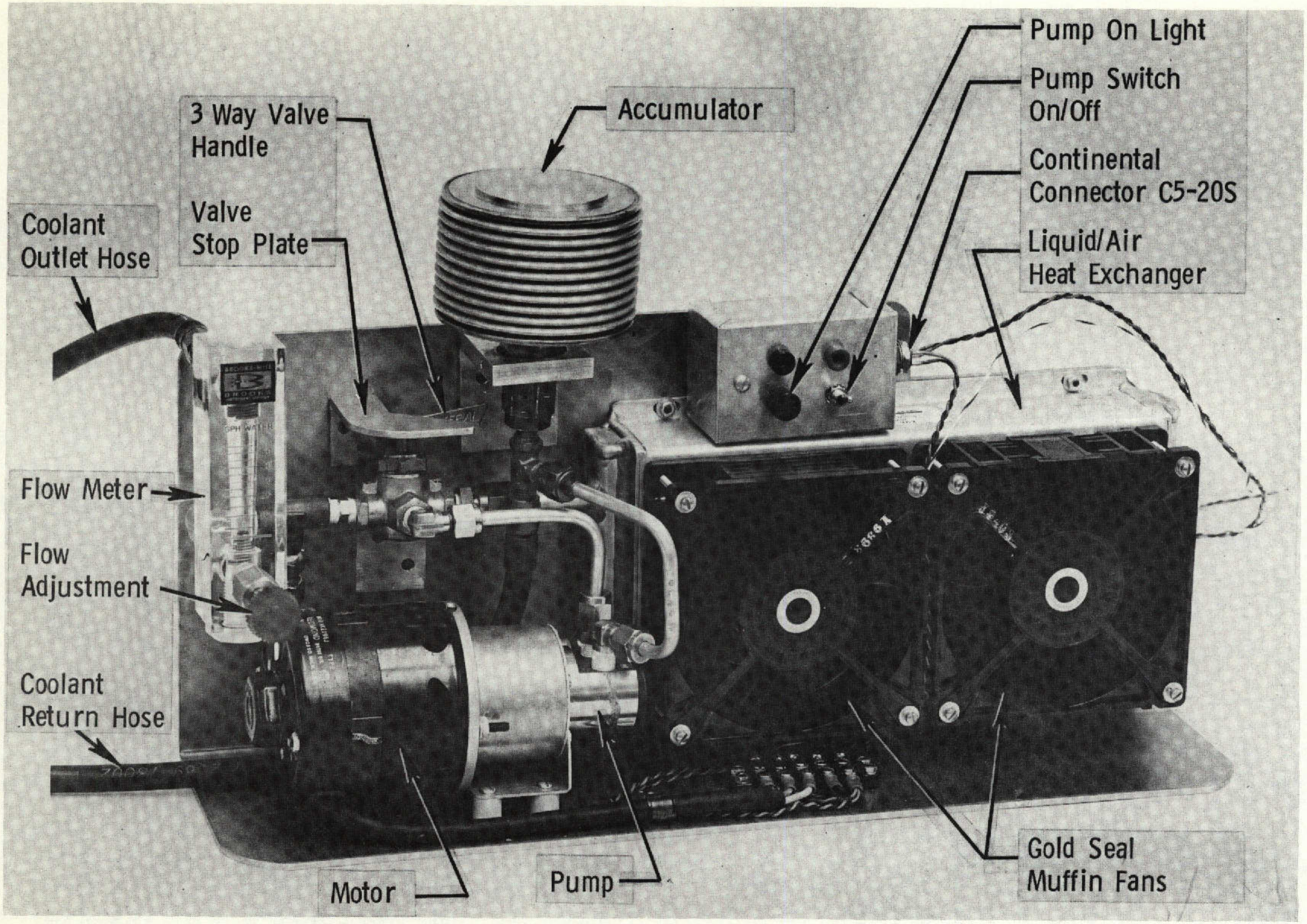

Fig. 3.4.3 SIRU Liquid to Air Heat Exchanger

from the front. A gasket spacer between the coldplate and the RIP allows adjustment of the thermal resistance between the π-frame and coldplate.

Use of a coolant loop provides the capability to regulate the amount of heat which is transferred from the π-frame to the coldplate (Fig. 3.2.7). Coolant temperature and flow rate may be adjusted to hold the π-frame at a nearly isothermal temperature, suitably lower than the inertial sensor control point. Such adjustment of the thermal resistance from the π-frame to the heat-sink can be accomplished to compensate for environmental conditions or system operating mode. Thus, in the standby mode, a high thermal resistance would minimize the power required to keep the π-frame at temperature. In the operate mode a lower thermal resistance would keep the instruments within the allowable controller temperature. This regulation capability was not instrumented in the SIRU system for laboratory operation.

The design of the coolant loop for laboratory operation of the system was based on operation at $70 \pm 5^{\circ}$ F ambient temperature to avoid the use of a refrigeration unit. Design goals were achieved by reaching a compromise in coolant flow rate and coldplate gasket width and material as discussed below.

A low coolant flow rate reduces π-frame to module temperature differences (gradients) for the gyro modules (which need more critical temperature control) at the expense of higher temperature gradients for the accelerometer modules. To maintain the same coldplate transfer, a low flow rate also requires a lower coolant inlet temperature. Narrower gasket width results in lower π-frame temperature differences for both type of modules, but also at the expense of lower coolant inlet temperature requirements. A gasket made of aluminum has a lower thermal resistance than one of titanium, offering the possibility of a higher coolant inlet temperature. These variables were optimized in the SIRU system by a small increase in the coolant flow rate, utilizing a gasket of 0.5 inch wide aluminum and accepting a slight increase in the π-frame temperature gradients.

A forced-air cooled π-frame had been considered, but it required too much space and blower power, and temperature control sensitivity was unsatisfactory.

For spacecraft operation, with a 45° F coolant supply, as specified in Apollo, an adaptive regenerative HX could be used for π-frame temperature control. The lower coolant temperature supply would, otherwise, dictate even higher inertial sensor thermal isolation to avoid excessive control power. Optimum thermal performance would be attained by using a regenerative HX and a thermal control by-pass valve operating as a function of gyro module temperature control power. The regenerative HX would interface with the spacecraft environmental control system with hot and cold liquid mixing occurring at the π-frame coldplate inlet. Other methods for controlling the coolant loop in the spacecraft environment are also feasible.

To attain the fine temperature control needed for both the gyros and accelerometers, proportional control loops are used. The control circuit is novel in that the control power is a linear function of control current. The control power in dc control loops typically corresponds to $I^2 R$. In the SIRU system linear control is achieved by mounting the output power transistors directly on the IC mounting block along with the control heaters. The control power then becomes a function of both the applied heater power and the power dissipated in the transistor. Since the major portion of the controller power is dissipated in the transistor the resulting control is both linear and efficient.

A ternary torque loop is used to drive the inertial instruments. In the zero torque mode, the torquing current is directed to a "dummy" heater, equal in resistance to the torquer, located at the TG end of the instrument. This arrangement results in a constant power input to the TG end of the instrument, thereby, reducing thermal gradients on the π-frame. Each gyro or accelerometer module is thermally and mechanically interchangeable.

The use of thermoelectric elements instead of heaters was considered with the objective of reducing control power. The concept was not implemented in the SIRU development model to avoid the impact of new technology for a non-essential purpose. Thermoelectrics should be reconsidered in future designs. Since thermoelectrics are bi-polar heat pump devices, the control point can be set at zero control power. For a heater system, zero control power means the system has just lost control.

3.4.4 Thermal Design of the Accelerometer Module

The thermal design of the accelerometer module was based on a multinodal thermal network, Fig. 3.4.4, and thermal model test analysis. The test results indicated what changes should be made to the first-cut design. Thermal resistance between control heater and mounting block was too high, while the thermal resistance between accelerometer and block was too low for good control action and minimal temperature variation at the block (see Fig. 3.2.4). One of the effects of these combinations was that the temperature variation at the PTE module mounted to the side of the block was unacceptable.

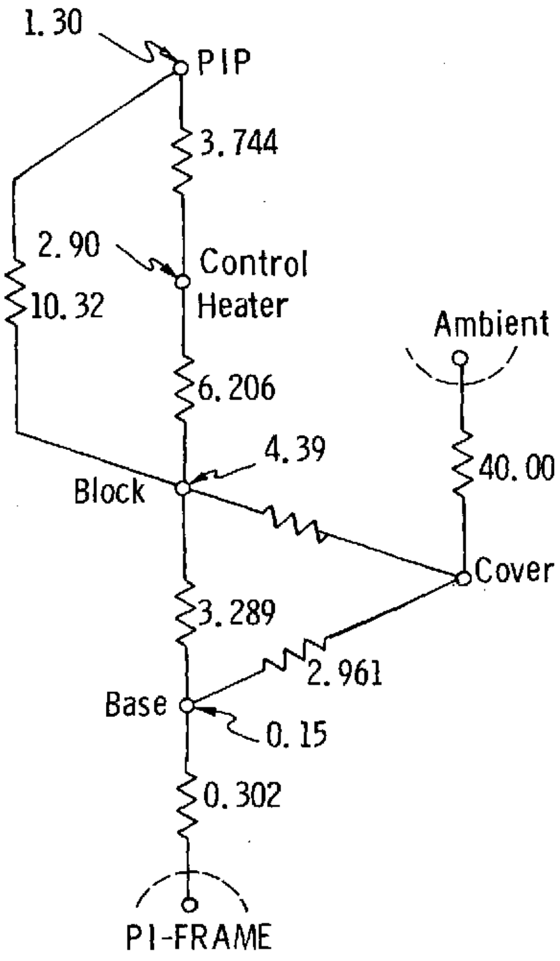

Fig. 3.4.4 SIRU PIP Module Thermal Model Network.

Recommendations resulting from these tests and incorporated into the final design were:

a) To decrease the control heater-to-block thermal resistance by changing the ring material from stainless steel to aluminum

b) To increase the accelerometer-to-block thermal resistance by increasing the clearance between the accelerometer body and block cavity

c) To increase the block-to-base thermal resistance by the use of Micalex washers instead of titanium under the mounting screws

d) To use an aluminum accelerometer mounting block

A nodal network representation of the accelerometer module thermal model as shown in Fig. 3.4.4 identifies the resistance values in units of $^{\circ}$F/watt. The numbers indicated by arrows are heat input values in watts. The ambient node can vary from 60°F to 110°F. Total dissipation is 5.7 watts excluding the control power of 2.9 watts. The resistance value of 40.0°F/watt from cover to ambient is a predicted value based on the assumption that a thermal jacket having 0.5 inch thick insulation will be provided for the RIP in the spacecraft. If this jacket is not present, this resistance value could be as low as about 8.0°F/watt.

The tested prototype accelerometer module can be represented in its simplest form by a nodal network of three equivalent resistors. Equivalent resistance for a 5.6 watt dissipation from control point to π-frame equals 9° F/watt (including 1.2°F/watt through greased pads). Equivalent resistance for 2.9 watt maximum control power from control point to π-frame equals 13.0° F/watt. Equivalent resistance from control point to ambient equals 12.0° F/watt without π-frame cover and 40.0°F/watt with 1/2 inch insulated π-frame cover.

Final thermal performance data shows that with bare modules (no insulated π-frame cover) in a laboratory ambient of 75°F, the accelerometer modules will stay within temperature control range (0-100% control power) over a π-frame temperature range of approximately 92°F to 125°F. In a spacecraft ambient of 60° F to 110°F, the accelerometer module will maintain temperature control over a π-frame temperature range from 77°F to 103°F if a 1/2 inch insulated π-frame cover is used (see Fig. 3.4.5). Temperature sensitive electronic modules in the accelerometer module, such as the PTE, will experience temperature excursions which are approximately 50% of the π-frame temperature excursions (see Fig. 3.4.6). The detailed description of the accelerometer temperature control circuit is presented in Volume IV.

A separate GSE heater and sensor assembly is mounted on the accelerometer alignment block. This heater and temperature sensor are used for GSE temperature control of the accelerometer module at 125°F, when the SIRU system is in the standby mode. A fourth accelerometer body wrap-around sensor is used in conjunction with the GSE to monitor accelerometer temperature at all times. Table 3.4.1. is a summary of the accelerometer temperature control circuit parameters.

3.4.5 Thermal Design of the Gyro Module

The final gyro module thermal design was based on a multi-nodal thermal network, Fig. 3.4.7, and model test analysis.

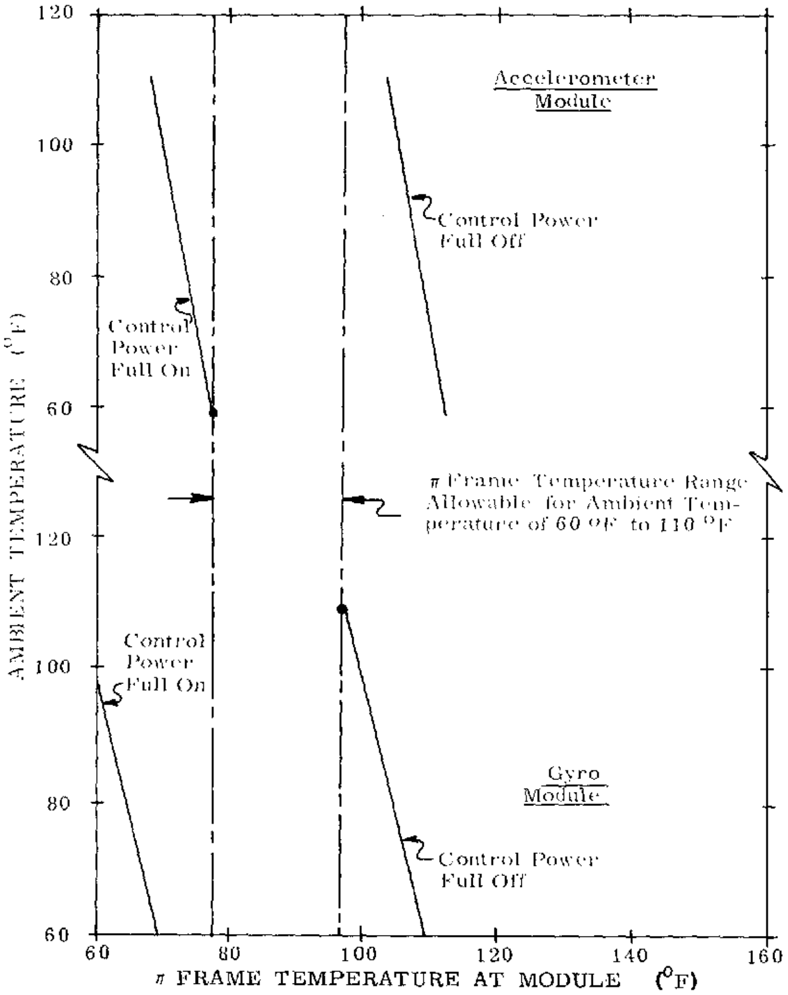

CONDITIONS: Coolant Temperature: 60°F.
Coolant Flow Rate: 0.2 to 0.3 GPM.
π Frame with Insulated Cover.
1.0 Inch Titanium Spacer.

Fig. 3.4.5 Module Temperature Control Range vs π-Frame and Ambient Temperatures

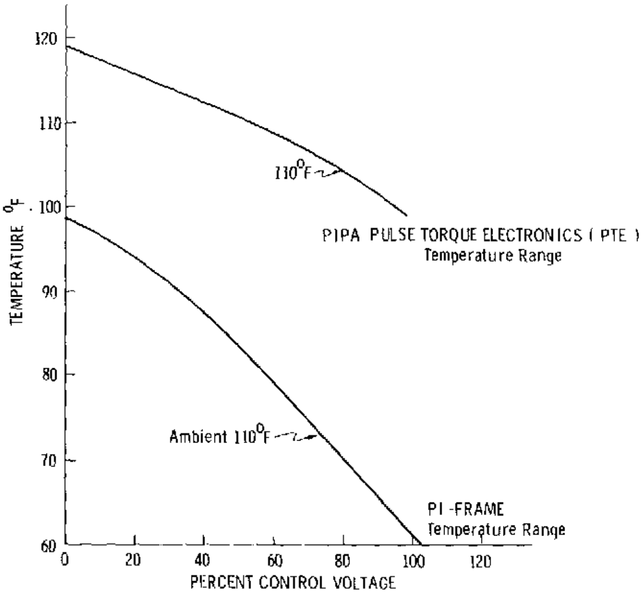

Fig. 3.4.6 PIPA PTE/π-Frame Temperature Range

Table 3.4.1 PIPA Module Temperature Control Parameters

Voltage:	28 vdc unregulated
Heater Power:	2.9 watts max @ 21.5 vdc
Power Transistor:	2N3752
Control Heater Resistance:	159 ohms
GSE Heater Resistance:	44 ohms
Control Sensor Resistance:	510 ohms @ 130°F
Monitor Sensor Resistance:	498.5 ohms @ 130°F
GSE Sensor Resistance:	510 ohms @ 130°F
Sensors Temp. Coefficient:	+0.00226 ohms/ohms/°F
PIPA Nominal Temperature:	130 + 1.6°F
PIPA Temp. Control Accuracy:	+0.1°F

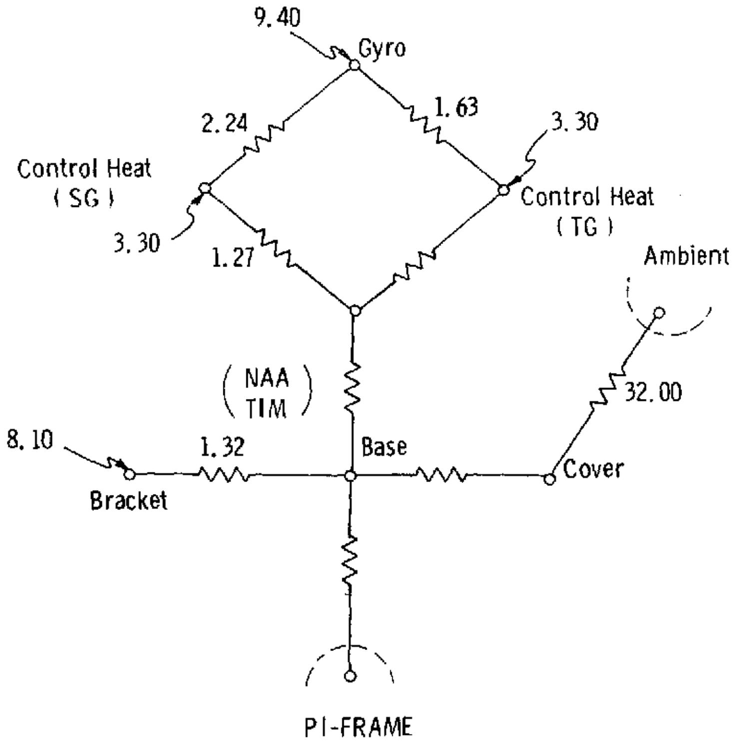

Fig. 3.4.7 SIRU Gyro Module Thermal Model Network

Results of these thermal test evaluations produced the following conclusions:

1) A variable-gap thermal interface material of high thermal conductance was needed between the gyro alignment plate and the module base plate to lower the thermal resistance.
2) The module could be successfully matched thermally to the accelerometer module on the π-frame by choice of suitable pad material in combination with the required thermal interface material (see Fig. 3.2.7).
3) The control heater power had to be increased to obtain a wider temperature control range.

The control heater power was increased by interchanging the 80 ohm GSE heaters with the 140 ohm control heaters. Thus, power was increased from 6.6 watts to 10.5 watts.

Tests were conducted to find a suitable thermal interface material (TIM) for module matching. The material chosen was a design by North American Aviation used on the Apollo program. This material consists of a copper foil helix wrapped around a one-eighth inch diameter silastic tubing. The copper helix provides the heat conduction path and the silastic tubing develops the necessary mechanical support. Thermal conductance can be varied to a small degree by the amount of compression applied and by maintaining the interface surface either dry or greased (see Fig. 3.4.8). The combination of this material and beryllium copper π-frame pad material accomplished the thermal matching.

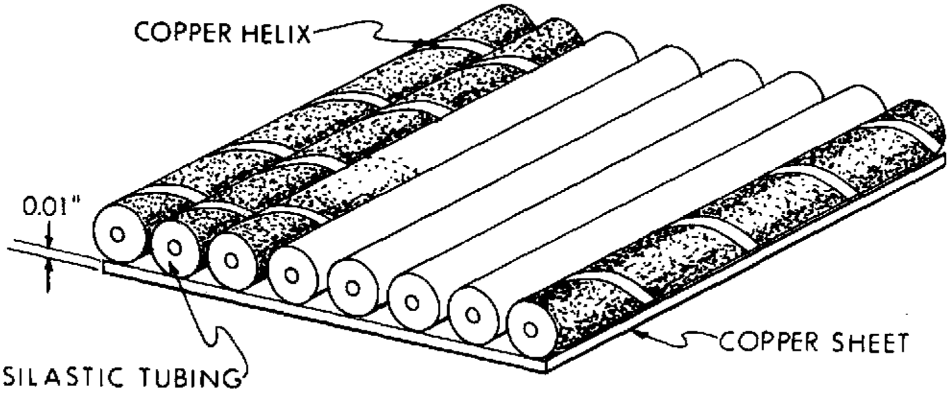

Fig. 3.4.8 Illustration of North American TIM.

The nodal network representation of the gyro module thermal model shown in Fig. 3.4.7 identifies the resistance values in units of °F/watt. The numbers indicated by arrows are the heat input values in watts. The ambient node can vary from 60°F to 110°F. Total dissipation is 17.5 watts excluding the control power of 10.5 watts. The resistance value of 32.0°F/watt from cover to ambient is a predicted value based on the assumption that a jacket having 0.5 inch thick insulation covers all modules on the π-frame. If this jacket is not present, this resistance value could be as low as about 7.0°F/watt.

The tested protoype gyro module can be represented in its simplest form by a nodal network of three equivalent resistors. Equivalent resistance for 17.5 watts dissipation (excluding control power) from control point π-frame is 2.6°F/watt (including 0.3°F/watt through greased pads). Equivalent resistance for 10.5 watts maximum control power, control point to π-frame equals 3.4°F/watt. Equivalent resistance, control point to ambient is 4°F/watt without π-frame cover and 20°F/watt with 1/2 inch insulated π-frame cover.

Final thermal performance data shows that with bare modules (no insulated π-frame cover) in a laboratory ambient of 75°F, the gyro modules will stay within temperature control range (0-100% control power) over a π-frame temperature range of approximately 88°F to 127°F. In a spacecraft ambient of 60°F to 113°F, the gyro modules will maintain temperature control over a π-frame temperature range of 69°F to 97°F, if a 1/2 inch thick insulated π-frame cover is used. Temperature sensitive electronics modules on the gyro module, such as the PTE, will experience temperature excursions which are 38% of π-frame temperature excursions (see Fig. 3.4.9).

The detailed description of the gyro temperature control circuit is presented in Volume II, Gyro Module.

3.4.6 Thermal Design of the π-Frame

Like the accelerometer and gyro modules, the final thermal design of the π-frame, Fig. 3.4.4, evolved from preliminary multinodal thermal network analysis by a computer program and thermal model tests. The test results indicated the following conclusions and recommendations;

a) A 4°F temperature variation between mounting pads on the π-frame could be expected at low control power for both gyro and accelerometer modules.

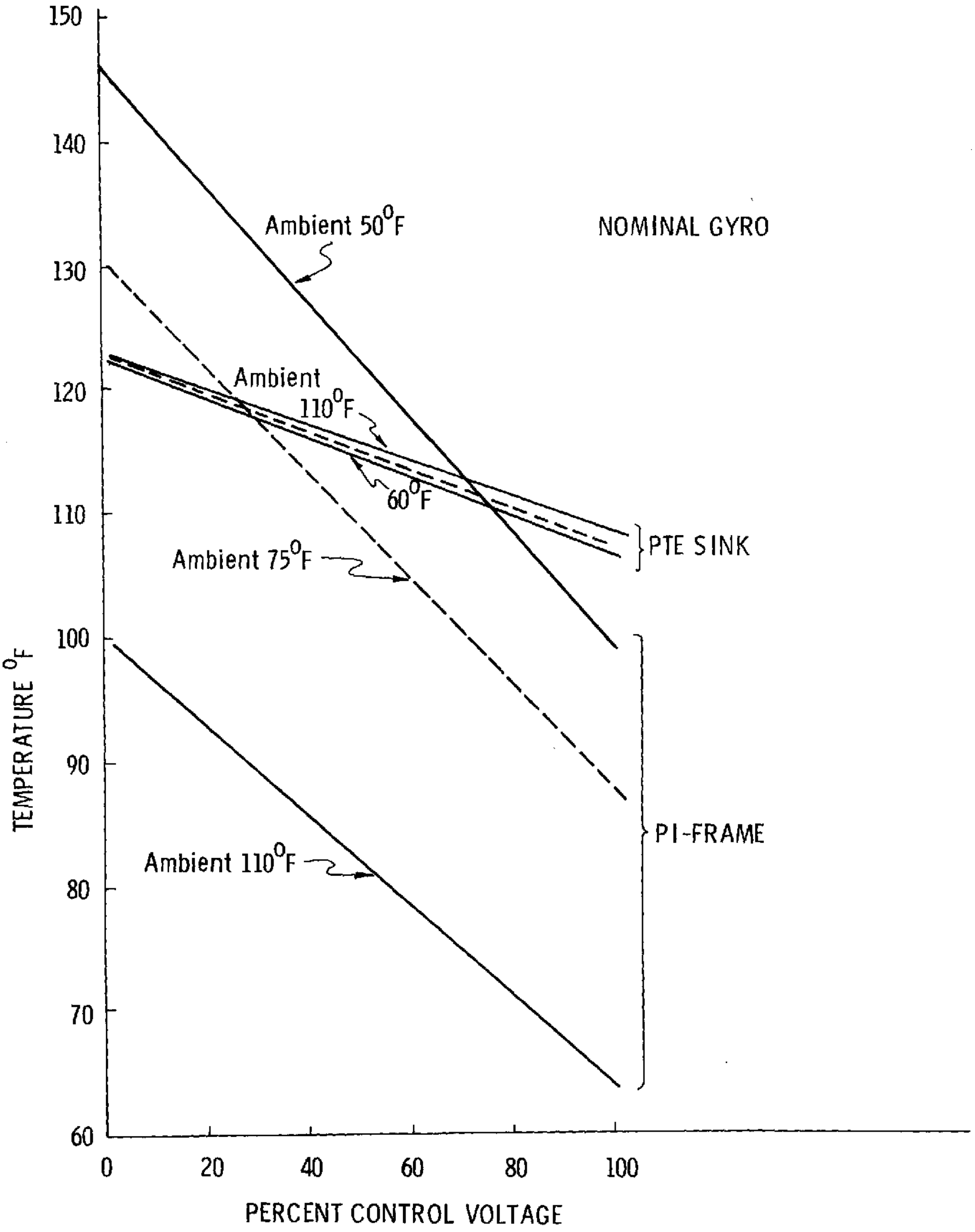

Fig. 3.4.9 Gyro PTE sink/PI Frame Thermal Comparison

b) Rearrangement of modules by moving the gyro modules to colder locations and the accelerometer modules to hotter locations would reduce the temperature variations occurring in these modules.

c) Reducing the coldplate contact area to about 1 inch width in the U -shaped heat exchanger pattern under the center part of the π-frame was necessary to minimize π-frame temperature variations.

d) Use of a gasket of titanium alloy, with greased interfaces, between the coldplate and the π-frame would provide the necessary thermal adjustment to permit use of a colder liquid coolant supply.

e) Thermal coupling between modules and π-frame could be adjusted by choice of pad material to provide a thermal match between the gyro and accelerometer modules. The pad materials must provide a hard surface to avoid wear and scratches which would affect alignment.

f) No changes in the basic π-frame structure were required.

g) For operation in 60°-110°F ambient, as required for flight, the module side of the π-frame would require a cover with 0.5 inch thick conventional foam insulation.

h) Relocating the coolant inlet to the left side of π-frame would reduce temperature differences at the gyro modules.

A sketch displaying temperature distribution at each inertial sensor module location on the π-frame is shown in Fig. 3.4.10. The average π-frame temperature varies from 93.0°F to 99.4°F at the module locations. Maximum temperature difference at the gyro module locations is 4.8°F, and at accelerometer module locations is 5.0°F. These results were obtained with a 74.4°F inlet coolant temperature and a flow rate of 0.20 gallons per minute (gpm).

π-frame temperature differences for accelerometer and gyro modules as a function of coolant flow rate and gasket width are shown in Fig. 3.4.11. The graph indicates that coolant flow rate and coldplate titanium gasket width are parameters which must be traded off. Reduced flow rate decreases π-frame temperature differences for the more critical gyro modules, but at the expense of higher π-frame temperature differences for the accelerometer modules and a lower inlet coolant temperature. Reducing the titanium gasket width decreases temperature differences for both type modules, but at the expense of a lower inlet coolant temperature.

For laboratory operations, ambient temperature is controlled at $75 \pm 5^{\circ}$F. Operation in this environment was achieved without refrigeration, using a liquid-to-air HX pumping unit (Fig. 3.4.3), by increasing the flow rate to 0.25 gpm and replacing the 1.0 inch titanium gasket material with 0.5 inch aluminum.

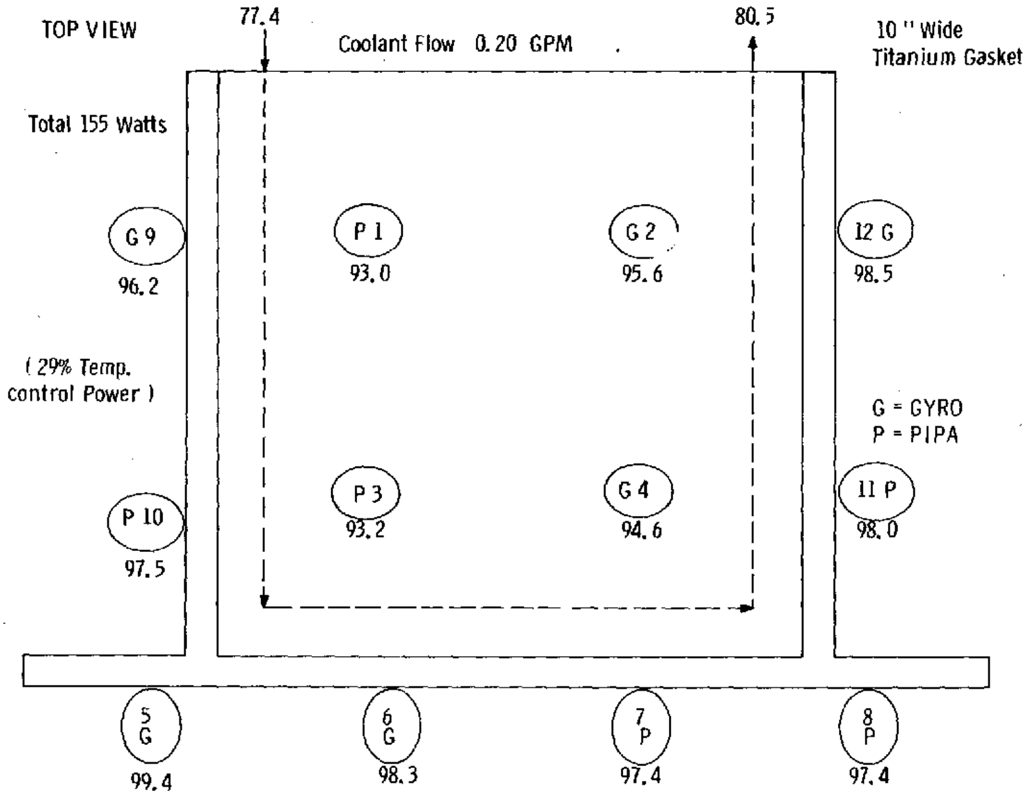

Fig. 3.4.10 SIRU π- Frame Temperatures, °F

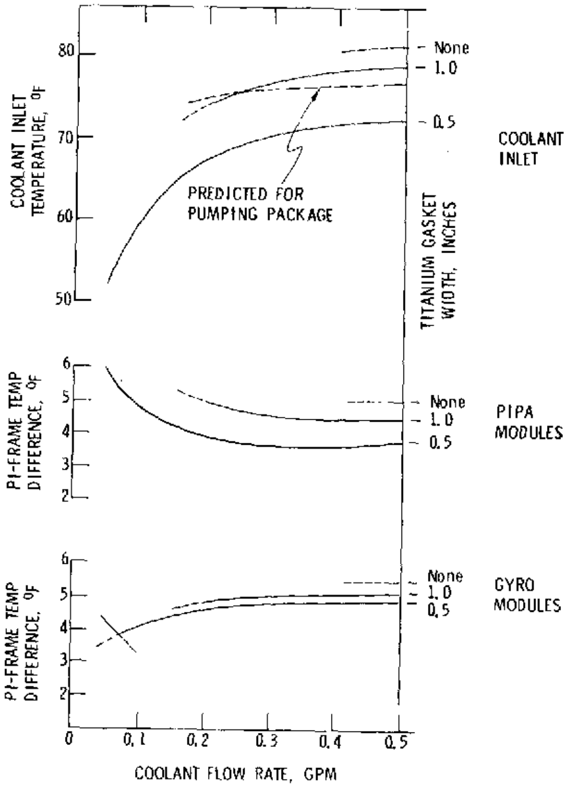

Fig. 3.4.11 SIRU π-Frame Cooling Performance

The curves of Fig. 3.4.5 show the π-frame temperature range allowable to maintain thermal control over an ambient temperature range of $60^{\circ}F$ to $110^{\circ}F$. Optimized parametric requirements for this figure are coolant temperature of $60^{\circ}F$, coolant flow rate of 0.2 to 0.3 gpm, an insulated π-frame cover and a 1.0 inch titanium gasket between the coldplate and the π-frame. Under these conditions, a maximum temperature variation of $9^{\circ}F$ at the base of the modules on the π-frame can be expected. This variation is composed of $5^{\circ}F$ for π-frame location, $2^{\circ}F$ for mounting interface resistance variation and $2^{\circ}F$ for liquid coolant supply temperature and flow rate changes. The π-frame and ambient temperature limits are established as follows.

Minimum Temperature Limit

1. Conditions
   Minimum π-frame temperature at module $78^{\circ}F$
   Minimum ambient temperature $60^{\circ}F$

2. Limiting Factor
   Accelerometer module control power full on

3. Penalty
   If either π-frame or ambient temperature is reduced, the affected accelerometer module's thermal demand will exceed its controller capability and the module temperature will drop.

Maximum Temperature Limit

1. Conditions
   Maximum π-frame temperature at module $97^{\circ}F$
   Maximum ambient temperature $110^{\circ}F$

2. Limiting Factors
   Gyro module control power full off

3. Penalty
   If either π-frame or ambient temperature is increased, the affected gyro module's thermal demand drops to zero and the module temperature will increase.

For applications requiring operation over a wider range of ambient temperatures, modification of the insulating spacer size and material, π-frame insulation, and implementation of a regulated coolant loop are required.

3.4.7 Thermal Design Features of the Liquid-To-Air Heat Exchanger

The SIRU liquid-to-air HX, Fig. 3.4.3, is a closed, pressurized system (5 psig) that supplies a fixed rate of coolant flow to the π-frame in any orientation. It is mounted on the rotary table in order to avoid liquid rotary joints.

The system consists of the following:

a) a pump for coolant circulation
b) a manually operated three-way valve for coolant flow direction (coolant outlet temperature setting)
c) a reservoir and expansion bellows (accumulator)
d) a flow meter for flow rate adjustment
e) a heat-sink consisting of a forced-air to liquid HX

The flow diagram of the coolant loop is shown in Fig. 3.4.1. The specifications for the unit are as follows:

1) Cooling Capacity: 200 watts at 70°F ambient, 0.46 gpm coolant flow and 75°F coolant outlet temperature (HX capacity of 22 watts/°F)
2) Coolant Flow: Adjustable from 0 to 0.46 gpm
3) Coolant: Inhibited Ethylene Glycol/Water mixture
4) Coolant Temperature: Adjustable, 75°F min. in 70°F ambient
5) Power: 115v, 60 cycles, 1 phase, 0.92 amps

The HX would not be used in the flight configuration of SIRU.

3.4.8 Thermal Design Features of the Electronic Assembly

The EA cooling system was designed for the laboratory environment only. Prime considerations were: simplicity of design, minimal effort, no active temperature control, avoidance of liquid coolant and easy dissassembly.

The final design, Fig. 3.4.2, consists of two separately removable, modular forced-air HXs mounted over the NAFI modules and a finned, natural convection heat-sink under the 40/5v power supplies. Each of the two identical, forced-air HX cools two rows of NAFI modules. Ambient cooling air (13 cfm) is drawn through the extruded aluminum finned plate and cover by a muffin fan operating on 115 vac, 60 cycle power. The HX surfaces are machined and greased for improved thermal conductance.

Since the EA is air cooled from the module side, removal of the NAFI modules requires the prior removal of the heat exchanger above that row of modules. The 40/5v power supplies, on the other hand, can be removed unimpeded from the module side.

At the 70°F room temperature, the maximum NAFI module frame temperature is 93°F. Under these conditions the semiconductor junction temperatures inside the modules remain below the 105°C reliability limit imposed on high reliability equipment in the Apollo program. The power supplies, however, operate slightly above (120°C) these established limits. Thermal resistance between NAFI modules and the structure is kept low by use of special clips (Bircher). Modules which dissipate the most heat are provided with more clips per module. Thermal analysis shows that temperature gradients along any row of NAFI modules is less than 2°F. Total power dissipated in the EA is 124 watts, 40 watts of which is at the 40/5v power supplies. Table 3.3.4 shows the distribution of power dissipation in the EA.

3.5 Documentation

The essential documentation of the RIP is contained in Fig. 3.5.1 which provides a simplified family tree showing the principal assembly and schematic drawings. Table 3.5.1 shows an index of the drawings identified with each of the electronic modules incorporated in the SIRU EA.

A review of the electrical and hardware items currently incorporated in SIRU shows that of approximately 350 items identified in the documentation by commercial designation, 250 are already qualified under military specifications or could readily be qualified by IDEP, previous military application or authenticated test data. Of the remainder, 50 items of miscellaneous hardware require some degree of effort to identify completely. It is estimated that one half of these (25 items) will turn out to be military specification equivalents. The remainder, approximately 75 items, require some degree of qualification action in order to meet a strict requirement for qualified parts selection.

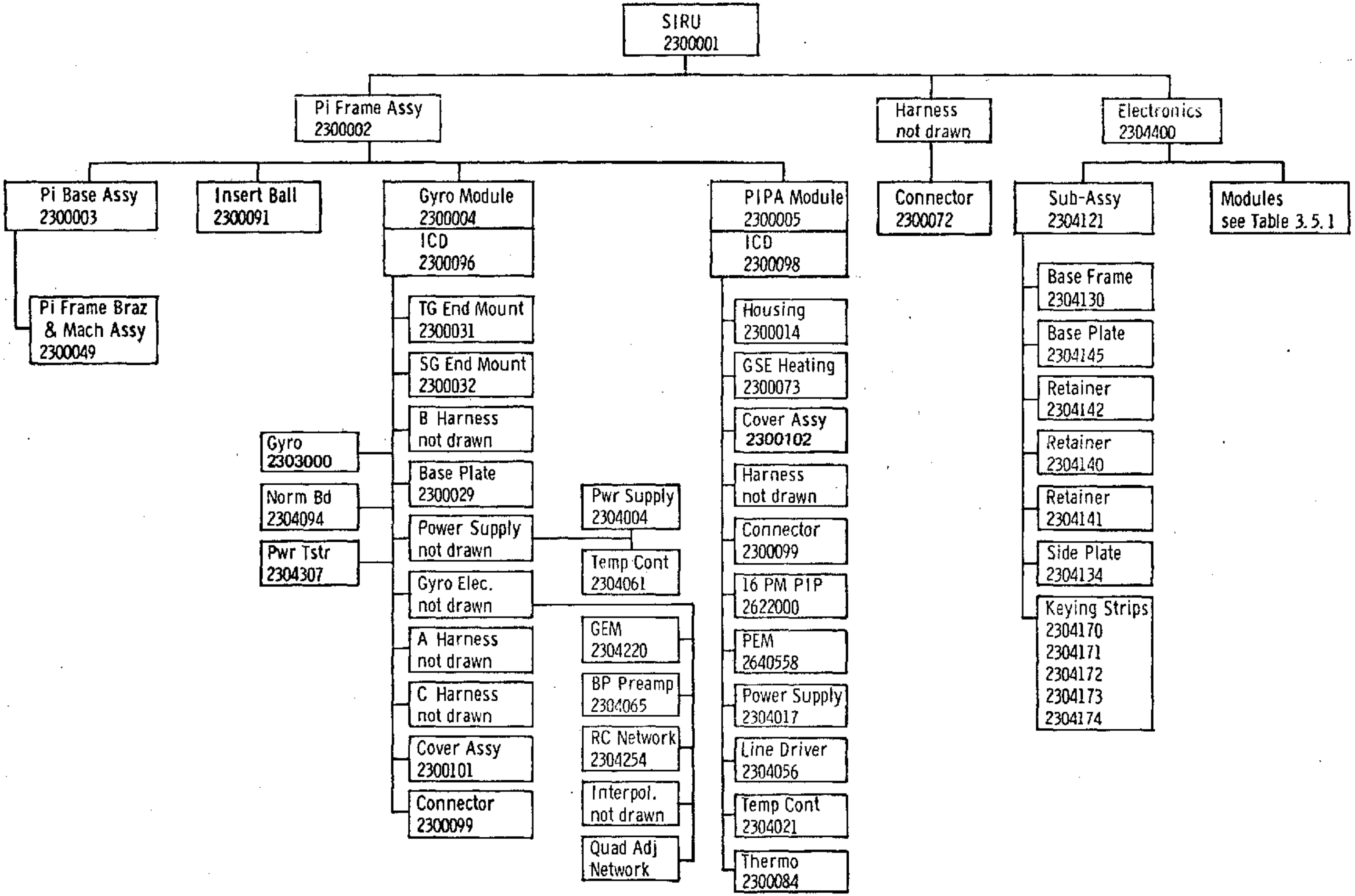

Fig. 3.5.1 SIRU Family Tree

Table 3.5.1 Electronic Assembly Documentation Index

MODULE TITLE	ASSEMBLY NO.	SCHEM.
DC AXIS SUPPLY	2304016	2304005
DC AXIS SUPPLY DRIVER	2304011	2304006
FUSE & DIODE	2304039	2304034
LOGIC TRANSFER HI/LO MONITOR	2304051	2304031
INTERROGATOR & SW LINE DRIVER	2304070	2304066
EXTERNAL CLOCK DR	2304074	2304071
5 VDC PULSE DR	2304079	2304067
40/5 V DC SUPPLY	2304086	2304033
TIMING & FUSE MOD	2304091	2304082
800 HZ WHEEL SUPPLY PWR AMP SECT II	2304097	2304098
9600 HZ SUSPENSION SUPPLY SECT II	2304105	2304095
800 HZ WHEEL SUPPLY PWR AMP SECT I/VI	2304108	2304250 2304251
9600 HZ SUSPENSION SUPPLY SECT IV	2304112	2304096
9600 HZ SUSPENSION SUPPLY SECT III	2304114	2304113
SCALER 1	2304236	2304204
SCALER 2	2304237	2304205
SCALER 3	2304238	2304206
SCALER 4	2304239	2304207
SCALER 5	2304240	2304208
900 HZ SECT I, 800 HZ SECT III	2304241	2304153
800 HZ SECT IV	2304242	2304150
800 HZ WHEEL SUPPLY PWR SECT V	2304255	2304106
CLOCK OSCILLATOR	2304308	—

4.0 Computation Facility and SIRU Software

The SIRU system was designed with an integral, dedicated computer in mind. The computer and its peripheral equipment were sized to support development and checkout including test software, and to carry out the full regime SIRU operational software. This chapter discusses the computational facility dedicated to the SIRU system, the test and operational software and the data handling and analysis programs written for this system.

4.1 SIRU Computation Facility

A computer facility was assembled to support, initially, the development, checkout and testing of the SIRU system including the development of SIRU software and software for the originally planned DCA. This same facility later supported the operational system. Major components of the facility are listed in Table 4.1.1.

The general purpose computer is a commercial DDP-516 manufactured by Honeywell. It is a 16-bit machine with a memory cycle time of 0.96 microsecond and includes the high-speed arithmetic package as well as 16,384 words of core memory. The Honeywell DDP-516 is compatible with current state-of-the-art airborne flight computers and as such serves as an excellent design demonstration and software verification vehicle. The computer has hardware interrupt and its structure incorporates direct, indirect and indexed addressing. The DDP-516 is relatively fast, its add time is 1.92 microseconds and the high-speed arithmetic package features a single precision multiply (5.82 microseconds) and divide (10.5 microseconds maximum) and double precision add and subtract (2.88 microseconds). The computer is compatible with the real-time processing requirements of the SIRU system running at a 100 update/second rate. In addition, the availability of a sophisticated disc operating system (DOS) developed for this particular computer by NASA/ERC enables operation with a large, moving head disc storage unit with backup capability. This combination of memory and versatile interactive capability provided a viable software development facility.

A detailed description of the computer peripherals listed in Table 4.1.1 as part of the Computation Facility is presented as follows.

Table 4.1.1

Major Components of the SIRU Computation Facility

Equipment Name	Identification
Computer	Honeywell DDP-516
Disc Drives	CDC 9433
Teletype	ASR-35
CRT Display	Sanders 720
Magnetic Tape I/O	Digistore W1-001
Paper Tape I/O	Remex
Dedicated Data Link to IBM 360/75	Bell 201A Data Phone
Test Table Interface	Wayne George Encoder

With the availability of DOS, a standard Honeywell disc control unit was added to the DDP-516. Two CDC 9433 drives are used, each capable of storing about 34 million words of data on line. The discs were used for the storage of: operational software programs, system calibration and data reduction programs and system test data for subsequent processing and error analysis. Programs were developed to "back-up" a disc by copying it on the second drive. Thus, a file copy of the current programs and data was always available.

User oriented input/output (I/O) capability is available either through the ASR-35 teletype unit or the Sanders 720 CRT. The CRT was procured to facilitate software development and for use as a real-time display. In all of the operational software described below in Section 4.2 (and in greater detail in Volume III), provision is made for real-time display of the system status.

Other I/O devices comprise a high speed Remex optical paper tape reader, a Digistore magnetic tape deck and a dedicated data phone link to MIT/CSDL's IBM 360/75 computer. A paper tape punch is available on the teletype, and all other forms of output (card decks, magnetic tapes, disc packs, etc.) are available at the IBM 360/75 through the data phone link. Initially, SIRU was dependent upon Digistore tape to transfer data to the IBM 360/75 complex, but the data phone link was incorporated midway through the program.

A final interface links the computer to the SIRU system and its test table. This interface contains an up-down counter for each inertial component, two interrogate pulse counters and a test table rotary axis readout. The up-down counters service the $\Delta\theta$ and ΔV outputs of the inertial components (IC). The gyro float angle interpolators are read separately.

An interface was planned for mating the SIRU system with the dual redundant Digital Computation Assembly (DCA). However, the DCA and its associated multiplexer were not implemented in hardware during this program period.

Figure 4.1.1 shows the computation facility as set up in the laboratory, Figure 4.1.2 is a block diagram of the operation, and Figure 4.1.3 shows additional detail of a typical ΔV or $\Delta\theta$ counter channel.

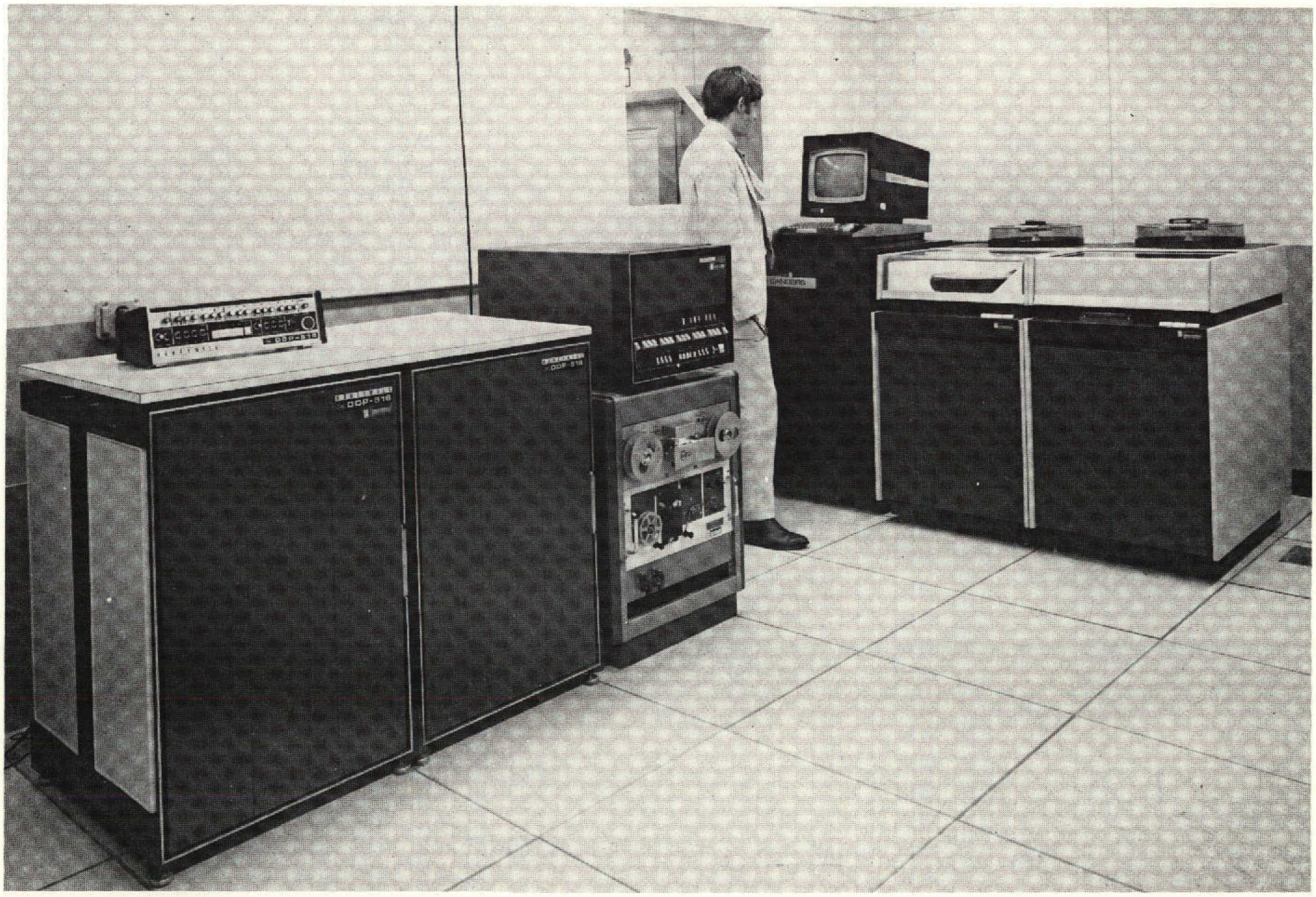

Fig. 4.1.1 SIRU Computation Facility

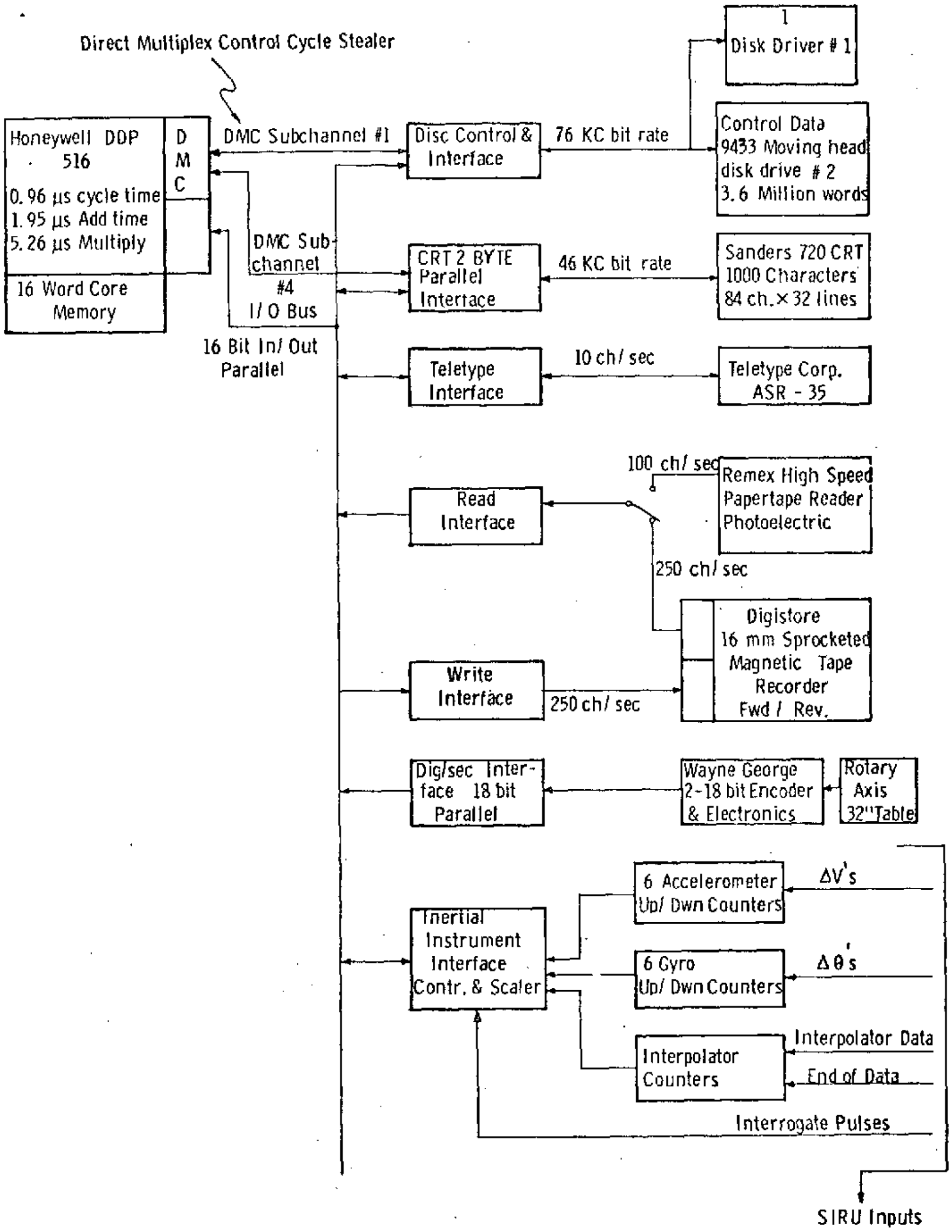

Fig. 4.1.2 Computation Facility Block Diagram

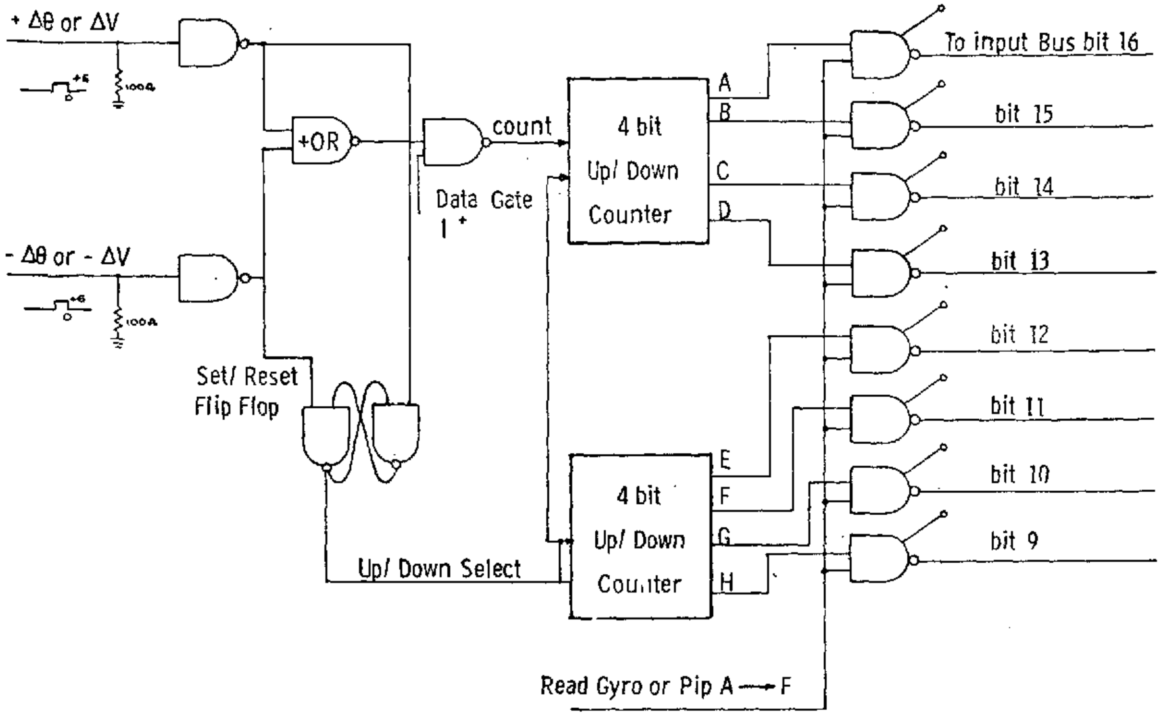

Note: 1* Data Gate Allows Counting Only During Interrogate Pulse.

Fig. 4.1.3 Typical Counter Channel Diagram.

4.2 SIRU Software Overview

A regime of modular, interacting programs was developed which functions, in general, to calibrate the system, verify its performance, provide failure detection and isolation (FDI) and develop navigation functions.

Using these programs the DDP-516 computation facility is used to perform the following specific tasks:

1. Direct and perform automatically (with the exception of table orientation positioning since digital table servo positioning was not available) the multiple position calibration test operation on the SIRU system during which a complete IC parameter determination is obtained, printed and stored. A single position sequence is designed to operate overnight and unsupervised.
2. Direct and perform real-time system testing during which the computer implements all the operational software for the following system tests:
   a) Pre-launch calibration sequence
   b) Pre-launch alignment (gyrocompassing) sequence

c) IC on-line compensation (static and dynamic)

d) Redundant six axes body measurements data to least-squares computational triad frame and implementation of adaption matrix for isolated faults

e) FDI equation computations to provide Fail Operational, Fail Operational, Fail Safe (FO, FO, FS) capability

f) Implementation of strapdown attitude and velocity algorithms supporting the navigation functions

3. Develop and checkout all of the software requirements for the previously described operations including data storage and transfer for subsequent analysis using Draper Laboratory's IBM 360/75 computation facility.

4.3 SIRU Software Description

The following description of the operational software is an abbreviated version of the detailed description provided in Volume III. Previous chapters in this volume have described the analytical theory and implementation of the software. The following material summarizes the software description contained in Volume III. All the operational software for the SIRU test system was developed on the DDP-516 computer facility, while complementary data analysis, data plotting and simulation programs were prepared for the IBM 360/75.

This development included the hardware checkout software, the system calibration and calculation programs, software development tools e.g., text editor and CRT display drivers, and an assembler for the DCA. A DCA self-test program was developed using the text editor and the DCA assembler.

4.3.1 Static Calibration Tests

SIRU performance is evaluated by comparison of system data with external references. The comparison is accomplished through the use of two parallel sets of computer programs, the SIRU DDP-516 software and an array of analysis, simulation and comparison programs available on MIT/CSDL's IBM 360/75. A dedicated link between the two computers facilitates the almost immediate evaluation of the SIRU real-time performance. The more important programs for each computer are explained in this section.

The simplest operating mode of the SIRU system is "static calibration" testing. Given the deterministic models of the ICs, it has been shown that a six position test (see Table 4.3.1) yields data necessary and sufficient to isolate and compute the static error parameters listed in Table 4.3.2. A DDP-516 program, STLOOP, used in each position, serves to collect instrument output in the form of elapsed time and torque pulse count for each of the twelve instruments. This data set is indexed serially by test position and date, and stored on the disc. In the calibration sequence, STLOOP is run in each of the six positions. Fig. 4.3.1 illustrates the engineering display. Table 4.3.2 lists the terms and engineering units shown in the figure.

Table 4.3.1 Static Testing Equations

$$\mathrm{Wij} = \mathrm{INTRATE} \cdot \mathrm{SF}_{\mathrm{nom}} \frac{(\mathrm{NGij}+)\ (1 + \mathrm{DSFi}+) - (\mathrm{NGij}-)\ (1 + \mathrm{DSFi}-)}{\mathrm{TGij}} \ (\mathrm{rad/sec})$$

where

Wij = total drift of the ith gyro in the jth calibrate position (i = A through F, j = 1 through 6)

DSFik = scale factor deviation from nominal of the ith gyro, where k denotes the + or - scale factor (ppm)

TGij = number of timing pulses for the ith gyro in the jth calibrate position

INTRATE = loop interrogate rate used for timing (4 800 pulses/sec)

$\mathrm{SF}_{\mathrm{nom}}$ = $2^{-13} + 2^{-14} + 2^{-15}$ rad/torque pulse = 0.213623 mrad/torque pulse

NGij = number of positive (+) or negative (-) $\Delta\theta$ pulses accumulated for the ith gyro in the jth calibrate position

$$\mathrm{ADIA} = \frac{(\mathrm{WA6} - \mathrm{WA5})\ \cos\alpha\,\mathrm{GA} - (\mathrm{WA1} - \mathrm{WA2})\ \sin\alpha\,\mathrm{GA}}{2} + \mathrm{WIEV}$$

$$\mathrm{ADSA} = \frac{(\mathrm{WA1}-\mathrm{WA2})\ \cos\alpha\,\mathrm{GA} + (\mathrm{WA6} - \mathrm{WA5})\ \sin\alpha\,\mathrm{GA}}{2}$$

$$\mathrm{ADOA} = \frac{(\mathrm{WA4} - \mathrm{WA3})}{2} + \mathrm{GSA}^*\mathrm{WIEV}$$

$$\mathrm{BDA} = \frac{\sum_{j=1}^{6} \mathrm{WAj} + 2\mathrm{WIEH}\ (\cos\alpha\,\mathrm{GA} + \sin\alpha\,\mathrm{GA} + \mathrm{GSA}^*)}{6}$$

$$\mathrm{A2DA} = \frac{\frac{(\mathrm{WA5} + \mathrm{WA6} - \mathrm{WA1} = \mathrm{WA2})}{2} + \mathrm{WIEH}\ (\mathrm{GSA}^* - \cos\alpha\,\mathrm{GA})}{\mathrm{Sin}\ (2\alpha + 2\mathrm{GOA}^*)}$$

where

$\alpha\mathrm{GA} = \alpha + \mathrm{GOA}^*$

Fig. 4.3.1 CRT Keyboard Display Equipment

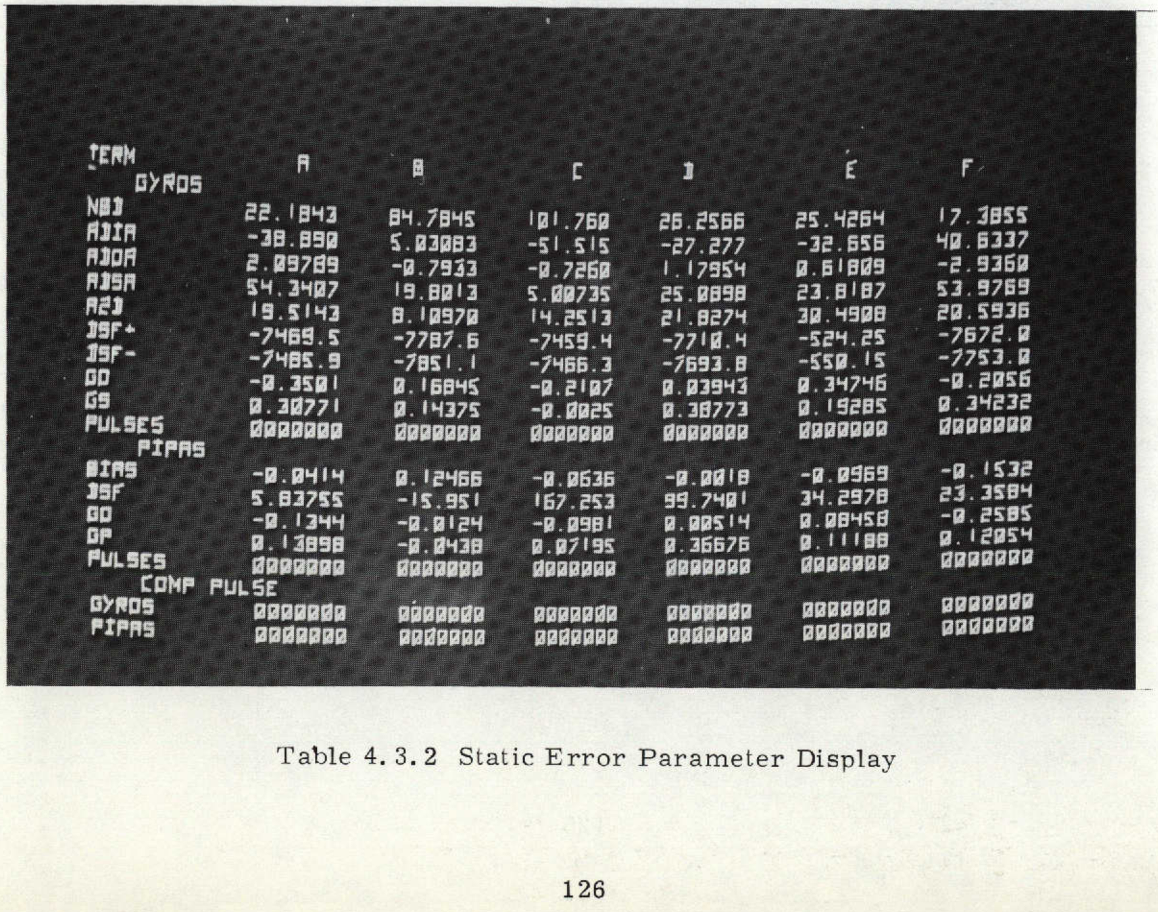

```
TERM            A          B          C          D          E          F
   GYROS
NBD          22.1843    84.7845    101.760    26.2566    25.4264    17.3855
ADIA         -38.890    5.03083    -51.515    -27.277    -32.656    40.6337
ADOA         2.09789    -0.7933    -0.7260    1.17954    0.61809    -2.9360
ADSA         54.3407    19.8013    5.00735    25.0898    23.8187    53.9769
A2D          19.5143    8.10970    14.2513    21.8274    30.4908    20.5936
DSF+         -7469.5    -7787.6    -7459.4    -7710.4    -524.25    -7672.0
DSF-         -7485.9    -7851.1    -7466.3    -7693.8    -550.15    -7753.0
DD           -0.3501    0.16845    -0.2107    0.03943    0.34746    -0.2056
GS           0.30771    0.14375    -0.0025    0.38773    0.19285    0.34232
PULSES       0000000    0000000    0000000    0000000    0000000    0000000
   PIPAS
BIAS         -0.0414    0.12466    -0.0636    -0.0018    -0.0969    -0.1532
DSF          5.83755    -15.951    167.253    99.7401    34.2978    23.3584
GO           -0.1344    -0.0124    -0.0981    0.00514    0.08458    -0.2585
GP           0.13898    -0.0438    0.07195    0.36676    0.11188    0.12054
PULSES       0000000    0000000    0000000    0000000    0000000    0000000
   COMP PULSE
GYROS        0000000    0000000    0000000    0000000    0000000    0000000
PIPAS        0000000    0000000    0000000    0000000    0000000    0000000
```

Table 4.3.2 Static Error Parameter Display

Two other programs are used to access this data and reduce it to modeled parameters (in engineering units). GYRCAL searches the filed data to retrieve the latest STLOOP data set for each of the six positions,[*] extracts the gyro information, and calculates the drift parameters.[**] A similar program, PIPCAL reduces accelerometer data to extract a_b, SF error and two misalignments for each functional axis. The results from GYRCAL and PIPCAL are filed on the disc for later use in the real-time compensation load.

STLOOP may be iterated to collect a continual record of system static performance in one position. In this case, the 11 minute test is used to collect 50 to 300 data sets which are identical in form to those discussed above. As before, they are filed serially for later analysis. At the command of the test technician, the data is transferred to the IBM 360/75. Several versions of a MAC 360 program, ICSASTAB, are resident there. These programs process the raw data into engineering units, subject it to statistical analysis and produce printed and plotted records of the performance stability of the twelve inertial components. This procedure is routinely followed and a substantial body of data is available to confirm system performance levels. Figure 4.3.2, for instance, graphically displays the stability of one gyro over a weekend run. The mean output represents a component of earth rate plus the gyro drift; the standard deviation of the data indicates the corresponding performance.

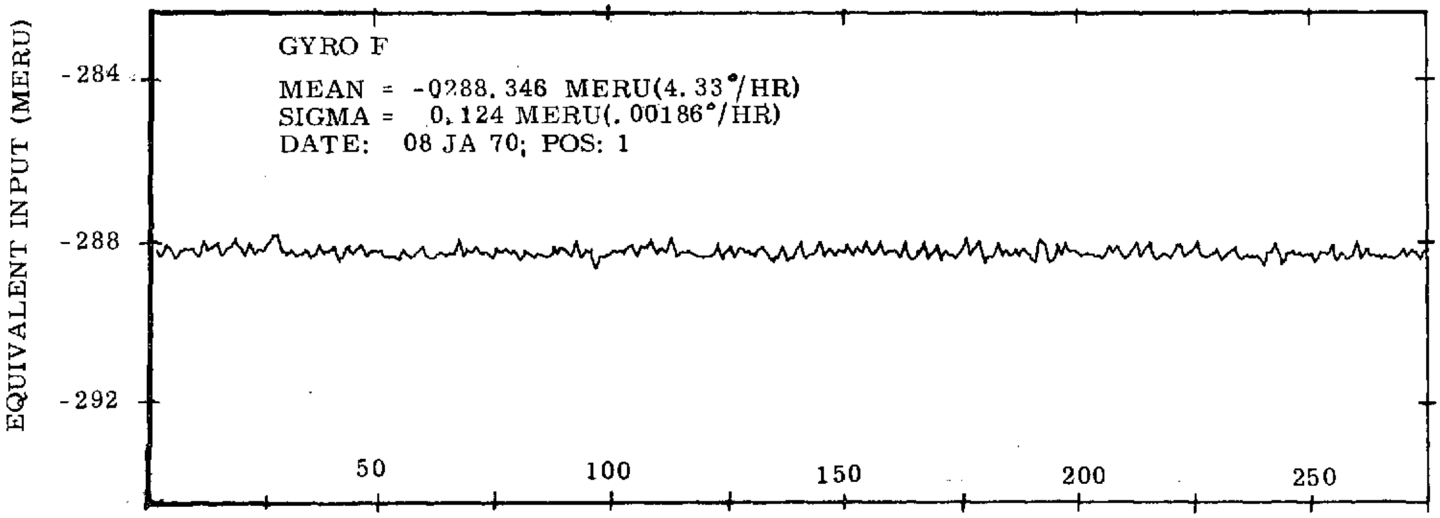

Fig. 4.3.2 SIRU Gyro Stability

---

[*] The user may, alternatively, specify earlier data sets by serial number.

[**] Gyro misalignment and SF calibration requires a dynamic test, which is described later.

Gyro scale factor (SF) error and misalignments can be determined only through dynamic tests as described below.

4.3.2 Dynamic Calibration Tests

Certain gyro parameters (SF error, misalignments about Spin Axis (SA) and Output Axis (OA), anisoinertia) are determined from dynamic calibration tests (test program JIMK). Data is taken in three test positions, with the table rotated in both positive and negative directions. Five rotation rates are used in each sense chosen so that:

$$\cos\alpha \ \omega_i = \sin\alpha \ \omega_{i+1}$$

Using this rule, the test conditions for all instruments reflect the same rate inputs.

Upon completion of data collection (3 positions, 2 senses, and 5 rates yielding 30 data sets), a DDP-516 program, DYNCAL, retrieves data from the disc, calculates the gyro error parameters (Table 4.3.3), and displays and stores these values.

Table 4.3.3 Rate Testing Equations

General format of the 4-simultaneous equations required

$$\begin{array}{llllllll}
A\ GOi^* & + & B\ Pi & + & C\ SFGi- & & = & D \\
E\ GOi^* & + & F\ Pi & + & G\ SFGi- & & = & H \\
I\ GOi^* & + & J\ Pi & & + & K SFGi+ & = & L \\
M\ GOi^* & + & N\ Pi & & + & P SFGi+ & = & Q
\end{array}$$

where GOi^* = output axis misalignment (Radians)

$$Pi = \text{anisoinertia} \left(\frac{I_{SA} - I_A}{H}\right) (\sec_t)$$

$$SFGi\pm = \text{gyro scale factors} \left(\frac{\text{Radians}}{\text{Pulse}}\right)$$

4.3.3 Real-Time Operational Software and Verification

The real-time operating software for the SIRU system comprises a complex of interacting routines coded in machine language. It is shown schematically in Fig. 4.3.3, SIRU Data Processing, and is described in detail in Volume III. This section bridges the gap between the schematic and the machine language routines. The routines themselves are also discussed.

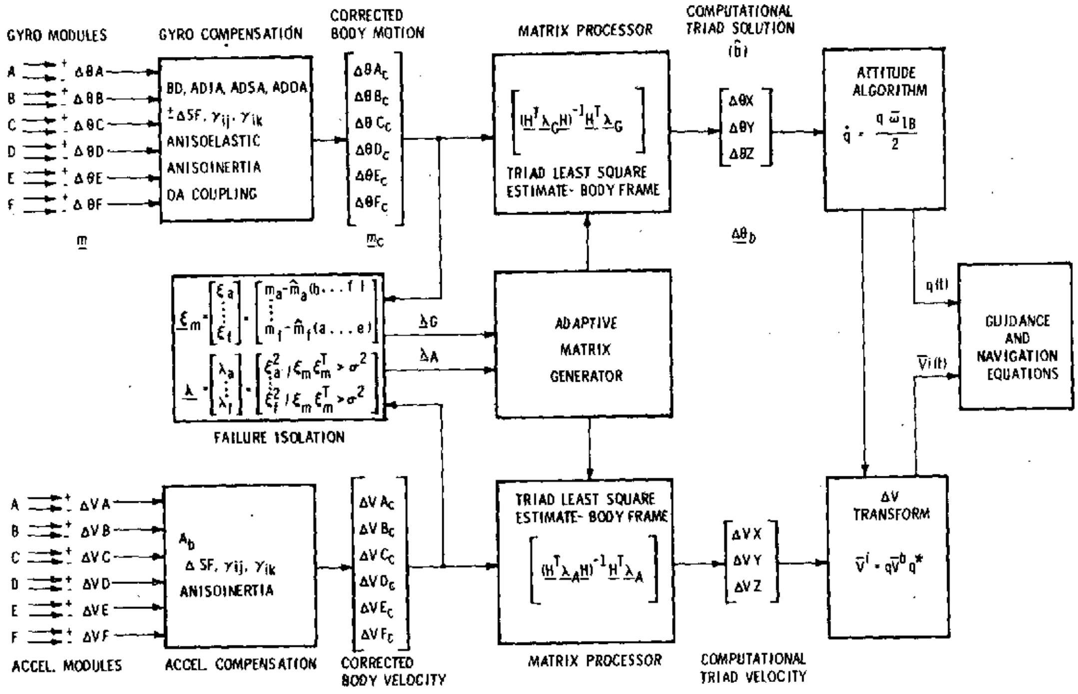

Fig. 4.3.3 SIRU Data Processing

The computational requirements of a strapdown system are as follows:

(1) Correct the raw gyro and accelerometer pulse counts by compensation routines to accommodate for the calibrated bias terms, misalignments, etc.

(2) Derive the computational triad solution for body rotation and velocity increments through the matrix processors

(3) Effect the failure detection and isolation equations, yielding current system failure status

(4) Adapt separate gyro and accelerometer matrix processors to reflect current failure status (λG - gyro axis failures and λA - accelerometer axis failures)

(5) Transform the body axis triad angular solution ($\Delta\theta_x$, $\Delta\theta_y$, $\Delta\theta_z$) to a body frame with respect to inertial reference attitude indication, quaternion (q) four parameter representation

(6) Transform the body triad velocity solution (ΔV_x, ΔV_y, ΔV_z) to an inertial velocity in the inertial frame

Other software subsequently added during the SIRU Utilization program and documented in R-747 included:

(1) Single position calibration
(2) Gyrocompassing routine
(3) Statistical FDI software with on-line recalibration
(4) Local vertical navigator

Although these operations were identified in Chapter 2, it must be recognized that the actual computation process is a complex procedure. The algorithms are divided into two sets, an accelerometer data processor and a gyro data processor.

The system accumulates ΔV and $\Delta\theta$ pulses from the torque- to-balance instrument loops after initialization. With the system operating at 100 iterations per second the accelerometer and gyro pulse counters are processed every 10 milliseconds (ms). Their processing, however, is interleaved so that the 10 ms of ΔV accumulation processing precedes the 10 ms of $\Delta\theta$ accumulation processing by 5 ms. The velocity and attitude algorithms are staggered in the same manner. This staggering is achieved immediately upon initialization by using the first 5 ms of $\Delta\theta$ data after initialization in the first attitude algorithm iterations prior to a full 10 ms velocity update.

The tasks accomplished during the accelerometer and gyro updates are listed here. To process the accelerometer outputs we require the system to perform the following tasks:

A1) Read the status of the six counters
A2) Compensate the output for average SF, bias and misalignments of each accelerometer's input axis about its output and penduluous reference axes
A3) Compensate the output for errors due to $R\omega^2$ and $R\dot{\omega}$ as a function of the accelerometer's position relative to the angular input
A4) Accumulate the corrected output for the purpose of FDI
A5) Perform FDI resulting in a current failure status
A6) Check the parity equations for third fail
A7) Create a least-squares matrix (as a function of fail status) to transform the six compensated ΔVs into the XYZ body frame
A8) Do the 6 x 3 matrix multiplication
A9) Unitize the attitude quaternion prior to velocity algorithm processing

A10) Do the velocity algorithm i.e., use the current attitude quaternion to generate the velocity transformation matrix and transform the incremental body velocity into the inertial frame

A11) Accumulate ΔV inertial for output processing

To process the gyro outputs we presently require the system to perform the following tasks:

G1) Read the table encoder, and the six gyros and interpolator accumulators

G2) Compensate the output for ±SF, Null Bias Drift (NBD), Acceleration Dependent Input Axis drift (ADIA), Acceleration Dependent Output Axis drift (ADOA), Acceleration Dependent Spin Reference Axis drift (ADSRA), anisoelasticity, misalignments, anisoinertia, Spin Reference Axis (SRA) cross-coupling and OA coupling

G3) Accumulate the corrected output for FDI

G4) Perform the FDI processing resulting in a current failure status

G5) Check the parity equation for third fail

G6) Create the least-squares matrix (as a function of failure status) to transform the six compensated $\Delta\theta$s into the XYZ body frame

G7) Do the 6×3 matrix multiplication

G8) Compensate for earth rate

G9) Update the attitude quaternion

In the time remaining, the system status is documented either on the teletype, the CRT display or on an incremental magnetic tape for further analysis (Fig. 4.3.4). The information outputted includes the attitude quaternion, ΔV_I accumulated over some interval, a squared error monitor and fail status for gyros and accelerometers, the test-table angle encoder output and time since initialization.

Coding of these operations is divided among thirty subroutines and a main program which sequences and controls communication between them. A brief description of the software at this level appears in Appendix D. Volume III presents a detailed description, including listings and load maps.

Each of these routines was subjected to extensive test verification and integrated system testing. For example end-to-end tests (12 to 60 hour duration) in a local vertical navigational mode have been repeatedly performed. In this test, the system software maintains an inertial reference by means of a quaternion, q_{IB}, which represents and quantifies the rotation from the inertial to the current body frame. A third order quaternion update algorithm is employed. The incremental

ΔV_B is transformed into the inertial frame, and used to update inertial velocity and position estimates.

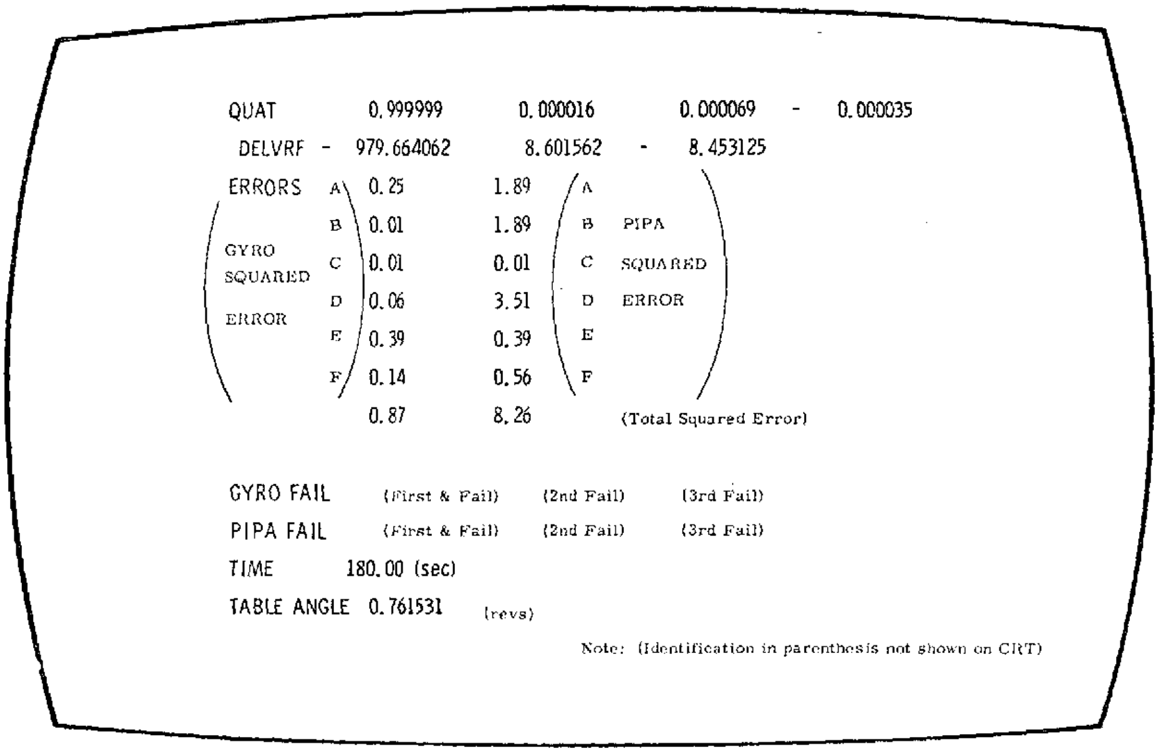

```
QUAT          0.999999        0.000016        0.000069   -   0.000035
 DELVRF  -  979.664062        8.601562   -    8.453125
ERRORS     A  0.25           1.89      A
           B  0.01           1.89      B  PIPA
GYRO       C  0.01           0.01      C  SQUARED
SQUARED    D  0.06           3.51      D  ERROR
ERROR      E  0.39           0.39      E
           F  0.14           0.56      F
              0.87           8.26         (Total Squared Error)

GYRO FAIL      (First & Fail)    (2nd Fail)    (3rd Fail)
PIPA FAIL      (First & Fail)    (2nd Fail)    (3rd Fail)
TIME        180.00 (sec)
TABLE ANGLE  0.761531   (revs)
                         Note: (Identification in parenthesis not shown on CRT)
```

Fig. 4.3.4 CRT System Status Display

The test results are typically evaluated using a series of evaluation programs resident in the IBM 360/75 computation facility.

Test data stored on the tape or disc and transferred to the IBM 360/75 for evaluation comprise real-time attitude, inertial velocity and inertial position estimates from SIRU software, and a record of table rotation over the test interval. Initial attitude, velocity and position are given. The record of table motion is processed by a third order quaternion update algorithm to yield a theoretical or "perfect" system attitude. This algorithm matches that of the SIRU software, but its input is free of gyro quantization and drift errors. The "perfect" attitude is used to process the specific force input due to gravity for "perfect" navigation. Comparison is made with the system's real-time record, both at the attitude and navigation (velocity and position) levels. As with the static tests discussed previously, the MAC language program includes a variety of options for reporting and plotting indices of performance. Thus this program provides a flexible tool for the analysis of SIRU system performance from a variety of tests. Static, constant slew and oscillatory tests have been processed, and show good agreement between measured (SIRU) and computed ("perfect") performance.

5.0 SIRU Reliability Appraisal

5.1 Observed Operational Reliability

Table 5.1.1 presents a summary of the SIRU system hardware reliability over the period beginning 27 January, 1970 and ending 19 November, 1971. During this period, the SIRU system was operated for 14,600 hours with a total of 71,000 gyro module operating hours and 88,000 accelerometer module operating hours. No simultaneous failures occurred. There were two gyro failures (January, 1971 and March, 1971) and one gyro module PTE failure (April, 1971). One of the gyro failures was a gas bearing wheel non-start after 2811 wheel hours of operation and 1745 wheel start/stop cycles. The other gyro evidenced intermittent float hangups after 5017 wheel hours of operation and 1914 wheel start/stop cycles. The PTE failure was due to a marginal solder joint (that degraded with time) at one of the scale factor (SF) resistor terminals. As a workmanship failure, it does not reflect on the PTE reliability as determined by the reliability of the PTE electronic components. It does, however, reflect a potential hazard that is not easily screened and represents a continuing reliability hazard to the system population.

Table 5.1.1 SIRU System Hardware Reliability

Data from 1/27/70 to 11/19/71	Component Failures	Operating Hours	System Failures
	3	14,600	0

	No. of Failures	MTBF Measured	MTBF 90% Conf	Operating Hours "Actual"	Operating Hours Req'd*
Gyro	2	35,500	13,400	71,000	185,000
PTE	1	159,000	40,700	159,000	620,000
Accelerometer	0	88,000	38,300	88,000	202,000

*Operating Hours required to demonstrate measured MTBF with 90% confidence

Table 5.1.2 is a tabulation of estimates of failure rates for SIRU hardware components. The failure rates for the electronics were estimated using a component parts count of each circuit with electronic component failure rates based upon Apollo experience. The conservative failure rate of 75×10^{-6} failures/hr shown in the gyro reliability range (Table 5.1.2) reflects the 13,400 hour MTBF value (at the 90% confidence level) from Table 5.1.1. The measured MTBF of 35,500 hours for the gyros (Table 5.1.1) was used to determine the lower failure rate value of 28×10^{-6} for the gyro shown in Table 5.1.2. (This estimate is also conservative because in this gyro population the wheel start problem was a known design deficiency that was subsequently resolved by a bearing material change). The failure rates shown for the accelerometer modules are conservative and were obtained by assuming that one failure did occur in the 88,000 hours of operation even though there were actually no failures during this period. The lower accelerometer failure rate given in Table 5.1.2 (11.4×10^{-6}), corresponds to an assumed one failure in 88,000 hours. The pessimistic accelerometer failure rate (26×10^{-6}) corresponds to the 90% confidence MTBF of 38,300 hours shown in Table 5.1.1.

Table 5.1.2 SIRU Failure Rate Estimates

	Failure Rate, λ (Failures per Hour)
Gyro Module:	
Gyro	$28\text{-}100 \times 10^{-6}$
Gyro PTE, Interpolator & 8v Supply	15×10^{-6}
Temperature Control	3×10^{-6}
Wheel Supply	11×10^{-6}
Net Gyro Module Each Axis = λ_1	$57\text{-}129 \times 10^{-6}$
Accelerometer Module:	
PIP	$11.4\text{-}50 \times 10^{-6}$
PIP PTE 8v Supply	12×10^{-6}
Temperature Control	3×10^{-6}
Net PIP Module Each Axis = λ_2	$26.4\text{-}65 \times 10^{-6}$
Electronics Assembly (6 Axes Support):	
9600 Hz Supply	10×10^{-6}
DC Axis Supply	12×10^{-6}
Fuse/Diode Module	1×10^{-6}
Net Electronics Assembly = λ_3	23×10^{-6}
Electronics Assembly (Dual or Triple Redundant):	
40/5 vdc Supply = λ_4	12×10^{-6}
28 vdc Pre-Regulated = λ_5	12×10^{-6}
Multiplexer = λ_6	10×10^{-6}
Clock = λ_7	1×10^{-6}
Scaler = λ_8	10×10^{-6}

5.2 Theoretical Reliability Calculations

Various SIRU reliability curves (reliability vs. mission time) are presented in Figs. 5.2.1 through 5.2.4 using the SIRU reliability criteria given in Table 5.1.3 for defining hard and soft failures and the failure rates listed in Table 5.1.2. Included for reference on each plot is the corresponding reliability of a triad system having non-redundant components with the same failure rates as the SIRU components. Fig. 5.2.1 presents SIRU reliability for the soft failure configuration using the 90% confidence failure rates for gyros and accelerometers. Fig. 5.2.2 presents SIRU reliability for the hard failure configuration using the 90% confidence failure rates for gyros and accelerometers. Figures 5.2.3 and 5.2.4 repeat the two previous figures using the failure rates experienced during the test programs for gyros and accelerometers.

These analyses are based on the following two assumptions:

1. The FDI coverage, defined as the probability that a failure, having occurred, will be detected and properly isolated, is 100%.*

   As described in Chapter 2, the FDI can not only detect and isolate two failures of gyroscopes and accelerometers and detect a third failure, but can also isolate the third failure if it results in a substantially greater squared error than the previous failures. The soft fail analyses presented here assume that two failures only are detected and isolated.
2. The SIRU equipment is in uninterrupted operation throughout the mission.

Equations are derived separately for what we termed soft and hard failure systems. The term soft failure is defined to encompass performance degradations which can be isolated only by measurement comparisons (voting or FDI algorithms). Hard failure is used to describe faults which do not require voting for proper isolation. In general, these are catastrophic failures which can be isolated by self-test hardware (BITE) or reasonability type software tests.

SIRU reliability equations are derived separately for systems which can tolerate different amounts of component failures. These two configurations are described in terms of what failures can be tolerated (Table 5.1.3). Soft failure systems are those in which FDI can isolate failures of only two measurement axes. Thus, up to two gyro and two accelerometer modules can be isolated automatically <u>or</u> two

---

* The reliability analysis in R-747 includes analysis of FDI coverage.

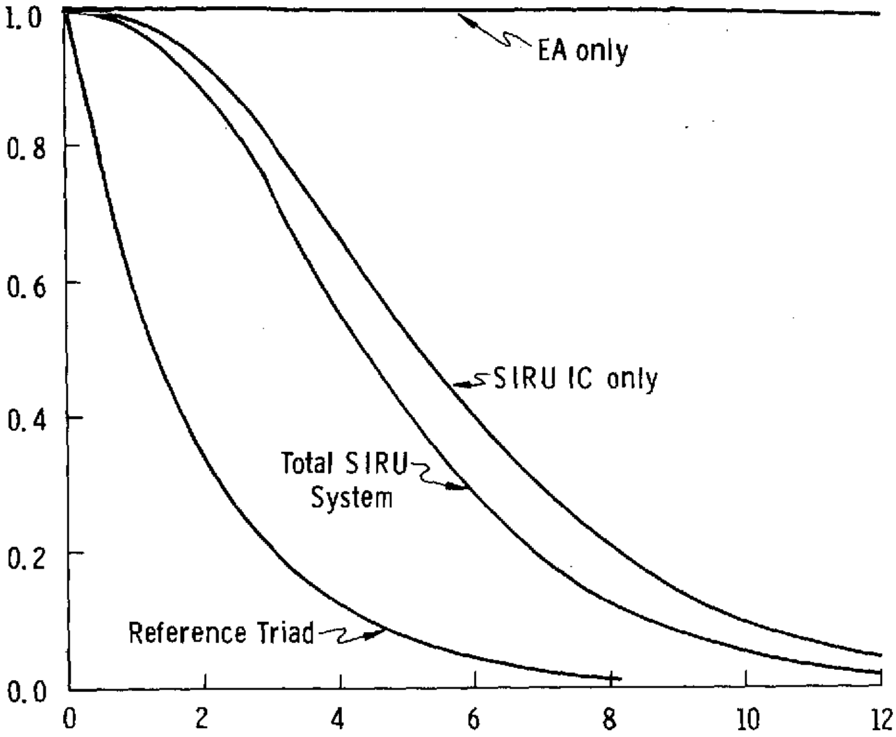

Fig. 5.2.1 SIRU Reliability - Soft Failures 90% Confidence Failure Rates for Gyros and Accelerometers

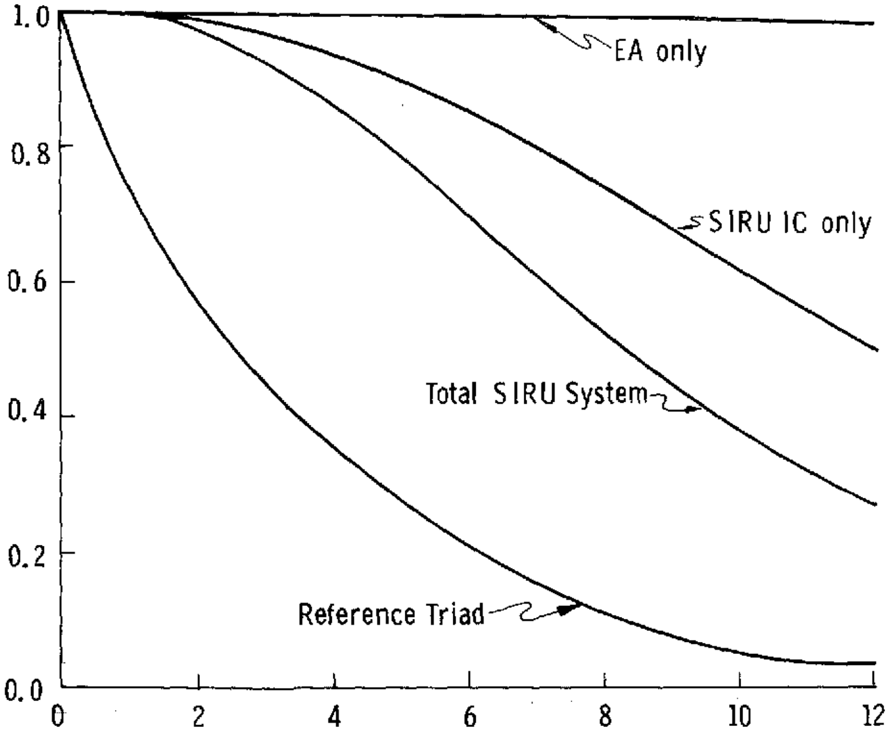

Fig. 5.2.2 SIRU Reliability - Hard Failures 90% Confidence Failure Rates for Gyros and Accelerometers

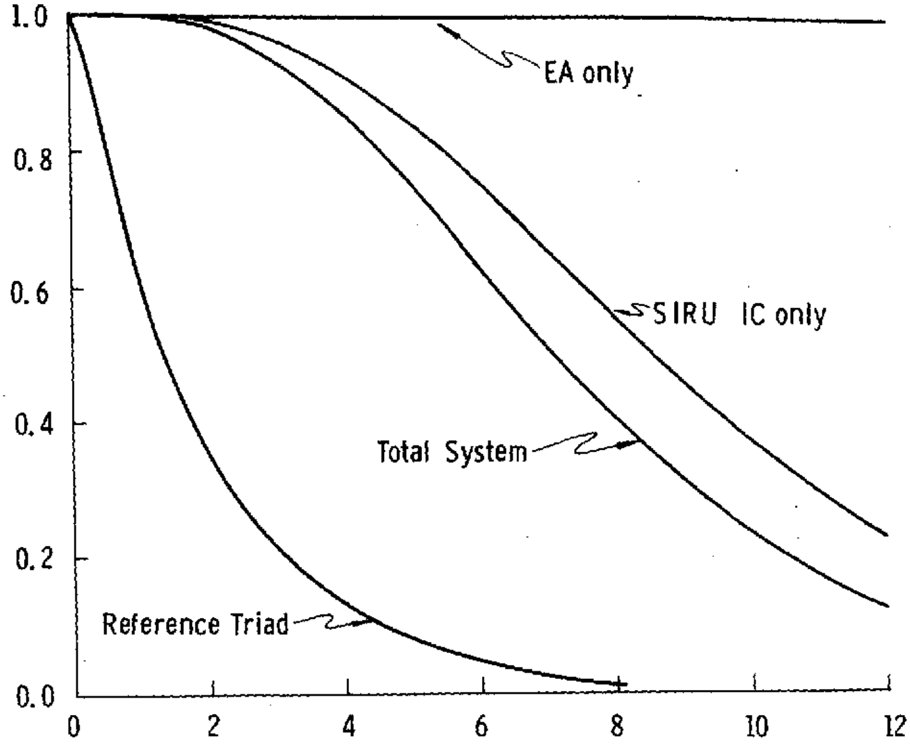

Fig. 5.2.3 SIRU Reliability - Soft Failures Experienced Failure Rates for Gyros and Accelerometers

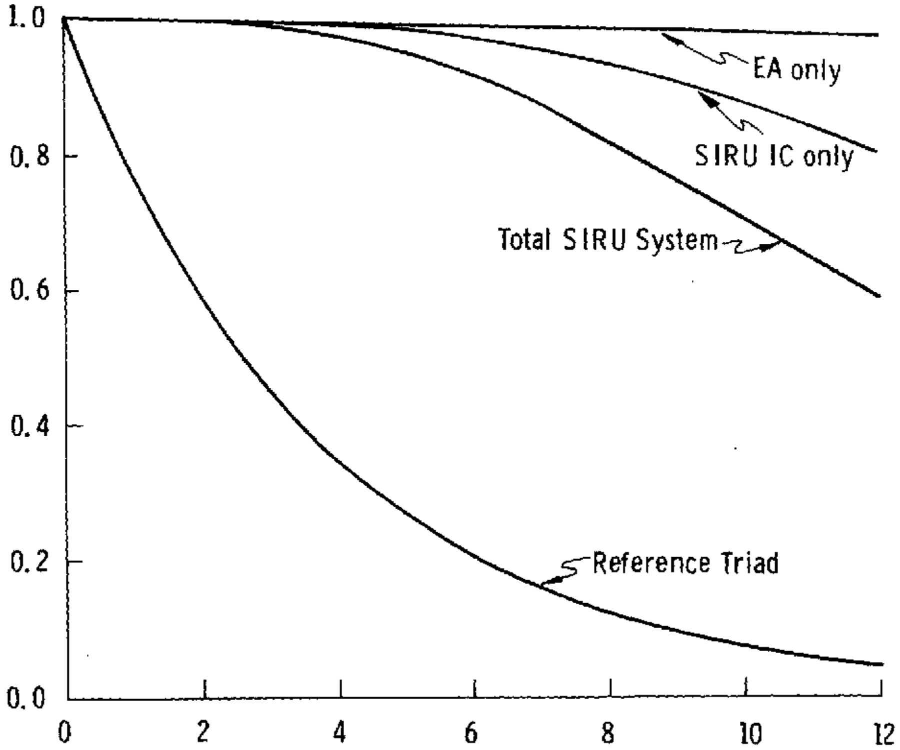

Fig. 5.2.4 SIRU Reliability - Hard Failures Experienced Failure Rates for Gyros and Accelerometers

electronic functional axes can be lost, with operation continuing. In addition, one of two scalers, one of two 40 vdc/5 dc supplies, one of two 28v supplies, one of two multiplexers and one of three clocks can fail without failing the system.

Table 5.1.3 SIRU Reliability Criteria

		Tolerable Failure Combinations	
Device	Redundancy Level	Soft Failure System	Hard Failure System
Gyro Module	6	(2 Fails and	(3 Fails and
PIPA Module	6	2 Fails)	3 Fails)
Electronic Assembly Functional Axes	6	OR 3 Fails and	OR 3 Fails
Scaler & 40v ps	2	1 Fail and	1 Fail and
Oscillator	3	1 Fail	2 Fails
Critical Path: Module & Axes		FO-FS	FO-FO-FS

FO = Fail-Operate

FS = Fail-Safe

Hard failure systems are those which include BITE and more extensive FDI (reasonability tests) etc. This hard category can tolerate the same non-axis-dedicated electronics failures, but will operate with up to three gyro or accelerometer modules, or three functional axes lost. The system will survive failure of two of the three clocks.

The reliability curves in Figs. 5.2.1 through 5.2.4 were calculated as follows. (All failure rates used are those given in Table 5.1.2).

5.2.1 Triad Reliability Calculations

The following reliability functions are calculated for the reference triad curves shown on Figs. 5.2.1 through 5.2.4. Reliability of a single gyro module:

$$R_G = e^{-\lambda_1 t} \tag{5.1}$$

where λ_1 = Net gyro module failure rate.

Reliability of a single accelerometer module:

$$R_A = e^{-\lambda_2 t} \tag{5.2}$$

where λ = Net accelerometer module failure rate.

Reliability of axis-dedicated electronics:

$$R_{AE} = e^{-\lambda_3 t} \tag{5.3}$$

where λ_3 = Net axis-dedicated electronics assembly failure rate.

Reliability of the non-axis-dedicated electronics:

$$R_{NAE} = e^{-\lambda_q t} \tag{5.4}$$

where λ_q = Net non-axis-dedicated electronics assembly failure rate.

$$\lambda_q = \lambda_4 + \lambda_5 + \lambda_7 + \lambda_8 \tag{5.5}$$

where (see Table 5.1.2) the failure rate of 40 vdc/5 dc supply is λ_4, that of the 28 vdc preregulator is λ_5, that of the clock is λ_7 and that of the scaler is λ_8.

The reliability, R_{EA}, of all of the triad electronics is given by:

$$R_{EA} = R_{AE}^3 \quad R_{NAE} \tag{5.6}$$

The reliability, R_T, of the complete triad is given by:

$$R_T = R_G^3 \quad R_A^3 \quad R_{EA} \tag{5.7}$$

5.2.2 SIRU Reliability Calculations

This section comprises the derivation of equations used in obtaining the specific SIRU reliability curves shown on Figs. 5.2.1 through 5.2.4. The derivation for soft and hard failure systems is presented later in this chapter.

The SIRU reliability calculations are complicated by the particular relationship of the axis-dedicated electronics to the gyros and accelerometers. For each functional axis three dedicated elements, a dc supply, a 9600 Hz supply and a fuse and diode module, support both the corresponding gyro and accelerometer modules. Since these electronic elements are not cross strapped, a failure in any of them results in the loss of both a gyro and an accelerometer. The reliability of the inertial package with no axis electronics failure is derived as shown in Eqs. 5.8 through 5.10. The reliability of the axis-dedicated electronics is shown by Eq. 5.3. The reliability of the complete inertial package including the axis-dedicated electronics for soft failures is as shown in Eq. 5.11.

This expression is conservative for it ignores several cases in which the system is unaffected by failures which Eq. 5.11 includes. For instance, if a gyro failure occurs followed by the failure of its axis electronics, the electronics failure, in effect, is partially forgiven. Another example is shown by a gyro failure followed by an axis electronics failure on another axis. While the limit of gyro failures has been reached, one more accelerometer failure can still be tolerated. Equation 5.11, to avoid computational complexity, does not include these small but definitely positive terms.

Soft Failure Systems

The reliability R_{6GS} of the six gyros modules in soft failure systems with no axis electronics failure is given by:

$$R_{6GS} = R_G^4 \; (15 - 24\,R_G + 10\,R_G^2) \qquad (5.8)$$

where R_G is given by Eq. 5.1. The reliability of the gyro package is given by the probability of four of the six gyros surviving.

The reliability, R_{6AS}, of the six accelerometer modules for soft failure systems with no axis electronics failure is given by:

$$R_{6AS} = R_A^4 \; (15 - 24R_A + 10R_A^2) \qquad (5.9)$$

where R_A is given by Eq. 5.2.

The reliability, R_{IS}, of the total inertial package (six gyro and six accelerometer modules) with no axis electronics failure is given by:

$$R_{IS} = R_{6GS} \; R_{6AS} \qquad (5.10)$$

The reliability R_{ISAE}, of the total inertial package including the axis-dedicated electronics (see Table 5.1.3) is given by:

$$\begin{aligned} R_{ISAE} = {} & R_{AE}^6 \; R_{6GS} \; R_{6AS} \\ & + 6R_{AE}^5 \; (1-R_{AE})(R_G^5 + 5R_G^4 \; (1-R_G))\,(R_A^5 + 5R_A^4 \; (1-R_A)) \\ & + 15\, R_{AE}^4 \; (1-R_{AE})^2 \; R_G^4 \; R_A^4 \end{aligned} \qquad (5.11)$$

where R_{AE} is given by Eq. 5.3.

The reliability, R_{DE}, of the dual redundant electronics is given by:

$$R_{DE} = R_4 \; R_5 \; R_6 \; R_8 \qquad (5.12)$$

where reliability of the 40/5 vdc supply is

$$R_4 = \left[1-(1-e^{-\lambda_4 t})^2\right] \qquad (5.13)$$

Reliability of the 28 vdc preregulator is

$$R_5 = \left[1-(1-e^{-\lambda_5 t})^2\right] \qquad (5.14)$$

Reliability of the multiplexer is

$$R_6 = \left[1-(1-e^{-\lambda_6 t})^2\right] \qquad (5.15)$$

and reliability of the scaler is

$$R_8 = \left[1-(1-e^{-\lambda_8 t})^2\right] \qquad (5.16)$$

λ_4, λ_5 and λ_8 are defined above, and λ_6 is the multiplexer failure rate.

The reliability of the clock for this system R_{CS}, is given by the probability of two of the three oscillators surviving:

$$R_{CS} = R_7^3 + 3R_7^2\,(1-R_7) \qquad (5.17)$$

where λ_7 is the clock failure rate and

$$R_7 = e^{-\lambda_7 t} \qquad (5.18)$$

The reliability, R_{EAS}, of the entire SIRU electronics assembly is given by:

$$R_{EAS} = R_{DE} R_{CS} \tag{5.19}$$

The overall SIRU system reliability, R_{TS}, for soft failure systems, is given by:

$$R_{TS} = R_{ISAE} R_{EAS} \tag{5.20}$$

where R_{ISAE} and R_{EAS} are given by Eqs. 5.11 and 5.19 respectively.

Hard Failure Systems

The discussion with respect to axis-dedicated electronics failures for soft failure systems presented above applies in a similar fashion to hard failure systems and the resulting derivation is presented below. Derivation of the reliability of gyro and accelerometer arrays, and of the axis electronics, is also similar. One additional failure, however, can be tolerated.

The reliability, R_{6GH}, of the six gyro modules in hard failure systems with no axis electronics failure is given by:

$$R_{6GH} = R_G^3 \ (20 - 45 R_G + 36 R_G^2 - 10 R_G^3) \tag{5.21}$$

where R_G is given by Eq. 5.1.

The reliability, R_{6AH}, of the six accelerometer modules with no axis electronics failure is given by:

$$R_{6AH} = R_A^3 \ (20 - 45 R_A + 36 R_A^2 - 10 R_A^3 \tag{5.22}$$

where R_A is given by Eq. 5.2

The reliability, R_{IH}, of the inertial package (six gyro and six accelerometer modules) in hard failure systems with no axis electronics failure is given by:

$$R_{IH} = R_{6GH} R_{6AH} \tag{5.23}$$

The reliability, R_{IHAE} of the total inertial package including the axis-dedicated electronics (Table 5.1.3) is given by:

$$\begin{aligned} R_{IHAE} = {} & R_{AE}^{6} \; R_{6GH} \; R_{6AH} + 6 R_{AE}^{5} \; (1-R_{AE}) (R_G^5 + 5 R_G^4 \; (1-R_G)) \\ & (R_A^5 + 5 R_A^4 \; (1-R_A)) \\ & + 15 R_{AE}^4 \; (1-R_{AE})^2 \; (R_G^4 + 4 R_G^3 \; (1-R_G)) \\ & (R_A^4 + 4 R_A^3 \; (1-R_A)) \\ & + 20 R_{AE}^3 \; (1-R_{AE}^3) \; R_G^3 \; R_A^3 \end{aligned} \tag{5.24}$$

where R_{AE} is given by Eq. 5.3.

The reliability of the dual electronics for this system is the same as for the soft failure case (Eq. 5.12).

The reliability, R_{CH}, of the clock for the hard failure case (failure of two oscillators may be tolerated) is given by:

$$R_{CH} = R_7^3 + 3 R_7^3 \; (1-R_7) + 3 R_7 \; (1-R_7)^2 \tag{5.25}$$

where R, is defined by Eq. 5.18.

The reliability, R_{EAH}, of the entire SIRU electronics assembly is given by:

$$R_{EAH} = R_{DE} \; R_{CH} \tag{5.26}$$

The overall SIRU system reliability, R_{TH}, in a hard failure system is given by:

$$R_{TH} = R_{IHAE} \; R_{EAH} \tag{5.27}$$

where R_{IH} and R_{EAH} are given by eqs. 5.23 and 5.26 respectively.

5.2.3 Theoretical Results

These equations have been evaluated and plotted using both 90% confidence level and experienced MTBF values. Results are plotted in Figs. 5.2.1 through 5.2.4. The conclusion which must be drawn from this study is that the SIRU configuration is notably more reliable than a gimbaled triad system built with similar components.

5.3 Reliability Analysis Summary

The equations presented above and graphs (Figs. 5.2.1 through 5.2.4) have been used to derive the probability of mission success and equivalent MTBF for the SIRU and triad systems for a period of 730 hours (one month). See Table 5.3.1 where the equivalent MTBF numbers were computed using the following equation:

$$\text{Equivalent MBTF} = \frac{-730}{\text{In } R} \tag{5.28}$$

where R is the corresponding system reliability at 730 hours as computed from Eqs. 5.7, 5.20, or 5.27.

Table 5.3.1 Reliability Analysis Summary

MISSION TIME 730 HRS.		MISSION SUCCESS		EQUIVALENT MTBF IN HRS.	
		SOFT FAILURES	HARD FAILURES	SOFT FAILURES	HARD FAILURES
SIRU SYSTEM	90% CONFIDENCE FAILURE RATES	.9779	.9981	32,767	347,619
	EXPERIENCED FAILURE RATES	.9959	.9997	178,000	2,433,333
TRIAD	90% CONFIDENCE FAILURE RATES	.5874		1370	
	EXPERIENCED FAILURE RATES	.7664		2740	

6.0 Test Facility

6.1 Introduction

This section contains a description of the facility and subsystem equipment developed to operate and evaluate the performance of the SIRU system. Section 6.2 describes the test table setup including the system optical alignment features. Section 6.3 provides descriptions of the GSE console and accessory electronic interfaces. Figure 6.1.1 shows the complete interface for SIRU and the associated support equipment. The computer facility components shown in the figure are an integral part of the overall test facility. See Chapter 4 for a discussion of the computer, its SIRU system interfaces and the associated peripherals.

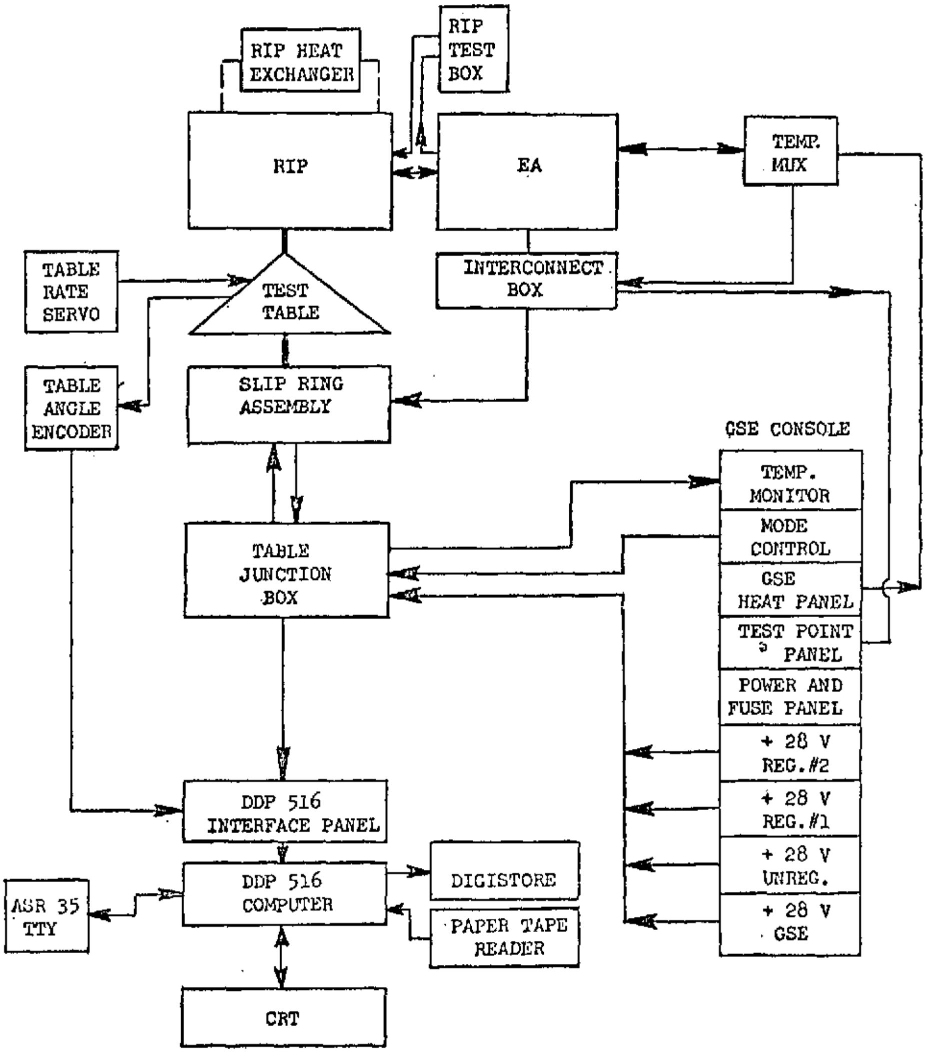

Fig. 6.1.1 SIRU System Block Diagram

6.2 Test Table

The test table provided to support the SIRU system consists of a 2-axis, 16-inch rotary table mounted on the rotating axis of a similar 2-axis 32-inch rotary table (both tables are manufactured by the International Machine and Tool Co.). Figure 6.2.1 shows the major components of the test table system. The four table axes are equipped with precision (0.5 $\widehat{\text{sec}}$ resolution, 2.0 $\widehat{\text{sec}}$ accuracy) optical readouts which allow positioning to a wide range of orientations including the six basic instrument calibration positions. The rotary axis of the 32-inch table is equipped with a rate drive system which can generate constant slew rates up to 1.0 rad/sec and oscillatory rates at frequencies up to 10 Hz. See Fig. 6.2.2 for a sketch of the slip ring and encoder assembly.

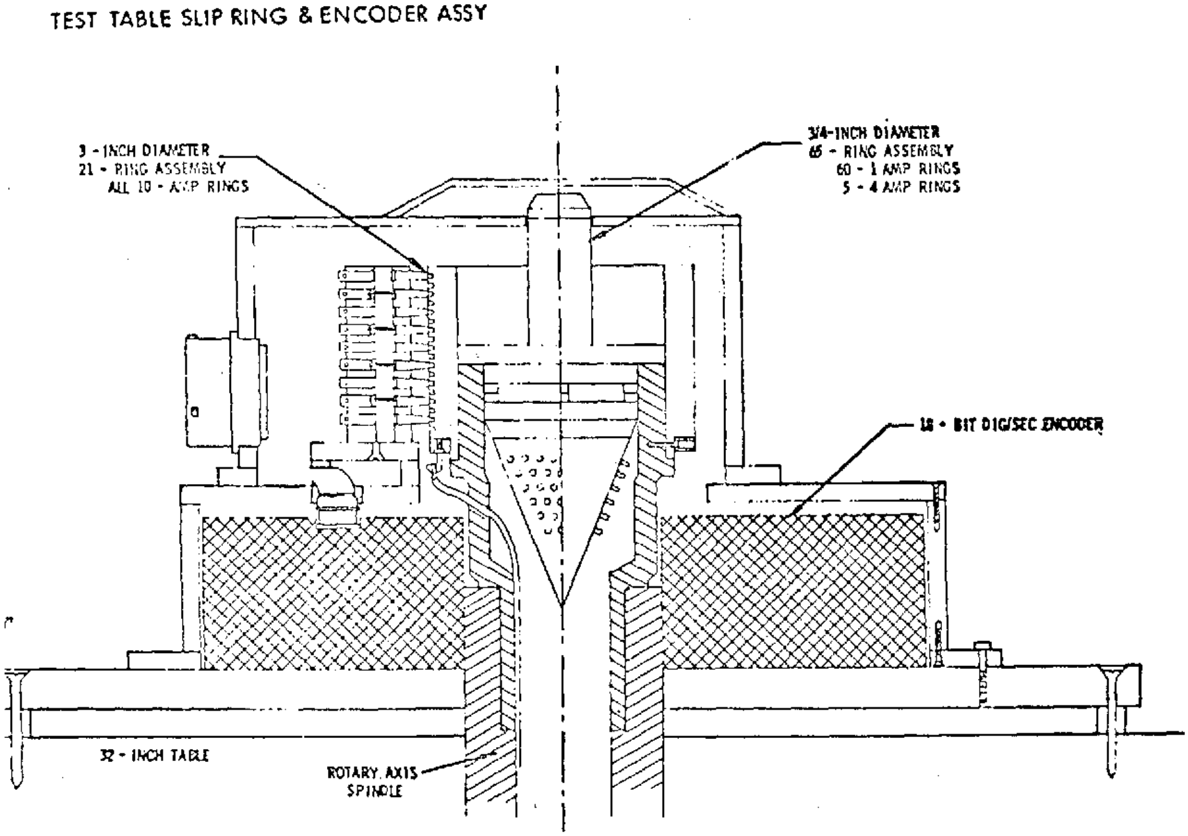

Fig. 6.2.2 Test Table Slip Ring & Encoder Assembly

The SIRU system can be aligned to within 10 $\widehat{\text{sec}}$ in azimuth and 5 $\widehat{\text{sec}}$ in elevation in all desired test positions. These alignments are accomplished by orienting the SIRU system (by autocollimation on the system reference cube) with respect to transfer lines from the azimuth reference (porro prism). See Fig. 6.2.3

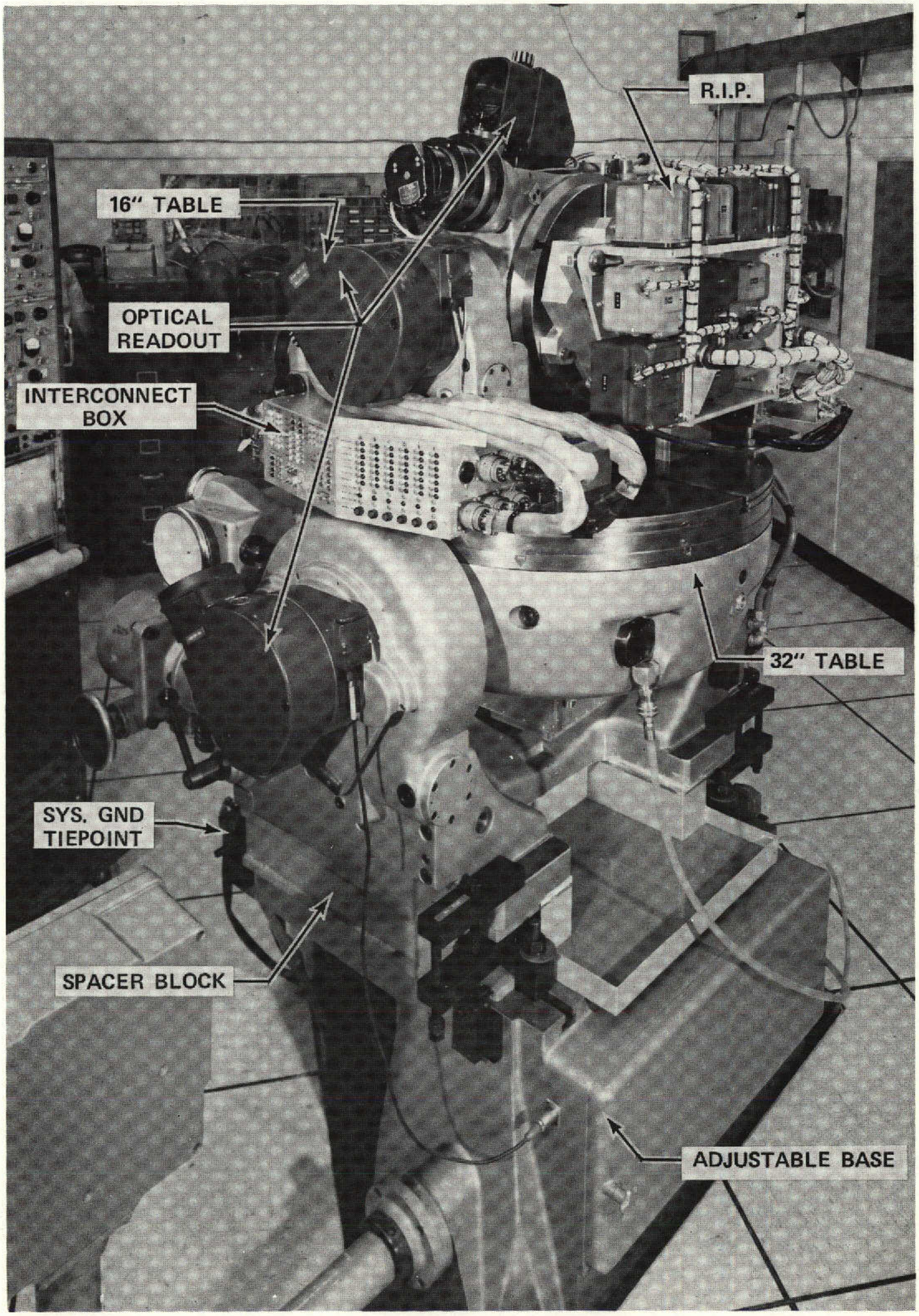

Fig. 6.2.1 Axis Test Table Assembly with SIRU System Installed

for the optical alignment layout. Figure 6.2.4 shows the SIRU system installed on the test table.

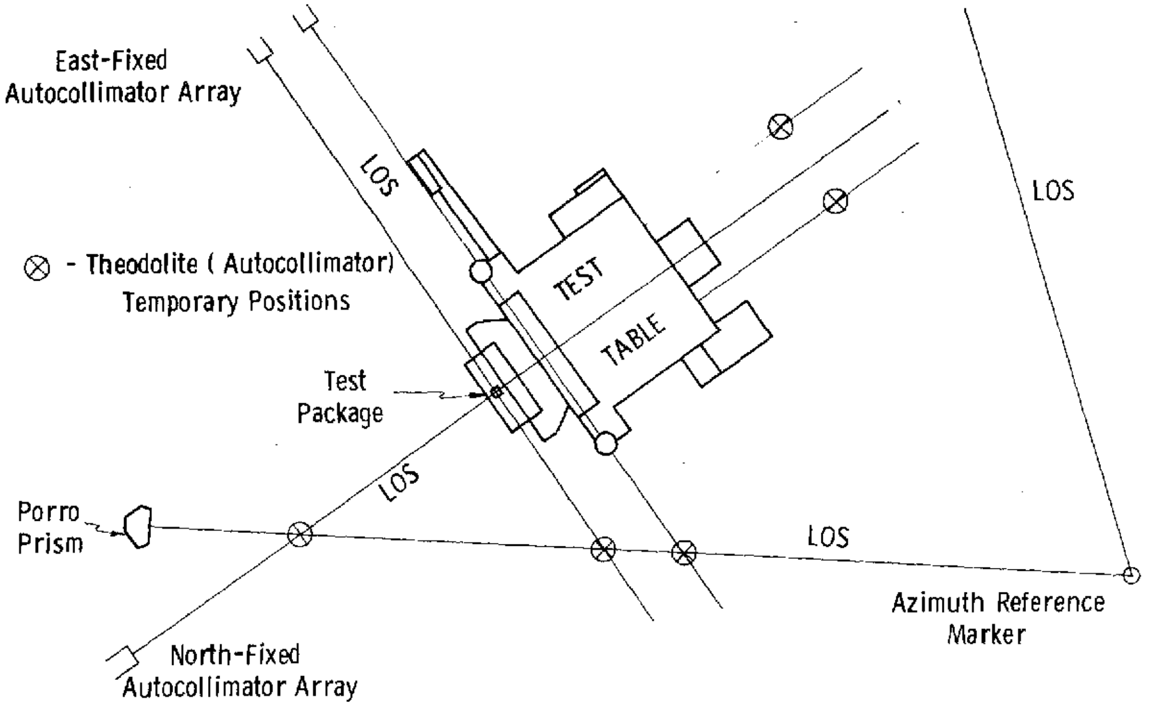

Fig. 6.2.3 Test Facility - Optical Alignment References

6.3 Support Equipment

Ground Support Equipment (GSE) for the SIRU laboratory installation consists of the following items of equipment:

I. GSE Console
II. Interconnect Box (ICB)
III. Table Junction Box (TJB)
IV. RIP Test Box
V. Monitor Console

A description of each item, their subassemblies and their application to the operation and test of the SIRU follows.

6.3.1 The GSE Console

The GSE console, Fig. 6.3.1, provides the necessary dc power sources and distribution for the SIRU system. It controls the moding of the system, provides

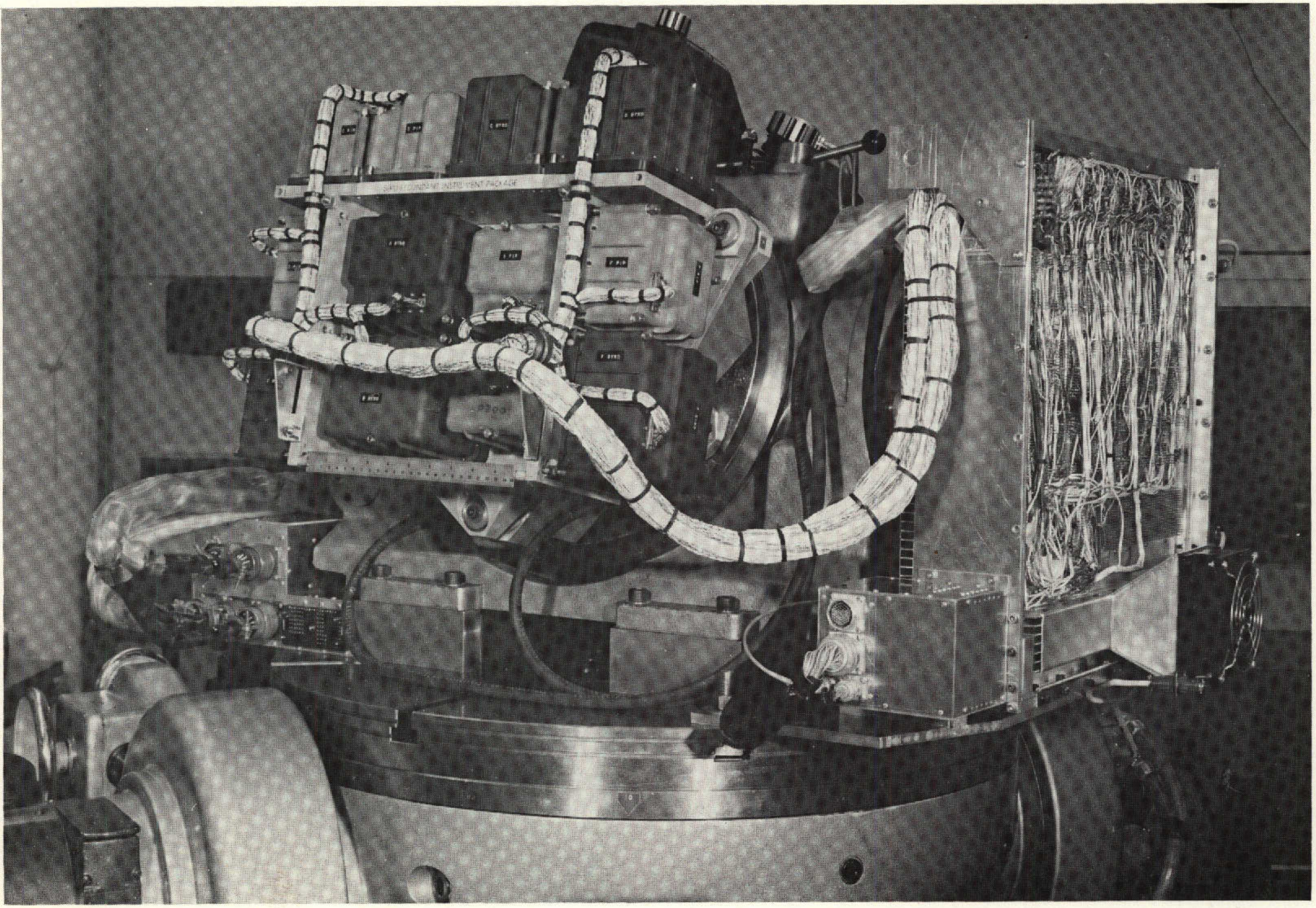

Fig. 6.2.4 SIRU System Installed on Test Table

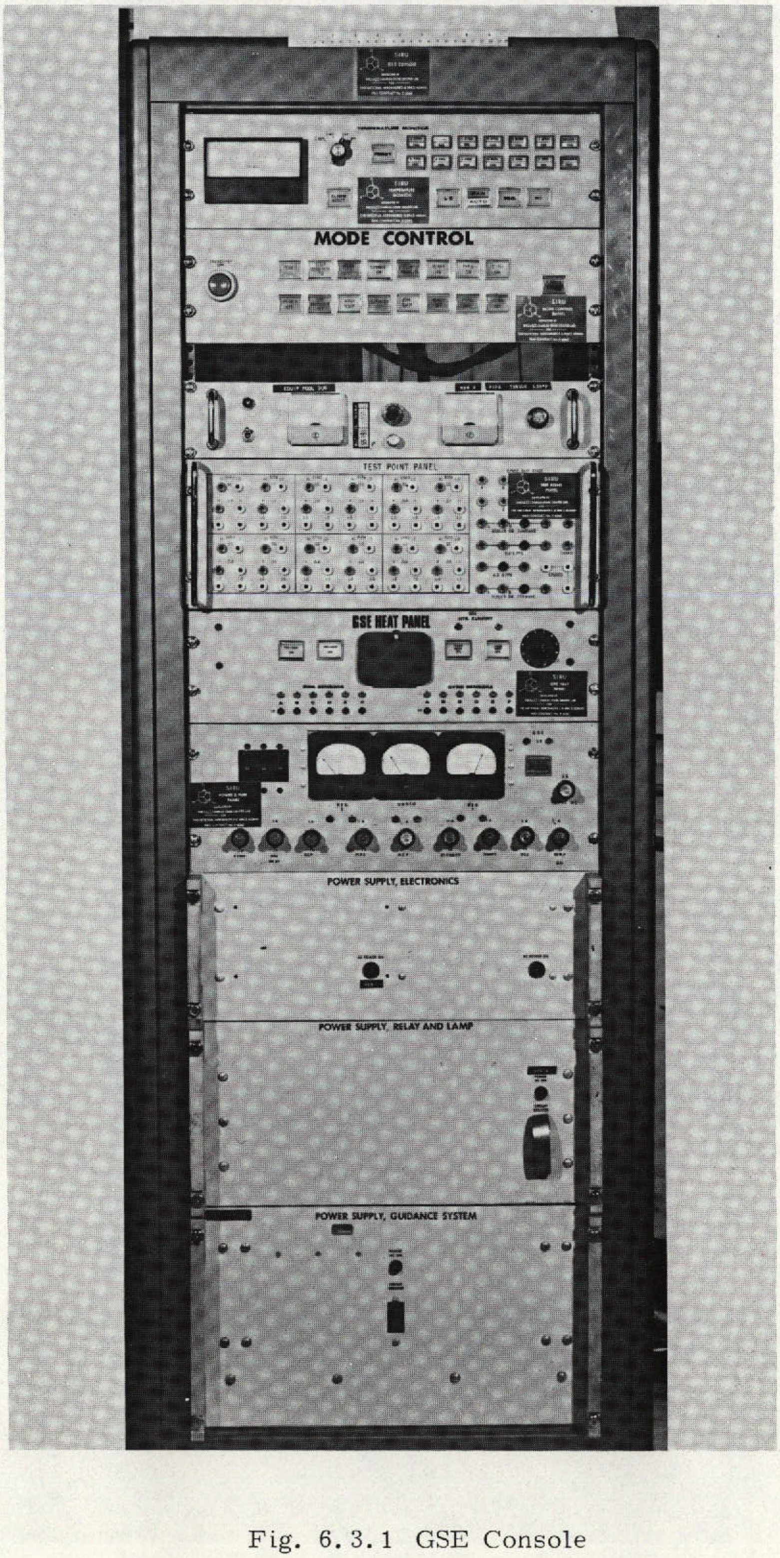

Fig. 6.3.1 GSE Console

auxiliary heat for inertial components, and monitors component temperatures. It also provides access to system test points and ac and dc power for GSE operation.

The console consists of six interlocking sections:

A. Temperature Monitor
B. Mode Control Panel
C. GSE Heat Control Panel
D. Power Distribution Panel
E. Power Supplies
F. Test Point Panel

Temperature Monitor

All inertial module temperatures are sensed in bridges and the amplified signal from each bridge is multiplexed to the monitor panel via the slip rings on the table once every 30 seconds. Signals are cycled through and displayed as a deviation from normal operating temperature. The inertial component being monitored is identified on the panel. Automatic scanning can be interrupted and manual sequencing invoked. Aural and visual alarms are activated if the temperature of any inertial component exceeds its specific limits, the faulty instrument is identified and the entire inertial system is automatically switched to a safe operating mode.

Mode Control Panel

The Mode Control Panel provides all the power switching devices required to control the various operational modes of the SIRU system. The Turn-On/Turn-Off sequence is interlocked and all critical points in the system and the GSE are channeled into the Mode Control Panel to insure safe system operation.

GSE Heat Control Panel

As described below, certain modes of operation require that extra heat be delivered to the inertial components. The GSE Heat Control Panel provides this extra heat individually to each component. This heat is adjustable and is available in two modes: preheat and fixed heat. Preheat is used when extra power is needed to bring the component up to operating temperature before turn on. Fixed heat was provided as an additional power source to assist the component temperature controllers when several modules have been removed to minimize the effect of a π-frame temperature gradient.

Power Distribution Panel

All the heavy current switching is done in the Power Distribution Panel under the command of the Mode Control Panel. Safety fusing and over-voltage crowbar circuitry are also located here. All power and grounds are distributed from this point to the GSE and SIRU system.

Power Supplies

The GSE console contains the following power supplies. The associated usages are identified.

1. +28 vdc - GSE relays and lamps
2. +28 vdc - SIRU temperature, control, clock, and scaler, 40/5 supply, 9600 Hz supply
3. +28 vdc - SIRU dc axis supplies
4. +28 vdc - SIRU accelerometer pulse torque electronics

Test Point Panel

The Test Point Panel provides necessary buffering for all available system test points used for troubleshooting and system monitoring. (This panel was used in Phase I only.)

6.3.2 Interconnect Box (ICB)

The ICB is mounted with the SIRU system on the test table and interfaces the system to the slip ring assembly. The circuitry in the ICB includes wheel current monitors with out-of-tolerance alarms, $\Delta\theta$ multiplexers, ΔV multiplexers, gyro interpolator multiplexers, pulse buffers, and mode controls for the clocks and scalers. All available system operational test points can be monitored through the buffers in the ICB.

6.3.3 Table Junction Box (TJB)

All the raw inertial data ($\Delta\theta$, ΔV, interpolator) which were multiplexed in the Interconnect Box for transmission through the slip rings are de-multiplexed in the TJB. This raw data are then buffered and sent to the computer for processing.

6.3.4 RIP Test Box

This small box is located between the Electronic Assembly (EA) and the Redundant Instrument Package (RIP) and contains dc current sensing resistors, wheel current sensing transformers, and switches to control the gyro and accelerometer pulse torque electronics.

6.3.5 Monitor Console

This single bay console contains oscilloscopes for monitoring all gyro and accelerometer error signal Lissajous patterns, a digital voltmeter for troubleshooting and test table rate servo power supplies and controls.

7.0 System Test Results

This chapter describes and presents the results of system tests performed to evaluate and confirm the operation of the SIRU system. A companion document, SIRU Utilization Report, R-747, describes in additional detail the test program and results for single position calibration (SPC), Local Level Navigation and Coarse and Fine Alignment. Thus, only selected samples of test results in these areas are included here.

The performance of the failure detection and isolation (FDI) and of the statistical FDI Classification and Recompensation (FDICR) is covered in the chapters of this report and R-747 which are devoted to those subjects, and does not appear in this chapter.

Test results from inertial components and gyro and accelerometer modules operated outside of the system environment are covered in the appropriate volume of this report; Volume II for gyros and gyro modules and Volume IV for accelerometer and accelerometer modules.

Reliability operating results and assessments are presented separately in Chapter 5 of this report and for the SIRU Utilization program in R-747.

With the exceptions described above, this chapter contains the principle results of the SIRU test and evaluation program for the entire period from July 1970 through December 1972.

7.1 System Operating Summary

This section presents the operating summary of the system over the entire test period. The SIRU gyros in the system, through December 1972, accumulated a total of 116,400 operating hours and a total of 694 system wheel stop-starts. The accelerometers accumulated a total of 147,800 operating hours with every instrument operating in the system in excess of 23,000 hours. Operating time for the system was 23,300 hours with a complete complement of instruments and the electronics assembly.

7.2 Calibration and Stability Data

This section presents results from calibration tests and shows short and long-term instrument stability and the effects of system cooldowns and module replacement. Accelerometer data, because of its security classification, have not been included in this volume but are presented in Volume IV of this report.

7.2.1 Gyro Torque-to-Balance Stability Statistics

Figures 7.2.1 and 7.2.2 summarize stabilities of bias drift (NBD), g-sensitive drifts (ADSRA, ADIA and ADOA), g^2 or compliance drift, scale factor (SF) and input axis alignments obtained across remounting, cooldowns and test repetition.

The delta drift, or change in drift magnitude, alignment and SF have been tabulated and an rms average calculated for the sample size to show the effect of module remounting (Column 1) and of system cooldowns (Column 2). The larger sample size of the cooldown data results because all installed instruments are affected by a system cooldown whereas remounting affects only individual instruments.

A comparison of the g-sensitive drift for these two cases shows nearly identical performance; that is, both the spread in delta magnitudes and the calculated rms values for each term are similar. This is to be expected, as the environmental impact on the instrument is nearly the same in each case (all power off). There is no apparent effect from the physical movement of the module during remounting. These g-sensitive drift changes across cooldown are a deficiency of the 18 IRIG Mod B gyro population used in SIRU. An improved instrument, the 18 IRIG Mod D, with a redesigned, integral wheel and gimbal (described in Volume II) has substantially reduced this sensitivity. The equivalent performance of the Mod D across cooldowns is documented to be on the order of $.015^{\circ}/hr$.

The tabulation of standard deviations (Column 3) for the various terms is derived from one to six months of calibration test results chosen to exclude all interposing cooldowns or remounts. This data is considered to be representative of the performance across cooldowns expected with the incorporation of the 18 IRIG Mod D or an equivalent instrument.

The SF and alignment stability performance, for all three cases, is very respectable, and the standard deviations are indicative of the stability of the hardware and the sensitivity or resolution of the calibration and data reduction process. As explained in subsequent sections, reductions in SF differences across mounting have been achieved through implementation of hardware modifications, and reductions in alignment differences across mounting can be achieved through the use of an optical calibration fixture.

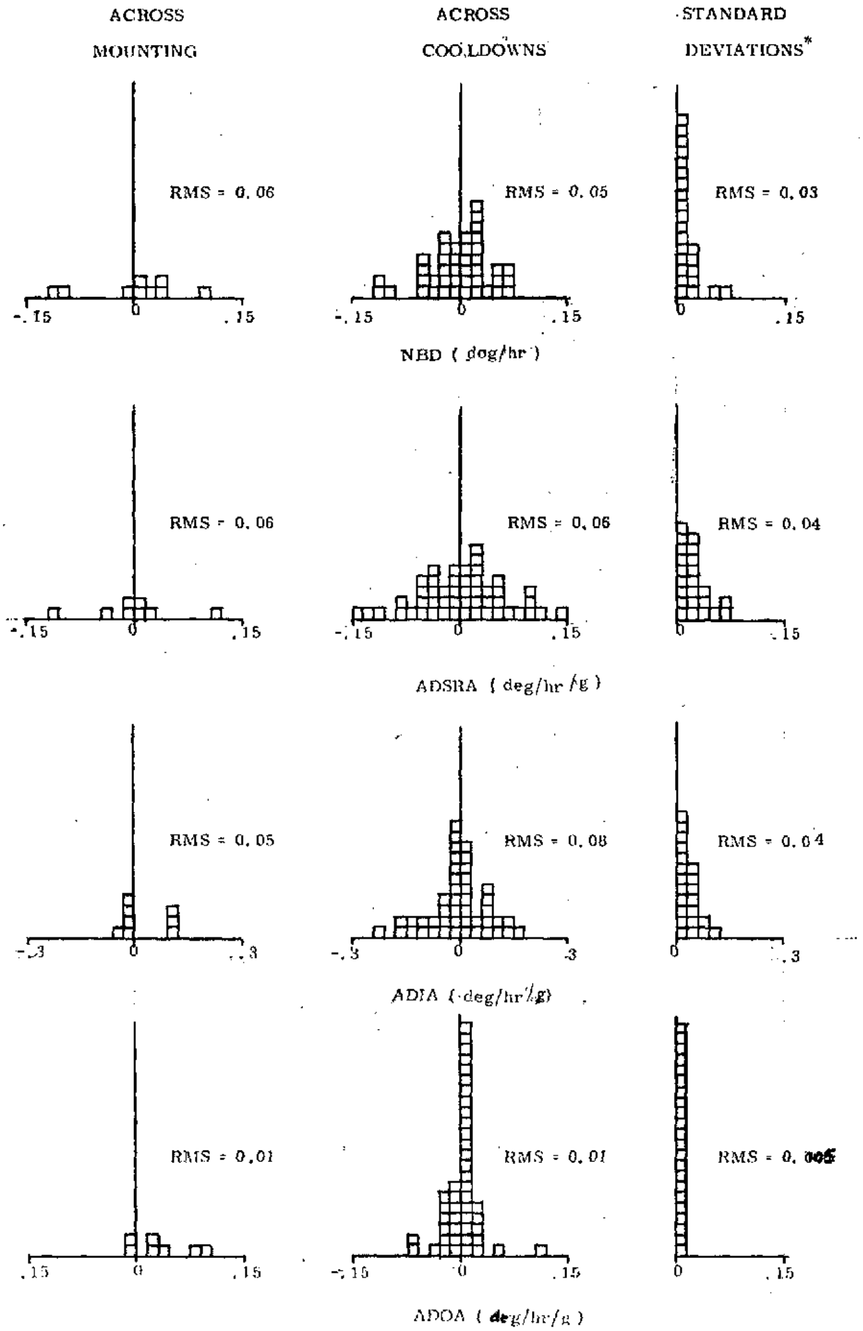

* No cooldowns or mountings 1 - 6 months.

Fig. 7. 2. 1 Gyro Drift Performance
18 IRIG Mod B

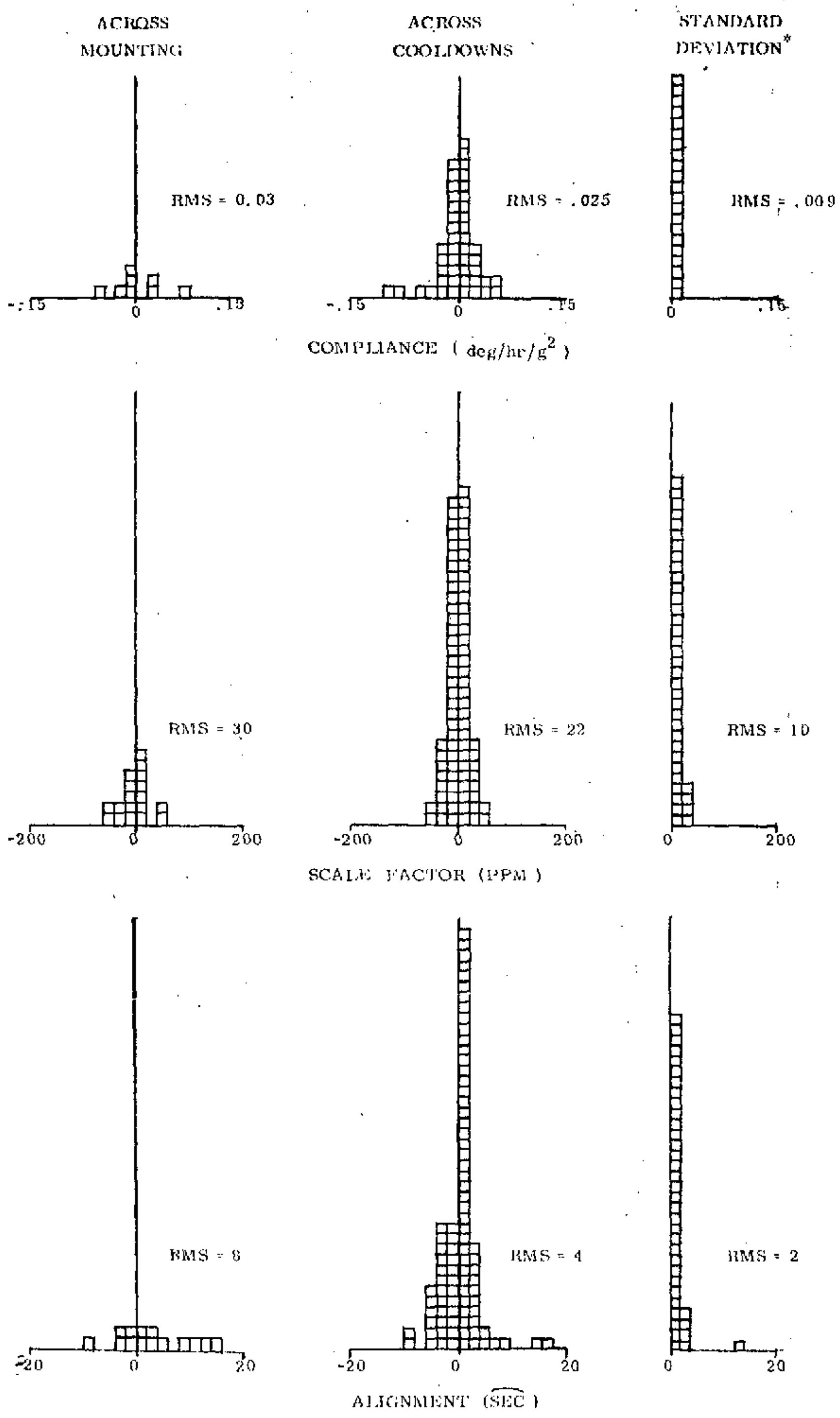

* No cooldowns or mountings 1 - 6 months.

Fig. 7.2.2 Gyro Compliance, Scale Factor, and Alignment Data 18 IRIG Mod B

Table 7.2.1 shows the average sigma of the drift stability applicable to each instrument in five of the test positions shown in Table 7.2.2. This data was derived from overnight and weekend test runs of approximately 16 hours to 60 hours duration. Statistically, the system performance is seen to be relatively unaffected by position with respect to gravity.

Table 7.2.1

Average Sigma of the SIRU System Overnight Stability Data

Axis	Gyro	Pos#1	N	Pos#2	N	Pos#3	N	Pos#4	N	Pos#6	N
A	MB-424A	6.08	7	6.06	11	1.98	3	2.97	3	3.16	6
B	MB-426A	9.39	7	8.68	10	5.67	3	1.78	4	3.06	7
C	MB-425	3.41	7	2.88	10	6.72	3	7.48	3	2.31	5
D	MB-428B	3.42	1	2.91	2	—	—	4.35	1	—	—
E	MB-421	6.00	4	4.20	9	3.48	3	2.49	1	5.31	4
F	MB-420A	3.14	6	2.43	9	2.02	3	1.71	3	3.90	7

Values in $^{\circ}/\mathrm{hr} \times 10^{-3}$

N: Number of Overnight or Weekend Test Runs

Representative data for the A, D and F axis gyros in calibration position 2 are shown in Figs. 7.2.3 through 7.2.10. Figures 7.2.3 through 7.2.5 show three drift stability calibration tests on the A gyro in calibration position 2 taken in May, September and November, 1972. The module is oriented with its output axis (OA) horizontal, sensing almost full negative earth rate and exhibiting gyro bias drift and both ADIA and ADSRA magnitudes and stabilities. The standard deviations of the drift stability data for the three samples are .0040, .0045 and .0041°/hr respectively. Figures 7.2.6 through 7.2.8 show the results of the same sequence of tests on the D gyro. In the calibration position 2, the D gyro module is oriented with its OA horizontal, sensing almost 9°/hr earth rate and exhibiting gyro bias drift and both ADIA and ADSRA magnitudes and stability. The standard deviations of the drift stability data for these three samples are .0027, .0020 and .0020°/hr respectively. Figures 7.2.9 and 7.2.10 show the F-gyro with a one sigma stability of less than 0.0015°/hr. In the calibration position 2, the F-gyro module OA is vertical and oriented so that it senses approximately 4°/hr of earth rate and exhibits essentially its bias drift magnitude and stability. When the F-gyro is placed in

RA1 = ROT. Axis 32" Table
RA2 = ROT. Axis 16" Table
TA1 = TRUN. Axis 32" Table
TA2 = TRUN. Axis 16" Table

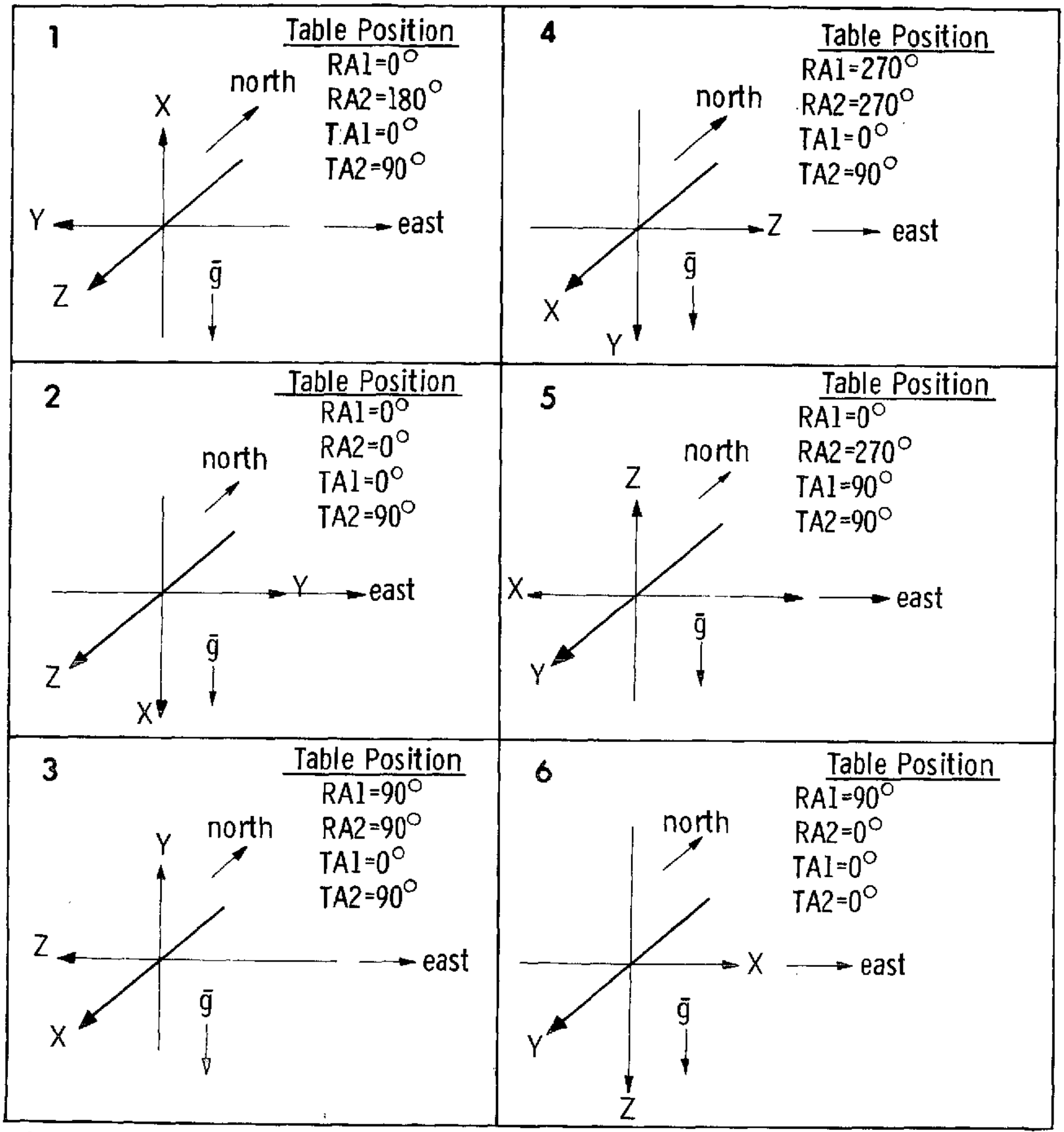

Note : Positions 2, 4 & 6 are the Basic Positions for Rate Testing

Table 7.2.2 Gyro and Accelerometer Static Calibrate Positions

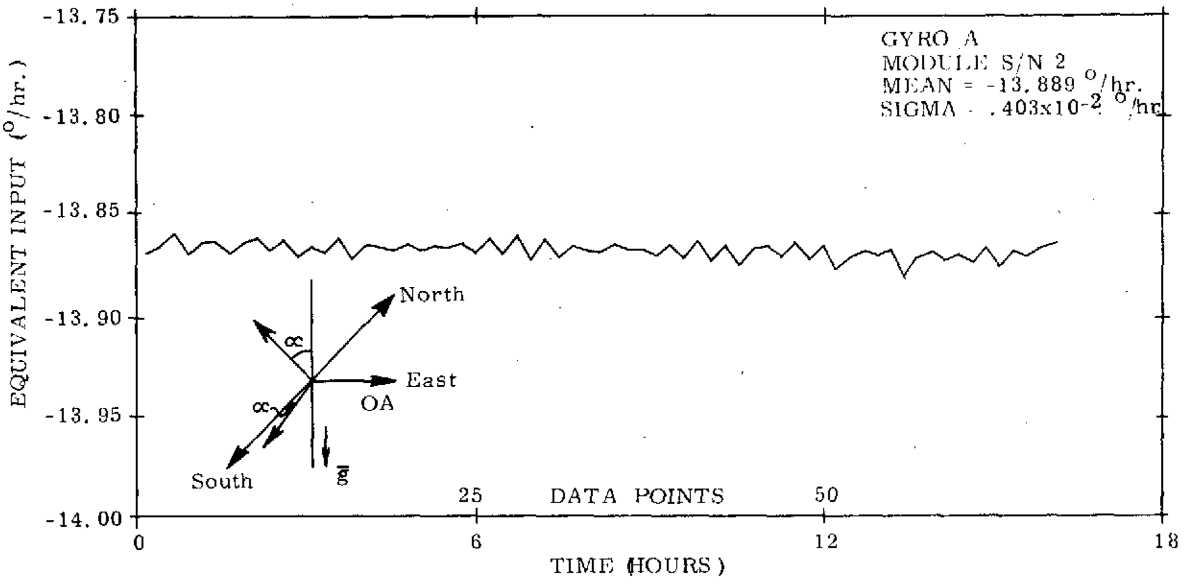

Fig. 7.2.3 A-Axis Gyro Drift Stability, May 3, 1972, Cal Pos 2

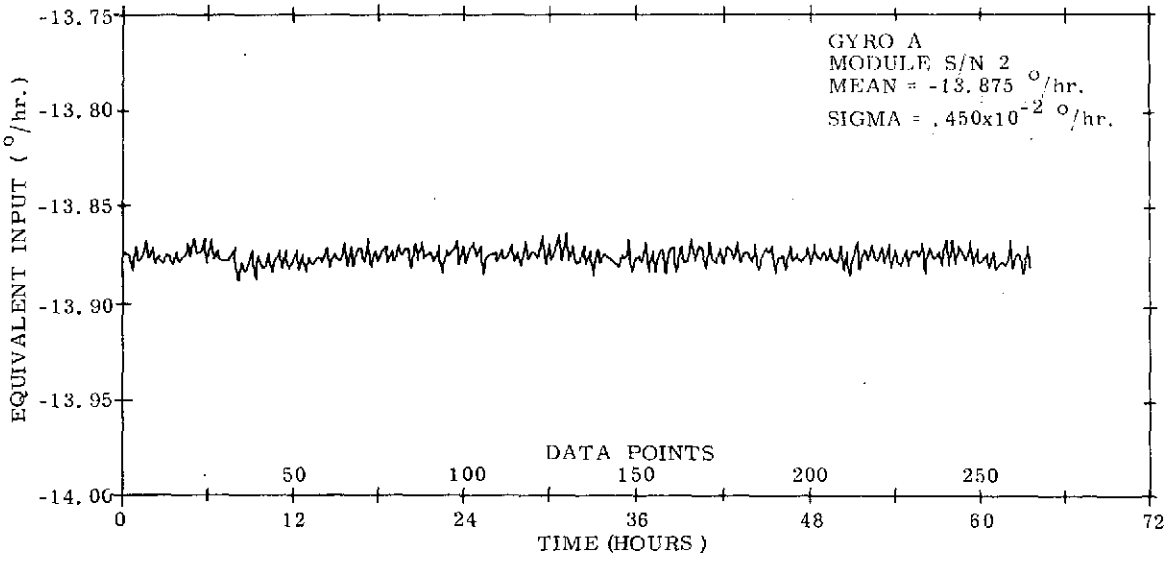

Fig. 7.2.4 A-Axis Gyro Drift Stability, September 18, 1972, Cal Pos 2

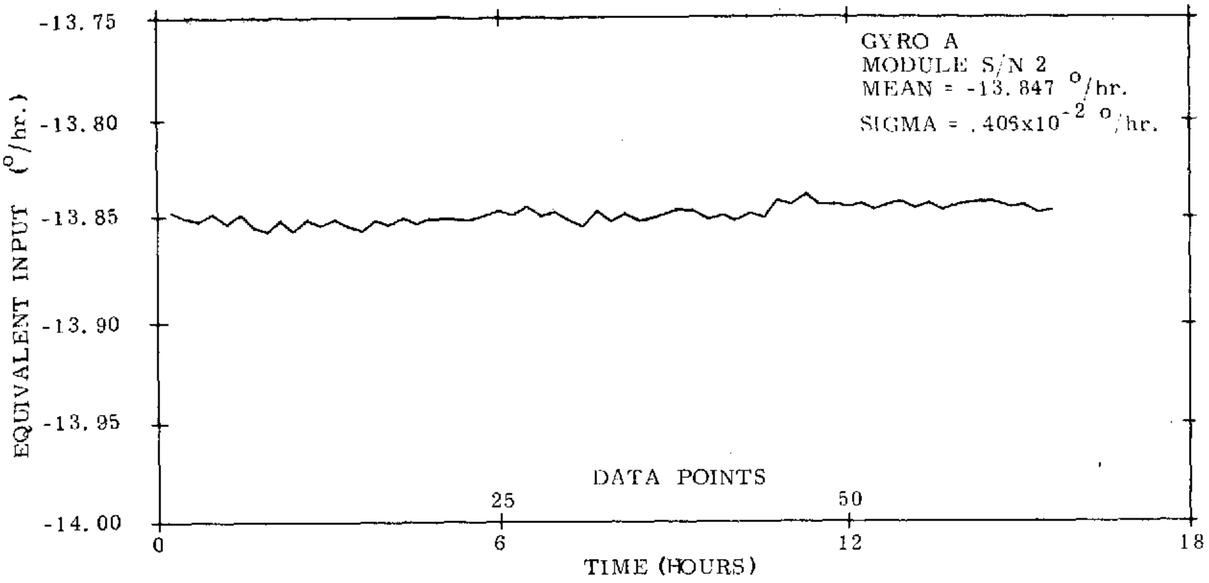

Fig. 7.2.5 A-Axis Gyro Drift Stability, November 9, 1972, Cal Pos 2

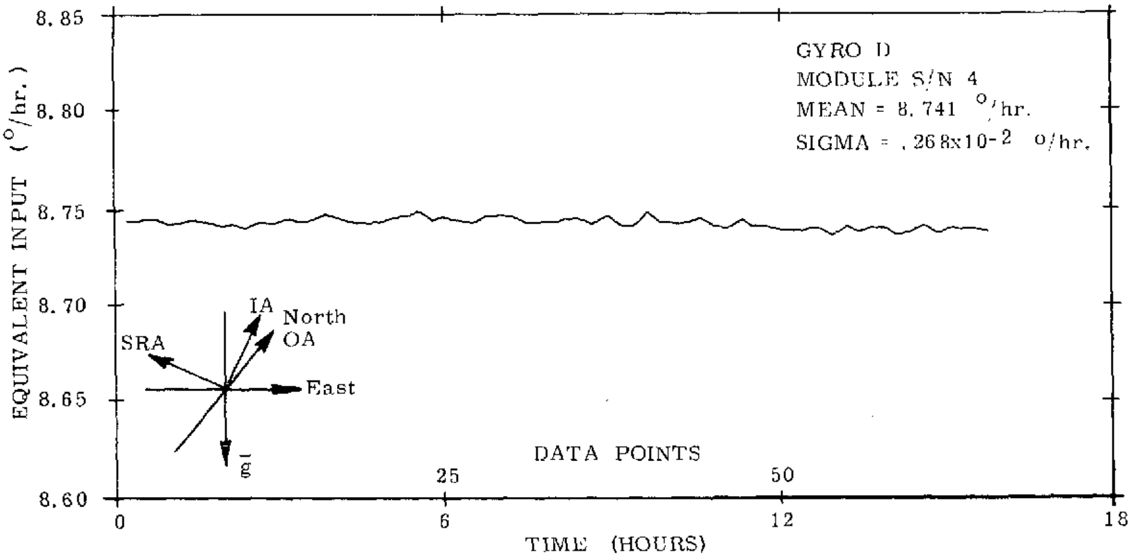

Fig. 7.2.6 D-Axis Gyro Drift Stability, May 9, 1972, Cal Pos 2

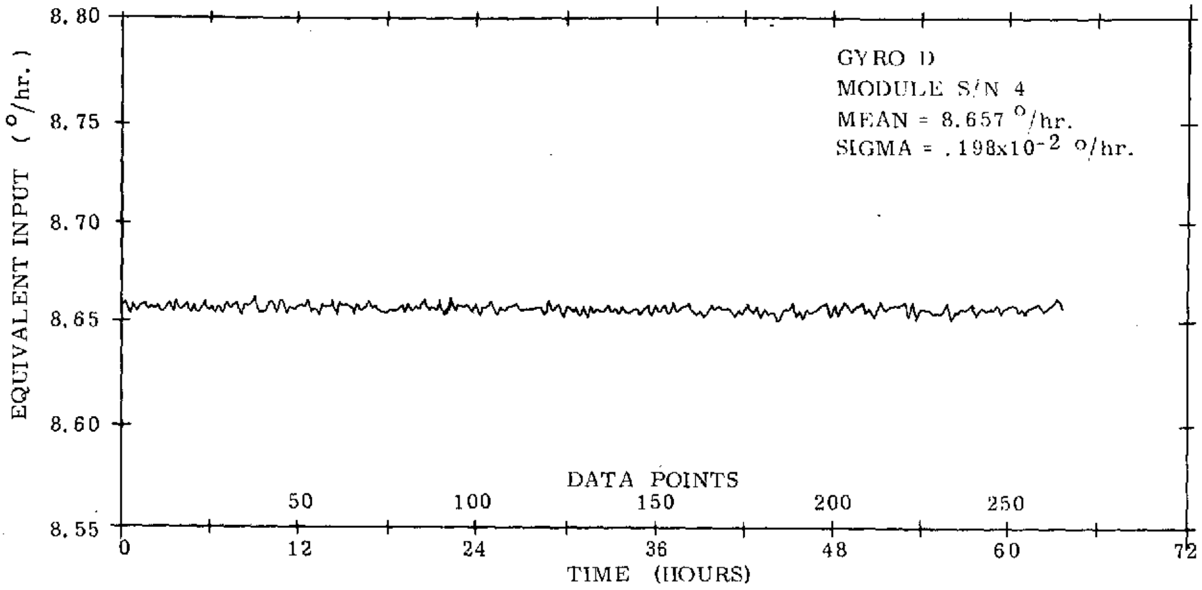

Fig. 7.2.7 D-Axis Gyro Drift Stability, September 18, 1972, Cal Pos 2

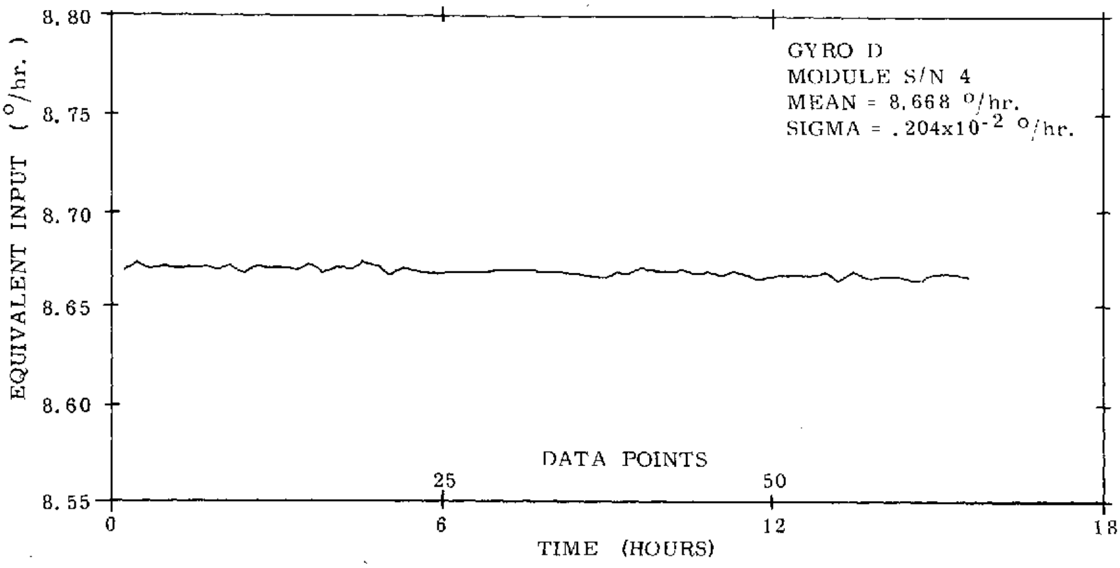

Fig. 7.2.8 D-Axis Gyro Drift Stability, November 9, 1972, Cal Pos 2

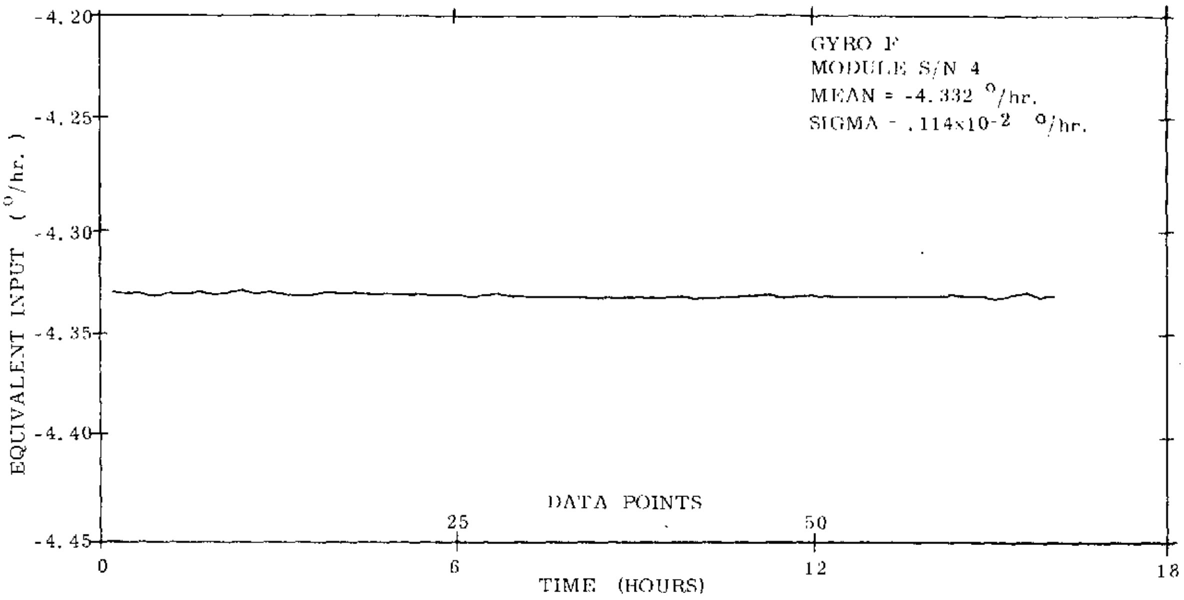

Fig. 7.2.9 F-Axis Gyro Drift Stability, July 28, 1971, Cal Pos 2

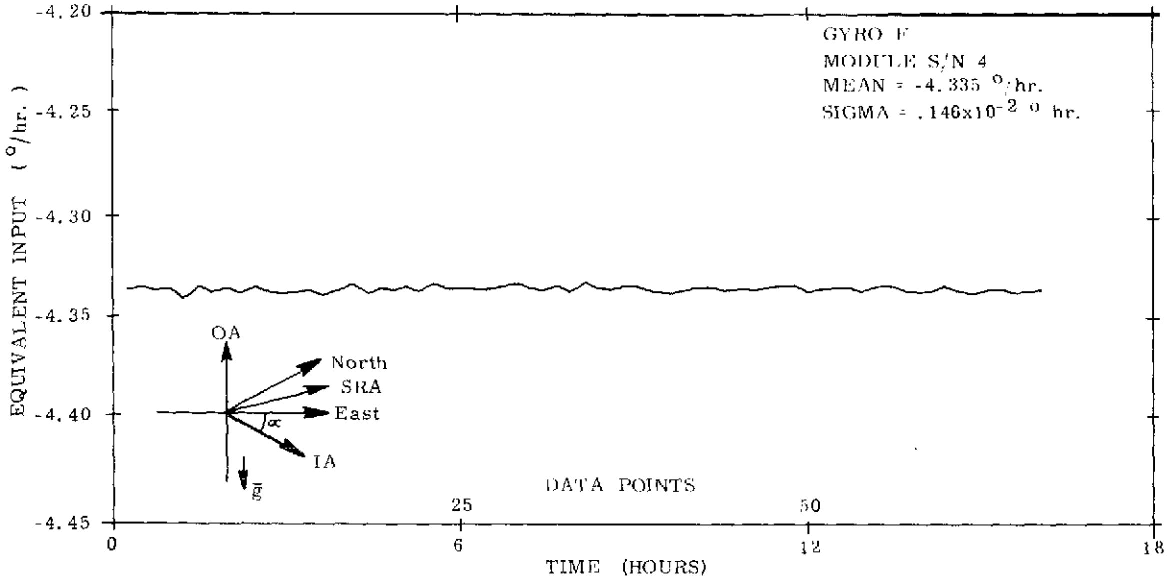

Fig. 7.2.10 F-Axis Gyro Drift Stability, June 1, 1972, Cal Pos 2

calibration position 6 (Fig. 7.2.11), the one sigma stability degrades to 0.0048°/hr. In calibration position 6, the F-gyro module is oriented with its OA horizontal sensing about 5.5°/hr of earth rate and exhibiting bias and both ADIA and ADSRA drift magnitudes and stabilities. Comparison of the F-gyro data in the two calibration positions illustrates the effect of the major g-sensitive drift terms on the short term performance of the instruments.

A transient type instrument failure that was observed in system testing is illustrated in Fig. 7.2.12. The data was taken on the E-gyro which had been randomly identified as a failure by the SIRU FDI software. This plot confirmed the transient failure phenomena. The unit remained in the system for continued monitoring, and additional random, real "soft" failure events were observed by the FDI software. The plot indicates that the instrument float was restrained at the initiation of the test and experienced an exponential return to the nominal drift level (for that orientation) over the first six to eight hours of the performance test. The one sigma drift value of 0.048°/hr and the visible roughness of the point-to-point performance during the remaining fifty hours of the test are indicators of a probable contaminant in the flotation fluid of this instrument. Subsequent teardown of this unit verified the presence of a contaminant.

7.2.2 Day-to-Day Gyro Drift Stability

The error in earth rate sensed by each of the system gyros in calibration position 2, on a day-to-day basis, is shown in Figs. 7.2.13 and 7.2.14. The instrument compensation routine (RPOTT) was utilized in these tests so that all the indicated rates are free of drifts caused by the nominal calibrated gyro drift, etc. parameters. There were no system cooldowns between the compensation updates.

For the entire population over the three month period, we observe from these curves that the maximum data spread was better than 0.09°/hr including the sudden shift in F-gyro performance and the ramping in the D-gyro. On the average, the day-to-day performance is better than 0.015°/hr. It should be noted that gyro axes A through D in this calibration orientation reflect g-sensitive as well as bias drift stabilities since their input axes (IAs) and spin axes (SAs) have sizable components along the g vector.

Both the E and F-gyros, whose OAs are vertical, indicate superior repeatable day-to-day drift performance, a maximum spread of 0.007°/hr (except for the F-gyro calibration shift); this data correlates closely with the overnight stability data (Figs. 7.2.9 and 7.2.10). If the stable drift shift of 0.09°/hr for the F-gyro occurred during

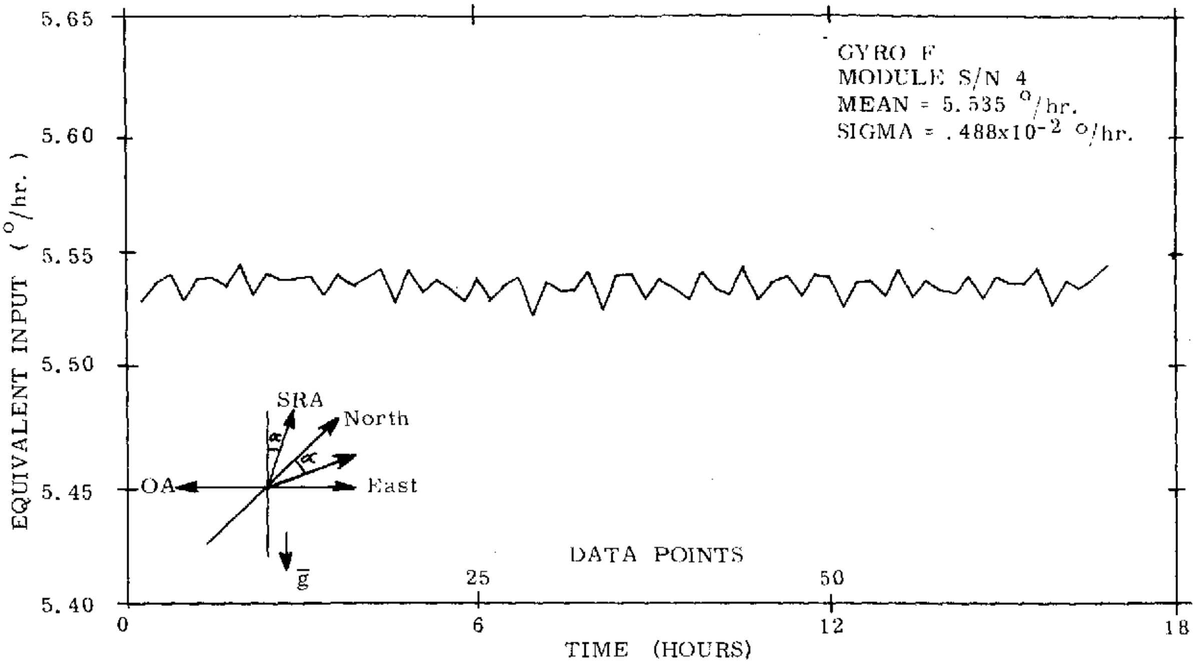

Fig. 7.2.11 F-Axis Gyro Drift Stability, September 19, 1972, Cal Pos 6

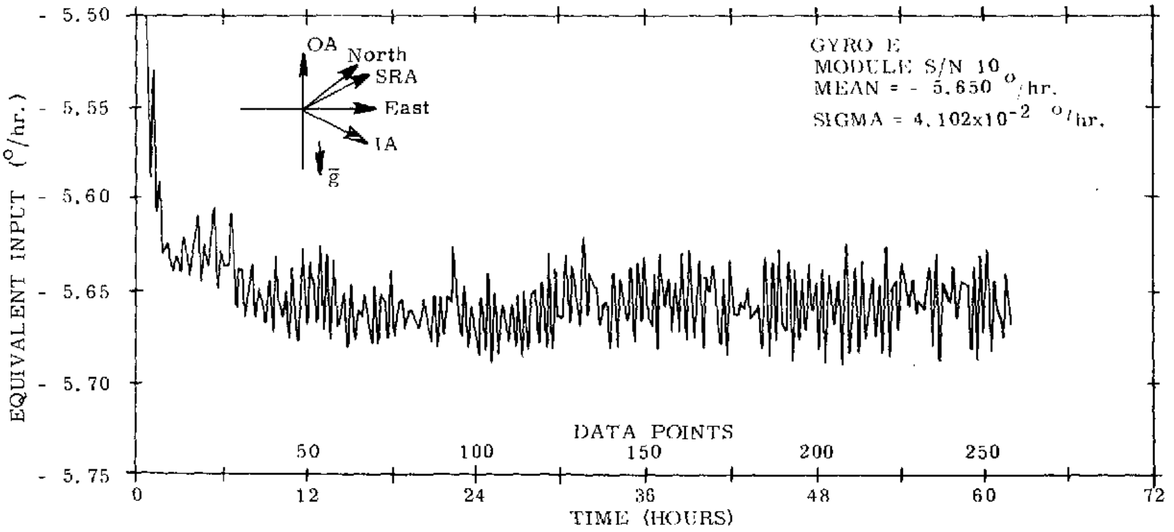

Fig. 7.2.12 E-Axis Gyro Drift Stability, March 15, 1971, Cal Pos 2

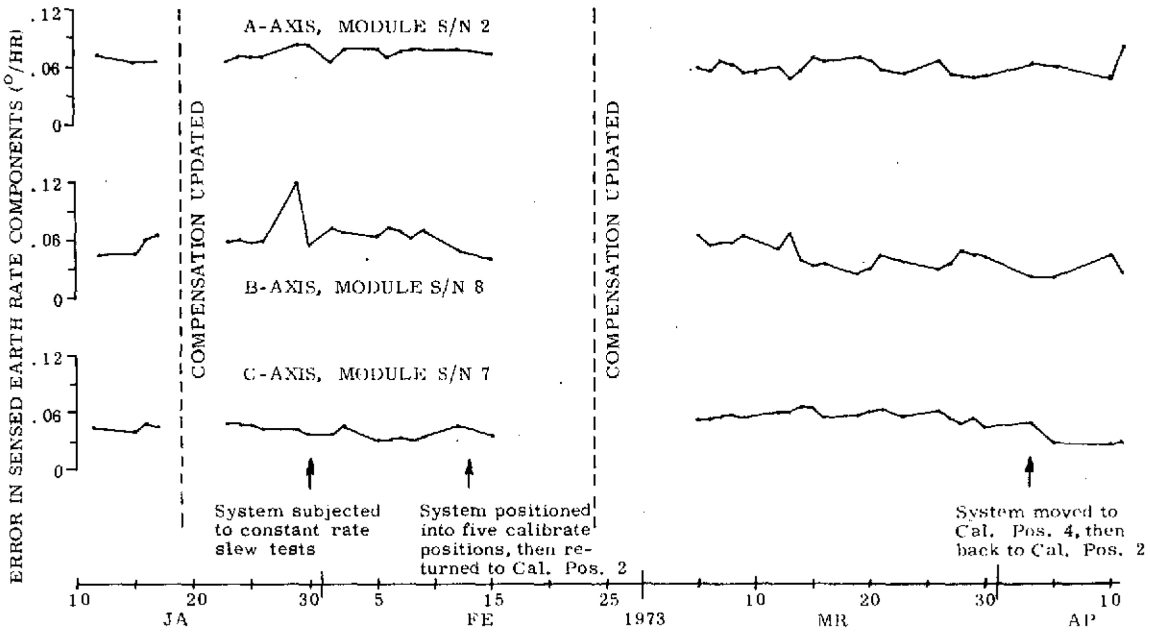

Fig. 7.2.13 Earth Rate Components Sensed by System Gyros in Cal Pos 2: Day-to-Day Stability for Compensated Gyros (Drift Terms, Scale Factor Errors and Misalignment Angles)

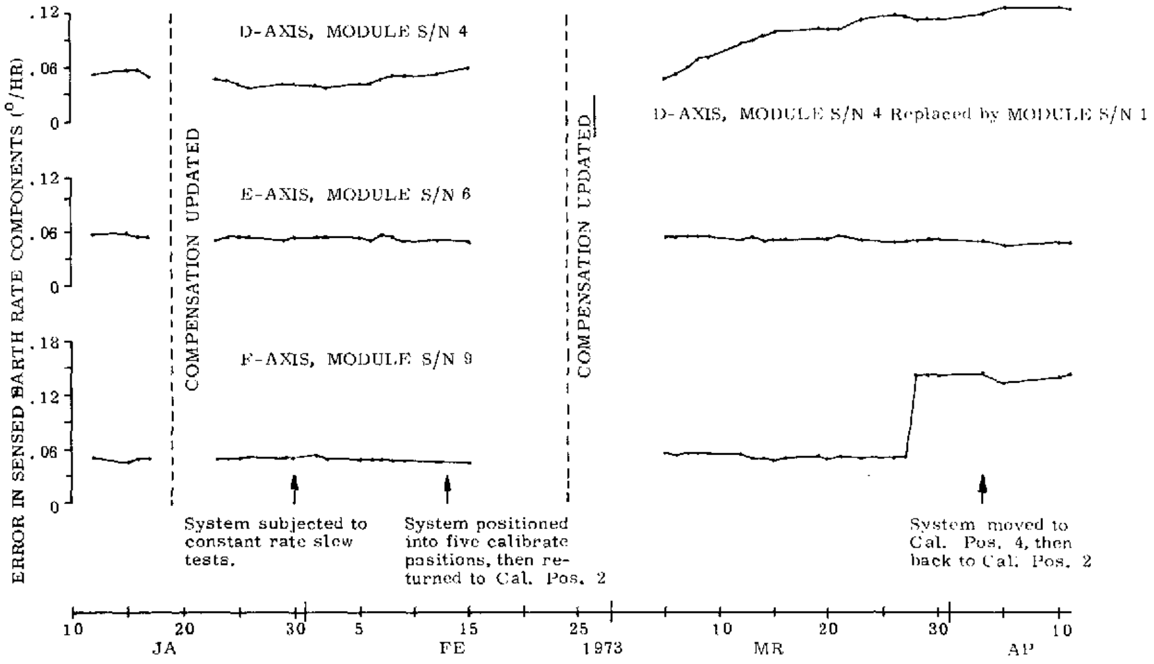

Fig. 7.2.14 Earth Rate Components Sensed by System Gyros in Cal Pos 2: Day-to-Day Stability for Compensated Gyros (Drift Terms, Scale Factor Errors and Misalignment Angles)

an operational period, the statistical failure detection routine would have detected, isolated, classified and recompensated this instrument. Recompensation to better than .007°/hr has been demonstrated in laboratory testing. This characteristically better performance in the OA vertical orientation provides the performance base for the self-calibration features of the SPC procedure that has been implemented under the SIRU Utilization program, R-747.

7.2.3 End-to-End Gyro Drift Summation Repeatability After "Dumping" System in the Gravitational Field

Table 7.2.3 shows the baseline net drift (all compensation terms applied and the a priori earth rate drift subtracted) sensed by the system gyros in calibration position 2. The system is then rotated about the Z-axis (horizontal) such that the X-axis is now vertical up (calibration position 1). The calibration position 1 data shows a maximum drift error of -0.0228°/hr in the E-gyro while the majority of units indicate better than 0.015°/hr. This stability across up-to-down rotation in the g field is indicative of a well calibrated system.

Table 7.2.3

SIRU Gyro Drift Rate Errors (With Drift Parameter Compensation Applied)—For the Cal Pos 2
System "Dumped" to Cal Pos 1 and then back to Cal Pos 2

System Orientation			System Axis			
	A	B	C	D	E	F
			°/hr			
Calibration Position 2 (Baseline)	-.0060	-.0111	-.0026	.0039	.0030	-.0015
Calibration Position 1 Positioned System 180° About Z-Axis	-.0032	-.0063	.0202	-.0054	-.0228	.0116
Calibration Position 2	-.0093	-.0034	-.0062	.0092	-.0062	-.0015
Calibration Position 2 Error With Respect To Baseline	-.0033	.0076	-.0036	.0052	-.0092	0

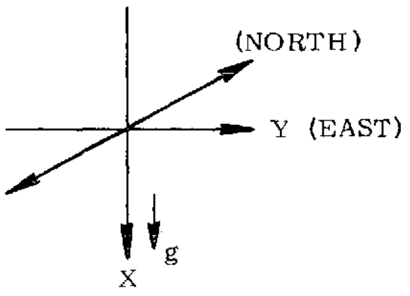

CAL. POS. 2

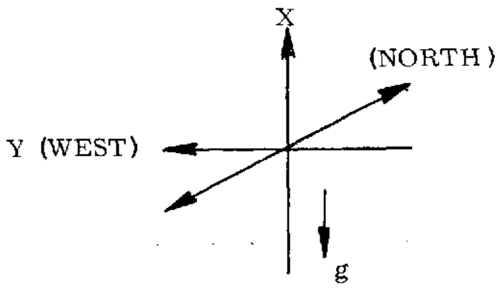

CAL. POS. 1

Upon returning again to calibration position 2, each gyro's net drift is again calculated. The maximum error with the gyros returned to their original orientation is .0092°/hr and the average return accuracy is within 0.005°/hr of the previous calibration position 2 drift summations. This small change is primarily due to the effect on the module electronics of the thermal gradients generated within the module by "dumping".

7.2.4 Gyro Scale Factor Linearity

Figure 7.2.15 is typical of the system's positive and negative SF linearity over the range of 0.09 rad/sec to 0.38 rad/sec for each of the SIRU gyro modules. Note that the plus and minus SF for each gyro is different, and each gyro's deviation from nominal is different. In the system implementation each gyro pulse update is corrected by the compensation software for a calibrated deviation from nominal for both its plus and minus SF corresponding to the plus and minus 0.125 rad/sec input. The linearity curves, therefore, reflect the error propagation from the calibrated value. This data was obtained by extending the dynamic calibration program (JIMK) to include the extra rate inputs required. The maximum spread for all system axes is approximately 50 ppm over the range of test rates. Incorporation of the point-slope compensation routine, developed and implemented on the SPOT program (NASA Contract NAS9-6823) and reported in Draper Laboratory report R-743, would reduce the SF deviation from the compensated value for these instruments to approximately 10 ppm for input rates up to 1 rad/sec.

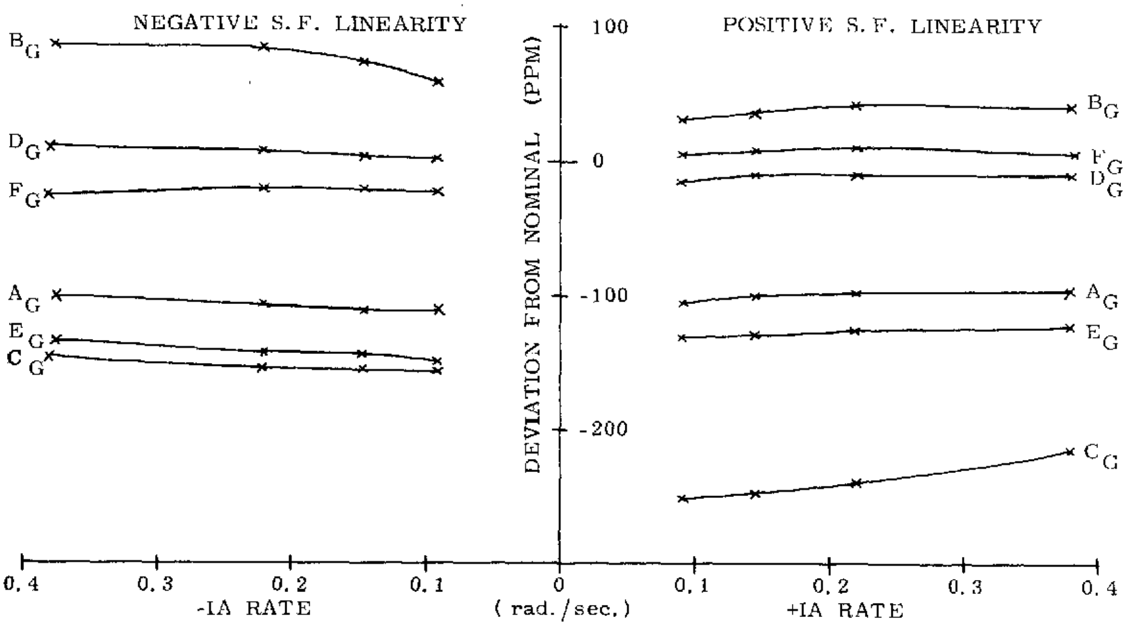

Fig. 7.2.15 Gyro Scale Factor Linearity Obtained at System Level Testing

7.3 Component Test to System Test Parameter Transfer

In general, transferability with reasonable performance has been achieved (see Figs. 7.2.1 and 7.2.2) during the course of the test program. However, problem areas were encountered in the demonstration of transferability of module calibration data between the gyro or accelerometer module normalization test area and in subsequent tests after installation in the system. These problems and corresponding recent test findings that indicate that significant improvements are obtainable are reviewed below.

7.3.1 Gyro Module

A review of the non-g-sensitive (BD) gyro drift across transfer from the gyro laboratory tests to SIRU system tests shows an rms value of .06 degrees per hour. Recent efforts have shown this discrepancy to be the result of variations in transistor leakage in the pulse torque-to-balance loop H switch dependent upon the residual polarity of the switch after torquing. In addition, an error in one of the data reduction programs was uncovered that introduced an uncertainty of approximately $0.12^{\circ}/\mathrm{hr}$. This error, when combined with the polarity dependency, appears to account for the BD transferability discrepancies. Special system tests conducted since isolation of these causes have shown a maximum delta BD of .03 degrees per hour between the module and system tests. This magnitude can be further reduced in the future by modifying the calibration and system compensation programs and the computer interface so that the BD compensation will be able to correct for H switch polarity leakage dependency. The interface modification would enable the separate accumulation of plus and minus $\Delta\theta$ pulses in each input/output (I/O) iteration. This I/O modification would enable tracking of the individual polarity states of the torquing circuits and permit the implementation of a precise software compensation routine for the dual BD magnitudes.

Torquer SF shifts (approximately 150 ppm) between module and system tests had been evidenced and were investigated. The SF magnitude was found to be sensitive to variations in the level of the 40v excitation between the component test area and the system test area. Tests were conducted with several pulse torque electronics (PTE) modules in SIRU gyro module #10 to evaluate:

1) DC amplifier circuit stability
2) SF sensitivity to 40v dc supply variations
3) SF stability
4) SF linearity
5) SF sensitivity to RC network tuning

Modification of the dc amplifier compensation, combined with an increase in the padded resistance of the torquer circuit and resistive tuning of the torquer circuit, has proven successful in desensitizing the SF to variations in the 40v excitation. Tests with a modified module have demonstrated a significant improvement; the delta SF between module and system tests was reduced to a maximum of 13 ppm.

Transfer of alignment from laboratory to system mounting has not been fully verified, although module alignment repeatability after a system alignment calibration and then across a subsequent removal of the module with a cooldown and remounting has been excellent, e.g., an rms of 8 $\widehat{\text{sec}}$ and a maximum spread of 20 $\widehat{\text{sec}}$. The demonstration of absolute transferability of alignment calibration between the laboratory and system has been limited by the non-availability of the precision optical calibration fixture mentioned earlier, (design and assembly of such a gauge was not effected during this program because of fiscal and time constraints) that could be installed in each system π-frame module location. This fixture would enable the determination of the frame pad alignments with respect to the system reference optical cube and allow correlation of laboratory and system data. In general, the limited correlated test work devoted to replacement of different modules in the same π-frame slot indicates that the absolute transferability is on the order of 4 $\widehat{\text{sec}}$.

7.3.2 Accelerometer Module

The variation in accelerometer bias from laboratory test to system test has been acceptable with an rms value of 21 micro g's. The rms value of SF deltas from laboratory to system operation is 29 ppm. No attempt has been made to reduce this value. If an application requirement for a better SF match existed, a task could be initiated to reduce this value to less than 15 ppm rms (conservatively estimated). The status of alignment transfer for the accelerometer module is the same as for the gyro module.

7.4 Real-Time Attitude Error Propagation

Tests were conducted with various combinations of zero, one and two instrument failures in static and dynamic environments to determine the error propagation characteristics of the redundant system. Tests were run with the body axes X, Y, and Z vertical and down. Constant angular rates of 0.4, 4, 10, 16, 26 and 40°/sec in both directions and oscillatory tests of 0.25 Hz,20° p-p, 0.50 Hz,15° p-p, 3.0 Hz, $3/4^{\circ}$ p-p, and 5.0 Hz,$1/4^{\circ}$ p-p were conducted.

The representative data included in this section are presented as the attitude error between the body (true) and computed (system error) reference frames as a function of time. The predominant dynamic errors appearing in the plots are due to OA coupling and pseudo-coning. Other dynamic errors due to SA cross coupling, anisoinertia, and SF errors are present to a lesser degree. A large repeatable error appearing in these plots is due to a test table encoder error of 80 $\widehat{\text{sec}}$ peak to peak over one table revolution.

7.4.1 Static Quaternion Attitude Tests

Figure 7.4.1 is typical of the static test results. Even though the test duration is only 14 hours, a 24 hour period in the X, Y and Z attitude errors can be observed. The error in the quaternion is quite small, a maximum of 2.5 milliradians in the 14 hour period is shown on the X-axis. This corresponds to a gyro drift miscompensation and cross coupling error that is equivalent to less than a $0.01^{\circ}/\text{hr}$.

7.4.2 Constant Angular Rate Tests

Inputs, during dynamic testing, were impressed about the X, Y, and Z body axes. No multiple axis testing was included.

Figures 7.4.2 through 7.4.4 present closure errors for the quaternion attitude expressed in terms of SF error for the X (input) axis and equivalent misalignment errors for the axes perpendicular to the rate vector. With respect to Figs. 7.4.2 and 7.4.3, the equivalent system alignment uncertainties correspond to those out-of-plane angles, which, when operated on by the total angle traverse accumulated about the X-axis, would yield the observed error in the output of the attitude algorithm axes that are orthogonal (Y and Z) to the rotational axis X. As seen from these figures, the equivalent system alignment uncertainty was well bounded, approximately 10 $\widehat{\text{sec}}$, regardless of the failure combination. It is very interesting to note, however, that when the E and F-gyro axes were failed, i.e., not used in the least-squares processing matrix for the triad solution, the equivalent misalignment errors were essentially nulled.

This result is indicative of a miscalibration load error in either the E or F instruments. Analysis of the equation structure for the four-instrument processing equations, Appendix A, shows that the F-gyro weighting becomes more dominant with the failure combinations that were exercised. The F-axis data in the Y-axis triad solution with gyro A and D failed increases in weighting from 0.425 with no failures to 0.638. Similarly, in the Z-axis solution, weighting increases from 0.425

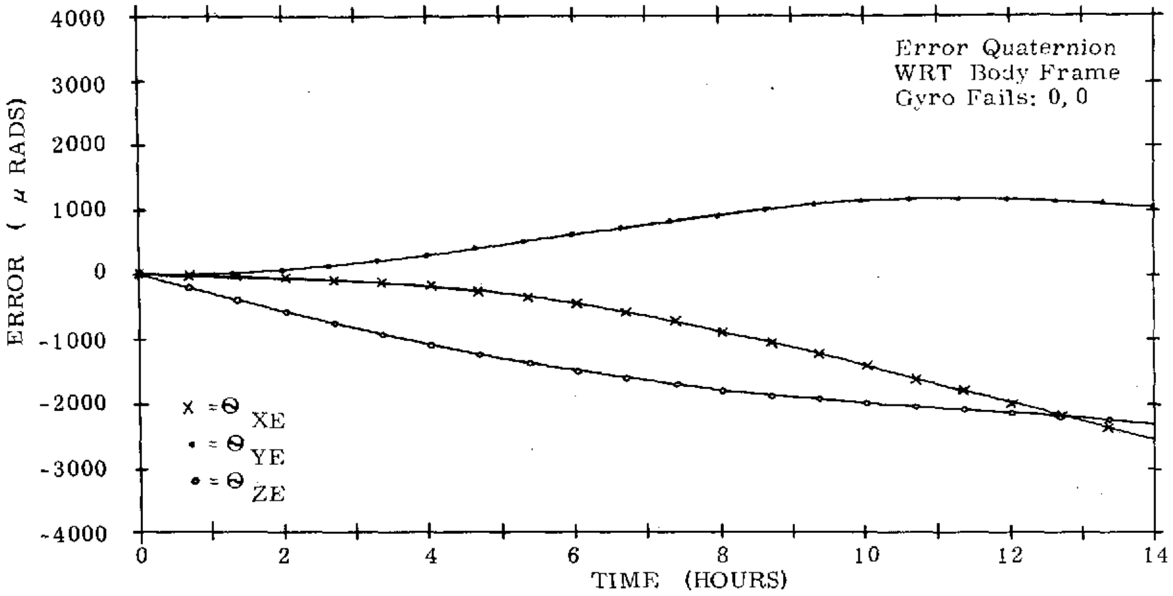

Fig. 7.4.1 14-Hour Attitude Test-No Instrument Failures (Cal Pos 2)

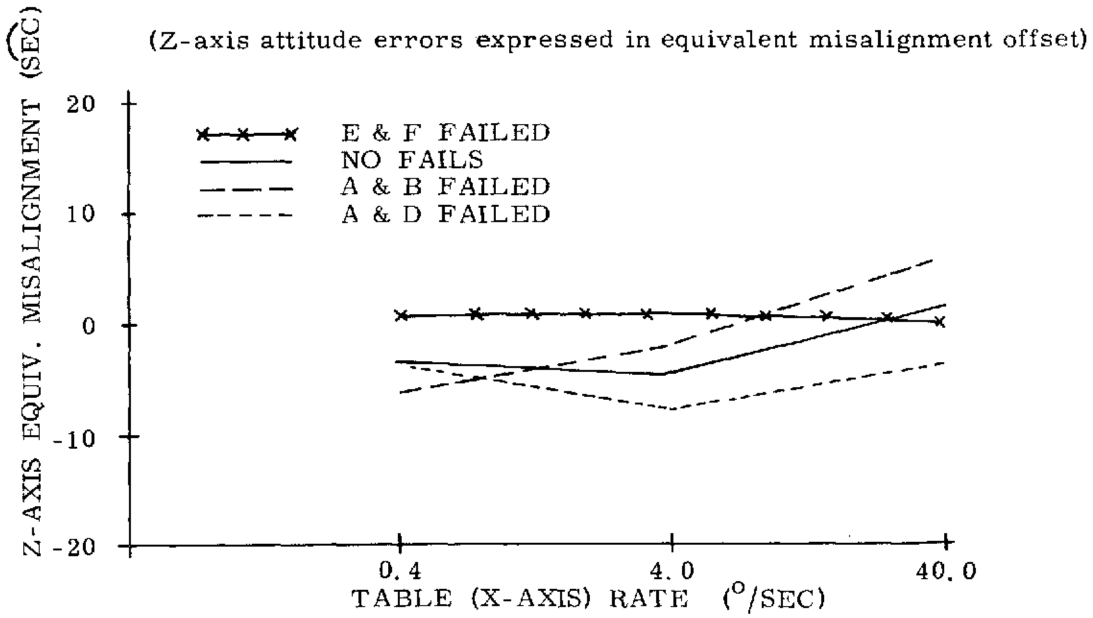

NOTES: 1 Rev. at 0.4 °/sec.
3 Revs. at 4 and 40 °/sec.
Compensation Load: NL109 (with OA Coupling Compensation)

Fig. 7.4.2 End-to-End Quaternion Attitude Tests (Cal Pos 2)

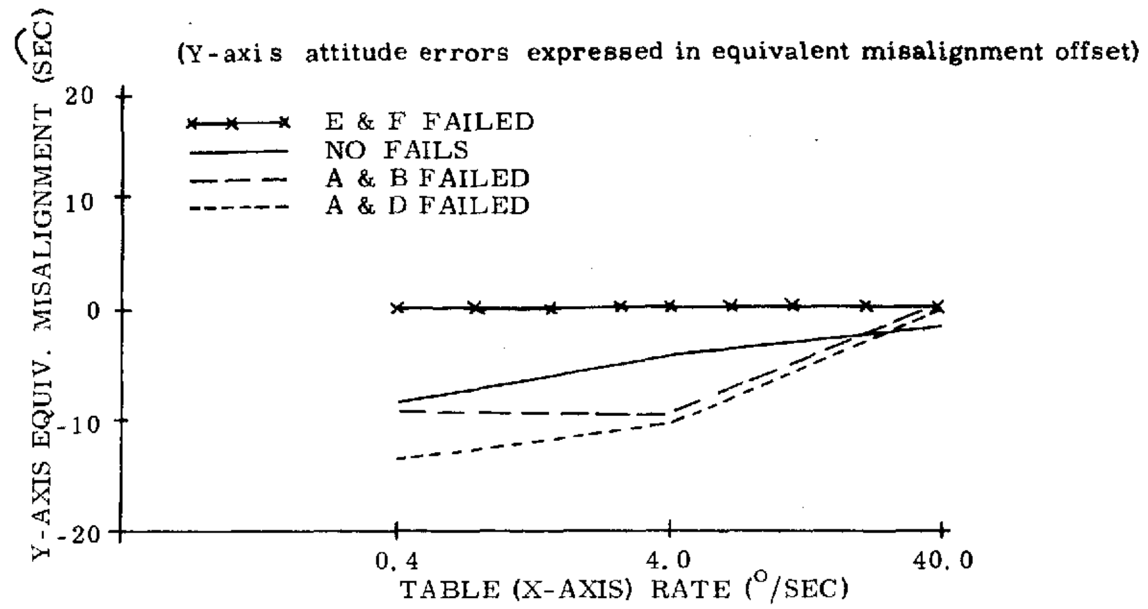

NOTES: 1 Rev. at 0.4 °/sec.
3 Revs. at 4 and 40 °/sec.
Compensation: NL109 (with OA coupling compensation)

Fig. 7.4.3 End-to-End Quaternion Attitude Tests, Cal Pos 2

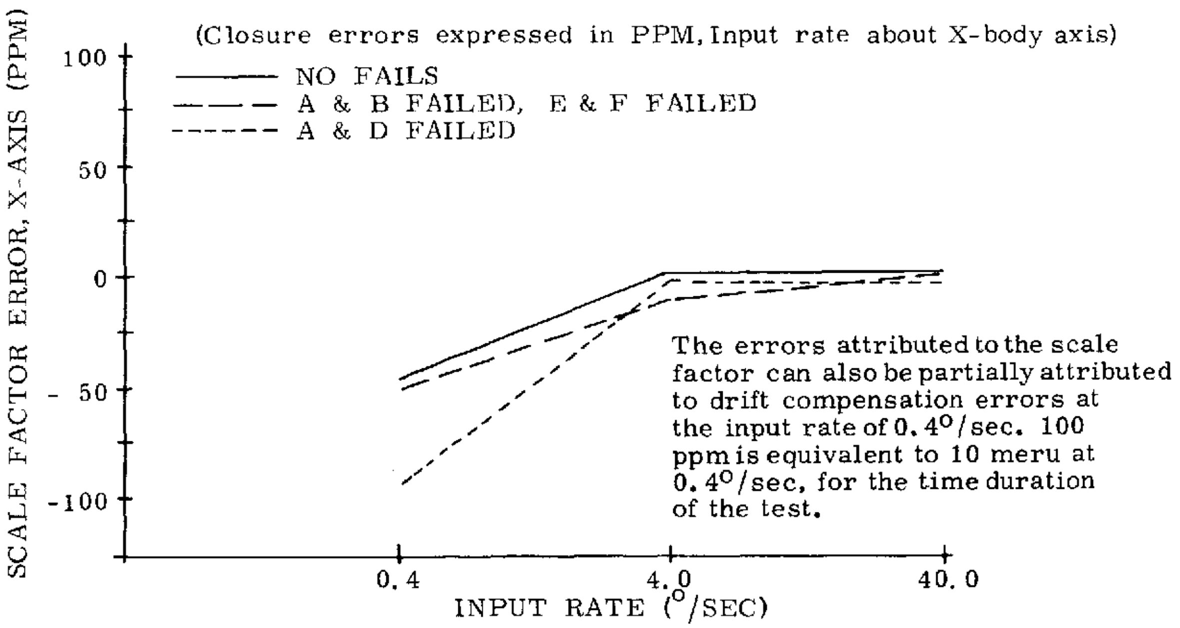

The errors attributed to the scale factor can also be partially attributed to drift compensation errors at the input rate of 0.4°/sec. 100 ppm is equivalent to 10 meru at 0.4°/sec, for the time duration of the test.

NOTES: 1 Rev. at 0.4 °/sec.
3 Revs. at 4 and 40 °/sec.
Compensation: NL109 (with OA coupling compensation)

Fig. 7.4.4 End-to-End Quaternion Attitude Tests, Cal Pos 2 to 0.607 with gyro A and D failed. Considering the foregoing factors, the relative test time for the different rotational rates and the number of revolutions, it appears that the equivalent system alignment spread in the data shown was primarily due to an approximately 0.03°/hr drift calibration error in the F-gyro. This is not unexpected since no special care was taken to obtain a precise calibration load prior to this test sequence. In addition, in the calibration sequence run 14 days after these performance tests, an F-gyro drift performance change from the previous calibration of 0.18°/hr was observed. The F-gyro instability was eventually traced to a random malfunction in the torquing electronics causing variance type bias performance failure phenomena.

With regard to Fig. 7.4.4, the equivalent system X-axis SF error was defined by comparing the attitude algorithm output X-axis error to the total angle rotation of the X-axis. Recall that the compensation algorithm used in SIRU corresponds to a nominal SF calibration at approximately 0.125°/sec. From the test data in the figure, across all of the combinations in the rate region between 4 and 40°/sec, the equivalent SF error is quite small, a spread of approximately 10 ppm. This performance is consistent with the SF linearity performance for individual instruments shown in Fig. 7.2.15. The roll off at lower rates (0.4°/sec) is also consistent with data observations on individual instruments and generally relates to the uncertainties introduced in the estimation of SF calibration at low rates by the gyro drift calibration uncertainties. The 50 ppm drop across the no failure and E and F-gyro failure conditions is therefore consistent with the test calibration condition. The system SF performance is well bounded and reflects the general quality of the system gyro torquing performance. Use of a SF linearity compensation routine, as discussed previously, would have yielded improved performance. It is interesting to note that the A and D-gyro failure combination resulted in an increase in the equivalent SF error at the low rates of about 40 ppm. Once again, this result appears to correspond to the bias compensation error in the F-gyro since the X-axis triad solution weighting does not use the F-gyro when there are no failures. However, with A and D-gyro failed, it is scaled to 0.557.

Figures 7.4.5 through 7.4.8 present quaternion attitude as a function of time with and without OA coupling compensation and with no failures.

The effect of OA coupling errors, resulting from a step rate input, in terms of the error in the indication of the inertial frame is evidenced in Fig. 7.4.5. As expected, an inertial frame error in the Y and the Z axes occurs that corresponds to the change in rate applied about the X reference triad axis. The rate change affects the E and F instruments which have their OAs colinear with the X-axis. It

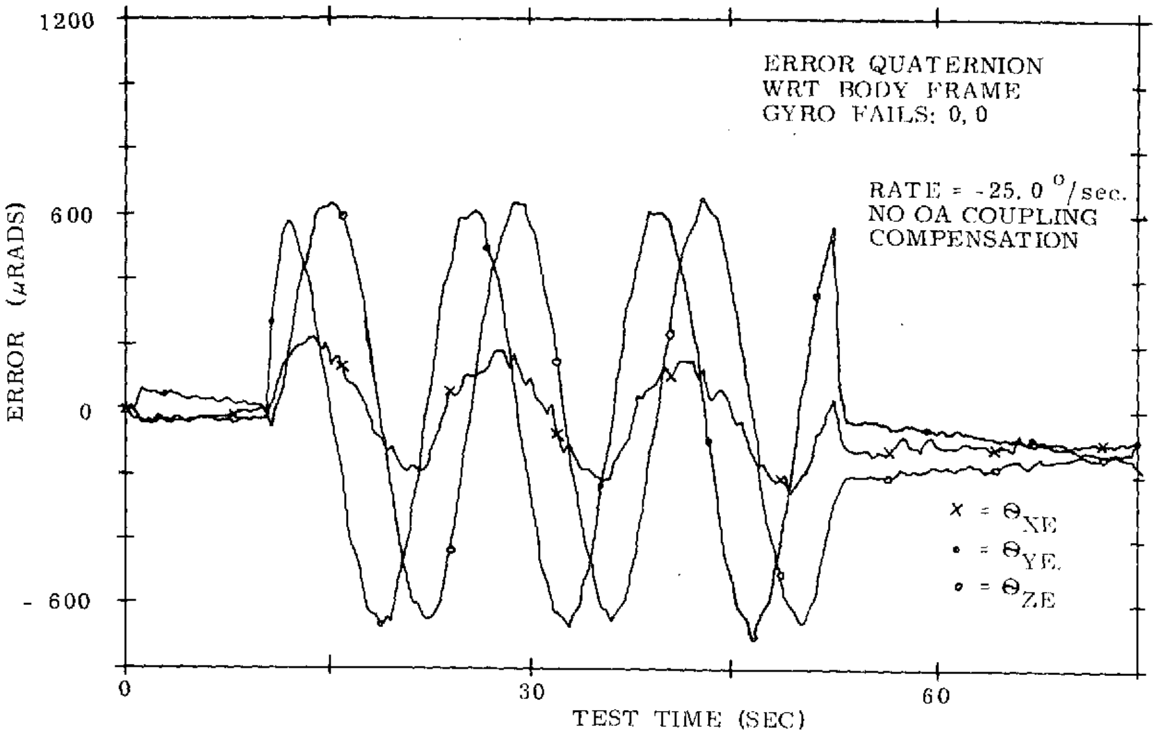

Fig. 7.4.5 Constant Rate Test about X-Body Axis (Static - 3 Rev Slew - Static), Cal Pos 2

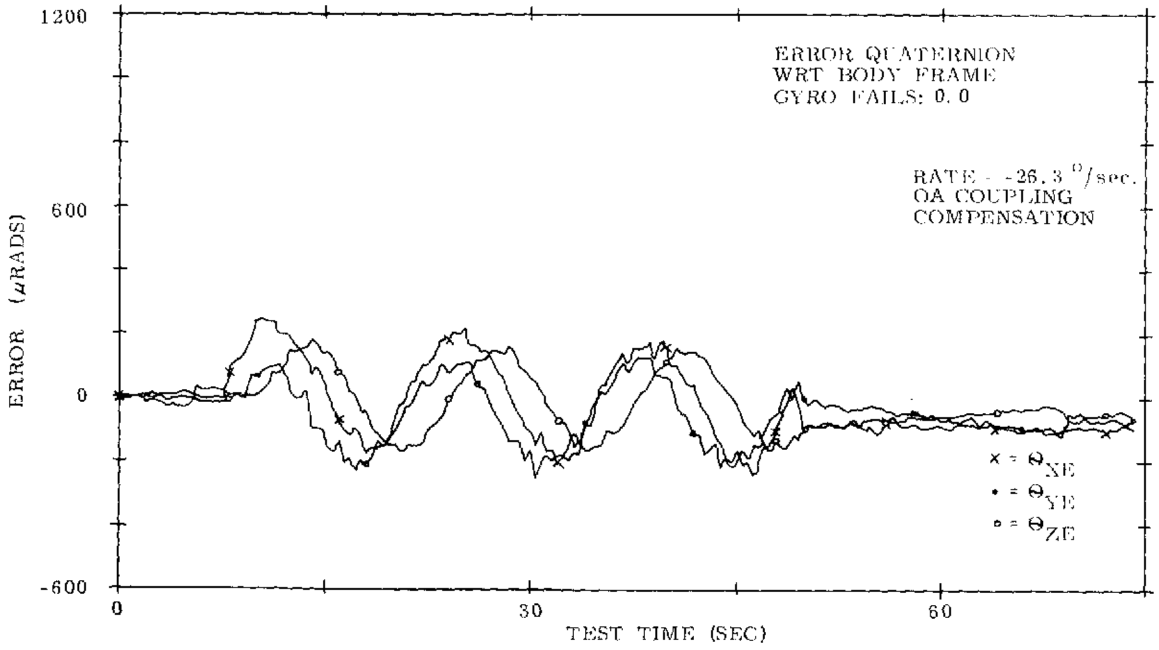

Fig. 7.4.6 Constant Rate Test about X-Body Axis (Static - 3 Rev Slew - Static), Cal Pos 2

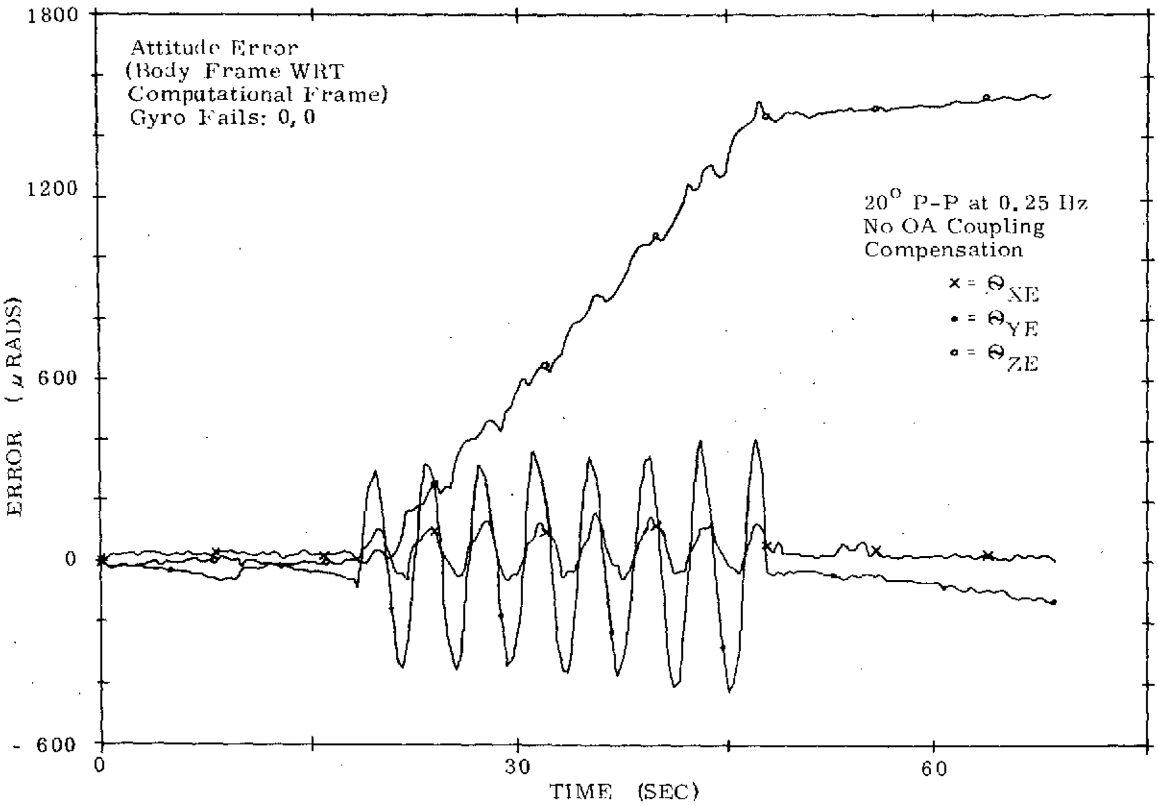

Fig. 7.4.7 Oscillatory Input about X-Body Axis, Cal Pos 2

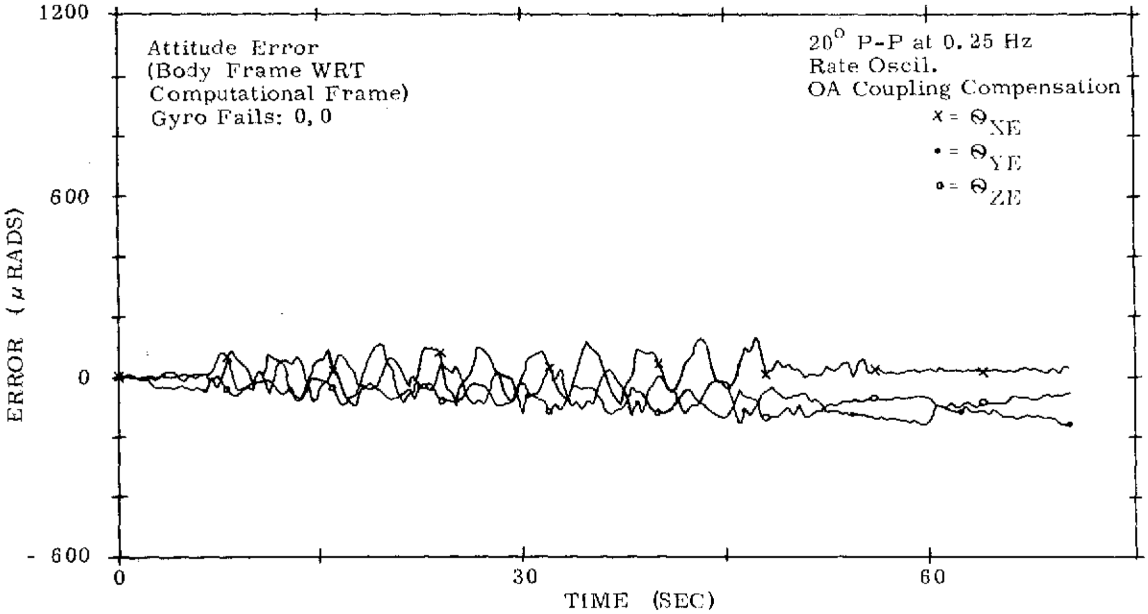

Fig. 7.4.8 Oscillatory Input about X-Body Axis, Cal Pos 2

results in an erroneous E and F-gyro output and a corresponding error in the Y and Z triad solution. This output is proportional to the OA coupling coefficient. The Y and Z axis solution error results in the sinusoidal Y and Z error curves, Fig. 7.4.5. These error curves correspond to the indication of the Y and Z body axis orientation with respect to a perfect non-rotating inertial frame. The Y and Z axis sinusoid errors are 1200 μrads peak to peak, and the sinusoidal error in the X axis corresponds to the table encoder calibration error (80 $\widehat{\text{sec}}$, 400 μrad). When the table rotation is stopped, an opposite polarity change of rate occurs with a corresponding E and F-gyro output that returns the inertial indication to the correct orientation with no net error due to OA coupling. The net offsets at the end of the test are primarily due to SF and alignment error propagation. With OA coupling compensation implemented in software, the magnitude of the attitude error in the Y and Z axes for the same input rate step was reduced to 400 μrads peak to peak, Fig. 7.4.6.

The variation in OA coupling error between tests is attributable to the manual setting of angular rate and rate magnitude (i.e., variation in w magnitude and time).

The effect of OA coupling error in an oscillatory environment is dramatically presented in the quaternion attitude plot of Fig. 7.4.7. The Z-axis attitude drift, termed pseudo-coning,[*] results when the algorithm receives information from the instruments for apparent oscillatory inputs 90° out of phase and of the same frequency about two axes (X and Y). The X-axis oscillation is the true sensed input and the Y-axis oscillation is the false information caused by the OA coupling error of the E and F-gyros. The Y-axis sinusoid is the direct result of the OA coupling error term and the X-axis sinusoid is a function of the encoder error. When OA compensation is effected, Fig. 7.4.8, the Y-axis OA coupling induced sinusoid is compensated and the Z-axis attitude drift error is essentially removed. The X-axis sinusoid error is essentially the table encoder error.

A comparison of the theoretical and measured pseudo-coning drifts for the five oscillatory inputs, presented in Table 7.4.1, indicates the high degree of correlation achieved in these tests.

---

[*] A complete description of the propagation and effects of pseudo-coning is presented in the Final Report, Strapdown System Performance Optimization Test Evaluations (SPOT) by Richard Blaha and Jerold Gilmore, R-743, February, 1973.

Table 4.1.1

SIRU Error Propagation Results for Oscillatory Inputs

	Without OA Coupling Compensation		With OA Coupling Compensation	
X-Axis Oscillatory Inputs	Approximate Theoretical Pseudo-Coning Drift ($^{\circ}$/hr)	Actual Pseudo-Coning Drift ($^{\circ}$/hr)	End-to-End Error Expressed in $^{\circ}$/hr	Attitude (sec)
15° p-p at 0.5 Hz	22.20	21.75	0.30*	16
20° p-p at 0.25 Hz	10.20	10.05	0.30*	16
$3/4^{\circ}$ p-p at 3.0 Hz	1.95	1.05	0.30*	16
2° p-p at 1.0 Hz	2.55	1.50	0.30*	16
$1/4^{\circ}$ p-p at 5.0 Hz	0.60	None Apparent	0.08*	4

*Within the quantization uncertainty of the test data

7.5 Self-Alignment and Navigation Performance Comparisons

Table 7.5.1 presents standard deviations for latitude, longitude, azimuth and leveling of the SIRU system calculated from the one sigma values of drift of the SIRU instruments derived from calibration testing. The first data column shows alignment and navigation performance calculated from the instrument one sigma values over a 6 month uninterrupted operating period. The second data column shows alignment and navigation performance based on instrument calibration shifts across system cooldown. The calculated results also reflect accelerometer performance in the SIRU module configuration. These calculations do not reflect the performance improvements that would be attained using the statistical self-calibration techniques or the SPC software developed in the SIRU Utilization Program, R-747. Similarly, the calculations are based on the population data, and the improvements inherent in the hardware/software modifications to correct for the torque loop H switch polarity (bias) leakage problem (Section 7.3.1) have not been factored in. Finally, incorporation of the redesigned gyro, 18 IRIG PM Mod D, with its reduced cooldown sensitivities, would yield significant improvements. For example, the Mod D bias stability across cooldowns demonstrates improvement by a factor of three and the ADIA and ADSRA stability by a factor of six to eight compared to Mod B performance.

Table 7.5.1

Projected Alignment and Navigation Performance

	Parameter	Gyro 1σ Error Models	
		No Cooldowns or Mountings (6 Months)	Across Cooldown
Instrument Calibration Data	NBD $(^\circ/\text{hr})$	0.015	0.05
	ADOA $(^\circ/\text{hr}/\text{g})$	0.005	0.01
	ADIA $(^\circ/\text{hr}/\text{g})$	0.02	0.08
	ADSRA $(^\circ/\text{hr}/\text{g})$	0.02	0.06
	Compliance $(^\circ/\text{hr}/\text{g}^2)$	0.009	0.025
	Alignment $(\widehat{\text{sec}})$	2.0	4.0
	Scale Factor (ppm)	10.0	22.0
Calculated System Performance	*North Axis Drift $(^\circ/\text{hr})$	0.016	0.058
	East Axis Drift $(^\circ/\text{hr})$	0.013	0.046
	Vertical Axis Drift $(^\circ/\text{hr})$	0.018	0.063
	**Latitude Error (nm/hr)	0.87	3.07
	**Longitude Error (nm/hr)	1.07	3.87
	***Initial Azimuth Alignment (mr)	1.18	4.15
	Leveling $(\widehat{\text{sec}})$	10.0	10.0

*System aligned X-axis down, Y-axis east, Z-axis south

**Slope for first two hours of navigation run

***At SIRU laboratory latitude

The system performance across cooldowns in alignment using the Mod D is projected to be equivalent to 1 mr in azimuth alignment.

Figures 7.5.1 and 7.5.2 present typical navigation test data for the SIRU system taken in the static test condition. A comparison of these plots with the calculated latitude and longitude errors of Table 7.5.1 indicates that the one sigma values of the static error sources used in the calculations represent a conservative system end-to-end performance.

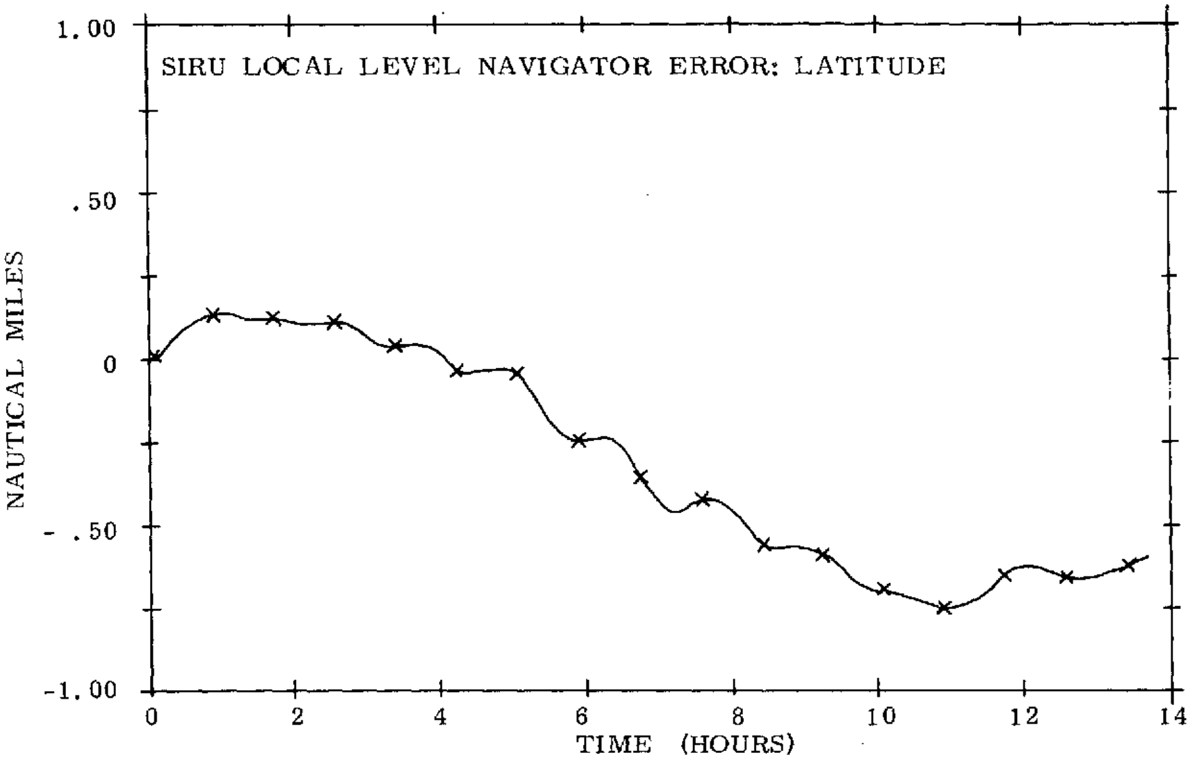

Fig. 7.5.1 Latitude Error for Compensated Local Navigation Axis Drift — Cal Pos 2

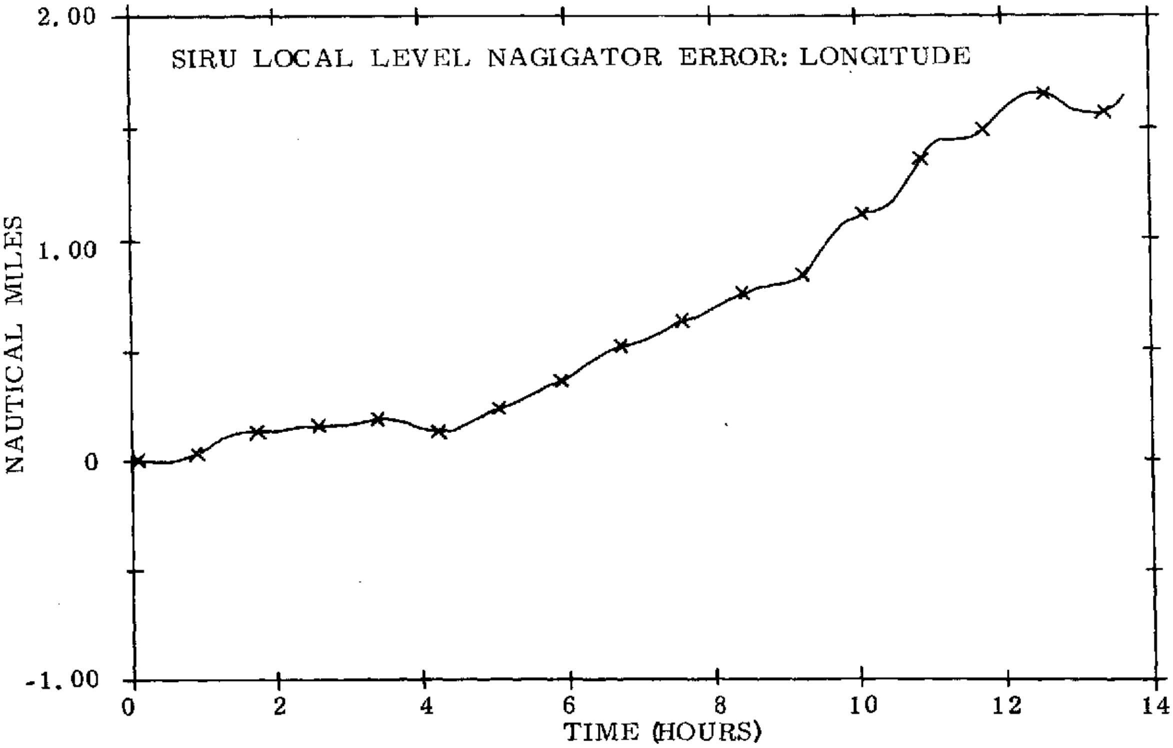

Fig. 7.5.2 Longitude Error for Compensated Local Navigation Axis Drift — Cal Pos 2

8.0 Program Milestone History

This chapter of the SIRU Development Final Report presents the history of the SIRU development as a series of significant milestones extending from May, 1968 through November, 1971. Subsequent history is summarized in the System Log, Volume III of the SIRU Utilization Report, R-747.

8.1 Program Initiation

Technical Proposal

In May, 1968, the Draper Laboratory in response to NASA RFP #BG131-47-8-533P submitted a Technical Proposal to NASA describing a strapdown system which would replace certain portions of the Apollo primary Guidance, Navigation and Control system as required to support the long term manned space flights contemplated for the Apollo Applications Program.

Contract Award

Work on the SIRU system commenced under contract NAS9-8242 in June, 1968. Delivery called for one developmental modular redundant strapdown system based on the dodecahedron geometric concept which, in a production version, would provide a capability to perform a 120 day mission with a .999 mission success probability followed by a one-half hour reentry phase with .9999 success probability.

The SIRU design configuration was specified to be compatible with mounting in an Apollo spacecraft in the same equipment bay, replacing the Apollo three gimbaled IMU. The design was to be compatible with the Apollo vibration and shock environment with a vacuum capability using conductive (liquid coolant) heat transfer. In addition, the system was to be compatible with a detachable coldplate.

The gyroscope specified by NASA for the SIRU design was the Draper Laboratory designed strapdown instrument, the 18 IRIG Mod B. This unit is a floated, single-degree-of-freedom (SDF) gyroscope, magnetically suspended, with a gas bearing wheel design and a 5 radian per second slew capability. Built with a permanent magnet torquer, it is scaled for torque-to-balance operation with input rates up to one radian per second. The accelerometer specified by NASA was the Draper Laboratory size 16 Permanent Magnet Torquer Pulsed Integrating Pendulous Accelerometer (PMT PIPA). This unit is a floated, SDF, magnetically suspended specific force receiver designed for operation in a torque-to-balance mode. It is distinguished

C3

from its predecessor, the Apollo PIPA, by inclusion of a PM torquer, a solid float and a more conventional bellows arrangement.

8.2 Design and Construction

Significant program milestones occurring during the design and construction of the SIRU engineering model were as follows:

a) September 1968, Initial Design Review.—The first of the two required design reviews with NASA was held September 16-18, 1968. The overall SIRU mechanical and electronic design including the computer (DCA) was presented and approved.

b) February 1969, Second Design Review.—The second design review with NASA was held at MIT February 4, 6 and 7, 1969. Specific mechanical and electronic design features were presented, modification direction was received and the plans approved as modified.

c) May 1969, Contract Review and Evaluation.—An MSC/MIT program review was held at MIT on May 6-9, 1969. The principle administrative actions were: elimination of the multiplexer from the deliverable hardware and approval of the GSE design.

d) July 1969, SIRU Progress Review.—An MSC/MIT progress review was held at MSC, Houston on July 28-29, 1969. Hardware status, completion schedules and problem areas were presented and discussed.

e) January 1970, First Six Position Calibration Test.—On January 27, 1970 the first six position calibration test was run. The second six position test was completed on February 13, 1970.

f) March 1970, IBM 360 Plotting Program Implemented.—On March 18, 1970 the IBM 360 plotting program became operative. Overnight stability data is placed on Digistore tape by the MDGO program and then processed by the IBM 360.

g) April 1970, Deletion of Digital Computational Assembly (DCA).—In accordance with modification No. 5 to NAS9-8242 the requirement for delivery of a breadboard DCA and associated software was eliminated as of April 1, 1970 for budgetary reasons. At that time a breadboard simplex model had been constructed, initial instruction capability checkout was completed and 60% of the instruction combinations had been run and verified.

h) June 1970, SIRU Assembly and Checkout Completed.—System hardware and software are in operating condition ready for NASA "selloff" demonstration.

i) July 1970, NASA Acceptance Testing Successfully Completed. — The SIRU demonstration and "selloff" tests were conducted at Draper Laboratory on July 22-24, 1970. The system was accepted subject to correction of minor discrepancies and instigation of configuration control. By mutual agreement between NASA and MIT, SIRU remained at Draper Laboratory to allow a demonstration for industry to be presented in September.

j) September 1970, Industrial Symposium on SIRU. — An Industrial Symposium was presented for space shuttle contractors and other interested parties at MIT on September 9-10, 1970. Titled "Design Principles for a Modular Redundant Inertial System" it included demonstrations of the operating SIRU system.

k) November 1970, Software Improvements Incorporated. — Attitude algorithm and failure isolation routines were speeded by 48% at a cost of 200 memory words. The change permitted improvement in adaptation time for a detected failure. Incorporation of the gyro interpolator into the attitude algorithm software eliminated pulse bursting in the loop performance.

l) March 1971, Gyro Module Interpolator/Compensator Retrofit Complete. — In March, 1971, the task of retrofitting all gyro modules with Interpolator/Compensators was completed. The system had been operating with a complete set of retrofitted modules since the first of the year.

m) November 1971, Close of SIRU Development. — All static and dynamic error compensation routines were in successful operation.

9.0 Conclusions and Recommendations

9.1 Introduction

This report has presented the hardware and basic software status of the SIRU Redundant Modular Strapdown system development program. The SIRU system achievements in both hardware and software demonstrate several original applications of new technology which represent significant state of the art inertial system milestones. Some of the more noteworthy achievements that have been developed and successfully demonstrated by the SIRU program are described in the following Conclusion section. Recommendations for further development and evaluation of the strapdown redundant, modularized, fault tolerant guidance and navigation system are provided in Section 3.0, Recommendations.

9.2 Conclusions

9.2.1 Hardware

SIRU is the first designed, fabricated and test evaluated, integrated, redundant strapdown inertial hardware mechanization. It has uniquely evolved and matured concepts of redundancy based on dodecahedron geometry. This hardware is free from single point failure mechanisms and its fault-tolerant operational features have been successfully demonstrated with multiple "hard" and "soft" failures.

The SIRU, pulse-torqued, strapdown, mechanization has demonstrated wide dynamic range (one rad/sec) with performance equivalent in many dynamic environments to that of commercial gimbal systems. During the course of this program significant strides in achieving stable and precise strapdown pulse weight scale factor and alignment performance were made in both single degree-of-freedom gyro and ternary pulse-torque control technology at the system test level, e.g., gyro electronics long term scale factor (SF) stability of 10 ppm rms over a six month test period (no cooldowns) and 22 ppm rms over two years operation was achieved.

SIRU represents an initial demonstration of instrument functional modularity. Concepts of functional instrument modularity with interchangeable mechanical and electrical interfaces, and prealigned and calibrated transferability were implemented, matured and demonstrated (e.g., across mountings and cooldowns gyro SF repeatability of 30 ppm rms and alignment repeatability of 8 $\overset{\frown}{\text{sec}}$ rms were achieved in system operation).

9.2.2 Software

SIRU represents the first hardware with an operating, integrated and evaluated redundancy management software system. This system includes self-contained fault detection and isolation (FDI) with reorganizational processing routines and recertification of "healed" or transient failures. The FDI algorithms have demonstrated reliable nonambiguous fault isolation with as many as two gyro and two accelerometer measurement axes failures and positive fault detection for a third failure.*

The SIRU program has demonstrated that a comprehensive inertial navigation and redundancy management software system for a strapdown dodecahedron redundant configuration can be successfully integrated in a representative minicomputer (DDP-516) operating at 50 iterations per second (36% machine time) with a reasonable memory allocation (7000 16-bit words). This software system includes the strapdown processing (twelve instrument static and dynamic compensation, attitude and velocity algorithms) redundancy management (FDI, processing, reorganization, etc.), system software (preflight calibration,** alignment,** and navigation),** and operating software (dedicated executive, I/O servicing and display).

Some discussion based on the total SIRU test experience, as it relates to and affirms the motivation for a redundant implementation, seems desirable.

The SIRU equipment, although a first development model, has proven to be remarkably reliable (over 20,000 hours of system operation with only 5 hardware failures (two of which would typically have been edited out of reliability estimates as workmanship or correctable design deficiencies). The fact that these failures did occur during the SIRU system testing and that they did not compromise continuing system operation is of significance. In each case the processing software automatically adapted to reflect the failure status and changed the processing structure to omit bad data and yield a minimum error propagation solution for continued satisfactory system performance. First, from a hardware point of view the failures did not result in any systematic degradation, i.e., the redundant hardware features retained their integrity and no secondary system operational or performance effects

---

* During the SIRU Utilization phase of this contract (R-747), third failure isolation capabilities were demonstrated for those situations in which a third performance failure error magnitude was worse than an already existing and isolated performance failure. In addition, the capability to recalibrate and thereby recertify a failure that corresponds to a stable performance change was also demonstrated.

** Described in SIRU Utilization Report, R-747.

were observed. Second, although several of the failures were of a performance degradation type that could not have been detected or isolated by self-monitoring electronics typically identified as BITE (Built-in Test Equipment), they were reliably detected and isolated by the FDI software algorithms.

The soft failures that did occur present a broad spectrum of different failure mode phenomena, e.g., a random float-freedom gyro problem; a malfunctioning preamplifier in the torque loop with attendent variance type data output performance and a gyro SF degradation due to a gradually deteriorating solder joint. In a simplex triad inertial system implementation, these types of failure modes would, in a space mission, probably cause a mission abort. Had the transient failures occurred in a critical mission phase, crew safety would probably be endangered. In a prelaunch or preflight phase, the transient gyro float-freedom and variance data output failure phenomena might possibly have been observed on a coincidental basis. Even if observed, verification and isolation diagnostics in the vehicle would be time consuming with limited probability of success. In comparison, the SIRU system using real-time continuous FDI detected and isolated the failures to the replaceable modular functional axes. In each case, as the system repair was being made, the utility and advantage of the interchangeable modular instrument module concept was clearly in evidence. The faulty instrument module was readily replaced by another module, within the tolerance described previously, usually in less than six minutes.

The motivating need for a redundant system implementation remains apparent for missions with time-critical reliability phases or long term missions, as characterized by the space shuttle, anticipated satellite space missions and current and anticipated commercial and military aircraft operations. The SIRU program has demonstrated a realizable and efficient solution to the high reliability operational readiness questions posed by these applications.

In the final summary the concepts formulated and developed in the SIRU dodecahedron redundant modular configuration have been successfully demonstrated and matured in both hardware and software. Commitment of strapdown technology for a variety of applications is forthcoming and the SIRU performance achievements in strapdown technology represent another significant step toward that realization.

9.2.3 Supplementary Conclusions

As noted in the introduction of this report, NASA in 1972, subsequent to the basic development activity described in this report, funded additional SIRU effort to further mature and utilize concepts of redundancy management and to implement other operational features such as preflight single position calibration, self-alignment and navigation. This report reflects the achievements in hardware and basic software prior to the program extension. Report R-747, a companion report, documents the technical concepts and achievements in the development of statistical failure detection, isolation, classification and recalibration (FDICR) techniques, as well as the operational software developments included in the SIRU Utilization program.

In recognition of the successful outcome of the effort in these areas some supplementary conclusionary comment is in order in this report, especially as a prelude to any recommendations regarding further coherent redundant system technology development.

Some of the most noteworthy achievements during the additional development demonstration effort were:

1) The implementation of a statistical FDICR technique based on the "Wald" sequential probability test. This technique enabled detection and isolation, with a specified coverage (reliability, false and missed alarm probabilities), of mean performance shifts at levels equivalent to 1.5 times the one sigma noise level of normal system operation. For example, in a quiescent maneuver environment, the detection and isolation of a bias shift as small as 0.07°/hr was routinely achieved with a background noise level of 0.045°/hr. The noise background corresponded to the $\Delta\theta$ quantization in the two minute sampling period. Similarly, performance standard deviation changes on the order of four times the nominal spread were also detected and isolated.

   The maximum attitude error accumulation prior to detection and isolation of a performance failure was bounded at 40 $\widehat{\text{sec}}$ independent of the magnitude of the performance degradation. Bias and ramp recompensation to better than $.015^{\circ}$/hr and $.0008^{\circ}$/hr/minute respectively were demonstrated repeatedly for the static environment. Accelerometer bias errors of 0.1 cm/sec^2 and ramp errors of 0.02 cm/sec^2/minute in a static environment were also detected and bias compensation to 0.02 cm/sec^2 or less effected.

2) A single position lumped parameter self-calibration to approximately 0.015°/hr or better in the static environment was consistently achieved using the technique developed and implemented.

3) The self-alignment software, implemented in a coarse/fine sequential program achieved totally acceptable magnitudes regardless of the environment input during testing. Coarse alignment to less than 1^{o} in a fixed 260 second period and fine alignment to less than 1 milliradian in 15 minutes were consistently attained.

4) End-to-end performance, demonstrated as the output of a local level navigator, was on the order of 0.5 nm/hr or less for all static tests.

9.3 Recommendations

The concepts of redundant modular strapdown technology have been clearly demonstrated and matured in the SIRU technology programs documented by these reports. The modular hardware implementation and the operating software have undergone a comprehensive laboratory evaluation. The obvious and next logical evolutionary program step to establish confidence in this technology and to demonstrate its unique advantages should be in the commitment of the SIRU system to a realistic broad-based flight test evaluation.

Such a flight test effort should seek to establish a base line for Guidance and Navigation performance of the strapdown implementation across the full spectrum of flight environments and mission phases. The utility of the redundant implementation with its fault tolerant operation and its ability to provide a direct measure of its operational readiness represents an important factor to evaluate and demonstrate in pre-flight and in-flight operations. Similarly, the logistic and maintenance enhancement offered by the comprehensive redundancy, self-test software, and hardware modularity should be assessed in an operational environment. With respect to the redundancy management design features, both the statistical reliability enhancement and the significance of the SIRU dodecahedron's fail-operational characteristics in time-critical mission phases can be evaluated and demonstrated.

Commitment of the SIRU technology to such a test program should be proceeded by the integration of the SIRU inertial hardware with a complementary redundant computer complex. Development of a special purpose redundant computer system does not appear to be realistic technically nor economically feasible. A concept based on the utilization of available general purpose computers replicated in triplicate with fail-safe input/output interfacing to achieve fault-tolerant, fail-operational mission performance for a single "soft" computer failure represents a practical and realizable flight demonstration approach. However, the more challenging and basic computer redundancy implementation approach requires the development of a high confidence FDI technique for a dual computer complex. For example, in a triplicate system, after the first computer failure, should one abort the mission if critical flight safety phases remain? Conversely, can one sufficiently characterize potential computer failure modes, as they relate to total system operation, to enable the development of a high confidence fail-operational FDI for the remaining duplex configuration? At a minimum, the formulation of a suitable dual redundant computer complex with special emphasis on a reliable FDI approach and means for re-initialization betweeen computers to resolve transient failure phenomena is highly recommended for integration with the SIRU inertial subsystem.

Consistent with the integration of SIRU with the computer complex is the need to fabricate and integrate a multiplexer interface unit with suitable, triplicate computer, expansion capabilities. The original SIRU multiplexer design (not fabricated due to program funding limitations) should be reviewed and revised to reflect the more advanced state of currently available electronics. The SIRU laboratory test experience, the computer complex FDI implementation as formulated, and flight operations interactive man-machine considerations should also be reflected in the advanced design. The built-in test equipment (BITE) features to be incorporated in the multiplexer should complement the software FDI by enabling automatic fault location diagnostics to the different axis functions (i.e., wheel supply, dc axis supply, etc.) to optimize system maintenance.

BITE should also incorporate failure status data display for those hardware functions that do not reflect as unique axis failures in the software FDI. This display would communicate to the mission operator in real-time the status of the triple redundant clocks and dual redundant scalers and 40v power supplies (these redundant elements use hardware FDI and active or passive switching provisions in their redundant mechanization).

Within the software area some limited development appears desirable to enable a more comprehensive evaluation of possible pilot/system interfacing. The current SIRU executive software is dedicated and non-interactive except for mode switching phases, i.e., alignment, navigation, etc. An interactive executive allowing flexible examination of different system parameters, modification of compensation loads, redundancy in processing conditions and maintenance diagnostics should be developed. In addition, the incorporation of the software compensation routines evolved in the SPOT program (MIT/DL Report R-743) for compensation of anisoinertia, SRA cross coupling and scale factor linearity appears to be desirable and a review of the OA compensation bandwidth characteristics should be effected.

In the area of advanced software development, the concepts evolved in the SIRU Utilization program can be advantageously matured. Studies to relate the FDI criteria automatically to mission phase and dynamics should be conducted and corresponding software demonstrations effected. The single-position self-calibration technique should be augmented to advantageously utilize optical alignment data as well as other alignment aids. The evolution of techniques to apportion drift change correction among the bias and g-sensitive coefficients should be initiated. Finally, the efficient utilization for flight operations of the total integrated redundant system with SIRU and the redundant computer complex as a core structure could be advantageously explored. For example, the SIRU sensing data could also redundantly provide flight control and stabilization sensing and attitude and heading display, thereby efficiently and reliably replacing a multiplicity of independent sensors. The integration of radio-navigation and landing aids with the SIRU concept in a redundant implementation should be explored to evaluate total system concepts and to develop and demonstrate operational inflight usage of such aids for inertial system alignment and compensation improvement. The entire concept of statistical fault detection, isolation, classification and recalibration evolved in the SIRU program should be reviewed for more comprehensive total guidance, navigation, and control system application.

Several hardware recommendations and studies appear to be desirable. The SIRU hardware technology demonstrated modular concepts within the boundaries of reasonable physical size and weight allocations that were possible using the electronic components and packaging technology of the 1960's. The modularity concept is a sound concept, creating both a building block system design and simplified logistic and maintenance operations. The application of the technology of the 70's (expected to include the maturing of medium-scale circuit integration, the advent of realizable large-scale integration, and the availability of improved hybrid circuit capabilities) to the modular concept would enable realization of a totally integrated modular concept. A completely self-sufficient instrument module using a single power source and a digital data bus concept for input and output could be realized. Preliminary studies of such a design using the Charles Stark Draper Laboratory 13 size instrument form factor and MSI/hybrid packaging techniques indicate that an entire SIRU system consisting of six each accelerometer and gyro self-contained modules (no supporting electronic assembly) could be developed in a volume of 0.25 cubic feet which would weigh less than 25 lbs. Basic to such a concept however is a second logistic objective; to provide in the module interchangeable sensor compatibility features, i.e., ability to interface with several different available inertial instruments. Study and development in this area as well as in the integrated modular approach is recommended.

Finally the continued evolution and improvement of strapdown inertial instruments is considered most important. The Draper Laboratory 18 IRIG Mod B gyroscope has been significantly matured during the course of the SIRU and recently Navy sponsored programs. The performance and reliability of the permanent magnet version of the 18 IRIG Mod D gyroscope has demonstrated significant potentials and should be evaluated for high reliability, high performance, moderate rate applications. Similarly, the size 13 gyro and accelerometer technology exhibits the ability to accomodate an extremely wide dynamic rate range, in excess of 200°/sec, and to provide moderate drift performance. Even smaller and more promising concepts are under investigation. Industrial technology is making similar advances and should also be encouraged. The cornerstone of future strapdown technology and its acceptance lies in today's instrument development and continued support is highly recommended.

APPENDIX A

MATRIX PROCESSOR

1.0 Introduction

For the six gyros, in the SIRU system, the relationship between angular rate inputs (ω) about the selected triad axes and the gyro measurements (m) is conveniently expressed in matrix form in terms of the geometry as

$$m = Hb \tag{1}$$

where

$$b^T = \begin{bmatrix} \omega_x & \omega_y & \omega_z \end{bmatrix}$$

$$m^T = \begin{bmatrix} m_a & m_b & m_c & m_d & m_e & m_f \end{bmatrix}$$

$$H^T = \begin{bmatrix} s & -s & -c & -c & o & o \\ o & o & -s & s & c & -c \\ c & c & o & o & s & s \end{bmatrix}$$

and

c = Cosine of the dodecahedron half angle
= 0.8506508083

s = Sine of the dodecahedron half angle
= 0.5257311122

Equation (1) clearly shows the redundant information of the rates about the triad axes (X, Y and Z) resident in the SIRU configuration. Data from any three gyros (accelerometers) may be used to determine the equivalent triad axis rate (acceleration).

The process structure used to obtain the equivalent triad solutions from the dodecahedron array corresponds to a weighted least squares solution form

$$b' = (H^T \psi^{-1} H)^{-1} H^T \psi^{-1} m$$

where b' is defined as the best triad solution estimate and ψ corresponds to a diagonal 6 × 6 matrix whose terms represent the individual variances. This solution provides a best estimate where both the geometric properties of the configuration and the individual instrument performance statistics are considered.

For the SIRU system, weighting of the instruments' data was not considered applicable and a status matrix λ was substituted for ψ^{-1}. All diagonal elements of λ are 1 when all instruments are performing satisfactorily, and the appropriate element is set to 0 when an instrument failure is detected.

In the actual computer mechanization, this is accomplished by storage of common constants (Kij) which are algebraically used to achieve the appropriate least squares solution based on the status of the instruments.

2.0 Implementation

To minimize computer operations, the matrix processor depicted in Figure A-1 was implemented.

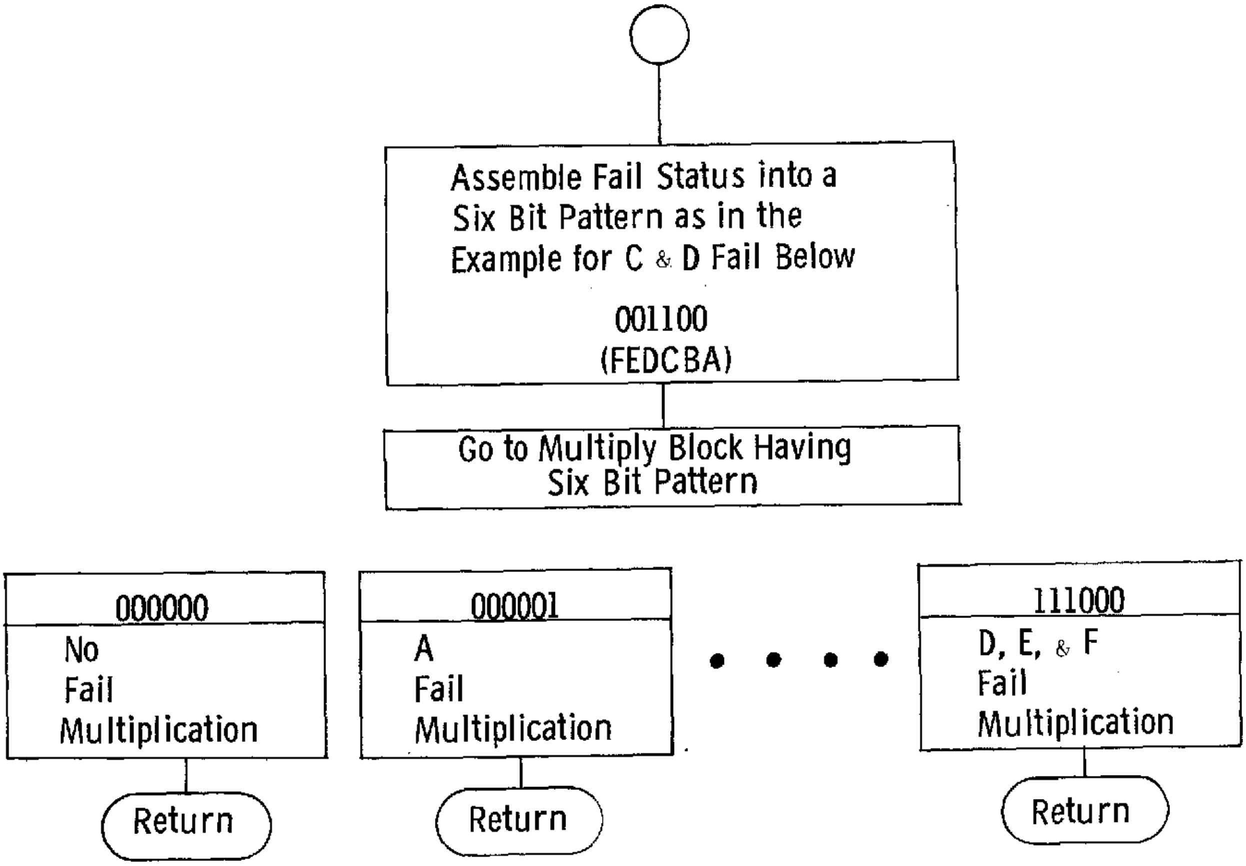

Fig. A-1 Matrix Processor

Figure A-2 presents an example of the "No Fail" multiply block with the desired matrix multiplication included for comparison. The matrix multiplication requires a total of 18 multiplys whereas the implemented method requires only 6 multiplys.

000 000

DESIRED MATRIX MULTIPLICATION:

$$\begin{bmatrix} MX \\ MY \\ MZ \end{bmatrix} = \begin{bmatrix} K1 & -K1 & -K2 & -K2 & 0 & 0 \\ 0 & 0 & -K1 & K1 & K2 & -K2 \\ K2 & K2 & 0 & 0 & K1 & K1 \end{bmatrix} \begin{bmatrix} MA \\ MB \\ MC \\ MD \\ ME \\ MF \end{bmatrix}$$

REQUIRES 18 MULTIPLYS

IMPLEMENTED:

$$MX = K1(MA - MB) - K2(MC + MD)$$

$$MY = K1(MD - MC) - K2(ME + MF)$$

$$MZ = K2(MA - MB) - K1(ME + MF)$$

REQUIRES 6 MULTIPLYS

$$K1 = \frac{S}{2} = 0.2628655561$$

$$K2 = \frac{C}{2} = 0.4253254042$$

FIGURE A-2 NO FAIL MULTIPLICATION

Figure A-3 compares the implemented manipulation with the desired matrix multiplication for an "A-gyro Fail".

000 001

DESIRED MATRIX MULTIPLICATION:

$$\begin{bmatrix} MX \\ MY \\ MZ \end{bmatrix} = \begin{bmatrix} 0 & -K4 & -K7 & -K7 & K3 & K3 \\ 0 & 0 & -K1 & K1 & K2 & -K2 \\ 0 & K8 & -K5 & -K5 & K6 & K6 \end{bmatrix} \begin{bmatrix} MA \\ MB \\ MC \\ MD \\ ME \\ MF \end{bmatrix}$$

REQUIRES 18 MULTIPLYS

IMPLEMENTED:

$$MX = -K4\ MB - K7(MC + MD) + K3(ME + MF)$$

$$MY = K1(MD - MC) + K2(ME - MF)$$

$$MZ = K8\ MB - K5(MC + MD) + K6(ME + MF)$$

REQUIRES 8 MULTIPLYS

$$K3 = s^2c/2$$

$$K4 = s^3$$

$$K5 = sc^2/2$$

$$K6 = s/2\ (c^2 + 1) = K1 + K5$$

$$K7 = c/2\ (s^2 + 1) = K2 + K3$$

$$K8 = c^3$$

FIGURE A-3 A FAIL MULTIPLICATION

As can be seen by the two examples given, this mechanization is more direct. Table A-1 summarizes the matrices, constants and multiplys for all possible combinations of failures (3 maximum).

Number of Failed Instruments	0	1	2	3	Totals
Number of Matrices	1	6	15	20	42
Number of Additional Constants	2	6	12	2	22
Number of Multiplys (Worst Case)	6	8	12	9	

TABLE A-1

MATRIX PROCESSOR SUMMARY

3.0 TABULATION OF CONSTANTS AND MATRICES

3.1 Stored Constants

K1: 0.2628655561
K2: 0.4253254042
K3: 0.1175570504
K4: 0.1453085056
K5: 0.1902113033
K6: 0.4530768594
K7: 0.5428824546
K8: 0.6155367074
K9: 0.5877852523
K10: 0.9510565163
K11: 0.0502028540
K12: 0.0812299241
K13: 0.3130684100
K14: 0.3440954801
K15: 0.3942983341
K16: 0.5065553283
K17: 0.5567581822
K18: 0.6069610362
K19: 0.63798810629
K20: 0.9820835864
K21: 0.3632712640
K22: 1.5388417686

3.2 Matrices

0 Fail

$$\begin{bmatrix} K1 & -K1 & -K2 & -K2 & 0 & 0 \\ 0 & 0 & -K1 & K1 & K2 & -K2 \\ K2 & K2 & 0 & 0 & K1 & K1 \end{bmatrix} \qquad 000000$$

1 Fail

A

$$\begin{bmatrix} 0 & -K4 & -K7 & -K7 & K3 & K3 \\ 0 & 0 & -K1 & K1 & K2 & -K2 \\ 0 & K8 & -K5 & -K5 & K6 & K6 \end{bmatrix} \qquad 000001$$

B

$$\begin{bmatrix} K4 & 0 & -K7 & -K7 & -K3 & -K3 \\ 0 & 0 & -K1 & K1 & K2 & -K2 \\ K8 & 0 & K5 & K5 & K6 & K6 \end{bmatrix} \qquad 000010$$

$$\text{C} \qquad \begin{bmatrix} K6 & -K6 & 0 & -K8 & K5 & -K5 \\ K3 & -K3 & 0 & K4 & K7 & -K7 \\ K2 & K2 & 0 & 0 & K1 & K1 \end{bmatrix} \qquad 000100$$

$$\text{D} \qquad \begin{bmatrix} K6 & -K6 & -K8 & 0 & -K5 & K5 \\ -K3 & K3 & -K4 & 0 & K7 & -K7 \\ K2 & K2 & 0 & 0 & K1 & K1 \end{bmatrix} \qquad 001000$$

$$\text{E} \qquad \begin{bmatrix} K1 & -K1 & -K2 & -K2 & 0 & 0 \\ K5 & K5 & -K6 & K6 & 0 & -K8 \\ K7 & K7 & -K3 & K3 & 0 & K4 \end{bmatrix} \qquad 010000$$

$$\text{F} \qquad \begin{bmatrix} K1 & -K1 & -K2 & -K2 & 0 & 0 \\ -K5 & -K5 & -K6 & K6 & K8 & 0 \\ K7 & K7 & K3 & -K3 & K4 & 0 \end{bmatrix} \qquad 100000$$

<u>2 Fail</u>

$$\text{A, B} \qquad \begin{bmatrix} 0 & 0 & -K9 & -K9 & 0 & 0 \\ 0 & 0 & -K1 & K1 & K2 & -K2 \\ 0 & 0 & 0 & 0 & K10 & K10 \end{bmatrix} \qquad 000011$$

$$\text{C, D} \qquad \begin{bmatrix} K10 & -K10 & 0 & 0 & 0 & 0 \\ 0 & 0 & 0 & 0 & K9 & -K9 \\ K2 & K2 & 0 & 0 & K1 & K1 \end{bmatrix} \qquad 001100$$

$$\text{E, F} \qquad \begin{bmatrix} K1 & -K1 & -K2 & -K2 & 0 & 0 \\ 0 & 0 & -K10 & K10 & 0 & 0 \\ K9 & K9 & 0 & 0 & 0 & 0 \end{bmatrix} \qquad 110000$$

$$\text{A, C} \qquad \begin{bmatrix} 0 & -K13 & 0 & -K20 & K17 & -K11 \\ 0 & -K12 & 0 & K11 & K19 & -K16 \\ 0 & K17 & 0 & -K14 & K18 & K15 \end{bmatrix} \qquad 000101$$

$$\text{A, D} \quad \begin{bmatrix} 0 & -K13 & -K20 & 0 & -K11 & K17 \\ 0 & K12 & -K11 & 0 & K16 & -K19 \\ 0 & K17 & -K14 & 0 & K15 & K18 \end{bmatrix} \quad 001001$$

$$\text{A, E} \quad \begin{bmatrix} 0 & -K11 & -K19 & -K16 & 0 & K12 \\ 0 & K14 & -K18 & K15 & 0 & -K17 \\ 0 & K20 & -K17 & -K11 & 0 & K13 \end{bmatrix} \quad 010001$$

$$\text{A, F} \quad \begin{bmatrix} 0 & -K11 & -K16 & -K19 & K12 & 0 \\ 0 & -K14 & -K15 & K18 & K17 & 0 \\ 0 & K20 & -K11 & -K17 & K13 & 0 \end{bmatrix} \quad 100001$$

$$\text{B, C} \quad \begin{bmatrix} K13 & 0 & 0 & -K20 & K11 & -K17 \\ K12 & 0 & 0 & K11 & K16 & -K19 \\ K17 & 0 & 0 & K14 & K15 & K18 \end{bmatrix} \quad 000110$$

$$\text{B, D} \quad \begin{bmatrix} K13 & 0 & -K20 & 0 & -K17 & K11 \\ -K12 & 0 & -K11 & 0 & K19 & -K16 \\ K17 & 0 & K14 & 0 & K18 & K15 \end{bmatrix} \quad 001010$$

$$\text{B, E} \quad \begin{bmatrix} K11 & 0 & -K16 & -K19 & 0 & -K12 \\ K14 & 0 & -K15 & K18 & 0 & -K17 \\ K20 & 0 & K11 & K17 & 0 & K13 \end{bmatrix} \quad 010010$$

$$\text{B, F} \quad \begin{bmatrix} K11 & 0 & -K19 & -K16 & -K12 & 0 \\ -K14 & 0 & -K18 & K15 & K17 & 0 \\ K20 & 0 & K17 & K11 & K13 & 0 \end{bmatrix} \quad 100010$$

$$\text{C, E} \quad \begin{bmatrix} K18 & -K15 & 0 & -K17 & 0 & -K14 \\ K17 & K11 & 0 & K13 & 0 & -K20 \\ K19 & K16 & 0 & K12 & 0 & K11 \end{bmatrix} \quad 010100$$

$$\text{C, F}\qquad\begin{bmatrix} K15 & -K18 & 0 & -K17 & K14 & 0 \\ -K11 & -K17 & 0 & K13 & K20 & 0 \\ K16 & K19 & 0 & -K12 & K11 & 0 \end{bmatrix}\qquad 100100$$

$$\text{D, E}\qquad\begin{bmatrix} K15 & -K18 & -K17 & 0 & 0 & K14 \\ K11 & K17 & -K13 & 0 & 0 & -K20 \\ K16 & K19 & -K12 & 0 & 0 & K11 \end{bmatrix}\qquad 011000$$

$$\text{D, F}\qquad\begin{bmatrix} K18 & -K15 & -K17 & 0 & -K14 & 0 \\ -K17 & -K11 & -K13 & 0 & K20 & 0 \\ K19 & K16 & K12 & 0 & K11 & 0 \end{bmatrix}\qquad 101000$$

<u>3 Fails</u>

$$\text{A, B, C}\qquad\begin{bmatrix} 0 & 0 & 0 & -2K9 & K21 & -K21 \\ 0 & 0 & 0 & 0 & K9 & -K9 \\ 0 & 0 & 0 & 0 & K10 & K10 \end{bmatrix}\qquad 000111$$

$$\text{A, B, D}\qquad\begin{bmatrix} 0 & 0 & -2K9 & 0 & -K21 & K21 \\ 0 & 0 & 0 & 0 & K9 & -K9 \\ 0 & 0 & 0 & 0 & K10 & K10 \end{bmatrix}\qquad 001011$$

$$\text{A, B, E}\qquad\begin{bmatrix} 0 & 0 & -K9 & -K9 & 0 & 0 \\ 0 & 0 & -K10 & K10 & 0 & 0 \\ 0 & 0 & -K22 & K22 & 0 & 2K10 \end{bmatrix}\qquad 010011$$

$$\text{A, B, F}\qquad\begin{bmatrix} 0 & 0 & -K9 & -K9 & 0 & 0 \\ 0 & 0 & -K10 & K10 & 0 & 0 \\ 0 & 0 & K22 & -K22 & 2K10 & 0 \end{bmatrix}\qquad 100011$$

$$\text{A, C, D}\qquad\begin{bmatrix} 0 & -2K10 & 0 & 0 & K22 & K22 \\ 0 & 0 & 0 & 0 & K9 & -K9 \\ 0 & 0 & 0 & 0 & K10 & K10 \end{bmatrix}\qquad 001101$$

$$\text{A, E, F} \quad \begin{bmatrix} 0 & 0 & -K9 & -K9 & 0 & 0 \\ 0 & 0 & -K10 & K10 & 0 & 0 \\ 0 & 2K9 & -K21 & -K21 & 0 & 0 \end{bmatrix} \quad 110001$$

$$\text{B, C, D} \quad \begin{bmatrix} 2K10 & 0 & 0 & 0 & -K22 & -K22 \\ 0 & 0 & 0 & 0 & K9 & -K9 \\ 0 & 0 & 0 & 0 & K10 & K10 \end{bmatrix} \quad 001110$$

$$\text{B, E, F} \quad \begin{bmatrix} 0 & 0 & -K9 & -K9 & 0 & 0 \\ 0 & 0 & -K10 & K10 & 0 & 0 \\ 2K9 & 0 & K21 & K21 & 0 & 0 \end{bmatrix} \quad 110010$$

$$\text{C, D, E} \quad \begin{bmatrix} K10 & -K10 & 0 & 0 & 0 & 0 \\ K21 & K21 & 0 & 0 & 0 & -2K9 \\ K9 & K9 & 0 & 0 & 0 & 0 \end{bmatrix} \quad 011100$$

$$\text{C, D, F} \quad \begin{bmatrix} K10 & -K10 & 0 & 0 & 0 & 0 \\ -K21 & -K21 & 0 & 0 & 2K9 & 0 \\ K9 & K9 & 0 & 0 & 0 & 0 \end{bmatrix} \quad 101100$$

$$\text{C, E, F} \quad \begin{bmatrix} K10 & -K10 & 0 & 0 & 0 & 0 \\ K22 & -K22 & 0 & 2K10 & 0 & 0 \\ K9 & K9 & 0 & 0 & 0 & 0 \end{bmatrix} \quad 110100$$

$$\text{D, E, F} \quad \begin{bmatrix} K10 & -K10 & 0 & 0 & 0 & 0 \\ -K22 & K22 & -2K10 & 0 & 0 & 0 \\ K9 & K9 & 0 & 0 & 0 & 0 \end{bmatrix} \quad 111000$$

$$\text{A, C, E} \quad \begin{bmatrix} 0 & K9 & 0 & -K22 & 0 & -K10 \\ 0 & K10 & 0 & -K9 & 0 & -K22 \\ 0 & K22 & 0 & -K10 & 0 & -K9 \end{bmatrix} \quad 010101$$

$$\text{A, C, F} \quad \begin{bmatrix} 0 & -K21 & 0 & -K10 & K9 & 0 \\ 0 & -K9 & 0 & K21 & K10 & 0 \\ 0 & K10 & 0 & -K9 & K21 & 0 \end{bmatrix} \quad 100101$$

$$\text{A, D, E} \quad \begin{bmatrix} 0 & -K21 & -K10 & 0 & 0 & K9 \\ 0 & K9 & -K21 & 0 & 0 & -K10 \\ 0 & K10 & -K9 & 0 & 0 & K21 \end{bmatrix} \quad 011001$$

$$\text{A, D, F} \quad \begin{bmatrix} 0 & K9 & -K22 & 0 & -K10 & 0 \\ 0 & -K10 & -K9 & 0 & K22 & 0 \\ 0 & K22 & -K10 & 0 & -K9 & 0 \end{bmatrix} \quad 101001$$

$$\text{B, C, E} \quad \begin{bmatrix} K21 & 0 & 0 & -K10 & 0 & -K9 \\ K9 & 0 & 0 & K21 & 0 & -K10 \\ K10 & 0 & 0 & K9 & 0 & K21 \end{bmatrix} \quad 010110$$

$$\text{B, C, F} \quad \begin{bmatrix} -K9 & 0 & 0 & -K22 & K10 & 0 \\ -K10 & 0 & 0 & -K9 & K22 & 0 \\ K22 & 0 & 0 & K10 & -K9 & 0 \end{bmatrix} \quad 100110$$

$$\text{B, D, E} \quad \begin{bmatrix} -K9 & 0 & -K22 & 0 & 0 & K10 \\ K10 & 0 & K9 & 0 & 0 & -K22 \\ K22 & 0 & K10 & 0 & 0 & -K9 \end{bmatrix} \quad 011010$$

$$\text{B, D, F} \quad \begin{bmatrix} K21 & 0 & -K10 & 0 & -K9 & 0 \\ -K9 & 0 & -K21 & 0 & K10 & 0 \\ K10 & 0 & K9 & 0 & K21 & 0 \end{bmatrix} \quad 101010$$

Appendix B

Gyro and Accelerometer Compensation Algorithms

This appendix provides a descriptive review of the gyro and accelerometer compensation algorithms.

Figure B-1 illustrates the sequence of compensation and the flow of compensated data through the matrix processor.

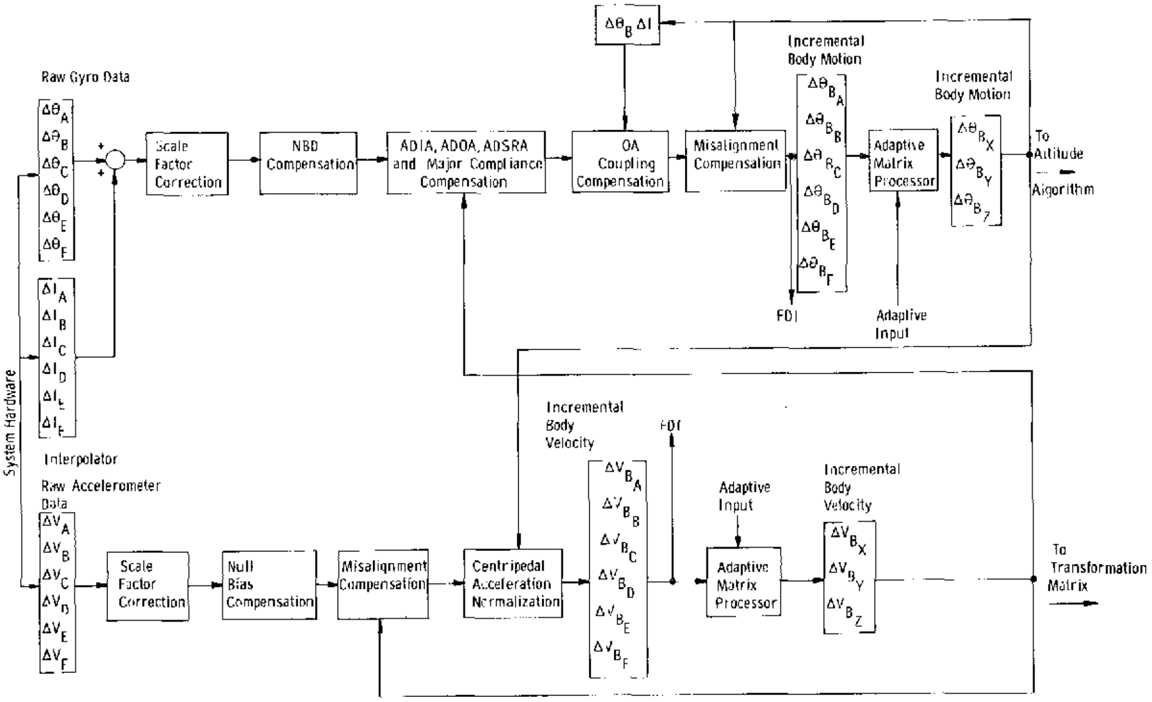

Fig. B-1 Compensation Software Flow Chart

The first step in gyro compensation adds the finer quantization information from the gyro interpolator electronics to the accumulated gyro pulses. This added information reduces the loop quantization from 44 $\widehat{\text{sec}}$ to approximately 5.5 $\widehat{\text{sec}}$ per pulse.

The resulting raw attitude data is scaled by the gyro scale factor to determine the input axis angular rotation. Scaling is accomplished by first sizing the accumulated pulses to a nominal scale factor (an even power of 2 for computational efficiency), and then, correcting for the deviation of the true scale factor from the nominal value. The scale factor correction is determined for each gyro from the calibration test data and stored in memory by a load making program.

Bias drift (NBD) is compensated with incremental corrections applied to the gyro pulse count. The magnitude of the correction is derived from the NBD calibration value (from static test) applied to the compensation iteration period.

Acceleration sensitive drift components (ADIA, ADOA, ADSRA, and major compliance) are corrected by triad referenced acceleration estimates derived from the accelerometer outputs. The gyro drift error magnitudes are calibrated using a six position procedure (discussed in Chapter 4), but are rescaled to the triad frame for compensation purposes. Thus, the accelerometer derived velocity increments in the triad frame are applied directly to effect the appropriate correction to the accumulated gyro pulses. The magnitude of correction is dependent on the drift error magnitude, the velocity increment estimate, and the iteration period. Since the correction is based on triad referenced velocity data, the compensation scheme is independent of first instrument failure and therefore is redundant.

Output axis coupling drift errors result from a lagging float motion in response to rate changes about the output axis (OA). Hence, extra torque pulses will occur to maintain the float at its null position as the gyro case is accelerated. Compensation is accomplished by using angular estimates about the OA of each gyro. These acceleration estimates are derived directly from the body triad data (XYZ) since each gyro's OA is colinear with the reference triad. The magnitude of the compensation is determined by weighing the OA rate change estimates by the gyro parameter ratio I/H (moment of inertia about OA divided by wheel angular momentum).

Spin axis cross coupling and the anisoinertia drift errors result from simultaneous rates applied about the input axis (IA) and the spin reference axis (SRA). For the 18 IRIG Mod B gyro the anisoinertia magnitude is approximately equal and of opposite effect to the spin axis cross coupling error. Thus, the two error sources cancel in the propagation of attitude errors. These error sources, while correctable, are not compensated in SIRU at this time.

Gyro misalignment angle errors are compensated by subtracting from the gyro pulse count the product of the estimated rate derived from the triad referenced vectors and the fixed misalignment (determined from dynamic test). The gyro misalignment calibration is obtained by each individual instrument referenced to the dodecahedron frame. However, for compensation purposes, the alignment magnitudes are projected to the triad configuration such that the triad derived rate estimate can be applied directly in the compensation process. The additional component of OA misalignment error, which represents the effect of float hangoff due to the applied input rate, is lumped with the dynamic error term (spin axis cross coupling) described above.

Accelerometer Compensations

The accelerometer accumulated pulse data is scaled to determine the magnitude of the velocity increment. An average scale factor, based on positive and negative acceleration input calibrations, is used.

Accelerometer bias is compensated by adding increments to the pulse count. The magnitude is based on the bias magnitude (from static test) and the duration of the compensation interval.

The accelerometer misalignment angles are fixed quantities dependent on the mounting alignment and determined by calibration tests. Misalignment errors are corrected by subtracting the estimated acceleration errors due to the misalignments from the input accelerometer pulse count.

Centripetal acceleration ($R\omega^2$) and tangential acceleration ($R\dot{\omega}$) normalization is required because of the dispersed locations of the individual accelerometers. Ideally, the mass elements of all accelerometers should be located at a single point. Since this condition is obviously impossible to obtain, corrections are introduced to account for the distance from an assumed single point to the actual location of each accelerometer mass element. The error correction is computed from this distance, the body angular rate, and the change in rate over the compensation interval. In SIRU, the A accelerometer mass element is the single point reference.

Accelerometer OA coupling, pendulous axis cross coupling and the G^2 error terms do not introduce substantial system errors and are not compensated in SIRU.

A complete software documentation package including detailed software flowgrams and descriptions is presented separately as Volume III of this report.

APPENDIX C

GYRO AND ACCELEROMETER MODULE SPECIFICATIONS

The principle parameters of the gyro and accelerometer modules as implemented for the SIRU system are specified in this appendix. They represent performance consistent with the goals contained in the original NASA Statement of Work and subsequent cost effective design tradeoffs. Design descriptions of the individual circuits and the module connector pin listings are provided in Volume II and Volume IV, respectively.

1. Gyro Module

a) Scale Factor (SF) Nominal Parameters

$\Delta\theta$ Pulse	$2^{-13} + 2^{-14} + 2^{-15}$ radians = 44.1 $\overset{\frown}{\text{sec}}$
SF Decay Characteristics	Nominal 40 ppm/decade, maximum 60 ppm/decade
Interrogation Rate (Max Pulse Rate)	4800 pps ± 1/2 ppm = F_1
Loop Torque Rate Capability	1.025 rad/sec (1.0 minimum)
Torquer Duty Cycle	$(15/16)(1/F_1)$ = 195 microseconds of 208 microseconds
Stability	0.25 rad/sec in 24 hours (15 ppm p-p)
Stabilization Time	One hour
SF Linearity	± 30 ppm p-p
SF Thermal Sensitivity	$1/2$ ppm/$^{\circ}$F
SF Voltage Sensitivities	
PVR Supply	1 ppm/.05%
40v Supply	1 ppm/1% (within ±5% range)
SF Dynamic Sensitivity	
Radial Displacement	25 ppm/rad/sec about OA
Axial or Radial g Loading	5 ppm/g

b) IA Alignment Stability

Thirty day stability with 3 room temperature cooldowns	5 $\widehat{\text{sec}}$ (rss)
Alignment Repeatability (removal and replacement)	10 $\widehat{\text{sec}}$ (rss)

c) Operational Characteristics

Power Supply Characteristics

DC	Source Level	Load (Max)	Ripple
1.	40.0 vdc ± 0.4 vdc	165 ma	$<0.43\ v_{rms}$
2.	15.000 vdc ± 0.008 vdc	11 ma	$<0.002\ v_{rms}$
3.	-10.0 vdc ± 0.5 vdc	25 ma	$<0.140\ v_{rms}$
4.	10.0 vdc ± 0.5 vdc	25 ma	$<0.140\ v_{rms}$
5.	5.25 vdc ± 0.25 vdc	140 ma	$<0.1\ v_{rms}$
6.	28 vdc ± 3 vdc	750 ma	$<0.5\ v_{rms}$
7.	28 vdc ± 0.5 vdc	55 ma	$<0.3\ v_{rms}$
8.	-20 vdc ± 1.0 vdc	25 ma	$<0.2\ v_{rms}$

b. AC

1. 9600 Hz, 8.0 v_{rms} ± 1%, 2.5 watts max, harmonic content < 2% sine wave
2. 800 Hz, 2 phase, 28 v_{rms} ± 5%, 2.6 watts max each phase, phase A leads phase B by $90^{o} \pm 0.5^{o}$, harmonic content < 20%
3. 9600 Hz and 800 Hz signals in synchronization

Timing Pulse Characteristics

Interrogate pulse	
Amplitude	4.5 ± 0.5 vdc
Width	0.4 microseconds
Repetition Rate	4.8 kpps
Switch pulse pair	
Amplitude	4.5 ± 0.5 vdc
Width	0.4 microseconds
Spacing	13 microseconds
Repetition Rate	4.8 kpps
Lag of reset pulse to interrogate pulse	2 microseconds ± 1/2 microseconds

Output Signal Requirements

$\Delta\theta$ pulses	5 vdc amplitude, 2 microseconds width
Interpolator pulses	4.5 ± 0.5 vdc amplitude, 0 to 31 pulses at 1.5 mc rate, 200 nanoseconds width, first pulse starts 10 microseconds ± 1 microsecond after interrogate pulse leading edge
Interpolator end-of-data pulse	4.5 ± 0.5 vdc amplitude, 200 nanoseconds width, 208.33 microseconds repetition rate, pulse occurs 31.34 microseconds after interrogate pulse leading edge.

Monitoring Line Identification

1. PVR power test point
2. Single ended SG monitor point, 1250 mv/milliradian of angular input about IA at 9600 Hz
3. SF resistance test point
4. Gyro temperature sensor #4, 500 ohms ± 0.5 ohms at operating temperature (+.00226 ohms/ohm/$^{\circ}$F).
5. DC amplifier test point

Auxiliary Input Requirements

1. 0 to 28 vdc at 0 to 0.4 amp (for adjustable fixed heat when used with GSE only).
2. Frequency and Timing Accuracy and Stability— All ac input voltage frequencies and input signal repetition rates are derived from a clock whose basic frequency is 3.6864000 mega Hz ± 1 part in 10^8 with a stability of ±3 parts in 10^7 per week.

Thermal Characteristics

Nominal Thermal Dissipation	21.5 watts
Thermal Dissipation Limits	17 watts to 30 watts
Nominal Average Module Mounting Pad Temperature	105°F Max p-p deviation between pads and average temperature ±3°F
Temperature Control Range	(at 70°F nominal free air ambient & 1/2 inch insulation) 60° to 110°F

2. Accelerometer Module

a) Operational Characteristics

Power Supply Characteristics

DC	Source Level	Load (Max)	Ripple
1.	28.0 vdc ± 0.3 vdc	100 ma	$0.07\ v_{rms}$
2.	15.000 vdc ± 0.008 vdc	11 ma	$0.002\ v_{rms}$
3.	-10.0 vdc ± 0.5 vdc	25 ma	$0.140\ v_{rms}$
4.	10.0 vdc ± 0.5 vdc	25 ma	$0.140\ v_{rms}$
5.	5.25 vdc ± 0.25 vdc	140 ma	$0.1\ v_{rms}$
6.	28 vdc ± 3 vdc	750 ma	$0.5\ v_{rms}$

b. AC

1. 9600 Hz, 4.0 v_{rms} ± 1%, 1.6 watts, maximum harmonic content <2%. Sine wave synchronized to interrogator pulse train.

Timing Pulse Characteristics

Interrogate pulse	
Amplitude	4.5 ± 0.5 vdc
Width	4 microseconds
Repetition Rate	4.8 kpps
Switch pulse pair	
Amplitude	4.5 ± 0.5 vdc
Width	0.4 microseconds
Spacing	13 microseconds
Repetition Rate	4.8 kpps
Lag of reset pulse to interrogate pulse	2 microseconds ± 1/2 microseconds

Output Signal Requirements

ΔV pulses 5 vdc amplitude, 2 microseconds width

Monitoring Line Identification

1. PVR power test point
2. Single ended SG monitor point—400 mv/milliradian rms about OA at 9600 Hz.
3. Scale factor resistance test point
4. Accelerometer temperature sensor #4—500 ohms ± 0.15 ohms at operating temperature (+00226 ohms/ohm/^{o}F).
5. DC amplifier test point.

Auxiliary Input Requirements

1. 0 to 28 vdc at 0 to 0.4 amps (available for adjustable fixed heat when used with GSE only).
2. Frequency and Timing Accuracy and Stability—All ac input voltage frequencies and input signal repetition rates are derived from a clock whose basic frequency is 3.6864000 mega Hz ± 1 part in 10^8 with a stability of ± 3 parts in 10^7/week.

APPENDIX D

The SIRU system software has been described in Chapters 2 and 4 of this volume. Volume III of this report contains detailed descriptions of the software, listings of the subroutines and load maps. This appendix is a precis of Volume III.

The principal programs and the tasks which each software element addresses (see Section 4.3.3) are shown in Table D-1. The indicated page number refers to the full description in Volume III. A short description of each program follows.

Table D-1 Software Program Listing

Program	Task	Page
MPRO	Main Program	7
ALPO		20
SFPOUT		31
SXOU	Output	36
SDGS		39
READ	A1, G1	43
ACOM	A2	47
GCOM		52
DCMT	G2	61
DCOA		65
ROMS	A3	69
PREX	A4	78
GARC	G3	81
GFIS		87
ERDE	G4	93
CFSE	A5	99
PFIS		112
GPRT	G5	115
PRTY		118
PPEX	A6	123
GMIN	G6	125
GPMA	A7	128
EMIN		138
MG63	G7	140
MV63	A8	146
SPUN	A9	149
VESP	A10	158
VACU	A11	169
ERC6	G8	171
AA6S	G9	174

The main executive of the system operating program (MPRO) calls the appropriate subroutines to accomplish the algorithms shown in Fig. 4.3.3 of Chapter 4 and the system tasks listed there It is divided into three sections. The first is initialization and the enabling of interrupt. Next is a waiting loop which checks to see if it is time for output and, if so, calls the proper output routines. When this waiting loop is interrupted (every 5 milliseconds), the program sequence goes to the third section which decides when the time has come to update the accelerometer or gyro algorithms, retains the processing registers as they were at the time of interrupt, calls the appropriate algorithms, restores the processing registers and returns to whatever was being processed at the time of interrupt.

The subroutines which accomplish these various activities are identified and described briefly as follows.

ALPO

ALPO provides system status information formatted as shown in Fig. 4.3.4 of Chapter 4 on teletype, CRT screen or as a block of 104 bytes on Digistore tape.

SFPOUT

SFPOUT and OUT100 provide the ALPO information in decimal numbers and seconds of time.

SXOU

This routine determines whether the ALPO information is displayed on teletype or CRT screen.

SDGS

This routine causes the information to be written onto the Digistore tape.

READ

READ causes either the gyro and accelerometer interface to interrupt the main program every 5 milliseconds. These interruptions start with the accelerometer and alternate between the accelerometer and the gyro. At each interruption the six appropriate pulse counters are read and the contents stored. Scaling is 2^{-6} pulses which represents 1 pulse ΔV as 4 cm/sec and 1 pulse $\Delta\theta$ as $7\text{x}2^{-15}$ radians.

ACOM

This subroutine compensates each accelerometer output for scale factor, bias and two misalignments.

GCOM

GCOM compensates each gyro output for SF, NBD, ADIA, ADOA, ADSRA major compliances and OA coupling.

DCMT

This subroutine modifies the misalignments of the gyro about the output axis as a function of the measured input rate at each update. The information is stored in the base sector where it is available for the gyro compensation program.

DCOA

DCOA calculates a compensation for the error resulting from the effect of a rotational input on the output gyro axis.

ROMS

When a strapdown system is subjected to a rotational input, accelerometers will sense acceleration due to $R\omega^2$ and $R\dot{\omega}$. Since the several accelerometers do not sense these rotations at the same point, they will appear to be in disagreement one to another. ROMS compensates the output to represent the origin as a single point. For convenience, the center of accelerometer A is the chosen single point which makes it necessary to compensate only the other five instruments.

GARC

This subroutine accumulates the six compensated gyro pulse counts and stores them for the squared error calculation. It also accumulates the total of the change in count for use in GFIS.

PREX

PREX accomplishes the same operation for accelerometers as GARC performs for the gyros.

GFIS

This subroutine controls the logic for the gyro FDI procedure. Once every update it decides which failure should be searched for by consideration of the gyro fail status and identification from the previous search. It then stores the maximum allowable total squared error for either the first or second failure search.

ERDE

ERDE is called up by either the gyro or accelerometer FDI logic and provides the information required to identify the failure.

CFSE

This subroutine calculates either the first or second squared error terms for instruments from the set of accumulated measurements, decides whether the total squared error exceeds a certain limit and, if it does, decides if any instruments squared error exceeds a certain percentage of the total. If the calculations show an error equalling or exceeding 2^{12} pulses or the total squared error exceeds 2^{24} an indication is provided that the calculations could not be completed due to huge errors in one or more instruments.

PRIS

This subroutine controls the logic for the accelerometer FDI procedure and is substantially the same as GFIS. The accelerometer maximum allowable squared errors are not modified prior to this operation as is the case of the gyro GFIS.

GPRT

This subroutine is a further extension of the gyro FDI. It determines the failure status and identifies the proper parity equations to solve.

PRTY

PRTY solves the proper parity equations to provide detection for a third gyro failure.

PPEX

This subroutine is the accelerometer equivalent of the PRTY routine for gyros.

GMIN

GMIN, using the gyro fail status instructions from the gyro least-squares matrix generator, calculates which of the 22 matrices to generate.

GPMA

This subroutine is the least-squares matrix generator for gyros and accelerometers.

EMIN

EMIN is the accelerometer equivalent of the gyro GMIN subroutine.

MG63

This subroutine performs the 6x3 matrix multiplications which transform the six gyro $\Delta\theta$ outputs into the XYZ frame.

MP63

MP63 is the accelerometer equivalent of the gyro MG63 subroutine.

SPUN

This subroutine corrects the quaternion to maintain it at a unity value, i.e.

$$\lambda^2 + P_x{}^2 + P_y{}^2 + P_z{}^2 = 1$$

VESP

This subroutine constructs a cosine matrix from the quaternion, transforming a vector in the body frame to the inertial frame. It then multiplies the ΔV in the body frame by this matrix to transform ΔV into the inertial frame.

VACU

VACU accumulates delta velocity in the inertial frame.

ERC6

This subroutine accomplishes the equivalent of torquing a gyro in a gimbal IMU. It essentially compensates the gyro for a drift in the inertial frame and is used to take out earth rate. It does this compensation by transforming the negative of the drift in the inertial frame into the body frame by adding it to the gyro output as an equivalent NBD.

AA6S

AA6S performs a third order attitude algorithm to update the quaternion of rotation.

SIRU BIBLIOGRAPHY

1. Weinstein, Warren D., Optimum Skew Angle Between Redundant Inertial Systems, Grumman Aerospace Corporation, Bethpage, L. I., N. Y.

2. Gilmore, J. P., A Non-Orthogonal Gyro Configuration, MIT/IL Report T-472, January, 1967.

3. Crisp, R., Gilmore, J. P., and Hopkins, A. L., SIRU—A New Inertial System Concept for Inflight Reliability and Maintainability, MIT/IL Report E-2407, May, 1969.

4. McKern, R. A., A Study of Transformation Algorithms for Use in Digital Computer, MIT/IL Report T-493, January, 1968.

5. Feldman, J., and Gilmore, J. P., The Gyroscope in Torque-to-Balance Strapdown Application, MIT/IL Report E-2392, April, 1969.

6. MIT/IL Apollo Staff, Control, Guidance, and Navigation for Advanced Manned Missions, Vol. IV Inertial Subsystems, MIT/IL Report R-600, September, 1968.

7. Lory, C. B., Compensation of Pulse-Rebalanced Inertial Instruments, MIT/IL Report T-495, January, 1968.

8. Feldman, J., Dynamic Testing of a Single Degree of Freedom Strapdown Gyroscope, MIT/CSDL Report E-2525, August, 1970.

9. Schneider, G. E., Studies on Dynamic Testing of a Single Degree Integrating Gyroscope Used in a Strapped-Down Environment, MIT/IL Report T-526, January, 1970.

10. Bukow, G. J., Alignment Optimization for Strapdown Systems, MIT/CSDL Report E-2481, January, 1970.

11. FBM/IC Staff, 18 IRIG Mod B 0420 Series Final Report, MIT/CSDL Report R-664, June, 1970.

12. Dove, D. W., A Performance Evaluation of a Strapdown Inertial Measurement Unit in the Presence of a Severe Dynamic Environment, MIT/CSDL Report T-544, January, 1971.

13. Lory, C. B., Feldman, J., and Sinkiewicz, J. S., Dynamic Testing of a Single Degree of Freedom Strapdown Gyroscope, MIT/CSDL Report E-2618, October, 1971.

14. Tze-Thong Chien, An Adaptive Technique for a Redundant-Sensor Navigation System, MIT/CSDL Report T-560, February, 1972.

15. Lory, C. B., Float Positions of Inertial Instruments Having Torque Applied in Quantum Increments, MIT/CSDL Report E-2622, December, 1971.

16. Schamp, T. A., Dynamic Errors in a Pulse-Rebalanced Single Degree of Freedom Integrating Gyroscope Undergoing Two Axis Angular Oscillations, MIT/CSDL Report T-566, June, 1973.